UNIVERSITÀ DEGLI STUDI DI PADOVA

Sede Amministrativa: Università degli studi di Padova
Dipartimento di Fisica

DOTTORATO DI RICERCA IN FISICA
CICLO XVI

"Search for multi–lepton events with the ZEUS detector at HERA"
and
"VCMVD: an algorithm for MVD tracking at TLT"

Coordinatore: Ch.mo Prof. Attilio Stella
Supervisore: Ch.mo Prof. Luca Stanco

Dottorando: Andrea Parenti

31 Ottobre 2003

A tutti coloro che mi sono stati vicini in questi anni.

L'infinito

Sempre caro mi fu quest'ermo colle,
e questa siepe, che da tanta parte
dell'ultimo orizzonte il guardo esclude.
Ma sedendo e mirando, interminati
spazi di là da quella, e sovrumani
silenzi, e profondissima quïete
io nel pensier mi fingo, ove per poco
il cor non si spaura. E come il vento
odo stormir tra queste piante, io quello
infinito silenzio a questa voce
vo comparando: e mi sovvien l'eterno,
e le morte stagioni, e la presente
e viva, e il suon di lei. Così tra questa
immensità s'annega il pensier mio:
e il naufragar m'è dolce in questo mare.

Giacomo Leopardi, *Idilli* (1819–1821)

Abstract

In the first part of this thesis I report about the search for events with two or more leptons in the final states of collisions collected by the ZEUS experiment at HERA. Multi–leptons are produced at HERA mainly through the two–photon process $ep \to e(\gamma\gamma)X \to el^+l^-X$. The cross section is very well predicted in the context of the Standard Model (SM) of particle physics, and various extensions to this model also predict production of di–leptons, therefore the search is a good test for the SM and opens a window on new physics beyond that.

121.30 pb^{-1} (101.47 pb^{-1}) of events recorded in the 1996–2000 running period were analysed for the multi–electron (di–muon) search. Good agreement was found between the ZEUS data and the expectation of the two–photon process. The total and various differential cross–sections were measured.

In the second part of the thesis I describe the development of a high level trigger which makes use of information from the new ZEUS vertex detector by updating the ZEUS tracking package into a new program. The algorithm considers tracks that have been found in the central tracker system and propagates them into the vertex detector, collecting hits and refitting track parameters.

Riassunto

Nella prima parte di questa tesi riporto i risultati della ricerca di eventi con due o più leptoni nello stato finale delle collisioni raccolte dall'esperimento ZEUS ad HERA. I multi–leptoni sono prodotti ad HERA prevalentemente nel processo a due fotoni $ep \to e(\gamma\gamma)X \to el^+l^-X$, la cui sezione d'urto è nota con grande precisione nel contesto del Modello Standard (SM) delle particelle elementari, inoltre varie estensioni al suddetto modello prevedono la produzione di di–leptoni, cosicché questa ricerca è un buon test per il SM e dà la possibilità di scoprire processi al di fuori di questo.

121.30 pb^{-1} (101.47 pb^{-1}) di eventi raccolti nella periodo di presa dati 1996–2000 sono stati analizzati per la ricerca di multi–elettroni (di–muoni). È stato trovato un buon accordo tra i dati di ZEUS e le previsioni del processo a due fotoni. La sezione d'urto totale e varie sezioni d'urto differentiali sono state misurate.

Nella seconda parte della tesi descrivo lo sviluppo di un *trigger* di alto livello che fa uso delle informazioni dal nuovo rivelatore di vertice di ZEUS, aggiornando la ricostruzione di tracce di ZEUS in un nuovo programma. L'algoritmo considera le traccie ricostruite nella camera di tracciamento centrale e le propaga all'interno del rivelatore di vertice, raccogliendo i punti da questo rivelati e ricalcolando i parametri della traccia.

Contents

Introduction

This thesis is composed by two independent parts. The first describes the study of multi–lepton production at the HERA accelerator in Hamburg.

The second part reports about the development of a high level trigger algorithm for tracking in the ZEUS Micro–Vertex Detector.

HERA (*Hadron–Elektron Ring Anlage*) is the first, and so far the only, electron–proton collider in the world. The main contribution to the production of lepton pairs at HERA comes from a pure Quantum Electro–Dynamics (QED) process, called Bethe–Heitler: a photon emitted by the electron and another photon coming from the proton (or a quark within it) are converted into a lepton–antilepton pair. This process is calculable with high precision by means of the QED. The study of lepton pair production is important because it is a good test ground for the Quantum Electro–Dynamics.

A second reason to study the process is the excess observed by the H1 experiment, also at HERA, in the number of multi–electrons produced at high–mass. The ZEUS collaboration has analysed its data in the search for di–muons and multi–electrons events, finding agreement of data and Standard Model expectation; these results were presented as preliminaries in some conferences.

With respect to the ZEUS released results, I have analysed a larger amount of the ZEUS data; the data taken in the years 1996–2000 were considered, which corresponds to almost all the available statistics. Moreover I have measured the cross section of the process. My analysis was carried on independently with respect to the one already public; my work will be the basis for the future publication of ZEUS on the di–muon and di–electron production.

The first part of the thesis is organised as follows:

- Chapter 1: the HERA physics, in particular the production of electrons and muons, is reviewed; H1 and ZEUS results for di–lepton production are reported;
- Chapter 2: the HERA accelerator and the ZEUS detector are described;
- Chapter 3: the Monte Carlo generators and the Monte Carlo samples that have been used in the analysis are enumerated;
- Chapter 4: the algorithms used for identifying electrons and muons and

for reconstructing the hadronic part of the event are presented; the event selection is also described;

- Chapter 5: the distributions of data variables are compared to the ones expected from the Standard Model processes;
- Chapter 6: the method used for the cross section measurements, and the measurements themselves, are reported; the effect of some sources of systematic uncertainties is evaluated;
- Appendix A: the trigger chains used for the di–lepton selection are described in detail;
- Appendix B: the differential cross sections presented in Chapter 6 are reported in tables.

The ZEUS experiment was originally equipped with a vertex detector, the VXD, which was removed in the 1995-96 shutdown. Since then, the closest detector to the interaction point has been the Central Tracking Detector.

In the 2000–01 shutdown a new vertex detector, the Micro–Vertex Detector (MVD) was installed in the region between the beam pipe and the CTD internal wall. The necessity arose, at this point, to update VCTRAK, the ZEUS tracking package, in a new program which was able to benefit from the information got by the newly installed detector. I had the responsibility to develop the algorithm to be used in the third level trigger.

The algorithm, called VCMVD, has been developed respecting the constraint of a "fast" execution time with respect to the existing tracking package.

The second part of the thesis is organised in this way:

- Chapter 7: an overview of VCTRAK and VCMVD is given; the formalism of a particle propagating in a magnetic field is introduced;
- Chapter 8: the MVD geometry and the effect of the inactive materials are described;
- Chapter 9: the clustering algorithm is presented;
- Chapter 10: the procedure of the pattern recognition and the update of the trajectory parameters are described;
- Chapter 11: the performances of the algorithm are shown;
- Appendix A: the data file which stores the results of the clustering, the pattern recognition and the parameter fit, is described;
- Appendix B: all the mathematical details skipped in the previous sections are reported here.

Finally a summary of the work is given.

Part I

Search for multi–lepton events with the ZEUS detector at HERA

Chapter 1

HERA Physics

In this first chapter the formalism of the *ep* interaction will be introduced. Some aspects of the scattering in the region of large 4–momentum transferred between the electron and the proton will be described, because the sensitivity to new phenomena is maximised there. In the last part of the chapter the production mechanisms of multi–leptons at HERA, and the results on multi–lepton search at the H1 and ZEUS experiments, will be reviewed.

1.1 Electron–proton scattering

In the Standard Model (SM) of particle physics the interaction between a proton and an electron (or a positron) occurs through the exchange of an electroweak vector boson. When the boson is a γ or Z^0 the process is called *Neutral Current* (NC) and the lepton is left unchanged by the interaction. The boson may also be a $W^{\pm}$; in this second case the lepton in the final state is a neutrino and the process is called *Charged Current* (CC). The inclusive process (the particles 4–momenta are indicated in parentheses),

$$e(k)\ p(P) \rightarrow l(k')\ X(P'), \tag{1.1}$$

schematically displayed in Fig. 1.1, can be described in terms of the following kinematic variables:

- the square of the centre–of–mass energy,

$$s = (P + k)^2; \tag{1.2}$$

- the square of the 4–momentum transferred by the electron (positron) to the proton, with reverse sign,

$$Q^2 = -q^2 = -(k - k')^2; \tag{1.3}$$

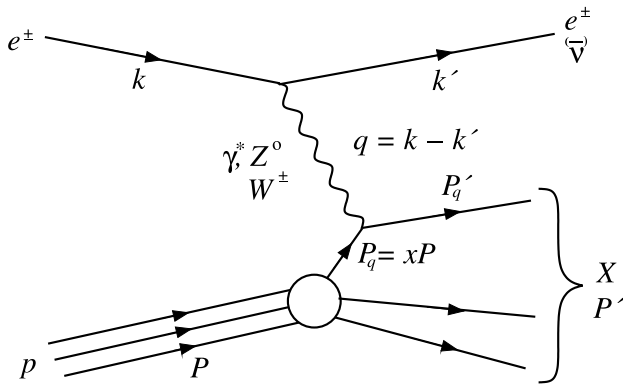

Figure 1.1: Electron–proton scattering in neutral current (γ or Z^0 exchange) and charged current ($W^{\pm}$ exchange) processes.

- the Bjorken–x variable,

$$x = \frac{Q^2}{2P \cdot q}, \tag{1.4}$$

  which, in the *infinite–momentum frame*[1], is the fraction of the proton momentum carried by the struck parton;

- the inelasticity,

$$y = \frac{P \cdot q}{P \cdot k} \simeq \frac{Q^2}{sx}, \tag{1.5}$$

  which, in the proton rest frame, is the fraction of the electron (positron) momentum transferred to the photon;

- the centre–of–mass energy W of the photon–proton system,

$$W^2 = (P + q)^2 \simeq Q^2 \frac{1 - x}{x}. \tag{1.6}$$

The kinematic variables given above are not independent. Once the centre–of–mass energy $\sqrt{s}$ is fixed, the kinematic of the event is completely determined by the knowledge of two of the other variables defined above. Usually the (x, y) or (x, Q^2) couple is chosen, from which the energy and direction of the outgoing lepton can be determined.

[1]The *infinite–momentum frame* is defined as a reference system in which the proton is moving with very high momentum, at limit *infinite*, so that the masses are negligible. In this frame the proton can be considered as a parallel stream of particles, all moving in the same direction, since the transverse momenta can be neglected. The relativistic time dilation slows down the characteristic time of the interactions between proton constituents (*partons*) so that in the scattering with the lepton they can essentially be considered as *free* particles.

Quark Type	Isospin T_3	Charge Q	"Current" Mass
u	$+\frac{1}{2}$	$+\frac{2}{3}$	$1.5 \div 4.5$ MeV
d	$-\frac{1}{2}$	$-\frac{1}{3}$	$5.0 \div 8.5$ MeV
c	$+\frac{1}{2}$	$+\frac{2}{3}$	$1.0 \div 1.4$ GeV
s	$-\frac{1}{2}$	$-\frac{1}{3}$	$80 \div 155$ MeV
t	$+\frac{1}{2}$	$+\frac{2}{3}$	174.3 ± 5.1 GeV
b	$-\frac{1}{2}$	$-\frac{1}{3}$	$4.0 \div 4.5$ GeV

Table 1.1: List of quarks and their properties.

1.1.1 The formalism of deep inelastic scattering

We usually talk about *Deep Inelastic Scattering* (DIS) when

$$Q^2 < 1 \text{ GeV}^2; \tag{1.7}$$

when this condition holds the virtual photon has a wavelength smaller or of the order of $1/Q \simeq 2 \cdot 10^{-16}$ m, i.e. less than the dimension of the proton ($\sim 10^{-15}$ m); the photon behaves like a probe of the internal structure of the proton. In the quark model introduced by Gell–Mann [1], the proton constituents are point–like spin–$\frac{1}{2}$ particles called *quarks* (q), which carry a fractional charge (in units of the positron charge e) e_q; they carry as well a *colour* charge, related to the strong interaction which keeps together the proton. The list of quarks and their properties is reported in Table 1.1 [2]. The proton is composed by three *valence* quarks (uud), plus a *sea* of $q\bar{q}$ pairs; more details on the quark content will be given in the following.

The formulae relative to the DIS can be derived from the *Quantum Electro–Dynamics* (QED) of spin–$\frac{1}{2}$ particles and the more suitable reference frame to work in is the infinite–momentum frame defined in Footnote 1; at HERA both the laboratory and the centre–of–mass frames can be classified in that category. In such a frame the interaction of the virtual photon (γ^*) with the proton constituents can be considered as *incoherent*[2]; conversely the partons, due to the relativistic time dilation, have their lifetime greatly increased and can be considered as "frozen". In this hypothesis the electron–parton scattering is identical to the scattering of an electron off a muon; this case is treated in detail in [3].

For example we can derive the cross section of the neutral current DIS. We start studying the $eq \to eq$ scattering, and we use the definition of momenta given in Fig. 1.1. The matrix element for this subprocess is

$$\mathcal{M} = -e^2 e_q \; \bar{u}(k')\gamma^\nu u(k) \; \frac{1}{q^2} \; \bar{u}(P'_q)\gamma_\nu u(P_q). \tag{1.8}$$

[2]The $\gamma^* q$ interaction becomes *incoherent* when its characteristic time is much shorter than the mean time of the interactions between partons.

If we are interested in the unpolarized cross–section, we can square and sum over electron and quark spins and over quark colours, to obtain

$$|\mathcal{M}|^2 = \frac{e^4 e_q^2}{q^4} L_e^{\mu\nu} L_{\mu\nu}^q, \tag{1.9}$$

where we have separated the electron and the quark contributions in two *currents*, $L_e^{\mu\nu}$ and $L_{\mu\nu}^q$. Using standard trace techniques and neglecting mass terms leads to

$$|\mathcal{M}|^2 = \frac{8e^4 e_q^2}{(k-k')^4} \left[(k' \cdot P_q')(k \cdot P_q) + (k' \cdot P_q)(k \cdot P_q') \right]. \tag{1.10}$$

The use of the Mandelstam variables s, t and u simplifies enormously the last equation. The Mandelstam variables for the ep scattering are defined by

$$\begin{array}{rcccccc} s & \equiv & (k+P)^2 & \approx & 2k \cdot P & \approx & 2k' \cdot P' \\ t & \equiv & (k-k')^2 & \approx & -2k \cdot k' & \approx & -2P \cdot P' \\ u & \equiv & (k-P')^2 & \approx & -2k \cdot P' & \approx & -2k' \cdot P \end{array} \tag{1.11}$$

while in the eq subprocess they are

$$\begin{array}{rcccccc} \hat{s} & = & (k+P_q)^2 & = & xs & & \\ \hat{t} & = & (k-k')^2 & = & t & = & -Q^2 \\ \hat{u} & = & (k'-P_q)^2 & = & xu & & \end{array} \tag{1.12}$$

and satisfy

$$\hat{s} + \hat{t} + \hat{u} = 0. \tag{1.13}$$

Their use makes it possible to rewrite $|\mathcal{M}|^2$ as

$$|\mathcal{M}|^2 = \frac{2e^4 e_q^2}{\hat{t}^2} (\hat{s}^2 + \hat{u}^2). \tag{1.14}$$

The matrix element can be converted to a cross section by using the standard formula for a $2 \to 2$ scattering:

$$\frac{\mathrm{d}\sigma_{eq}}{\mathrm{d}\hat{t}} = \frac{1}{16\pi \hat{s}^2} |\mathcal{M}|^2 = \frac{e^4 e_q^2}{8\pi \hat{s}^2 \hat{t}^2} (\hat{s}^2 + \hat{u}^2). \tag{1.15}$$

A double differential cross section can be obtained by using the delta function $\delta(\hat{s} + \hat{t} + \hat{u})$

$$\frac{\mathrm{d}^2\sigma_{eq}}{\mathrm{d}\hat{t}\ \mathrm{d}\hat{u}} = \frac{e^4 e_q^2}{8\pi \hat{s}^2 \hat{t}^2} (\hat{s}^2 + \hat{u}^2)\ \delta(\hat{s} + \hat{t} + \hat{u}). \tag{1.16}$$

This can be expressed in terms of s, u and t:

$$\frac{\mathrm{d}^2\sigma_{eq}}{\mathrm{d}t\ \mathrm{d}u} = \frac{2\pi\alpha^2 x e_q^2}{s^2 t^2} (s^2 + u^2)\ \delta(t + x(s+u)), \tag{1.17}$$

where $\alpha = e^2/4\pi$ is the fine–structure constant.

Let $f_i(x)$ be the density distribution, inside the proton, of quark i between x and $x + \mathrm{d}x$; we can now write the total NC ep cross section as the incoherent sum of all possible eq scatters

$$\frac{\mathrm{d}^2\sigma_{ep}^{\mathrm{NC}}}{\mathrm{d}t\ \mathrm{d}u} = \sum_i \int f_i(x) \left(\frac{\mathrm{d}^2\sigma_{eq_i}}{\mathrm{d}t\ \mathrm{d}u} \right) \mathrm{d}x. \tag{1.18}$$

Substituting (1.17) and evaluating the integral leads to

$$\frac{\mathrm{d}^2\sigma_{ep}^{\mathrm{NC}}}{\mathrm{d}t\ \mathrm{d}u} = \sum_i f_i(x) \frac{2\pi x \alpha^2 e_{q_i}^2}{s^2 t^2} \frac{(s^2 + u^2)}{s + u}. \tag{1.19}$$

An alternative approach to obtain the NC cross section is to start from (1.9), and substitute the quark tensor $L_{\mu\nu}^q$ with a proton tensor $W_{\mu\nu}$; this tensor must contain some *structure functions* because of the finite dimensions of the proton. $W_{\mu\nu}$ is defined in the most general way compatible with relativistic invariance:

$$\begin{aligned} W_{\mu\nu} &= \left(-g_{\mu\nu} + \frac{q_\mu q_\nu}{q^2} \right) F_1(x, Q^2) + \frac{\hat{P}_\mu \hat{P}_\nu}{P \cdot q} F_2(x, Q^2) - \\ &- i\epsilon_{\mu\nu\alpha\beta} \frac{q^\alpha q^\beta}{2P \cdot q} F_3(x, Q^2), \end{aligned} \tag{1.20}$$

where

$$\hat{P}_\mu = P_\mu - \frac{P \cdot q}{q^2} q_\mu, \tag{1.21}$$

ϵ is the completely antisymmetric tensor and

$$g_{\mu\nu} = \begin{pmatrix} 1 & 0 & 0 & 0 \\ 0 & -1 & 0 & 0 \\ 0 & 0 & -1 & 0 \\ 0 & 0 & 0 & -1 \end{pmatrix}. \tag{1.22}$$

The structure functions F_1, F_2 and F_3 describe the unknown structure of the proton. The antisymmetric ϵ tensor shows that the last part of $W_{\mu\nu}$ is parity violating; we will ignore F_3 for the moment, restricting the discussion to low–Q^2 neutral current events where the effects of Z^0 exchange (the parity violating part) can be neglected. The contraction of $W_{\mu\nu}$ with the leptonic tensor $L_e^{\mu\nu}$ leads to

$$\frac{\mathrm{d}^2\sigma_{ep}^{\mathrm{NC}}}{\mathrm{d}t\ \mathrm{d}u} = \frac{4\pi\alpha^2}{s^2 t^2 (s + u)} \left[(s + u)^2 x F_1(x, Q^2) - su F_2(x, Q^2) \right], \tag{1.23}$$

which can now be compared with (1.19); the comparison fixes the expressions for the structure functions:

$$F_2(x, Q^2) = \sum_i e_{q_i}^2 x f_i(x), \tag{1.24}$$

$$F_1(x, Q^2) = \frac{1}{2x} F_2(x, Q^2). \tag{1.25}$$

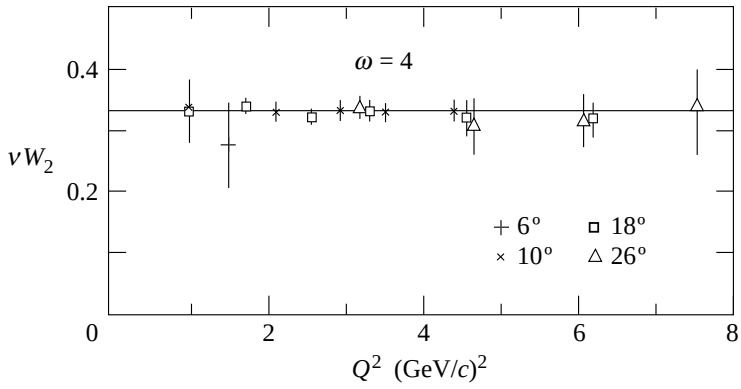

Figure 1.2: The $\nu W_2 (\equiv F_2)$ structure function at $\omega = 1/x = 4$ as a function of Q^2 as measured by the SLAC–MIT group. Data taken at four different scattering angles are shown. All data are consistent with being independent of Q^2. ν is defined by $\nu = P \cdot q / M_p$ (M_p is the proton mass) and represents the energy of the exchanged boson in the proton rest frame.

The relation between F_1 and F_2 is know as the *Callan–Gross relation* [4]. Equations (1.24)–(1.25) also imply that F_1 and F_2 are functions of x only, a phenomenon know as *scaling*. In particular, in the NC scattering,

$$\begin{aligned} F_2(x) &= x\left\{\frac{4}{9}\left[f_u(x) + f_{\bar{u}}(x) + f_c(x) + f_{\bar{c}}(x)\right] + \right. \\ &+ \left. \frac{1}{9}\left[f_d(x) + f_{\bar{d}}(x) + f_s(x) + f_{\bar{s}}(x)\right]\right\}. \end{aligned} \tag{1.26}$$

The scaling was clearly observed in the original SLAC experiments [5] as shown in Fig. 1.2, and is also clearly visible in the ZEUS data shown in Fig. 1.3 (from [6]) at similar values of x. However, when one looks at other values of x, it is clear that scaling becomes progressively more and more violated. I will analyse the reasons of this violation in the next section.

Making use of the identity

$$x \equiv \frac{Q^2}{2P \cdot q} = -\frac{t}{s+u}, \tag{1.27}$$

we can re–write (1.23) as a function of x and Q^2 as

$$\begin{aligned} \frac{\mathrm{d}^2\sigma_{ep}^{\mathrm{NC}}}{\mathrm{d}x\ \mathrm{d}Q^2} &= \frac{2\pi\alpha^2}{xQ^4}\left[2\frac{(s+u)^2}{s}xF_1(x,Q^2) - 2\frac{u}{s}F_2(x,Q^2)\right] = \\ &= \frac{2\pi\alpha^2}{xQ^4}[2xy^2F_1(x,Q^2) + 2(1-y)F_2(x,Q^2)]. \end{aligned} \tag{1.28}$$

Then, we rearrange the terms and introduce the longitudinal structure func-

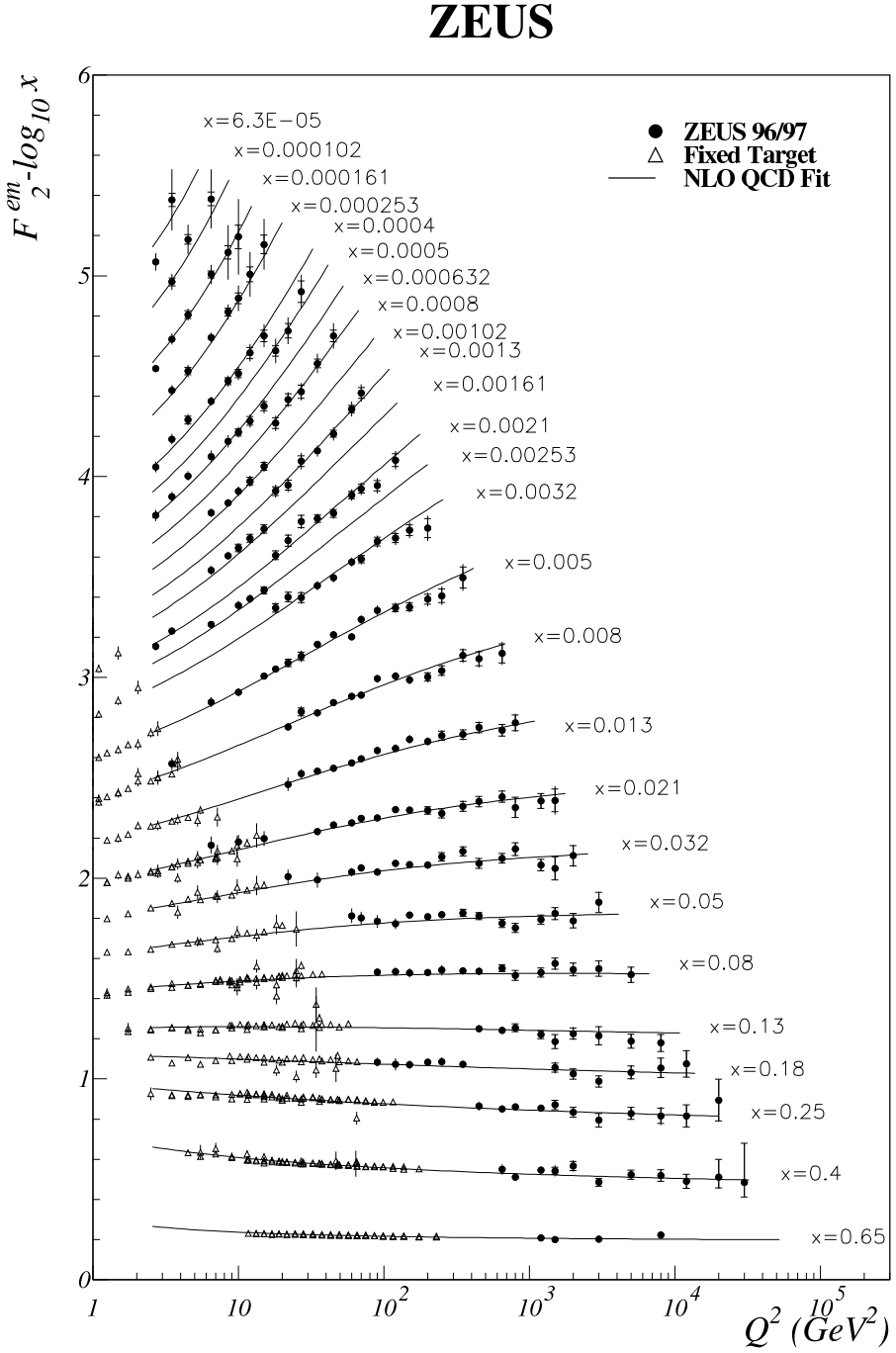

Figure 1.3: The F_2 structure function as measured by the ZEUS and some fixed target experiments as a function of Q^2. The bins centred around $x = 0.25$ are where scaling was originally observed in the SLAC experiments. Clear scaling violation is observed in the ZEUS data outside this region, particularly at lower values of x.

tion $F_L = F_2 - 2xF_1$:

$$\frac{\mathrm{d}^2\sigma_{ep}^{\mathrm{NC}}}{\mathrm{d}x\ \mathrm{d}Q^2} = \frac{2\pi\alpha^2}{xQ^4}\left\{-y^2F_L(x,Q^2) + [1+(1-y)^2]F_2(x,Q^2)\right\}. \tag{1.29}$$

The longitudinal structure function is zero in the quark–parton model since the quarks have zero transverse momentum.

Finally we re–introduce the parity–violating term to write down the most general form for the unpolarized cross–section

$$\frac{\mathrm{d}^2\sigma_{ep}^{\mathrm{NC}}}{\mathrm{d}x\ \mathrm{d}Q^2} = \frac{2\pi\alpha^2}{xQ^4}(1+\delta)\left[Y_+F_2(x,Q^2) - y^2F_L(x,Q^2) \pm Y_-xF_3(x,Q^2)\right], \tag{1.30}$$

where the $\pm$ before F_3 is taken as positive for electron scattering and negative for positron scattering, $Y_\pm$ are kinematic factors given by

$$Y_\pm = 1 \pm (1-y)^2, \tag{1.31}$$

and δ is the QED radiative correction.

The generalization of (1.24)–(1.25) which incorporates also the effect of Z^0 exchange is [7]

$$\begin{aligned}
F_1(x,Q^2) &= \frac{1}{2x}F_2(x,Q^2), & (1.32)\\
F_2(x,Q^2) &= \sum_i x[f_{q_i}(x,Q^2) + f_{\bar{q}_i}(x,Q^2)]C_{q_i}(Q^2), & (1.33)\\
xF_3(x,Q^2) &= \sum_i x[f_{q_i}(x,Q^2) - f_{\bar{q}_i}(x,Q^2)]D_{q_i}(Q^2), & (1.34)
\end{aligned}$$

where the coefficients C and D depends on the quark charges and on the electroweak couplings, V_f and A_f:

$$\begin{aligned}
C_{q_i}(Q^2) &= e_{q_i}^2 - 2e_{q_i}V_eV_{q_i}P_Z + (V_e^2+A_e^2)(V_{q_i}^2+A_{q_i}^2)P_Z^2, & (1.35)\\
D_{q_i}(Q^2) &= -2e_{q_i}A_eA_{q_i}P_Z + 4V_eA_eV_{q_i}A_{q_i}P_Z^2, & (1.36)\\
P_Z &= \frac{Q^2}{Q^2+M_Z^2}. & (1.37)
\end{aligned}$$

For $Q^2 \ll M_Z^2$, where M_Z is the mass of the Z^0 boson, $C_{q_i} \simeq e_{q_i}^2$ and $D_{q_i} \simeq 0$. V_f and A_f are the vector and axial couplings of the fermions to the Z^0, and are defined by:

$$\begin{aligned}
V_f &= T_f^3 - 2Q_f\sin^2\theta_W, & (1.38)\\
A_f &= T_f^3 & (1.39)
\end{aligned}$$

(T_f is the isospin, Q_f the electric charge, θ_W the electroweak mixing angle); they are listed in Table 1.2.

Fermion	Q_f	V_f	A_f
u, c, t	$+\frac{2}{3}$	$\left(+\frac{1}{2} - \frac{4}{3}\sin^2\theta_W\right) \simeq +0.191$	$+\ \frac{1}{2}$
d, s, b	$-\frac{1}{3}$	$\left(-\frac{1}{2} + \frac{2}{3}\sin^2\theta_W\right) \simeq -0.345$	$-\ \frac{1}{2}$
ν_e, ν_μ, ν_τ	0	$+\ \frac{1}{2}$	$+\ \frac{1}{2}$
e, μ, τ	-1	$\left(-\frac{1}{2} + 2\sin^2\theta_W\right) \simeq -0.036$	$-\ \frac{1}{2}$

Table 1.2: Couplings of fermions to the Z^0 boson. The numerical values of V_f are for $\sin^2\theta_W = 0.232$.

In the naïve quark–parton model, the proton is built up by three *valence* quarks (uud) and a *sea* of light $q\bar{q}$ pairs; when probed at a scale Q, the sea contains all the flavours with $m_{q_i} \ll Q$. For example, at the scale $\mathcal{O}(1\ \text{GeV})$, assuming that the sea is symmetric in all the quark flavours, we would have

$$f_u(x) = f_{u_V}(x) + S(x), \tag{1.40}$$
$$f_d(x) = f_{d_V}(x) + S(x), \tag{1.41}$$
$$S(x) = f_{\bar{u}}(x) = f_{\bar{d}}(x) = f_s(x) = f_{\bar{s}}(x), \tag{1.42}$$

with the sum rules

$$\int_0^1 \mathrm{d}x f_{u_V}(x) = 2, \tag{1.43}$$
$$\int_0^1 \mathrm{d}x f_{d_V}(x) = 1; \tag{1.44}$$

these equations indicate that the proton contains two u valence quarks and just one valence d. It has been found experimentally that

$$\sum_i \int_0^1 \mathrm{d}x x[f_{q_i}(x) + f_{\bar{q}_i}(x)] = \sum_i \int_0^1 \mathrm{d}x x[f_{u_V}(x) + f_{d_V}(x) + 6S(x)] \approx 0.5, \tag{1.45}$$

this implying that only half of the proton momentum is carried out by the quarks; it is a hint that other particles, electrically neutral, exist within the proton.

1.1.2 QCD evolution of structure functions

The scaling violation observed, for example, at HERA (Fig. 1.3) is explained by the *Quantum Chromo–Dynamics* (QCD), the theory of strong interactions between quarks; in this context, the interaction is mediated by a neutral, massless

particle called *gluon* (g) which carries the strong charge, the so–called *colour*. The effect of QCD on the DIS is the presence of additional Feynman diagrams of the type $\gamma^* q \to qg$ which contribute with a cross section

$$\sigma_{eq\to qg} \propto \alpha_s \ln \frac{Q^2}{\mu^2}; \tag{1.46}$$

μ being a cut–off and α_s the strong coupling constant. Let $P_{qq}(z)$ be the probability to emit a gluon with a fraction $(1-z)$ of the quark momentum; if we consider the additional contribution from (1.46), the structure function F_2 becomes

$$F_2(x,Q^2) = \sum_i x e_{q_i}^2 \int_x^1 \frac{\mathrm{d}\xi}{\xi} f_{q_i}(x,\mu^2) \left[\delta\left(1-\frac{x}{\xi}\right) + \frac{\alpha_s}{2\pi} P_{qq}\left(\frac{x}{\xi}\right) \ln \frac{Q^2}{\mu^2} \right]. \tag{1.47}$$

Therefore, the effect of the gluon emission is to introduce a Q^2 dependence in F_2. The behaviour at large Q^2 can be explained qualitatively as follows: when Q^2 becomes large the resolution of the probing photon is such that we start to see the structure of the quark. The quark, which appeared as point–like at a larger spatial scale, is now surrounded by a sea of soft gluons and quark–antiquark pairs; the momentum of the valence quark is shared between all these soft particles and the low–x region is enhanced against the high–x region.

If we define $t \equiv \mu^2$ and take the $\ln(t)$ partial derivative of (1.47) we obtain

$$t\frac{\partial}{\partial t} f_{q_i}(x,t) = \frac{\alpha_s(t)}{2\pi} \int_x^1 \frac{\mathrm{d}\xi}{\xi} P_{qq}\left(\frac{x}{\xi}\right) f_{q_i}(x,t). \tag{1.48}$$

That is known as *Dokshitzer–Gribov–Lipatov–Altarelli–Parisi* (or DGLAP) *equation* [8] and is one of the most important in perturbative QCD. The derivation given above is not completely rigorous, but more precise treatments based on the renormalisation group equation give the only difference that $P_{qq}(z)$ is substituted by a perturbative expansion in powers of the running coupling constant α_s

$$P_{qq}(z,\alpha_s) = P_{qq}^0(z) + \frac{\alpha_s}{2\pi} P_{qq}^1(z) + ... \tag{1.49}$$

More generally, DGLAP equation is a $(2n_f+1)$–dimensional matrix equation in the space of quarks (n_f being the number of quark flavours), antiquarks and gluons,

$$\begin{aligned} t\frac{\partial}{\partial t} \begin{pmatrix} f_{q_i}(x,t) \\ f_g(x,t) \end{pmatrix} &= \frac{\alpha_s(t)}{2\pi} \sum_j \int_x^1 \frac{\mathrm{d}\xi}{\xi} \\ \times \begin{pmatrix} P_{q_iq_j}(x/\xi,\alpha_s(t)) & P_{q_ig}(x/\xi,\alpha_s(t)) \\ P_{gq_j}(x/\xi,\alpha_s(t)) & P_{gg}(x/\xi,\alpha_s(t)) \end{pmatrix} &\begin{pmatrix} f_{q_i}(x,t) \\ f_g(x,t) \end{pmatrix}. \end{aligned} \tag{1.50}$$

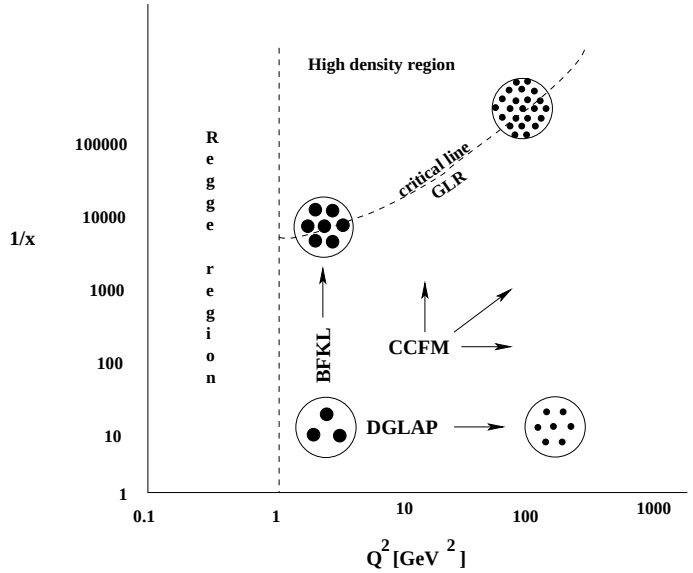

Figure 1.4: Schematic diagram showing different regions of the $\ln(1/x)$–$\ln(Q^2)$ plane and the evolution equations expected to hold therein. The "size" and density of partons within the proton are also indicated in different kinematic regions.

These equations are usually solved by numerical integration.

The validity of the DGLAP evolution is limited to the region away from small x; in fact the splitting functions contain logarithms $\ln(1/x)$, neglected for example in (1.49), which become important and spoil convergence as $x \to 0$:

$$xP(x,\alpha_s) = \sum_{n=0}^{\infty} \left(\frac{\alpha_s}{2\pi}\right)^n \left[\sum_{m=0}^{n} A_m^{(n)} \left(\ln\frac{1}{x}\right)^m + x\bar{P}^{(n)}(x)\right] \tag{1.51}$$

($A_m^{(n)}$ are coefficients, and the splitting functions $\bar{P}^{(n)}$ are finite for $x \to 0$).

As can be seen in Fig. 1.4 more approaches are available to describe the evolution in different kinematic regions; for example the BFKL equations (Balitsky–Fadin–Kuraev–Lipatov, [9, 10, 11, 12]) hold at low–x, while the CCFM equations (Ciafaloni–Catani–Fiorani–Marchesini, [13, 14, 15]) are derived in a more general approach, and both DGLAP and BFKL can be regarded as a special case of them.

On the figure some schematic indications of the "size" and density of partons in the proton in different kinematic regions are shown.

1.2 High–Q^2 phenomena

We now proceed by illustrating the new aspects of DIS provided by the last generation of colliders, in particular the HERA one.

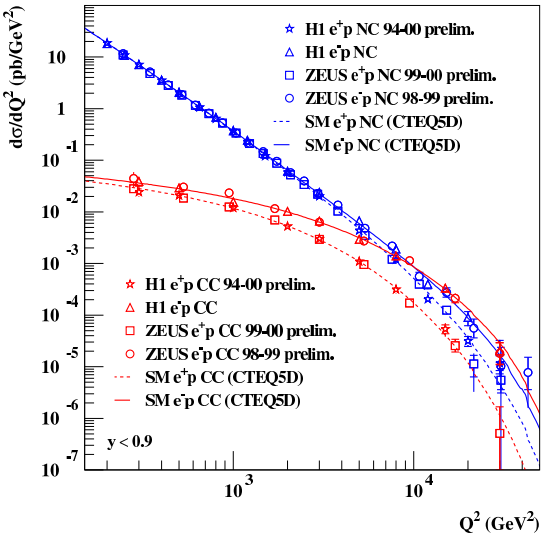

Figure 1.5: Differential cross section, as a function of Q^2, for charged and neutral current scattering of $e^{\pm}$ off protons. Experimental points are from H1 and ZEUS experiments.

HERA provides the unique opportunity to inspect QED in the region where the charged and neutral current interactions have a similar strength. In Fig. 1.5 the differential cross section as a function of Q^2, as measured by H1 and ZEUS experiments at HERA, is shown. In the $e^- p$ scattering the NC and CC have a comparable cross section from around $Q^2 = M_Z^2 \sim 10^4$ GeV^2; in the $e^+ p$ interaction the CC is everywhere below the NC.

This can be understood by comparing the differential cross sections for the CC processes:

$$\left.\frac{\mathrm{d}^2\sigma}{\mathrm{d}x\mathrm{d}Q^2}\right|_{e^-p}^{\mathrm{CC}} = \frac{G_F^2}{2\pi}\left(\frac{M_W^2}{M_W^2+Q^2}\right)^2 \times 2x\left\{f_u(x)+f_c(x)+(1-y)^2[f_{\bar{d}}(x)+f_{\bar{s}}(x)]\right\}, \quad (1.52)$$

$$\left.\frac{\mathrm{d}^2\sigma}{\mathrm{d}x\mathrm{d}Q^2}\right|_{e^+p}^{\mathrm{CC}} = \frac{G_F^2}{2\pi}\left(\frac{M_W^2}{M_W^2+Q^2}\right)^2 \times 2x\left\{f_{\bar{u}}(x)+f_{\bar{c}}(x)+(1-y)^2[f_d(x)+f_s(x)]\right\}. \quad (1.53)$$

There are two reasons why (1.52) is greater than (1.53); the first is that the density of the quark u in the proton is greater than the one of the quark d (there are two u valence quark but only one d); the second is that in the e^+ case, the term involving the quark d is suppressed by the factor $(1-y)^2$, due to the $V-A$ structure of the weak interaction.

The different behaviour of e^+ and e^- in the neutral current scattering allows to obtain the parity violating structure function xF_3 (see, for example, [16]).

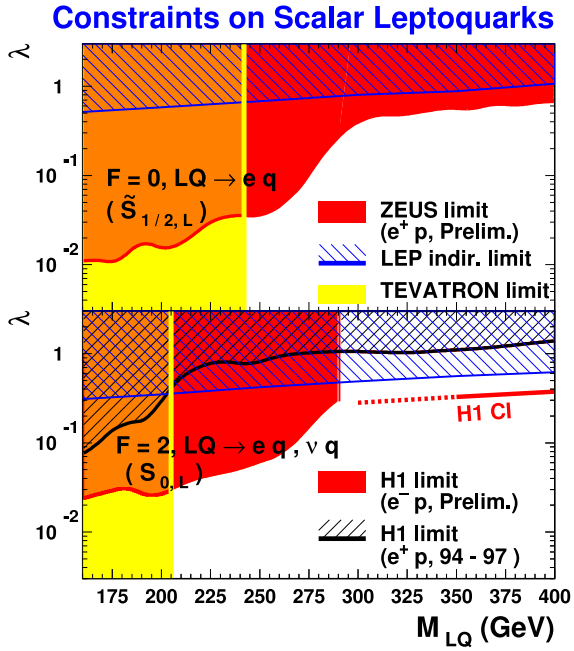

Figure 1.6: Limits on the coupling constant λ of leptoquarks to ordinary leptons and quarks, as a function of the leptoquark mass. $F \equiv L + 3B = 0, 2$ is the fermion number. H1, ZEUS, LEP and TEVATRON results are shown.

The interest of the high–Q^2 region is also due to the fact that possible new states from electron–quark fusion (leptoquarks, or squarks in $\not{R}_P$ SUSYs) are expected to have high mass and therefore high Q^2 (since $Q^2 \simeq yxs = yM$); another reason is that the sensitivity to the effect of new currents is maximised at high Q^2. An example of the sensitivity of HERA is given in Figure 1.6, where the limit on the coupling constant λ of leptoquarks to the ordinary leptons and quarks is shown, as a function of the leptoquark mass. H1 and ZEUS reach similar results, and HERA has a higher sensitivity than LEP and TEVATRON.

Beyond the possibility to set limits on new phenomena, HERA furnished as well some unexpected results which may be signatures of new physics. For example, both H1 and ZEUS showed an excess in the number of neutral current events recorded in 1994–96 [17, 18].

H1 observed 12 neutral current events with $Q^2 > 15000$ GeV^2, whereas 4.71 ± 0.76 were expected (Fig. 1.7); the probability to observe 12 or more events were 6×10^{-3}. ZEUS observed 2 events with $Q^2 > 35000$ GeV^2, whereas 0.145 ± 0.013 were expected (see Fig. 1.8).

A second example of a search in which an excess was found, is the one done by H1 for events with isolated charged leptons and large missing momentum in the final state. In 1994–2000 e^+p collisions, H1 found 8 events while 2.55 (with low uncertainty) were expected from SM processes [19].

The last example is more strictly related to the topic of this thesis. H1 analysed 1994–2000 collisions in the search for multi–electron events [20]; they found

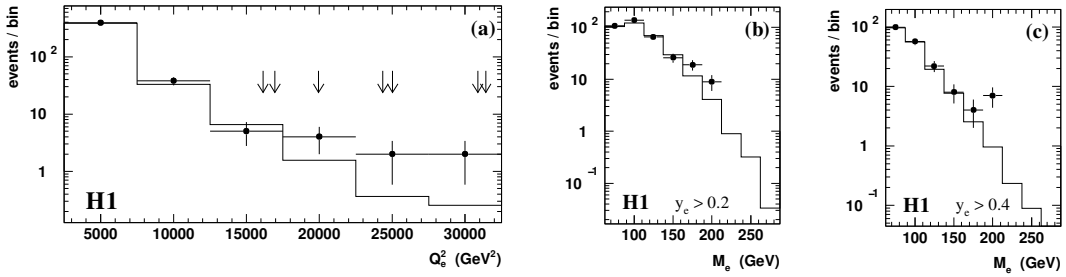

Figure 1.7: (a) Q^2 distribution of NC–DIS events at H1 (1994–96); dots (•) represents data, histogram is the Monte Carlo expectation. Invariant mass distribution of the eq system, with the cuts $y > 0.2$ (b) and $y > 0.4$ (c).

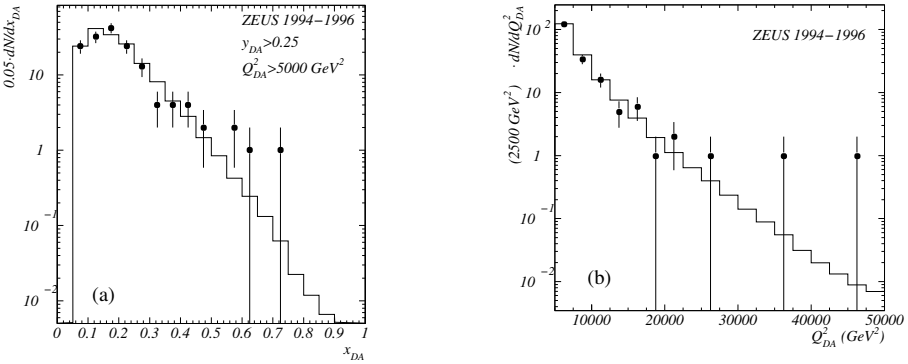

Figure 1.8: (a) The $x(= M_{eq}/s)$ distribution of NC–DIS events at ZEUS (1994–96), and (b) the Q^2 distribution of the same events.

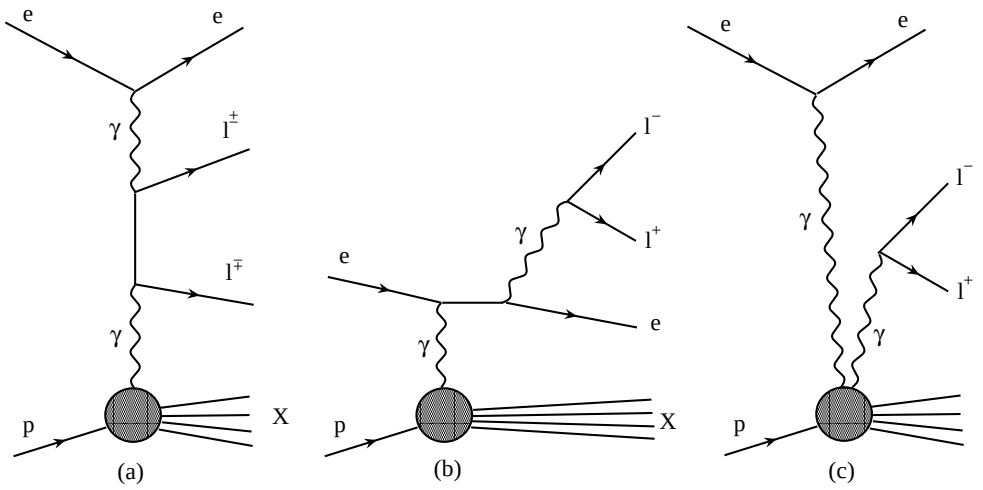

Figure 1.9: The three types of leading order graphs for lepton pair production in *ep* interactions: (a) Two photon (or Bethe–Heitler) process, (b) Cabibbo–Parisi type (radiation of a massive lepton pair from the electron line) and (c) the corresponding graph for the radiation from the proton side.

3 events with 2 electrons of invariant mass $M_{12} > 100$ GeV (they expected 0.30 ± 0.04 from SM) and 3 events with 3 electrons and $M_{12} > 100$ GeV (with an expectation of 0.23 ± 0.04).

1.3 Lepton pair production at HERA

Lepton pairs are produced at HERA via non–resonant electroweak processes, and through the decay of vector meson resonances; moreover single leptons are produced by decays of heavy quarks, τ leptons and $W^{\pm}$ bosons. The electroweak contribution is dominant in the integrated cross section.

1.3.1 Electroweak production

In between the non–resonant diagrams, the predominant contribution comes from the *two photon* or Bethe–Heitler process, Fig. 1.9a; the process took the name after Bethe and Heitler made the first calculations [21] of lepton pair production by an electron in the field of a fixed target nucleon. At the same time Landau and Lifshitz did the same [22] in Moscow.

The second type diagram (Fig. 1.9b) corresponds to the QED–Compton–like radiation of a lepton pair from the initial or final state electron; this diagram is usually called "Cabibbo–Parisi", after their attempts to interpret this kind of events in an ADONE experiment [23]. Some authors also call it Compton–like or radiative lepton pair conversion or virtual bremsstrahlung.

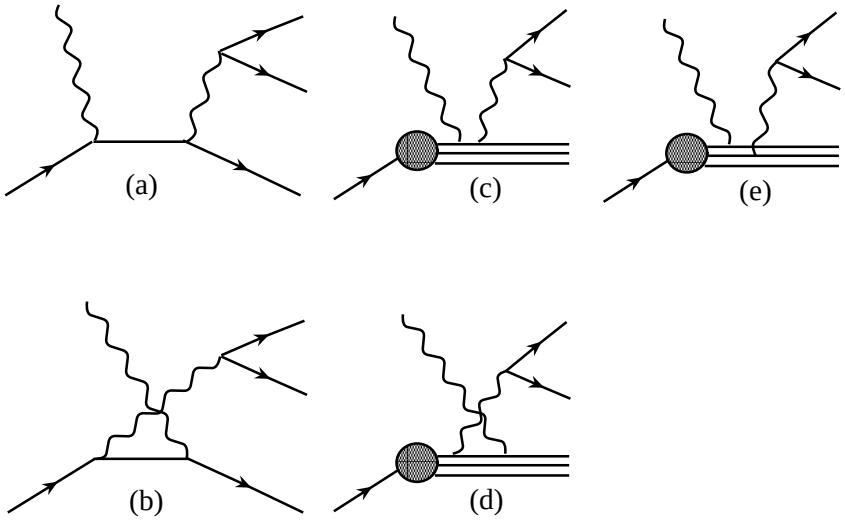

Figure 1.10: Diagrams for lepton pair production on the proton side: (a) and (b) are elastic (coherent) interactions with the entire proton, (c)–(e) are interactions with a parton within the proton.

The diagram in Fig. 1.9c represents the generation of a lepton pair from the photon radiated from the proton or quark line. For the latter, due to the composite structure of the proton, there are five possible graphs, as depicted in Fig. 1.10: in (a) and (b) the scattering is elastic (coherent) and the proton remains intact; the diagrams (c)–(e) show the interaction of the photon with a parton within the proton. Figure 1.10e represents a higher twist diagram: the emission of the lepton pair from the "middle" quark requires an additional interaction (e.g. a gluon exchange with another quark). The remaining diagrams, (c) and (d), represent the main contribution and are referred to as Drell–Yan type reactions; however these processes, which would offer the theoretical possibility to probe parton densities, are much suppressed at HERA. This is not true at pp or $p\bar{p}$ colliders, where the Drell–Yan dominates the lepton pair production. In addition to the diagrams depicted in Figs. 1.9 and 1.10, QED foresees three times more diagrams: they can be obtained by substituting one or both the photons with a Z^0.

Arteaga–Romero, Carimalo and Kessler have calculated the contribution of the three more important processes [24]. They made use of the equivalent photon approximation (EPA, [25]) to compute the vertices like $e \to e\gamma$ and $\gamma \to l^+l^-$, and in the Cabibbo–Parisi term they took into account the effect of the Z^0 exchange. The total transverse momentum of the lepton pairs is null ($p_T^{l^+} = p_T^{l^-}$) due to the collinear approximation of the central process. A summary is presented in Figure 1.11 (from [26]), where the cross sections as a function of the single lepton transverse momentum p_T are shown.

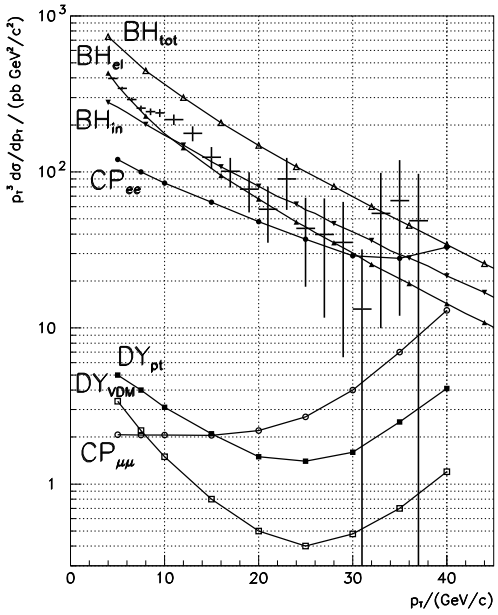

Figure 1.11: Contribution of the different processes to the differential cross section of lepton pair production at HERA. The cross section is presented as a function of the single lepton transverse momentum p_T. The curves represent: Bethe–Heitler (BH), elastic (el), inelastic (in) and total (tot), Cabibbo–Parisi (CP) and Drell–Yan (DY); the latter is divided into a point–like (pt) and a Vector Meson Dominance (VDM) contribution from the photon structure. For $p_T < 25$ GeV, CP and DY are negligible. For comparison the p_T distribution of a Monte Carlo simulation (LPAIR) of the elastic BH is shown (crosses).

Resonance	Mass [GeV]	BR($\rightarrow e^+e^-$) [%]	BR($\rightarrow \mu^+\mu^-$) [%]
J/ψ	3.09687	5.93 ± 0.10	5.88 ± 0.10
$\Upsilon(1s)$	9.46030	2.38 ± 0.011	2.48 ± 0.06
$\Upsilon(2s)$	10.02326	1.34 ± 0.20	1.31 ± 0.21
$\Upsilon(3s)$	10.3552	seen	1.81 ± 0.17

Table 1.3: Vector mesons decaying in lepton pairs. The masses and the branching ratios into e^+e^- and $\mu^+\mu^-$ are given.

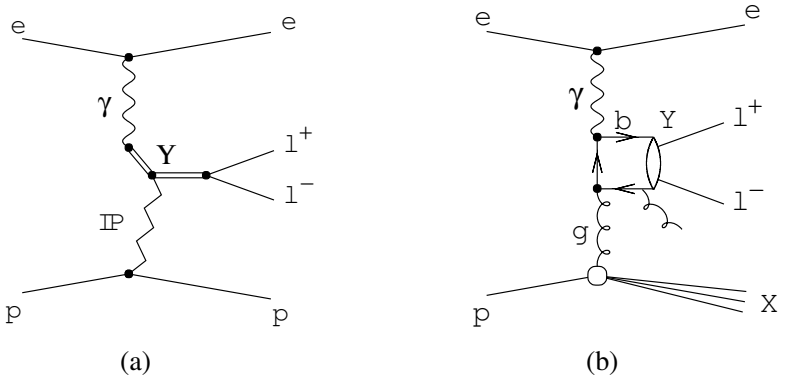

Figure 1.12: Mechanisms of production of vector mesons. On the left the diffractive process is shown, while on the right the inelastic process is sketched out.

1.3.2 Vector mesons decays

The production of lepton pairs may take place at HERA via the decay of a vector meson resonance, J/ψ or Υ (Table 1.3, from [2]). In turn, the vector meson may be produced via diffraction, Fig. 1.12a, or by photon–gluon fusion, Fig. 1.12b. In the diffractive production, the exchanged photon fluctuates into a meson, which interacts with the proton under the exchange of a colourless object, the *pomeron*. In QCD this object can be realized by the exchange of two gluons. Since we are interested to the region where the mass of the di–lepton is high, only the contribution from the Υ (interpreted as a $b\bar{b}$ bound state), has to be considered.

1.4 Single muon production at HERA

1.4.1 Boson–Gluon fusion

The production of a heavy quark via boson–gluon fusion, which leads to the production of a pair of heavy quarks q–$\bar{q}$, is shown in Fig. 1.13; each heavy quark can decay into a lighter quark q' ($\bar{q}'$) and a W boson, which may subsequently decay semi–leptonically into a charged lepton–neutrino couple. The branching ratio of W into leptons is quite high: $BR(W^+ \rightarrow l^+\nu_l) = (10.68 \pm 0.12)\%$, the

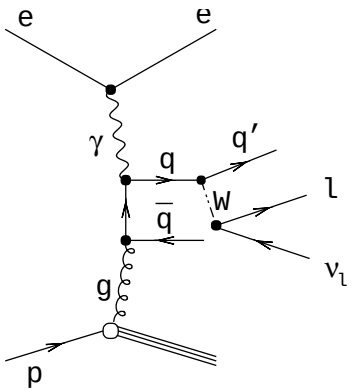

Figure 1.13: Boson–gluon fusion followed by a semi–leptonic decay of the heavy quark.

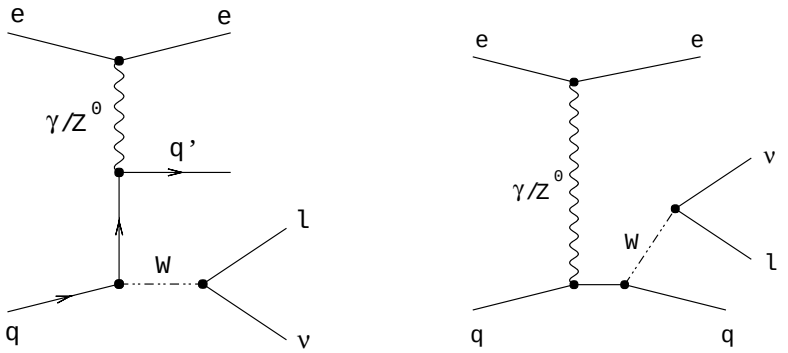

Figure 1.14: Dominating Feynman diagrams for the W production at HERA.

same for the charge conjugate.

The dominant contributions are $b \to cW^-$ and $c \to sW^+$, whereas the decay $b \to uW^-$ is suppressed because of the smallness of the element V_{ub} of the CKM matrix.

Additional contributions come from the cascade decays initiated by a b quark ($b \to cW^-$) and followed by a semi–leptonic decay of the daughter quark ($c \to sW^+ \to sl^+\nu_l$), or by the conversion of the W boson into light quarks which in turn decay semi-leptonically ($W^- \to \bar{c}s$, $\bar{c} \to \bar{s}W^- \to \bar{s}l^-\bar{\nu}_l$).

If both the produced quarks decay semi-leptonically, two leptons are found in the final state.

1.4.2 W–production at HERA

W production at HERA can take place via neutral or charged current interactions:

- $e^{\pm}p \to e^{\pm}W^{\pm}X$,
- $e^+p \to \bar{\nu}_e W^+X$ and $e^-p \to \nu_e W^-X$.

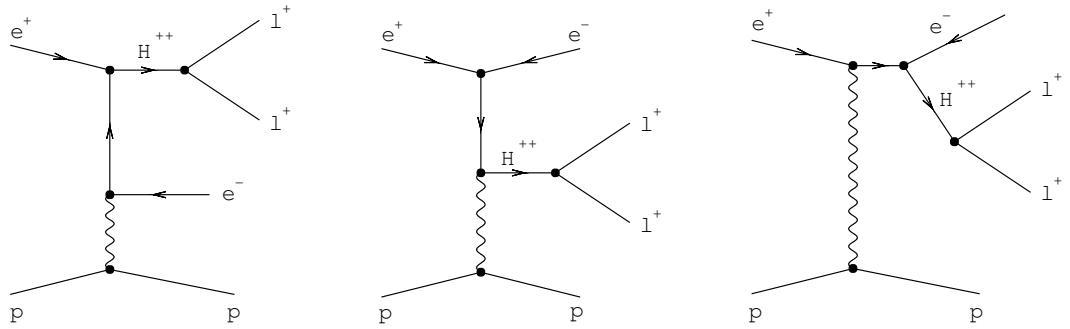

Figure 1.15: Feynman diagrams for doubly charged Higgs production at HERA.

The neutral current interactions dominate the cross section ($\sigma_{\rm NC} \sim 1.0 \div 1.3$ pb, [27]); in particular the main diagrams are depicted in Fig. 1.14.

These diagrams, in which a real W boson is emitted from the incoming or outgoing quark line, have the same topology as the Z^0 production in the Drell–Yan mode. The other processes are largely suppressed due to the large mass of the boson in the propagator.

1.4.3 τ decays

τ leptons, which are produced in two photon collisions (Fig. 1.9a), decay into muons and electrons with high branching ratios: $BR(\tau^- \to \mu^- \bar{\nu}_\mu \nu_\tau) = (17.36 \pm 0.05)\%$ and $BR(\tau^- \to e^- \bar{\nu}_e \nu_\tau) = (17.84 \pm 0.06)\%$.

If both the taus decay into leptons, two leptons (ee, $e\mu$ or $\mu\mu$) are present in the final state. In τ decays mainly low momenta leptons are produced.

1.5 Beyond the Standard Model

Various extensions to the Standard Model predict the production of equally charged lepton pairs. This appears as a promising discovery channel especially in the muon channel, which is almost background free, whereas in the electron channel the electron from the beam can be detected together with the like–sign electron from the SM process, giving the same signature as the non–standard reaction.

1.5.1 Doubly charged Higgs

Supersymmetric left–right models (SUSYLR) deserve attention since they solve many theoretical problems: they imply baryon and lepton number conservation, solve the CP problem of the Minimal Supersymmetric Standard Model (MSSM) and implement the see–saw mechanism by giving heavy mass to the right–hand Majorana neutrino [28]. In these theories right or left–handed Higgs triplets

$H_{R,L} = (H^0_{R,L}, H^+_{R,L}, H^{++}_{R,L})$ are introduced, which contain the doubly charged Higgs particle H^{++}. In Fig. 1.15 the Feynman diagrams for doubly charged Higgs production at HERA [29, 30] are depicted.

At HERA energies the doubly charged Higgs decay dominantly into lepton pairs; in principle there exist two leptonic decay modes: one which produces two leptons of the same flavour and one with two leptons of different flavour ($H^{++} \to e^\pm\mu^\pm, e^\pm\tau^\pm, \mu^\pm\tau^\pm$) in the final state. The muonium experiment [31] disfavours the latter decay mode. Limits for the same flavour decay mode stem from OPAL [32], which has excluded doubly charged Higgs with masses below 98.5 GeV at 95% C.L. Discovery potential is left for a doubly charged Higgs with a mass $M_{H^{++}} > 100$ GeV.

1.6 The study of lepton-pair production

The lepton pair production has been studied by the H1 and ZEUS collaborations, which presented preliminary results at the ICHEP 2002 conference [33]. H1 results on multi–electron production [20] have subsequently been submitted to the European Physical Journal. ZEUS results have been obtained by scientists in the collaboration other than me; my results, which have been derived independently and represent an extension of the ICHEP ones, will be presented in Chapters 5 and 6.

1.6.1 Multi–electron search at H1

All data recorded in years 1994 to 2000 by the H1 experiment (115.2 pb^{-1}), were analysed in the search for multi–electrons.

The electroweak di–electron production was simulated by the GRAPE Monte Carlo (see Sect. 3.2). The main experimental backgrounds are processes in which, in addition to the true electron, one or more fake electrons are reconstructed in the finale state. The dominant contribution comes from the NC DIS ($ep \to eX$), where hadrons or radiated photons are misidentified as electrons. The QED Compton scattering ($ep \to e\gamma X$) can also contribute if the photon is incorrectly identified as an electron.

The electron candidates are searched between electromagnetic deposits in the calorimeter, which are selected by a pattern recognition algorithm based on the geometrical profiles expected for electrons. The following requirements are applied to these candidates:

- $E_e > 5$ GeV;
- $5^\circ < \theta_e < 175^\circ$;
- $D^\mu_{\text{Trk,Jet}} > 0.5$[3];

[3] $D^\mu_{\text{Trk,Jet}}$ is the distance of the electron to the nearest track (or jet) in the CTD in the $\eta\phi$

Type	Data	SM	GRAPE	DIS + QEDC
All $2e$	108	117.1 ± 8.6	91.4 ± 6.9	25.7 ± 5.2
$2e$ and $M_{12} > 100$ GeV	3	0.30 ± 0.04	0.21 ± 0.03	0.09 ± 0.02
All $3e$	17	20.3 ± 2.1	20.2 ± 2.1	0.1 ± 0.1
$3e$ and $M_{12} > 100$ GeV	3	0.23 ± 0.04	0.23 ± 0.03	< 0.02
"$\gamma\gamma$" subsample	42	44.9 ± 4.2	43.7 ± 4.2	1.2 ± 0.4

Table 1.4: Observed and predicted multi–electron yields at H1. The errors on the predictions include model uncertainties and experimental systematic errors added in quadrature.

- an hadronic energy less than 2.5% of E_e, in a cone of radius $R_{\eta\phi} = 0.75$ in the $\eta\phi$ plane centred around the electron.

For central electrons ($20^\circ < \theta_e < 150^\circ$) a track matched to the calorimetric deposit (both geometrically and in energy) is required, and no tracks other than the electron itself in a radius $R_{\eta\phi} = 0.5$ around the deposit position. For forward electrons ($\theta_e > 150^\circ$) the energy threshold was raised to 10 GeV in order to reduce the fake electrons arising from hadrons in DIS events.

In the final selection at least two central electrons, one with $P_T^{e1} > 10$ GeV and the other one with $P_T^{e2} > 5$ GeV, were required. In Table 1.4 the number of events with two ($2e$) and three ($3e$) electrons is shown, for data and expectations from of the Standard Model; the agreement is good at low invariant mass M_{12} of the two highest–P_T electrons, whereas a modest excess is observed at high mass: three $2e$ and three $3e$ events are observed with $M_{12} > 100$ GeV, while the SM expectation is less than one. The distribution of events as a function of M_{12} and the correlation of M_{12} and the sum of electron's P_T are shown in Fig. 1.16.

All six events with $M_{12} > 100$ GeV occurred in e^+p collisions, and were studied in detail by H1. The electromagnetic shower shapes were found to be similar to those expected from the calorimeter response to electrons. All central tracks yield a specific ionisation in the central drift chamber as expected for single electrons. The measurements of the central electron momenta by the tracker and the calorimeter are compatible within the resolution. The forward electron candidates in the $3e$ events have at least one track pointing to the calorimetric energy cluster, although no such requirement is made in the identification procedure. For all the events the measurement of track charges is compatible with a presence of one e^- and two e^+ in the final state, as expected from pair production processes. The masses M_{12} are incompatible with the hypothesis of six high mass events coming from a narrow resonance; the same is true, in the $3e$ events, for the invariant mass M_{123} of the tri–electron.

plane. η is the pseudorapidity, related to the polar angle by $\eta = -\ln\tan(\theta/2)$.

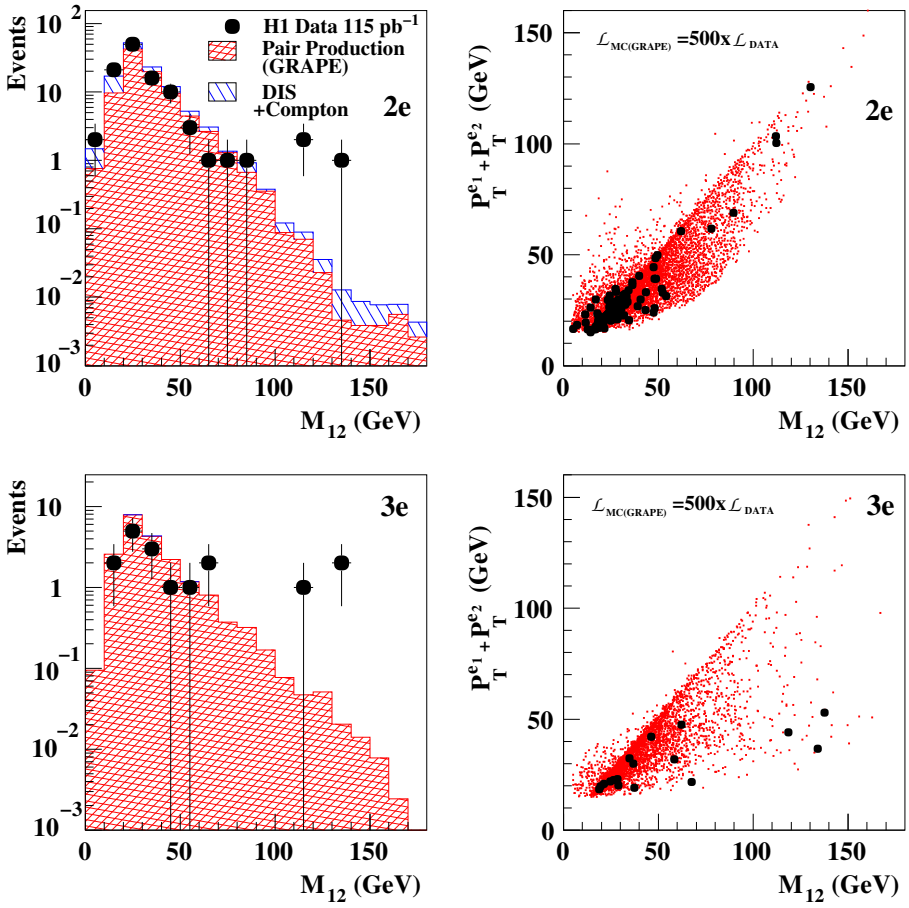

Figure 1.16: Distribution of the invariant mass M_{12} of the two highest–P_T electrons (left) and correlation of M_{12} with the scalar sum of the P_T of the electrons (right) for events classified as "2e" (top) and "3e" (bottom).

Cross section measurement

A subsample of the 2e sample labelled $\gamma\gamma$, was selected in order to measure the pair production in a well defined phase space region dominated by photon–photon collisions with low background. In this subsample, the two electrons had to be of opposite charge and a significant deficit compared to the initial state had to be observed in the difference $(E - P_z)$ of the energy and longitudinal momentum of all visible particles ($E - P_z < 45$ GeV[4]). These two conditions ensure that the incident electron is lost in the beam pipe after radiating a quasi–real photon of squared four–momentum Q^2 lower than 1 GeV^2. Summarizing, the phase space

[4]For fully contained events or events where only longitudinal momentum along the proton direction ($+z$) is undetected, one expects $E - P_z = 2E_e^0 = 55.2$ GeV, where E_e^0 is the energy of the incident electron. If the scattered electron is undetected, the threshold $E - P_z < 45$ GeV corresponds to a cut on the fractional energy loss $y = (E - P_z)/2E_e^0 < 0.82$.

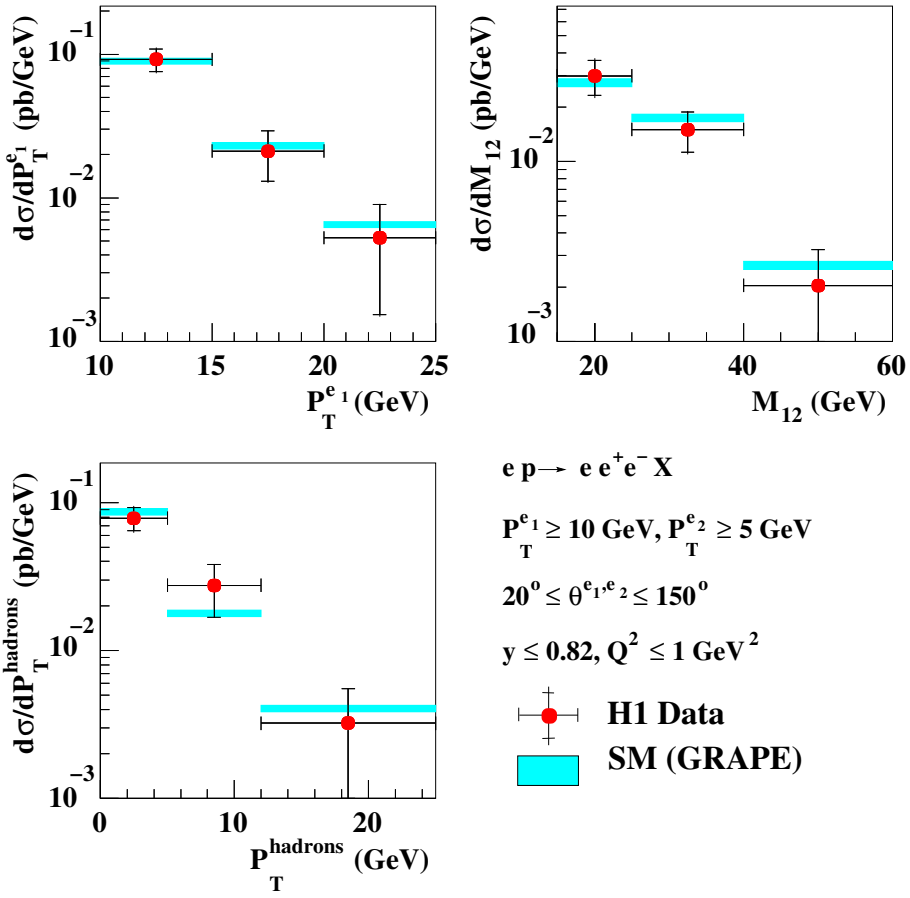

Figure 1.17: Cross section measurement for the $ep \to eeeX$ process, in the kinematic region defined in the figure itself. The inner error bars on the data points represent the statistical error, the outer error bars show the statistical and systematic uncertainties added in quadrature. The band around SM is one standard deviation uncertainty in the SM prediction.

of the $\gamma\gamma$ sample is

$$P_T^{e1} > 10 \text{ GeV}, \; P_T^{e2} > 5 \text{ GeV}, \; 20^\circ < \theta_e < 150^\circ, \; y{\leq}0.82, \; Q^2 < 1 \text{ GeV}^2;$$

the cross section measured by H1 in the above phase space is

$$\sigma = (0.59 \pm 0.08 \pm 0.05) \text{ pb},$$

where the first error is statistical and the second systematic; this result agrees well with the SM prediction

$$\sigma_{\text{SM}} = (0.62 \pm 0.02) \text{ pb}.$$

The differential cross sections are plotted in Fig. 1.17.

1.6.2 Di–muon search at H1

Isolated muon pair production has been studied by H1 using the data collected in years 1999 and 2000 (70.9 pb^{-1}).

Muon candidates were selected among charged tracks measured in the central tracker at polar angles between 20° and 160°, which were linked to a track measured by the muon chambers. In order to increase the efficiency for low momentum muons, also minimum ionising particles found by the calorimeter, which were linked to a central track, were accepted. Further cuts applied are:

- invariant mass of di–muon: $M_{\mu\mu} > 5$ GeV;
- transverse momentum of the muons: $P_T^{\mu 1} > 2$ GeV, $P_T^{\mu 2} > 1.75$ GeV;
- isolation of the muon: $D^{\mu}_{\text{Trk,Jet}} > 1.0$ (or $D^{\mu}_{\text{Trk,Jet}} > 0.5$ if $P_T^{\mu} > 10$ GeV).

The electroweak process was simulated by the GRAPE MC, while the LPAIR generator, which simulates only the Bethe–Heitler component (see Sect. 1.3.1), was used as a cross check. The $\gamma\gamma \to \tau\tau$ process (followed by the leptonic decay of the taus into muons), the Υ–resonance, as well the open heavy flavour contribution ($b\bar{b}$ and $c\bar{c}$) were also considered. The differential cross sections as a function of the di–muon mass $M_{\mu\mu}$ (Fig. 1.18, left), the muon transverse momentum and the hadronic transverse momentum, were extracted and found in agreement with the Standard Model.

The inelastic component was separated by tagging the proton remnant in the forward detectors. The differential cross section $\text{d}\sigma^{\text{inel}}/\text{d}M_{\mu\mu}$ is also in agreement with the SM prediction (Fig. 1.18, right).

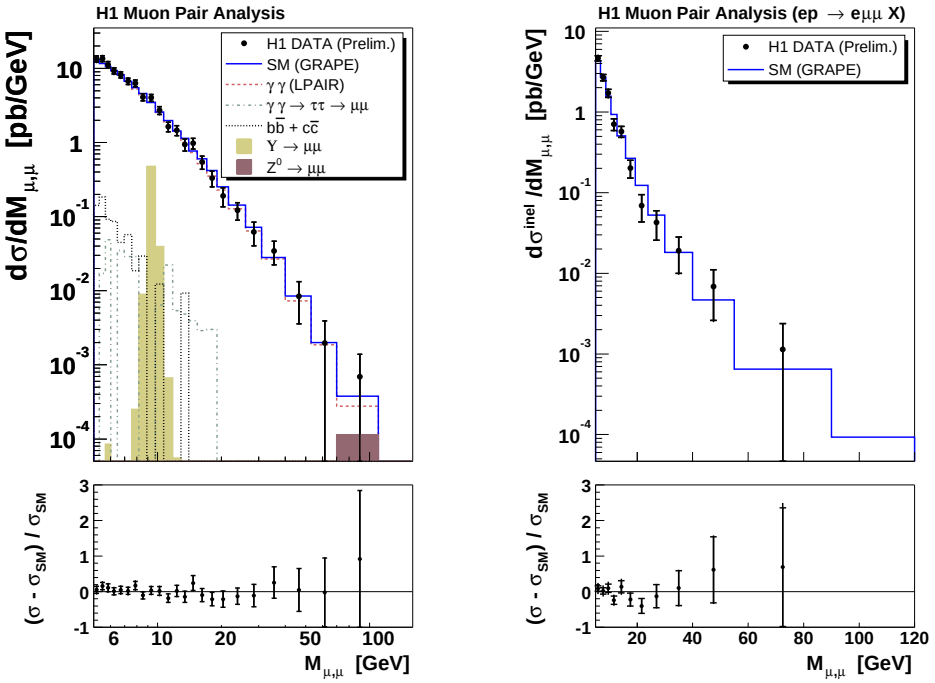

Figure 1.18: Differential cross section for di–muon production as a function of the di–muon invariant mass (upper left plot), and relative difference between data and all Standard Model contributions (lower left). The inner error bars represent the statistical error, whereas the outer error bars show the statistical and systematic uncertainties, added in quadrature. On the right, only the inelastic contribution is shown.

Type	Data	SM	GRAPE	NC DIS	QEDC
All $2e$	191	213.9 ± 3.9	182.2 ± 1.2	23.9 ± 3.7	7.8 ± 0.5
$2e$ and $M_{12} > 100$ GeV	2	0.77 ± 0.08	0.47 ± 0.05	0.12 ± 0.06	0.18 ± 0.03
All $3e$	26	34.7 ± 0.5	34.7 ± 0.5	–	–
$3e$ and $M_{12} > 100$ GeV	0	0.37 ± 0.04	0.37 ± 0.04	–	–

Table 1.5: Number of events selected at ZEUS with two ($2e$) or three ($3e$) electrons in the data and expectations of Standard Model processes. The latter (labelled "SM") is given by the sum of electroweak production ("GRAPE"), neutral current DIS ("NC DIS") and QED–Compton ("QEDC").

1.6.3 Multi–electron search at ZEUS

The whole data collected by ZEUS between 1994 to 2000, corresponding to an integrated luminosity of 130.5 pb^{-1}, were used in the search.

The electrons were identified by using the EM finder, described in Sect. 4.1, among the electromagnetic deposits in the calorimeter. The electron candidates were accepted when fulfilling:

- no tracks, other than the electron itself, in a cone of radius $R_{\eta\phi} = 0.4$ around the electron;
- a total calorimetric energy, not assigned to the electron, smaller than 0.3 GeV in a cone of radius $R_{\eta\phi} = 0.8$ around the electron;
- for central electrons ($0.3 < \theta_e < 2.86$ rad):
  - $E_e > 10$ GeV,
  - a track matched in position (DCA < 8 cm[5]) and $P > 5$ GeV;
- for forward electrons ($0.1 < \theta_e < 0.3$ rad), $E_e > 10$ GeV;
- for rear electrons ($2.86 < \theta_e < 3.05$ rad), $E_e > 5$ GeV.

The events were accepted if the vertex had $|z| < 50$ cm, and two or more central electrons were present, at least one with transverse energy $E_T > 10$ GeV. The electroweak production was simulated by the GRAPE Monte Carlo.

The number of events with two ($2e$) or three ($3e$) electrons in the final state was found in agreement with the expectation from the Standard Model, as shown in Table 1.5 and Fig. 1.19 (left). No events were found with more than three detected electrons.

[5]DCA is the distance of closest approach of the track to the energy deposit in the calorimeter.

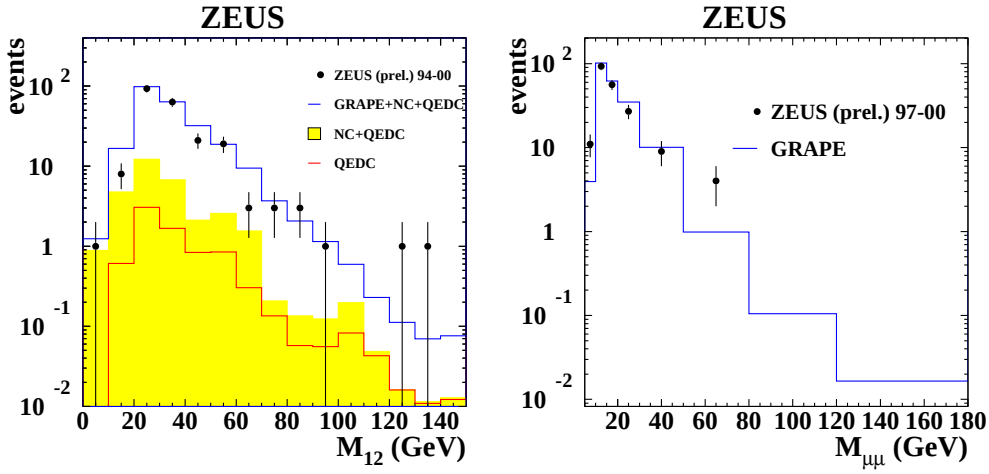

Figure 1.19: Invariant mass distribution of the two highest–E_T electrons (left), and of the two muons (right) in the multi–lepton search performed by ZEUS.

1.6.4 Di–muon search at ZEUS

A major subset of the data collected in the years 1997 to 2000 was used, corresponding to an integrated luminosity of 105.2 pb^{-1}.

Muons were identified by requiring:

- a track pointing toward an energy deposit in the calorimeter, compatible with a minimum ionising particle;
- at least three superlayers of the central tracker (Sect. 2.2.1) passed by the track;
- a polar angle of the track in $0.35 < \theta_\mu < 2.79$;
- a transverse momentum of the track $P_T^\mu > 5$ GeV;
- no tracks, other than the muon itself, in a cone of radius $R_{\eta\phi} = 1$ around the muon track.

Two or more muons were required, at least one of which had to be matched to a hit in the muon chambers. To reject cosmics, the reconstructed vertex was asked to have $|z| < 40$ cm and $\sqrt{x^2+y^2} < 0.5$ cm, and the angle between the two muons to be less than 174.2°.

After this selection 200 events were found in the data, while 213 ± 11 are expected from the GRAPE simulation of the electroweak process. Agreement is also found in the invariant mass distribution of the di–muons, Fig. 1.19 (right).

Chapter 2

The experimental setup

In this chapter I will describe the HERA accelerator and the ZEUS detector. A particular emphasis will be given to the components of ZEUS which were used for the multi–lepton search: the Central Tracking Detector (CTD), the Uranium–scintillator CALorimeter (UCAL), the muon detectors (FMUON and B/RMUON), the LUMInosity monitor (LUMI) and the trigger system. A more complete description of the detector can be found in [34].

2.1 The HERA accelerator

HERA (Hadron–Elektron Ring Anlage, [35]) is a unique facility, since collides beams of electrons (or positrons) and protons. It is located at the DESY (Deutsches Elektronen SYnchrotron) laboratory, in Hamburg, northern Germany, and operates since 1992. The HERA machine accelerates electrons[1] to an energy of 27.5 GeV, and protons to 820 (920) GeV (the energy of the proton beam has been raised from 820 up to 920 GeV at the beginning of 1998). The resulting centre–of–mass energy is 300 (318) GeV, more than an order of magnitude higher than the previous fixed–target experiments. As a consequence a new and wider kinematic region is accessible at HERA (see Fig. 2.1): the kinematic range has been enlarged by approximately three orders of magnitude in both the x and Q^2 variables.

The HERA tunnel is 6.3 km long and is located 15–30 m under the ground level. Electrons and protons are accelerated in two different rings. The magnetic system of the $e^{\pm}$ ring consists of conventional magnets with a maximum field of 0.165 T, whereas the proton beam is made of superconducting magnets with a maximum field of 4.65 T.

There are two *general purpose* detectors at HERA: H1 and ZEUS; they are located in the North and South Hall, respectively. The HERMES experiment is located in the East Hall and studies the spin structure of the nucleon using the

[1] Throughout this chapter I will refer to both electrons and positrons beams by using "electron".

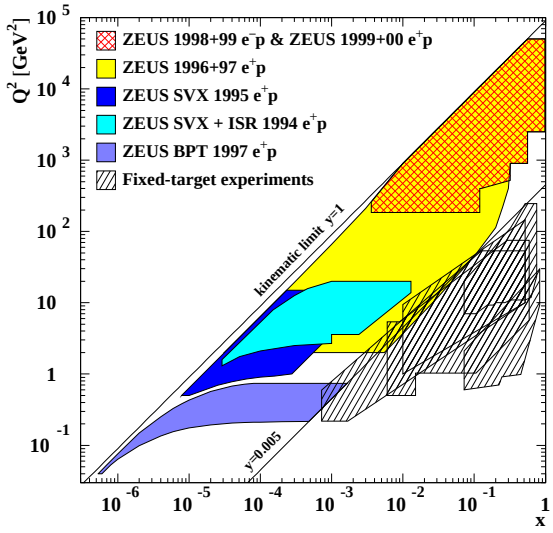

Figure 2.1: The x–Q^2 region covered by ZEUS and by fixed target experiments. ZEUS dramatically enlarge the phase space available for studies.

collisions of polarised electrons on an internal polarised gas target. The HERA–B experiment, located in the West Hall, was built to use collisions of the proton beam halo with a wire target to produce B–mesons for the study of CP violation in the B–$\bar{B}$ system.

Fig. 2.2 shows a layout of the HERA facility and of its pre–acceleration system. The proton acceleration chain starts with negative hydrogen ions (H^-) accelerated in a LINAC up to 50 MeV. The electrons are then stripped off the H^- ions to obtain protons, which are injected into the proton synchrotron DESY III, accelerated up to 7.5 GeV, and then transferred to PETRA, where they are accelerated to 40 GeV. Finally they are injected into the HERA proton storage ring, where they reach the nominal beam energy of 920 GeV.

The e^+ (e^-) pre–acceleration chain starts in a linear accelerator, LINAC I (LINAC II), where the electrons are accelerated up to 450 MeV. They are then injected into DESY II, accelerated to 7 GeV and then transferred to PETRA II, where they reach an energy of 14 GeV. They are then injected into HERA where they reach the nominal electron beam energy of 27.5 GeV. HERA can be filled with a maximum of 210 bunches of each electrons and protons spaced by 96 ns. Some of these bunches are kept empty (*pilot* bunches) in order to study the background conditions. When either the electron or the proton bunch is empty, the beam–related background, originating from the interaction of the electron or the proton beam with the residual gas in the beam pipe, can be studied, whereas when both the bunches are empty the non–beam–related background (e.g. the cosmic rays) can be estimated. The main design parameters of HERA are reported in Table 2.1.

In Fig. 2.3 and in Table 2.2 the performances of HERA during the years are

Main General Design Parameters of HERA		
Construction time	May 1984–November 1990	
Circumference of the HERA tunnel	6335.83 m	
Depth underground	15–30 m	
Number of pre–accelerators for HERA	6 (LINAC I, LINAC II, DESY II, PETRA II, H–LINAC, DESY III)	
Number of interaction points	4	
The HERA beams	**Electron**	**Proton**
Centre–of–mass energy (actual)	318 GeV	
Nominal energy (actual)	27.52 GeV	920 GeV
Magnetic field	0.165 T	4.65 T
Relative energy spread $\Delta E/E$	10^{-3}	10^{-4}
Injection energy	14 GeV	40 GeV
Luminosity per interaction point	1.6×10^{31} cm^{-2}s^{-1}	
Design Average Current	58 mA	163 mA
Particles per bunch	3.65×10^{10}	10^{11}
Maximum number of bunches	210	210
Beam crossing angle	head–on collisions, 0 mrad	
Bunch distance	96 ns (28.8 m)	
Beam length at maximum energy (σ_z)	0.85 cm	19 cm
Beam width at maximum energy (σ_x)	0.286 mm	0.28 mm
Beam height at maximum energy (σ_y)	0.06 mm	0.058 mm
Synchrotron radiation loss per turn	125 MeV	6×10^{-6} MeV
Polarization time at 30 GeV	35 min	–
Filling time	15 min	20 min

Table 2.1: Main design parameters of HERA.

Years	**Collisions**	**HERA Luminosity (pb^{-1})**
1992-94	e^-p	2.19
1994-97	e^+p	70.92
1998-99	e^-p	25.20
1999-00	e^+p	94.95

Table 2.2: Overview of the luminosity delivered by HERA from 1992 to 2000.

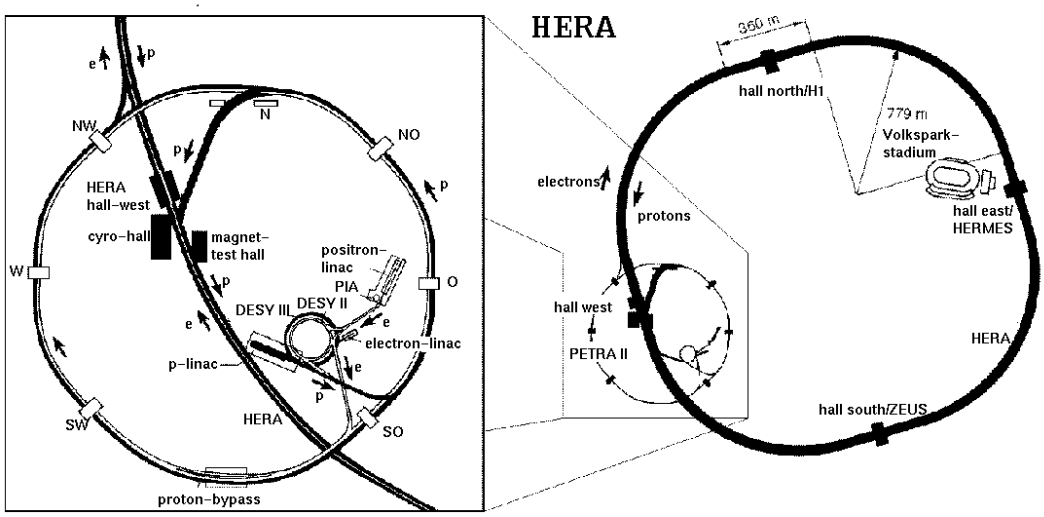

Figure 2.2: The HERA storage ring with its pre–accelerating system.

shown. The running operations began in 1992 with an electron (e^-) beam, but in 1994 it was realized that the electron beam current was limited by positively ionised dust particles getting into the beam pipe through the pumps, reducing the lifetime of the beam. For this reason HERA switched to positrons (e^+) in July 1994, achieving a more stable electron beam and a significant increase in the integrated luminosity of the collected data. During the 1997–98 shutdown period, new pumps were installed in the electron beam to improve the e^- beam lifetime, and therefore during 1998 and part of 1999 HERA was running again with e^-. It was also in 1998 that the energy of the proton beam was raised from 820 up to 920 GeV.

2.1.1 HERA II

After some years of operation HERA had reached a luminosity of $1.4{\cdot}10^{31}$ cm$^{-2}s^{-1}$, very close to the original design value. Although a lot of important measurements had already been performed at HERA, the desire was expressed by the experiments for an increase in the luminosity. The motivations for this increase were studied in a one–year workshop held between 1995 and 1996 [36], when it was concluded that having 1 fb^{-1} of integrated luminosity would have opened the possibility for new interesting measurements.

The HERA luminosity can be written as

$$\mathcal{L} = f\frac{n_e n_p}{4\sqrt{\epsilon_x\beta_x\epsilon_y\beta_y}}, \tag{2.1}$$

where f is the bunch crossing rate, n_e and n_p are the numbers of particles contained in the electron and proton bunches, respectively, β is the *amplitude func-*

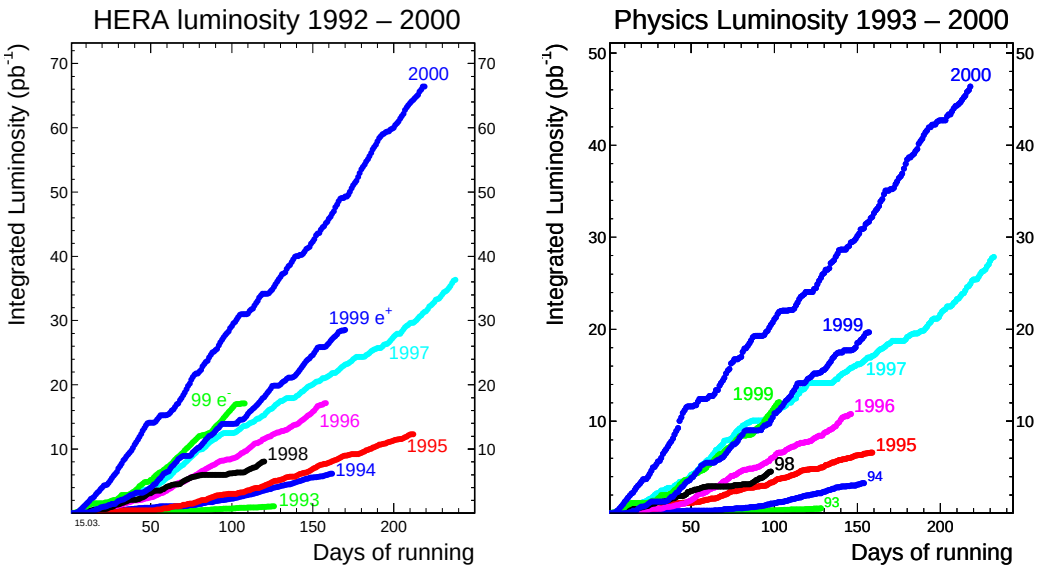

Figure 2.3: Integrated luminosity delivered by HERA (left) and usable for ZEUS physical analyses (right) in the 1993–2000 running period.

tion and ϵ is the *transverse emittance*. The amplitude function is a beam optics quantity and is determined by the accelerator magnet configuration. The transverse emittance reflects the beam quality; in the case of electrons mostly depends on synchrotron radiation. The beam size is related to β and ϵ by:

$$\pi\sigma^2 = \beta\epsilon. \tag{2.2}$$

The most affordable way to increase the luminosity at HERA was to reduce the spot size by a stronger focusing, thus to have smaller β functions, and to reduce the electron emittance.

The concept of the HERA upgrade is based on an early separation of the two beams with combined function magnets that are installed inside the experimental detectors, 2 m from the interaction point. The first exclusive proton focusing magnet is positioned at 11 m distance, to be compared with a distance of 26 m as it was installed previously. A summary of the post–upgrade parameters is given in Table 2.3, from [37]. The luminosity can be raised by a factor 4.7 compared to the original HERA design, assuming that the design currents can be reached in both machines.

2.2 The ZEUS detector

The ZEUS detector is a multipurpose detector designed to study electron–proton scattering at HERA. It is a quasi–hermetic detector since it covers most of the

	e–beam	p–beam
Energy [GeV]	27.5	920
Beam current [mA]	58	140
Emittance ϵ [nm]	22	$5000/\gamma$
Emittance ratio ϵ_y/ϵ_x	0.18	1
Amplitude functions β_x, β_y [m]	0.63, 0.26	2.45, 0.18
Spot size $\sigma_x \times \sigma_y$ [μm^2]	118×32	118×32
RMS bunch length [mm]	12	128
Luminosity [$cm^{-2}s^{-1}$]	$7.00 \cdot 10^{31}$	

Table 2.3: Start–up parameters for the HERA upgrade.

4π solid angle, with the exception of small regions around the beam pipe. ZEUS was commissioned and upgraded during the years of data–taking keeping into account the needs for physics and the technical understanding gained during the running period.

The original shape of the detector was driven by the different processes that can be observed at HERA. The detector can measure energies from few MeV to hundreds of GeV in the forward region. For low–momentum particles the tracking on a magnetic field is very precise (the resolution behaves as $\sigma(p_T)/p_T \sim p_T$), while high energy particles are well measured by the calorimetric system (the resolution goes as $\sigma(E)/E \sim \sqrt{E}/E$).

Particle identification is needed in a wide momentum range: in neutral current DIS events the scattered electron has to be identified and measured with high precision; the identification of electrons, positrons and muons is needed in order to study the semi–leptonic decay of heavy quarks and exotic processes involving leptons.

In charged current DIS processes a hermetic detector is needed in order to reconstruct the missing transverse momentum carried by the outgoing neutrino. In this kind of events and also in untagged photoproduction events the precise reconstruction of the final state energy is important in order to determine the event kinematic.

The ZEUS coordinate system (Fig. 2.4) is a right–handed, orthogonal system, with the origin at the nominal interaction point (IP), the z axis pointing in the proton direction (also referred to as the *forward* direction), the x axis pointing toward the centre of HERA and the y axis pointing upward. Because of the large momentum imbalance between the electron and the proton beams, most of the final state particles are boosted in the forward direction, and therefore the sub–detectors that build up ZEUS are coaxial but asymmetric for z reflection. The detector layout is shown in Fig. 2.5 (longitudinal view) and Fig. 2.6 (transverse view). The main detector is approximately 20 m long, 12 m large and 11 m high, and it weights around 3.6×10^6 kg.

A brief outline of the various detector components is given below, whereas

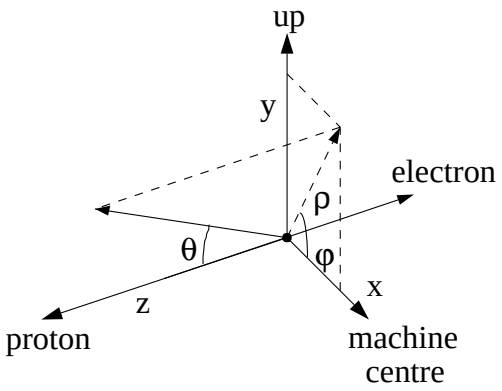

Figure 2.4: The ZEUS coordinate system.

a more detailed description of the sub–detectors of particular interest for the multi–lepton analysis will be given in the next sections.

The innermost detector that can be seen in Figs. 2.5 and 2.6 is the VerteX Detector (VXD), that was removed during the 1995–96 shutdown. Therefore during 1996–2000 data–taking the closest detector to the interaction point was the Central Tracking Detector (CTD), which is surrounded by a super–conducting solenoid providing a magnetic field of 1.43 T, for the determination of the charge and momentum of the particles. The forward (FTD) and rear (RTD) tracking detectors complete the tracking system.

Outside the super–conducting solenoid the ZEUS calorimeter is located, a compensating high–resolution uranium–scintillator calorimeter, divided into forward, barrel and rear sections (FCAL, BCAL, RCAL), with different thickness. The calorimeter is enclosed by an iron yoke that provides the return path for the solenoidal magnetic field flux, and serves as absorber for the BAcking Calorimeter (BAC), which measures the energy that escapes detection from the main calorimeter. The muon detectors are located inside (inner muon chambers, FMUI, BMUI and RMUI) and outside (FMUO, BMUO, RMUO) the yoke.

The Small angle Rear Tracking Detector (SRTD) is a scintillator strip detector located on the front face of the rear calorimeter, around the beam pipe, used to measure the impact point of the scattered electrons with high accuracy. The C5 counter, located at the rear end of the calorimeter ($z = -314$ cm), consists of two planes of scintillators, one above and one below the beam pipe. The timing information given by these two sub–detectors are used to reject proton–beam gas events.

Other detectors are located several meters away from the main detector along the beam pipe. The Leading Proton Spectrometer (LPS), consisting of six silicon strip detector stations located at distances of 24–90 m from the interaction point, measures protons scattered at very small angles. The VETO wall, located around $z = -7.5$ m before the interaction point, and consisting of an iron wall supporting scintillator hodoscopes, is used to reject background from beam–gas

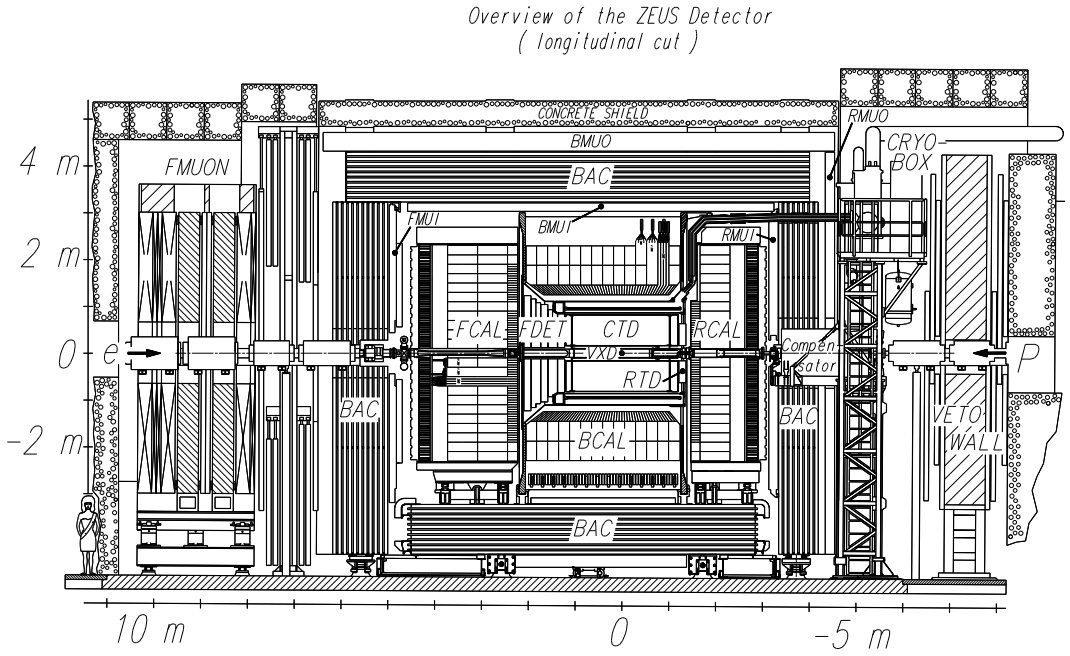

Figure 2.5: Cross section of the ZEUS detector along the beam axis.

interactions. The LUMI detector, made of two small lead–scintillators calorimeters, at $z = -35$ m and $z = -(104 \div 107)$ m, detects electrons and photons from bremsstrahlung events for the luminosity measurement.

2.2.1 The Central Tracking Detector (CTD)

The Central Tracking Detector (CTD) [38] is a cylindrical wire drift chamber used to measure the direction and momentum of the charged particles and to estimate the energy loss $\mathrm{d}E/\mathrm{d}x$ to provide information on particle identification. The inner radius of the chamber is 18.2 cm, the outer is 79.4 cm, and its active region covers the longitudinal interval from $z = -100$ cm to $z = 104$ cm, resulting in a polar angle coverage of $15° < \theta < 164°$. The CTD is filled with a mixture of argon (Ar), carbon dioxide (CO_2) and ethane (C_2H_6) in the proportion 85:5:1. The basic structure of the CTD is the *cell*, which consists of eight sense wires surrounded by drift wires. The sense wires are 30 μm thick, while the field wires have different sizes. Several cells are placed side by side to form *superlayers* (SL); the nine superlayers of the CTD are one cell thick in the radial direction. A total of 4608 sense wires and 19584 field wires makes up the CTD. The field wires are tilted of 45° with respect to the radial direction, in order to compensate the Lorentz angle of 45° due to the electric and magnetic field. One octant of the CTD is shown in Fig. 2.7.

A charged particle crossing the CTD produces ionisation of the gas in the chamber. The electrons from the ionisation drift toward the sense wires (positive), whereas the positively charged ions drift toward the negative field wires. The drift

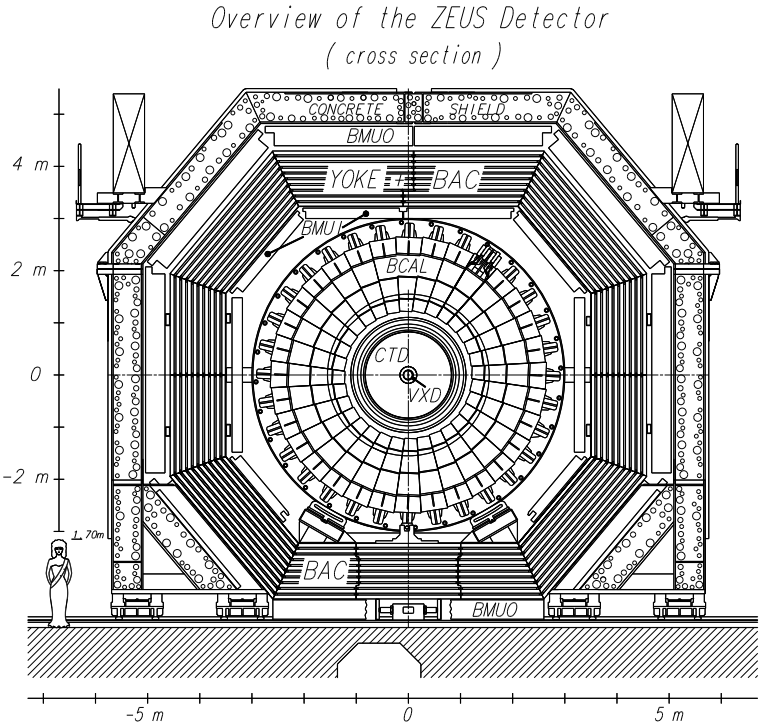

Figure 2.6: Cross section of the ZEUS detector orthogonal to the beam axis.

velocity of the electrons is approximately constant and equal to 50 μm/ns; during the drift an avalanche effect occurs, giving an amplification factor on the electrons of $\sim 10^4$, so that a readable pulse is induced on the sense wires.

The superlayers are numbered so that the number 1 is the innermost SL, whereas the outermost is number 9. Odd numbered SLs have wires parallel to the z direction (axial superlayers), while wires in even numbered SLs are at a small stereo angle of $\pm 5°$ (stereo superlayers) to achieve a better resolution in z. The achieved resolution is ~ 200 μm in the $r\phi$ plane and ~ 2 mm in the z coordinate.

For trigger purposes, the three inner axial superlayers (SL1, SL3, SL5) are equipped with a system that determines the z positions using information on the arrival time of the particle (z–by–timing system). The resolution achieved on the z coordinate with this system is ~ 4 cm.

The resolution on the transverse momentum p_T, for tracks fitted to the interaction vertex and passing at least three CTD superlayers, and having $p_T > 150$ MeV, is given by:

$$\frac{\sigma(p_T)}{p_T} = 0.0058 \cdot p_T \oplus 0.0065 \oplus \frac{0.0014}{p_T}, \tag{2.3}$$

where the symbol $\oplus$ indicates the quadratic sum, and p_T is measured in GeV. The first term is the hit position resolution, while the second and the third depend on the multiple scattering inside and before the volume of the chamber, respectively.

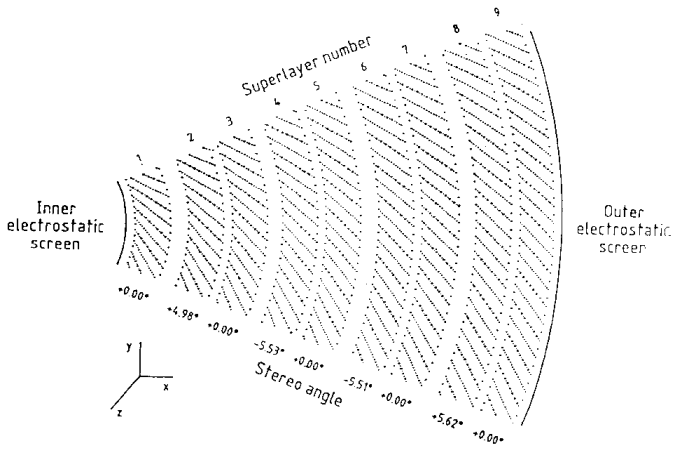

Figure 2.7: xy cross section of one octant of the CTD. The sense wires are indicated with dots.

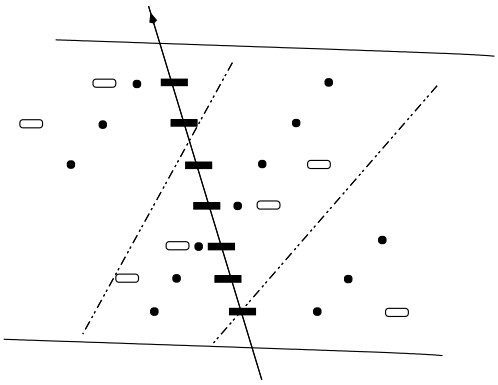

Figure 2.8: Hits coming from a genuine track (full rectangles) tend to cross the cell boundaries within a superlayer. The open rectangles are ghost hits.

Track reconstruction

The information used to determine the spatial position of a particle, needed for the track reconstruction, come from the time of arrival of the ionisation electrons on the sense wire. If the drift velocity is approximately constant and equal to u_d, the relation between the drift time, t_d, and the distance from the sense wire, d_s, is given by:

$$d_s \simeq u_d \cdot t_d \tag{2.4}$$

where t_d is defined as the difference between the time t_f at which the pulse appears on the sense wire, and the time t_i of passage of the charged particle, calibrated for every wire, $t_d = t_f - t_i$. However, this kind of information is not sufficient to determine from which side of the wire the particle comes, therefore a left–right ambiguity is still present. The 45° tilt of the sense wires can solve

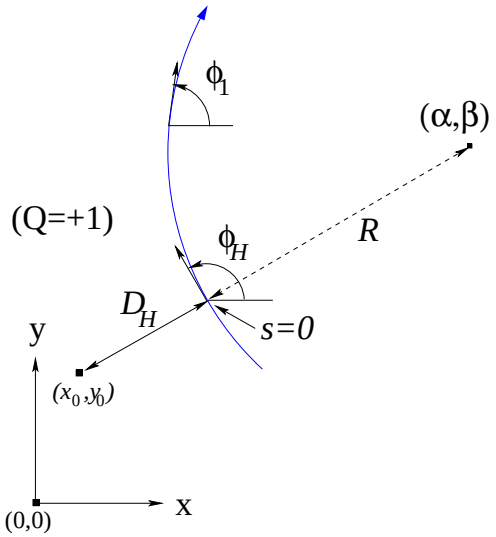

Figure 2.9: The track helix in the xy plane.

this ambiguity, since tracks coming from the interaction point tend to pass the boundary of adjacent cells within a superlayer, as shown in Fig. 2.8.

The pattern recognition of the track begins looking for a *seed*, a group of hits in the outermost superlayer (SL9). To these hits a virtual hit at $x = y = 0$ is added, keeping into account the transverse dimension of the beam as an error on this hit. The two hits are enveloped with a circle arc, and inner hits on the axial superlayers are added on the way, updating the circle parameters and refining the trajectory determination. Once that the pattern recognition is completed in axial superlayers, stereo hits are selected that match with the arc after being rotated. The pattern recognition begins with the longest tracks, those going from SL9 to SL1, then continues with shorter tracks, reaching inner superlayers (SL7, SL5...), and finally includes tracks with no hits in the innermost superlayer, that can come from the decay of long lived particles.

When the pattern recognition is done, all the candidate tracks are fitted with a helix, starting with the innermost superlayer and adding the outer ones on the way. If (x_0, y_0) is the *reference point* of the helix, its five parameters are (Fig. 2.9):

- $a_1 = \phi_H$, the azimuthal angle of the tangent to the helix, in the point of closest approach to (x_0, y_0);
- $a_2 = Q/R$, where Q is the charge and R the radius of the helix;
- $a_3 = Q\ D_H$, where D_H is the distance of the helix from the reference point;
- $a_4 = Z_H$, the z position of the point of closest approach;
- $a_5 = \cot\theta$, where θ is the polar angle of the tangent.

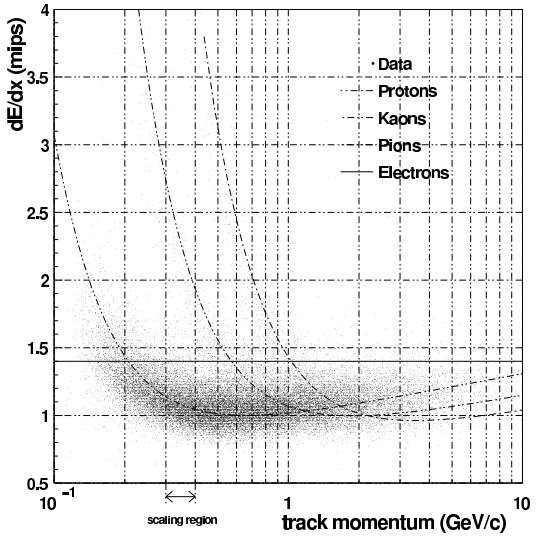

Figure 2.10: The energy lost by different particles, as reconstructed by the CTD, as a function of the particle momentum. The curves indicate the particle type.

The event vertex is then reconstructed from the information on the fitted tracks. Tracks too far from the determined vertex are discarded, the surviving tracks are constrained to the vertex and the helix parameters recalculated.

$\mathrm{d}E/\mathrm{d}x$ measurement

The CTD is also used to estimate the ionisation energy loss of a particle in the gas, in order to have information on the particle identification.

The ionisation energy loss is parametrized by the Bethe–Bloch equation:

$$-\frac{\mathrm{d}E}{\mathrm{d}x} = 4\pi N_A r_e^2 m_e c^2 z^2 \frac{Z}{A}\frac{1}{\beta^2}\left[\ln\left(\frac{2m_e c^2\gamma^2\beta^2}{I}\right) - \beta^2 - \frac{\delta}{2}\right] \qquad (2.5)$$

for a particle with charge ze passing through a medium with atomic number Z and mass number A. The energy loss is a function of the speed βc of the particle: at low momenta the energy loss is high and different for different masses of the particles; for increasing β, $\mathrm{d}E/\mathrm{d}x$ decreases steeply, down to a minimum for $\gamma = (1-\beta^2)^{-0.5} \simeq 3$. Then the energy loss rises as a logarithm up to a plateau at very high γ. The behaviour as observed by the CTD is shown in Fig. 2.10.

2.2.2 The Uranium–scintillator Calorimeter (UCAL)

The ZEUS calorimeter (UCAL) [39] is a high–resolution compensating calorimeter. It completely surrounds the tracking devices and the solenoid, and covers the 99.7% of the 4π solid angle. It consists of 3.3 mm thick depleted uranium plates (98.1% U^{238}, 1.7% Nb, 0.2% U^{235}) as absorber alternated with 2.6 mm thick organic scintillators (SCSN–38 polystyrene) as active material. The thickness of

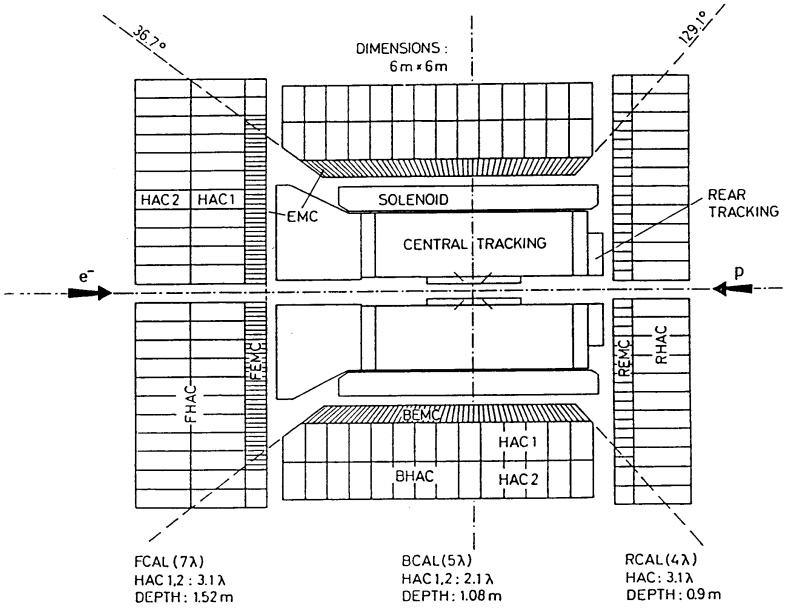

Figure 2.11: Schematic view of the UCAL along the beam axis.

the absorber and of the active material have been chosen in order to have the same response for an electron or a hadron of the same energy ($e/h = 1.00 \pm 0.02$) passing through the detector. This mechanism is called *compensation*, and allows to achieve good resolution in the determination of both the electromagnetic and the hadronic energy. The achieved electromagnetic resolution is

$$\frac{\sigma(E)}{E} = \frac{18\%}{\sqrt{E}} \oplus 2\%, \tag{2.6}$$

while the hadronic resolution is

$$\frac{\sigma(E)}{E} = \frac{35\%}{\sqrt{E}} \oplus 1\%; \tag{2.7}$$

E is the particle energy, measured in GeV.

The UCAL is divided into three parts: the forward (FCAL), barrel (BCAL) and rear (RCAL) calorimeters (Fig. 2.11). Since most of the final state particles in a electron–proton interaction at HERA are boosted in the forward (proton) direction, the three parts have different thickness, the thickest one being the FCAL ($\sim 7\ \lambda$, where λ is the interaction length), then the BCAL ($\sim 5\ \lambda$) and finally the RCAL ($\sim 4\ \lambda$).

Each part of the calorimeter is divided into *modules*, and each module is divided into one electromagnetic (EMC) and two (one in RCAL) hadronic (HAC) sections. These sections are made up of *cells*, whose sizes depend on the type (EMC or HAC) and position (in FCAL, BCAL or RCAL) of the cell, as reported in Table 2.4.

UCAL Part	Angular coverage	EMC $x \times y$	HAC $x \times y$
FCAL	$2.5° - 39.9°$	20×5 cm^2	20×20 cm^2
BCAL	$36.7° - 129.2°$	20×5 cm^2	20×20 cm^2
RCAL	$128.1° - 178.4°$	20×10 cm^2	20×20 cm^2

Table 2.4: Angular coverage of the UCAL parts and dimensions of the cells.

The FCAL consists of one EMC (first 25 uranium–scintillator layers) and two HAC (remaining 160 uranium–scintillator layers) sections. The electromagnetic section has a depth of 26 radiation lengths X_0, while each hadronic section is 3.1 λ deep. The EMC and HAC cells are superimposed to form a rectangular module, one of which is shown in Fig. 2.12. 23 of these modules make up the FCAL.

The BCAL consists of one EMC and two HAC sections, the EMC being made of the first 21 uranium–scintillator layers, the two HACs of the remaining 98 layers. The resulting depth is 21 X_0 for the electromagnetic section, and 2.0 λ for each hadronic section. The cells are organized in 32 wedge–shaped modules, each covering 11.25° in azimuth.

The RCAL is made up of 23 modules similar to those in the FCAL, but it consists of one EMC and only one HAC section. Therefore its depth is 26 X_0 for the EMC part and 3.1 λ for the HAC part.

The light produced in the scintillators is read by 2 mm thick wavelength shifter (WLS) bars at both sides of the module, and brought to one of the 11386 photomultiplier tubes (PMT) where it is converted into an electrical signal. These information are used for energy and time measurement. The UCAL provides accurate timing information, with a resolution of the order of 1 ns for tracks with an energy deposit greater than 1 GeV. These information can be used to determine the timing of the particle with respect to the bunch–crossing time, and it is very useful for trigger purposes in order to reject background events, as it will be illustrated later, in the Sect. 2.2.7.

The stability of the PMTs and of the electronics is monitored with lasers and charge pulses. In addition, the small signal coming from the natural radioactivity of the depleted uranium (wrapped in stainless steel foils not to interfere with the physical particles measurements) gives a very stable signal, also used for the calibration. The achieved accuracy is better than 1%.

2.2.3 The Muon Detectors

The main aim of these detectors is the measurement of the tracks coming from the interaction region (*pointing tracks*) and that are able to cross the whole calorimeter and the iron yoke (*penetrating tracks*). This behaviour is characteristic of muons, that can cross large amount of material without being absorbed since, being much heavier than the electrons and not interacting strongly, they lose

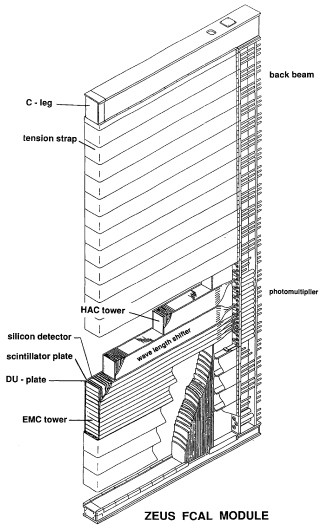

Figure 2.12: A FCAL module.

their energy just by ionisation.

The muon detection system, as the other detectors in ZEUS, has to keep into account the boost of the particles in the forward direction. The momenta of the muons can be very different depending on their polar angle: in the forward region muons with more than 10 GeV momentum are easily found, whereas in the barrel and rear regions the average momentum of the muons is expected to be much smaller. Therefore the muon detection system is split into two detectors, designed and realized in different ways: the Forward Muon Detector (FMUON) and the Barrel and Rear Muon Detector (BMUON and RMUON).

2.2.4 The Forward Muon Detector (FMUON)

The Forward Muon Detector is made up of two modules (Fig. 2.13): one is located between the FCAL and the BAC (inner detector, FMUI), the other is positioned outside the BAC (outer detector, FMUO). The FMUON detector consists of:

- a system of four limited streamer tubes [40] trigger planes (LST1÷LST4), with digital ρ and ϕ readout;
- two coverage planes of limited streamer tubes with digital (ρ, ϕ) and analog ρ readout, in the large polar angle region (LW1, LW2);
- four planes of drift chambers (DC1÷DC4);
- two large toroidal iron magnets providing a magnetic field of 1.7 T for the momentum separation and measurement in the angular region $5° < \theta < 16°$.

The first LST plane and the first drift chamber make up the FMUI detector, while the FMUO detector consists of the rest of the system.

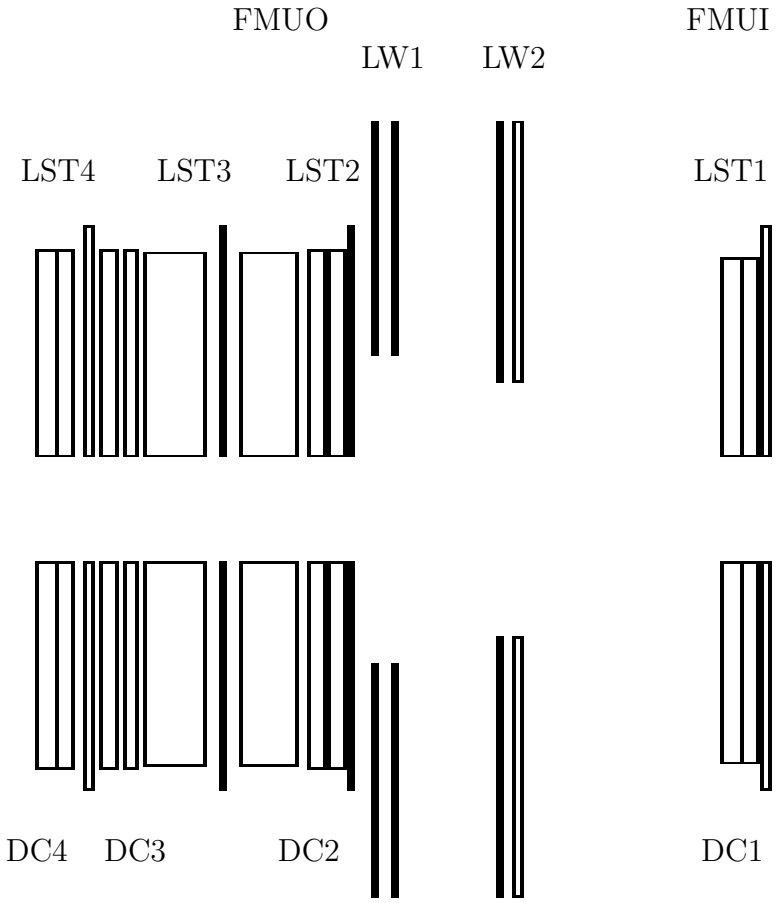

Figure 2.13: Schematic view of the forward muon detector along the beam axis.

The Limited Streamer Tubes (LST) Planes

The aim of the limited streamer tubes (LST) planes is to trigger on muon candidates and to reconstruct their position in terms of the azimuthal and radial coordinates of the track.

A trigger plane is made of four LST chambers, grouped by two in two half–planes. A quadrant consists of two layers of LST, positioned horizontally inside a plastic sheath. The tubes of the two planes are slightly displaced (0.5 cm) in order to achieve a complete geometrical acceptance. Each quadrant is contained in an aluminum air tight box. The signals generated by the LST are induced on copper strips with polar geometry, glued on the outer side of the plastic sheath. The number of radial ρ strips, 1.9 cm wide, is 132, and they are divided along the bisector of the quadrant so that the simplest unity of the trigger plane to be read is the octant. The last 64 strips far away from the beam line are OR'ed two by two since as θ becomes larger a coarser resolution is needed. Therefore the number of channels needed for each octant is 96. The number of ϕ strips is 32 per octant: each covers a 1.4° interval in azimuth.

The drift chambers (DC)

The drift chambers are needed in order to obtain a good momentum resolution. Each plane consists of four chambers, grouped two by two in two half planes, fixed on a sustain panel. The basic constituent of the chamber is the *cell*, made up of four sense wires and of the layers needed to generate the appropriate electric field. The four sense wires measure the radial coordinate. The information gathered by the wires are sent to a TDC, which converts them into a time distance, connected to the space distance by a known relation.

The Large Angle Coverage Planes (LW)

The two large angle coverage planes (LW) are needed in order to achieve the desired geometrical acceptance also in the region left uncovered by the toroids ($16° < \theta < 32°$). Each plane consists of eight aluminum tight wrappings that contain a LST layer. The LST signal is induced on copper strips with radial geometry, spaced of 0.7° in the ϕ coordinate and of 1.8 cm in the ρ coordinate. The number of ϕ strips is 64 per octant, while the ρ strips are 192 per octant. The achieved resolution in the ρ coordinate using a charge barycentre method is ~ 1 mm.

2.2.5 The Barrel and Rear Muon Detector (B/RMUON)

The Barrel and Rear Muon Detector [41] has to cover a very large area, of the order of two thousands squared meters, so a modular structure was chosen. The basic element is the *chamber*. The chambers covering the inner barrel part, between the CAL and the iron yoke, are called BMUI, whereas the chambers situ-

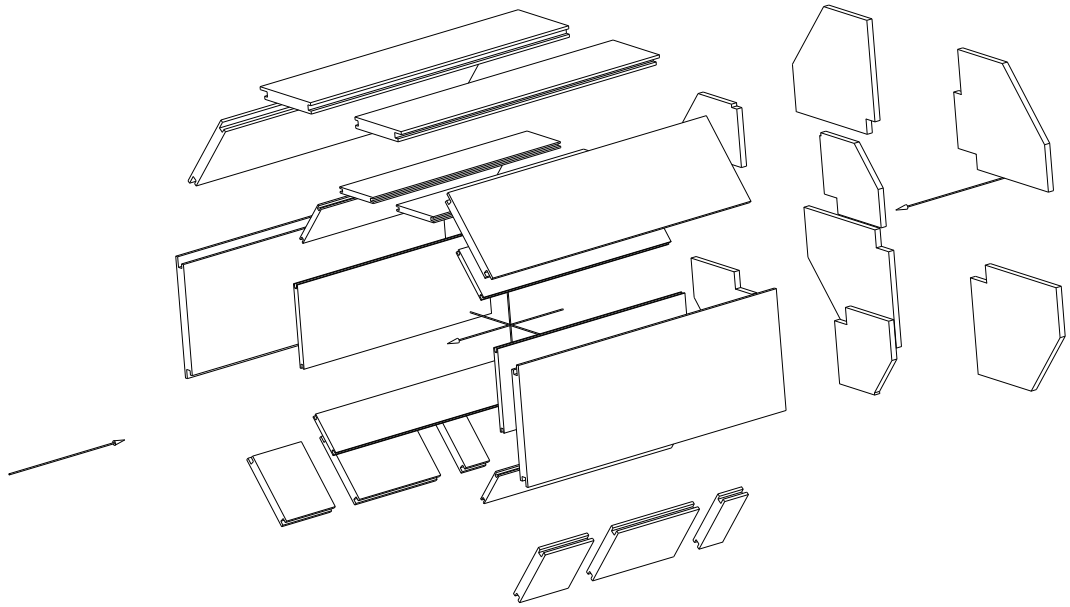

Figure 2.14: An exploded view of the Barrel and Rear Muon Detector, showing the positioning of the chambers.

ated in the outer barrel part, outside the yoke, are denoted as BMUO. In a similar way, in the rear region the detector is divided into RMUI and RMUO chambers. In Fig. 2.14 the layout of B/RMUON is schematically shown. The chambers have different shapes and dimensions depending on where they are located, but their internal structure is kept the same: the element bearing the weight of the chamber is an aluminum honeycomb structure, 20 cm thick in the rear chambers, 40 cm in the barrel ones. On both sides of the honeycomb a couple of planes of limited streamer tubes (LST) [40] is placed (see Fig. 2.15). The choice of LST planes was due to the large area to be covered, joined with the necessity of a good spatial resolution, of the order of ~ 1 mm. Each tube contains eight cells, each with one sense wire; the distance between two sense wires is 1 cm. During

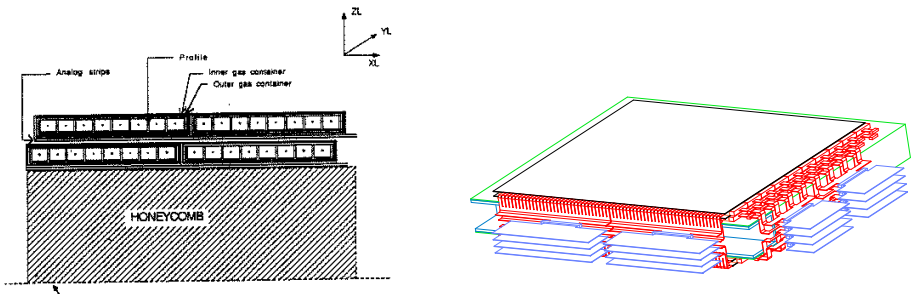

Figure 2.15: Transverse section of a B/RMUON chamber, with the honeycomb structure visible (left). Scheme of a BMUO chamber (right).

the data–taking the sense wires are brought to $\sim$ 4500 V so that they behave as anodes, while the inner cell walls, covered by graphite, act as cathodes. The cells are filled with a mixture of carbon dioxide (CO_2), argon and isobutane (C_4H_{10}). On one of the outer walls of the LST plane conductive strips orthogonal to the wires are placed. The pitch between two adjacent strips is 1.5 cm. The signal read by the wires is also induced on the strips, so that a single plane of wires and strips is sufficient to determine the particle position. For redundancy each chamber has two LST planes on each side of the honeycomb. The cells in one plane are displaced with respect to those in the other plane by half cell, in order to have good acceptance also for the particles passing near the boundary of two cells in a plane. In the BMUI and BMUO chambers the LST are parallel to the beam direction, whereas in RMUI and RMUO they are horizontal (parallel to the ZEUS x direction).

The determination of the position of a particle passing through the muon chambers proceeds by collecting the information coming from the wires, read by electronic cards called SGS, and from the strips, with readout cards named STAR. The reading of the cards depends on the presence of a trigger signal in the event. There are two types of trigger signals in an event:

(1) when the muon chambers identify a *penetrating* track, with activity in the inner and outer muon chambers, and *pointing* to the central tracking devices, the trigger signal is called *strong*;

(2) if the muon chambers find activity in at least one of the inner chambers, the trigger signal is called *weak*.

The trigger signal is determined by the analysis of the wires and strips hit in the event. First of all, the adjacent wires in the same LST plane are OR'ed in groups of 16, and the same is done with the strips. The signal obtained from these groups is further analysed in order to obtain information on the polar and azimuthal position of the wires and strips that have been hit. Coincidence matrices designed for this purpose analyse the information coming from the inner and the outer muon chambers, and select configurations generated by tracks coming from the volume specified by the inner tracking detectors (*pointing tracks*). In the case of positive response by the matrices, a strong trigger signal is present.

When there is a strong or weak trigger signal in the event the following information are recorded: the positions of the hit wires, the drift distance wire by wire, the positions of the hit strips and the charge collected by each strip (analog readout). With the analog readout the achievable spatial resolution on the coordinate orthogonal to the wires is 200 μm, while it is 700 μm for the coordinate parallel to the wires.

If there is no trigger signal in the event, the recorded information are the positions of the hit wires and of the OR of four adjacent strips, called *quadruplets* (digital readout). In this case the resolution on the single hit is $1/\sqrt{12}$ cm in the direction orthogonal to the wires, $6/\sqrt{12}$ cm along the wires.

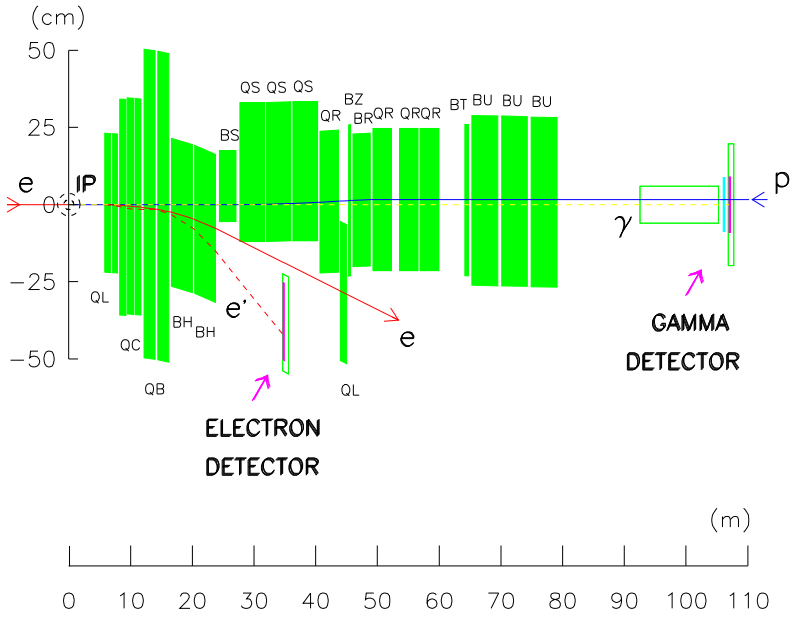

Figure 2.16: Schematic view of the luminosity monitor.

2.2.6 The luminosity monitor

The luminosity measurement at ZEUS is done by studying the bremsstrahlung events $ep \to ep\gamma$, where the electron and the photon are scattered at very small angle. The cross section of this process is described by the Bethe–Heitler formula [42, 43] and is known with an accuracy of $\sim 0.5\%$, allowing a precise determination of the collected ep luminosity.

The luminosity monitor consists of a photon and a electron calorimeter, located along the beam line at $z = -(104 \div 107)$ m and $z = -35$ m, respectively (Fig. 2.16). To protect the photon calorimeter against synchrotron radiation, it has been shielded by a carbon–lead filter. The resulting calorimeter resolution is $\sigma(E)/E = 23\%/\sqrt{E/\,\mathrm{GeV}}$. The bremsstrahlung event rate is determined by counting the number of photons above a fixed energy threshold, and not by the simultaneous identification of the electron and the photon, because of the dependence of the electron calorimeter acceptance on the beam position and angle. The luminosity is then extracted by dividing the evaluated rate by the bremsstrahlung cross section, corrected for the detector acceptance.

The main contribution to the background is given by the bremsstrahlung of electrons on the residual gas in the beam pipe. This can be estimated using *pilot* bunches, i.e. electron bunches with no paired proton bunches, evaluating for these the rate of bremsstrahlung events.

The achieved precision on the luminosity measurement is about 1.5–2%.

2.2.7 The ZEUS trigger system

The ZEUS trigger [44] is a three–level system, each level being differently sophisticated: the first level, having to deal with very high event rates, handles simpler information from the events, while the second can use more refined objects, and in the third even part of the offline reconstruction software can be run, in order to decide whether an event has to be written to disk or not. The aim of the ZEUS trigger system is to reject background events, coming mainly from beam–gas interactions and from cosmics, and at the same time to keep events coming from *ep* interactions, which have a rate, $\mathcal{O}(1\text{ Hz})$, which is much smaller than the background.

The First Level Trigger (FLT)

The First Level Trigger (FLT) has to strongly suppress the following classes of background events, in order to pass a cleaner sample to the other trigger levels:

- events coming from interactions of electrons or protons with the residual gas in the beam pipe, near the interaction point. The estimated rate of this kind of events, assuming a sensitive region of 100 m before and after the interaction point, with the nominal beam currents and with a vacuum of 10^{-7} Pa, is 50 kHz;

- events coming from interactions of the protons in the beam halo with the collimators, that can produce secondary hadrons decaying into high energy muons, crossing all the detector; these events, however, have a typical topology (the muons are typically parallel to the proton beam direction) and usually can easily be distinguished from *ep* events;

- cosmic ray muons, with a rate of the order of 1 kHz on the volume of the CTD.

The First Level Trigger has to deal with the HERA bunch crossing so it has to handle events at a rate of 10 MHz, giving as output events at a rate of the order of 1 kHz, the design rate of the Second Level Trigger. The FLT is a hardware trigger, designed to analyse one event for every bunch crossing. The data of each bunch crossing are stored into pipelines that are 46 bunch crossing deep and allows the FLT a time of 4.4 μs to accept or discard an event. The FLT operates on a subset of the full data coming from an event and makes use essentially of calculations of crude event observables (regional energy sums, number of tracks, timing information...).

Each detector component has its own first level trigger processor, and the 4.4 μs interval has to be shared between the components trigger and the Global First Level Trigger (GFLT). After 26 bunch crossing times (2.5 μs) all the components send their FLT signal to the GFLT, which uses the remaining 20 crossing times (1.9 μs) to take the final decision. The components data are processed and

combined in parallel in eight Trigger Logic Modules of the GFLT, and 64 individual sub–triggers (*slots*) are generated. The GFLT accepts or refuses the event looking at the OR of these 64 sub–triggers.

If the event is accepted, all the components have to digitize their data in order to send them to a system of digital CPUs for the next analyses. This operation takes ~ 10 μs after the GFLT decision, and during this time no event acquisition is possible. This is the only dead–time of the GFLT chain, and is of the order of 1%.

The Second Level Trigger (SLT)

The Second Level Trigger (SLT, [45]) has the aim to further reduce the background rate with respect to the *ep* events rate. The SLT, which receives events from the FLT with a rate of 1000 Hz, has an output rate of 100 Hz. The SLT is software–based and runs on a network of transputers [46]. The analysis of the events is done in parallel so that the available processing time is much larger than at the FLT, being of the order of some milliseconds. As in the FLT, each detector component has its own SLT processor, and all the information from the single components are sent to the Global Second Level Trigger (GSLT) after the processing.

The information the GSLT uses to distinguish between *ep* and background events are based mainly on the time of arrival of the particles to the calorimeter. As was said in Sect. 2.2.2, the UCAL can give timing information with a resolution of the order of 1 ns. The time is calibrated so that a physical event originating from the interaction point has zero time in the whole calorimeter, when the produced particles arrive at it. Therefore, a proton–gas event, originating upstream of the detector, will produce particles arriving to the RCAL before than the FCAL, and times in FCAL and RCAL differ by ~ 10 ns. In the same way, events coming from electron–gas interactions downstream the detector will produce particles arriving to the FCAL before than the RCAL, and the time difference is much larger than the UCAL timing resolution. Also cosmic events and electronic noise will appear as asynchronous to the HERA time and would therefore be suppressed.

The timing information from the UCAL is available when at least one cell above threshold (200 MeV) has been read by PMTs on both sides. The times are calculated by a weighted average on all the cells above threshold, for the different regions, with a bigger weight for the more energetic cells. In more detail, the filters applied to separate *ep* and background events are:

- *RCAL timing:* used to reject events coming from proton beam interactions with the residual gas in the beam pipe. Events are rejected if $|T_{RCAL}| > 8$ ns.

- *FCAL timing:* used to reject events coming from interactions of the electron beam with residual gas in the beam pipe. Events are rejected if $|T_{FCAL}| > 8$ ns.

- *F–RCAL timing:* events coming from real *ep* interactions have particles with the same time in FCAL and in RCAL, so that $(T_{FCAL} - T_{RCAL}) \simeq 0$, while beam–gas events upstream the interaction point have times in FCAL and RCAL that differ of ~ 10 ns. The events are rejected if $(T_{FCAL} - T_{RCAL}) > 8$ ns.

- *Up–down timing:* used to reject cosmic muon events, that reach the upper part of the BCAL before than the lower one. The event is rejected if both the halves of the BCAL have valid timing, if there isn't any activity nor in the FCAL neither in the RCAL and if $(T_{\rm up} - T_{\rm down}) < -10$ ns.

- E and P_z: used to reject beam–gas interactions occurring near the interaction region. Since these events can essentially be thought as proton collisions on a fixed target, the produced particles have a small polar angle so that

$$\frac{\sum_i E_i \cos\theta_{\rm i}}{\sum_i E_i} \sim 1 \tag{2.8}$$

  where E_i is the energy of the ith cell of the calorimeter and θ_i is its polar angle. The event is rejected if

$$\frac{\sum_i E_i \cos\theta_{\rm i}}{\sum_i E_i} > 0.96. \tag{2.9}$$

- *Global timing:* if one of the calorimeter times is valid and greater than 10 ns the event is rejected.

The Third Level Trigger

If the event is accepted by the GSLT all the components send their information to the event builder (EVB), which combines their data, writes them in a standard format and makes them accessible to the Third Level Trigger (TLT). The input rate to the TLT is 100 Hz, while the output rate is 3–5 Hz, similar to the rate of the *ep* interactions. Therefore the aim of the TLT is not only to reject background events but also to select the particular classes of *ep* interactions under investigation.

The TLT consists of a series of algorithms written in FORTRAN, running on a PC farm, where a partial event reconstruction is done. The analysis of the events is not parallel, but the events are distributed to all the CPUs of the farm. In addition to the reconstruction program, also some selection programs are run on the data in order to select good *ep* events. The main information that the reconstruction program sends to the selection algorithms are the addresses and the energies of the calorimeter cells above threshold, and the parameters (momentum and position) of the tracks reconstructed by the CTD. Of course the resolutions on the energy and on the track parameters are worse than that obtained with the final reconstruction program.

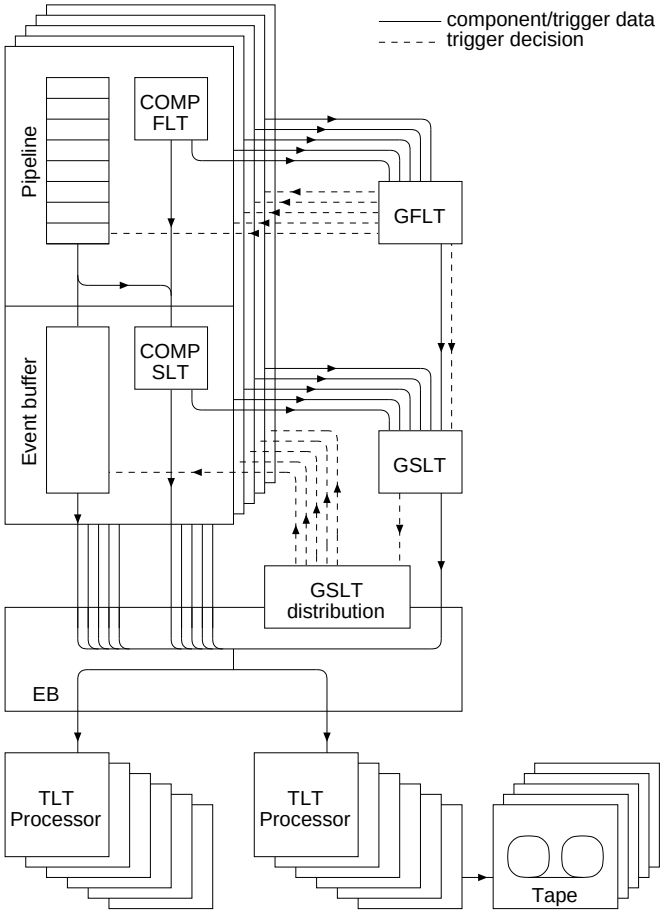

Figure 2.17: Schematic diagram of the ZEUS trigger and data acquisition system.

After having accepted an event, the TLT sends the data via an optical link to the DESY computing centre, where the events are written to disk to be available for further offline reconstruction and data analysis.

A schematic view of the ZEUS trigger and data acquisition system is shown in Fig. 2.17.

DST bits

Whenever an event has been accepted by the trigger system, its variables are reconstructed by the ZEPHYR[2] program. Being this an offline reconstruction, the physical observables are more precisely known than at TLT. A filter called DST (Data Summary Tapes) is based on this quantities and permits a further reduction of the data. In most of the cases a DST bit is obtained simply applying cuts similar to the ones of a TLT bit, just a bit more stringent, in order to further reduce the background.

[2]ZEus PHYsics Reconstruction.

2.3 Upgrades to ZEUS for HERA II

During the 2000–01 shutdown period of HERA, the ZEUS layout has been modified with the installation of new components. The upgrades were concentrated in three main areas: the vertex and the forward regions, and the luminosity measurement.

2.3.1 The Micro–Vertex Detector (MVD)

The tagging of the large flux of heavy quarks (charm and beauty) produced at HERA II can be greatly enhanced by the installation of a high–precision charged–particle detector as close as possible to a thin beam pipe. The silicon Micro–Vertex Detector (MVD, [47]), has been designed to address this issue.

The design of the MVD has been carried on fulfilling the following requirements:

- angular coverage of the region $10^\circ < \theta < 160^\circ$ around the interaction point;
- measurement of three points per track, in two projections each;
- 20 μm intrinsic hit resolution;
- two track separation of 200 μm;
- physical space available limited by the inner volume of the CTD ($r = 20$ cm), and by the beam pipe volume.

Accordingly to these specifications, the MVD has been divided into two parts, the barrel (BMVD) and the forward (FMVD) detectors (see Figure 2.18).

BMVD Layout

The barrel section is about 640 mm long; in Fig. 2.18 a cross section in the $r\phi$ plane is shown. In order to have a high efficiency for pattern recognition and the possibility to estimate momenta of the tracks at the trigger level, the design foresaw three layers of detectors.

The first layer, placed at $r = 3$–5 cm from the CTD axis follows the elliptical shape of the beam pipe; the second and third layers have circular shape and are placed at $r \sim 8.6$ and $r \sim 12.3$ cm.

The distribution of material in the BMVD is shown in Table 2.5.

BMVD impact parameter resolution

A test beam program has been set up to understand the performances of the silicon detectors and front–end electronics [48]. Fig. 2.19 shows the intrinsic resolution measured on a single detector as a function of the incident angle (with

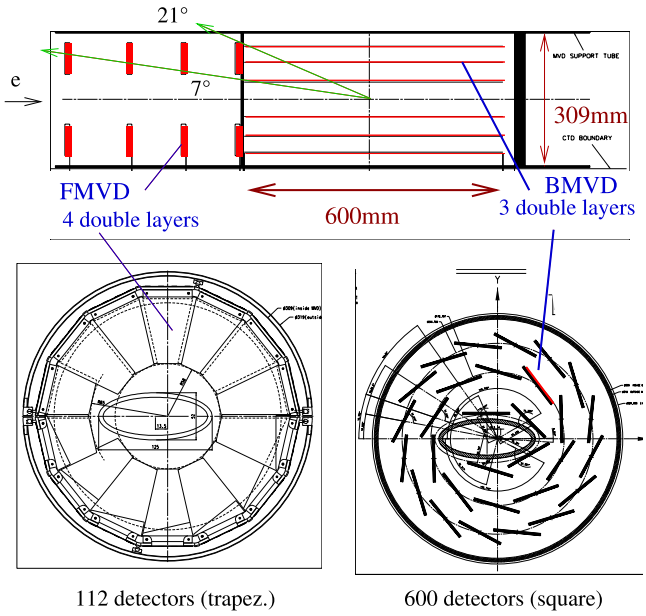

Figure 2.18: Layout of the MVD along the beam line (upper figure). A MVD forward wheel (lower left) and a BMVD section in the $r\phi$ plane (lower right).

Al–Be alloy beam pipe	1.1	
Ladder (per layer)	2.2	
Module		0.92
Support ladder		0.24
Cooling (water+pipes)		0.26
Cabling		0.78
Outer support	0.9	

Table 2.5: Average material in percentage of X_0 as seen by tracks perpendicular to the beam line in the BMVD section.

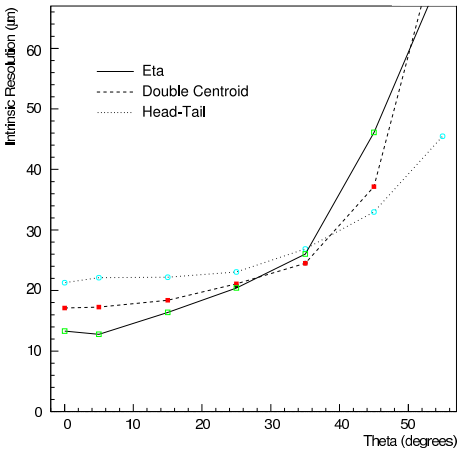

Figure 2.19: Intrinsic resolution as a function of the incident angle, measured with different hit reconstruction algorithms.

respect to the normal direction) with different hit reconstruction algorithms and a 6 GeV beam.

The improvement in resolution combined with the secondary vertex identification (not available with the pre–upgrade setup of ZEUS) will significantly enrich the heavy flavour physics program. As an example, the MVD will allow charm tagging with an efficiency between 10% and 20%, with purity around 30%, whereas charm identification via D^* mesons results in a very low efficiency, around 1% with the same purity (Fig. 2.20, [49]).

Silicon sensor design

The detectors are single sided made of high–resistivity (3–6 kΩ) n–type silicon, 300 μm thick (see Fig. 2.21). One side of the detector (64 mm × 64 mm) is n^+ doped and aluminized. The opposite face is covered by p^+ doped strips, 12 μm wide (14 μm for readout strips), with 20 μm pitch; one strip over six is AC coupled to an aluminum readout line. The number of readout strips is 512 per single detector. The coupling capacitance of the readout strips is achieved with a double layer of SiO_2 and Si_3N_4. The biasing of the strips is implemented by using poly–Si resistors which alternately connect even and odd strips to either of the two bias lines placed below the resistors and near the detector edges; the first and the last readout strips complete the bias ring being directly connected to the bias lines. Three guard rings surround the bias line. An additional n^+ doped ring is placed beyond the last guard ring, on the edges of the detector.

Capacitive charge division is used between the readout strips in order to limit the number of readout channels and achieve 10 μm spatial resolution for minimum

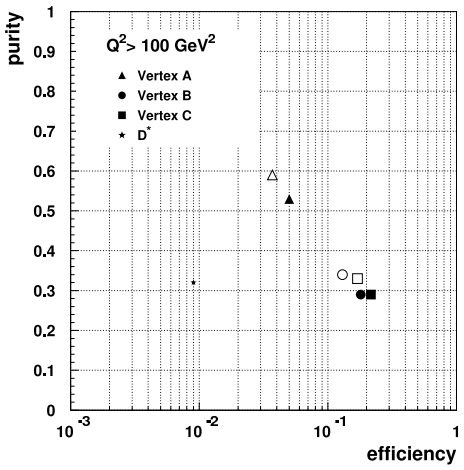

Figure 2.20: Purity versus efficiency for different selection criteria for charm in DIS ($Q^2 > 100$ GeV^2), as obtained on Monte Carlo simulations. The star ($\star$) shows results obtained by tagging the $D^\star$; this method was used in the pre–upgrade time. The full points (●, ■ and ▲) represent results from the baseline MVD configuration, whereas open points (○, □ and △) show results obtained by using the barrel part only; "Vertex A", "B" and "C" mean different tagging criteria.

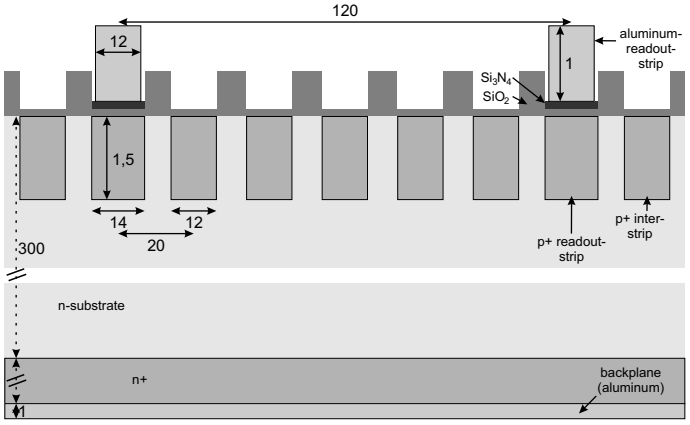

Figure 2.21: Cross section of a MVD silicon sensor.

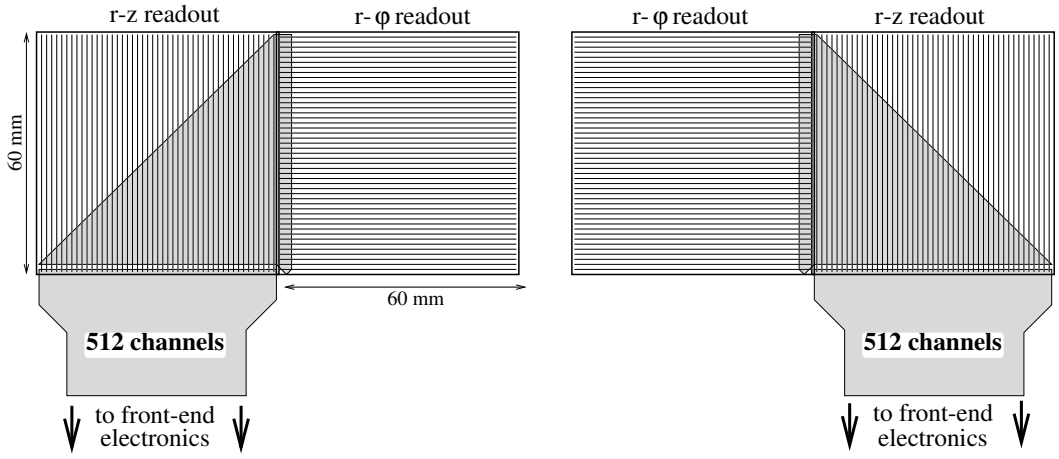

Figure 2.22: Two BMVD *half–modules*. They are mounted one on top of the other to form a *module*.

ionising particles crossing the detector with angles bigger than 30° with respect to the surface. By means of capacitive coupling between strips, the charge collection at intermediate strips induces charges on the readout strips which are inversely proportional to the distance between intermediate and readout strips [50]. Uniformity in charge collection can be achieved keeping all the strips (readout and intermediate) at the same potential. Charge losses to the ground planes can be significantly reduced by imposing the interstrip capacitance much larger than the capacitance to the detector backplane [50].

BMVD ladders

As shown in Fig. 2.22 two sensors are glued together to form a *half–module*. The two sensors (called $r\phi$ and z) are orthogonal and the strips of the first are connected to the one of the second via a kapton foil of triangular shape; the detectors have a small overlap in order to minimize the dead area of the cell. The resulting readout cell is approximately 120×60 mm^2. An additional fanout kapton, glued to the r–z plane, connects the strips to the front–end electronics. Two half–modules are placed on top of each other forming a readout *module* of 1024 channels and providing two coordinate reconstruction for a track traversing the module. Five readout modules are placed on a support ladder as shown in Fig. 2.23, left; due to its triangular shape, the fanout kapton is bent and the hybrid with the front–end electronics is positioned over the detector (see Fig. 2.23, right, for a cross section of the ladder). The total thickness of a ladder (module, support, cables) is 2.2% X_0.

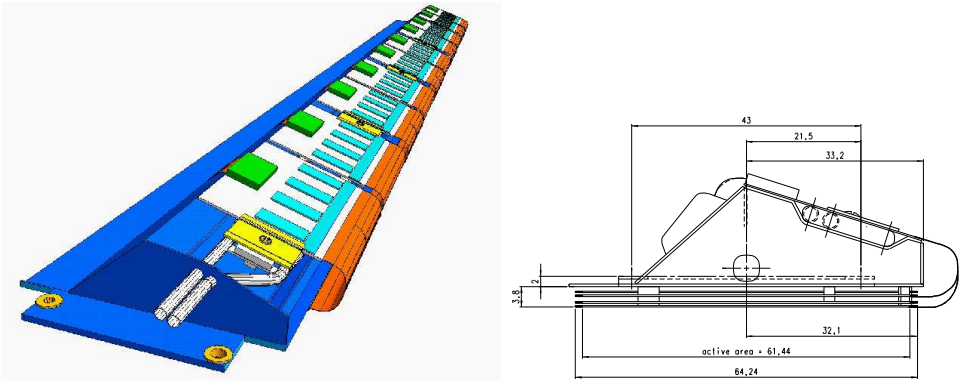

Figure 2.23: Layout of a complete ladder with five modules (left). Cross section of a barrel ladder (right); the detectors are located on the bottom of the structure while the hybrid is located on one edge of the triangular structure.

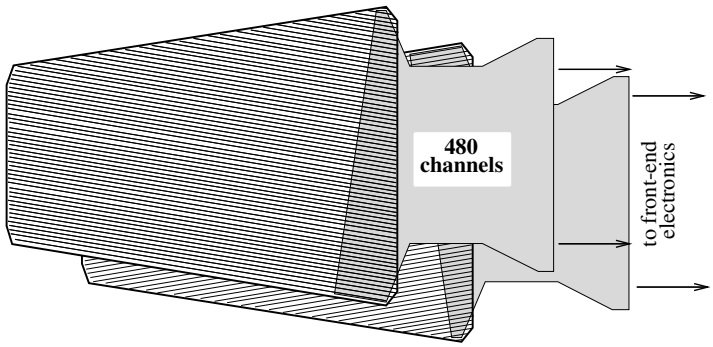

Figure 2.24: FMVD readout cell.

FMVD Layout

The forward vertex detector which is arranged in wheels extends to a polar angle $\theta = 0.15$ rad. The wheels provide essential tracking and vertexing information in regions which were not covered by the pre–upgrade tracking system. A wheel is made of two layers of 14 silicon planes of the same type of the barrel sensors and with a *wedge* shape, two sides being parallel and two tilted by 13° in opposite directions. One plane incorporates 480 readout strips. Fig. 2.18 shows a cross section of a forward wheel. By using two overlapping planes with strips oriented along the two tilted edges, one wheel provides r and ϕ coordinates per track (see Fig. 2.24). A small overlap between adjacent detectors in a wheel is used in order to minimise dead regions. The four wheels are positioned at $z = 32$, 45, 47 and 75 cm.

As for the BMVD, a kapton foil connects the readout strips with the front–end chips. Each detector is read separately using the same hybrid structure of the barrel section.

Readout electronics

The MVD silicon planes are read out by HELIX [51], an analog chip initially designed by ASIC laboratories in Heidelberg. The HELIX 2.2 version was specifically designed for the HERA–B experiment, whereas the 3.0 is an upgraded version from ZEUS. The chip integrates 128 channels with a charge–sensitive amplifier/shaper; the signals are then sampled in an analog pipeline with a maximum latency of 128 sampling intervals. The chip has an additional amplifier per each channel which is used to read the pipeline and is followed by a multiplexer and a buffer used to transfer the data on a serial bus. An important feature of HELIX is the possibility to synchronize the data transfer of more chips on a serial bus by using a daisy–chain mechanism; the first chip of the chain sends a token to the next chip after having transmitted all the data. The token moves on the chain and is sent back by the last chip through the chain until it reaches the first chip which generated it. The HELIX 3.0 chip implements a failsafe token which allows to exclude a bad chip from the readout chain without perturbing the functioning of the remaining chips of the chain.

The signal coming out of the HELIX chip is transferred via an analog link to the ADC cards about 10 m away from the detector hybrids. The ADC performs the pedestal and common mode subtractions and a preliminary reconstruction of the hit clusters. The signal is then transferred to the MVD second–level trigger processors and to the ZEUS event builder.

Radiation monitoring

The radiation monitor system (RadMon) for the MVD has the following main tasks:

- provides continuous monitoring data and generates warning signals to the ZEUS shift crew in case of a moderately high radiation;
- provides a fast dump signal to the electron kicker of HERA in case the radiation be too high;
- calculates the total integrated dose.

The maximum tolerable dose in the electronics is 3 kGy, with degradations in the S/N ratio already above 1 kGy (it can be partially recovered by tuning of the front end parameters). The design lifetime is 5 years of operation in the HERA environment, which sets the acceptable dose to 250 Gy/yr. The detectors chosen for the RadMon are 8 pairs of oxygen enriched silicon PIN diodes (1 cm^2 active surface, 300 μm thickness), placed near the beam pipe in the forward and rear part of the MVD. The two diodes forming a pair are mounted back to back with 1 mm of lead in between, to discriminate background of charged particles from synchrotron radiation.

In addition, in the rear region six plastic tubes have been glued on the beam pipe shield and are used to insert TLD dosimeters, providing a monthly dose measurement.

2.3.2 The Straw Tube Tracker (STT)

The higher luminosity expected at HERA II will increase the number of very high–Q^2 events in which the electron or positron is scattered in the forward direction. It will also give access to rare processes, including possible physics beyond the Standard Model, which tend to have forward jets and/or electrons. The pattern–recognition capabilities of the ZEUS Forward Tracker have therefore been improved by the replacement of two layers of transition–radiation detector by layers of straw tubes (Straw Tube Tracker – STT). The straws are approximately 7.5 mm in diameter and range in length from around 20 cm to just over 1 m. They are constructed from two layers of 50 μm kapton foil coated with a 0.2 μm layer of aluminum, surrounding a 50 μm wire at the centre. The straws are arranged in wedges consisting of three layers rotated with respect to each other, to give a three–dimensional reconstruction. Each of the two "supermodules" consists of four layers of such wedges.

2.3.3 The luminosity monitor

The measurement of luminosity at HERA II must cope with the greatly increased synchrotron–radiation background and the higher probability for multiple bremsstrahlung photons in a single beam crossing. To compensate for the latter, two devices have been constructed with very different systematic uncertainties. Both devices use the information from a small calorimeter placed around 6 m from the interaction point which detects the radiating electron. Hopefully a reduction of the systematic errors can be obtained from independent luminosity measurements by using very different techniques to attain a precision of about 1%.

Chapter 3

Simulation of the physical processes

The use of simulation programs is essential in physical analyses. In fact a better understanding of the data and the detector behaviour can be achieved by simulating the full detector response to physical events. Moreover, the theoretical models implemented in the simulations can be tested by comparisons to real data.

The simulation of physical events at HERA is done in two main steps. First, the *ep* scattering process is simulated using an *event generator*. This program, following the prescriptions of the implemented theoretical models, provides the the four–momenta of all the final state particles. In a second step, all the detector and the trigger systems are simulated, in order to determine their response to the particles produced in the physical process. These simulations are based on Monte Carlo (MC) techniques, which turn out to be an essential tool to understand the actual complexity of high energy physical processes and particle detectors.

3.1 General structure of an event generator

The factorization theorem for hard processes [52] is the main theoretical justification for Monte Carlo event generators. Following the prescriptions of the theorem, an *ep* scattering process characterized by a hard scale can be factorized into the following distinct stages (Fig. 3.1):

- *hard sub–process:* is the main feature of the event, the interaction between a parton, extracted from the proton, and the electron or a photon (or a photon constituent in resolved photon events). This kind of process can be calculated in a fixed order perturbative expansion since it involves a hard scale μ;

- *initial and final state radiation:* in processes involving charged and coloured objects the topology of an event can be strongly influenced by the emission of gluons and photons in the initial or final state. These perturbative corrections are usually modelled by the so called *parton shower method*: the

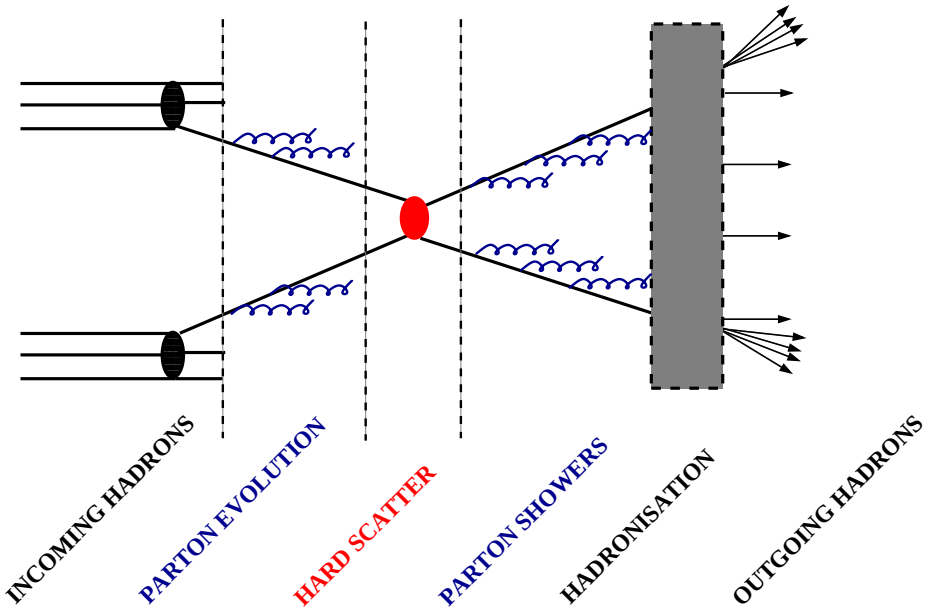

Figure 3.1: Schematic representation of the processes involved in a typical hard interaction.

radiation is simulated by an arbitrary number of branchings of one parton into two, like $e \to e\gamma$, $q \to qg$, $q \to q\gamma$, $g \to q\bar{q}$. The kernel $P_{a\to bc}(z)$ of a branching gives the probability distribution of the energy sharing, with daughter b taking a fraction z and daughter c the remaining $(1-z)$ of the initial energy E_a. The two daughters may branch in turn, producing other partons, and so on. Via the *initial state radiation* a parton, constituent of the incident hadron (photon), having low space–like virtuality, radiates time–like partons, increasing its space–like virtual mass. On the other hand, via the *final state radiation* an outgoing virtual parton with large time–like mass generates a shower of partons having lower virtuality. The shower evolution stops at some fixed scale μ_0, typically of the order of 1 GeV;

- *hadronisation:* it is the process in which colourless hadrons are formed starting from coloured partons. It is a non–perturbative phenomenon and is still not completely understood. Therefore simulation programs model the hadronisation process using phenomenological inputs. The main hadronisation models currently available are the cluster model, implemented in the HERWIG Monte Carlo [53] and the string model, implemented in the PYTHIA Monte Carlo program [54];

- *beam remnant:* in *ep* interactions, the simulation programs reconstruct the particles that have gone through the initial state radiation and have then generated the partons involved in the hard sub–process. These initial particles, one from each beam, are a parton extracted from the proton and an

electron or a photon or, in resolved photon processes, a parton from the photon. They carry only a fraction of the initial beam energy, the rest is taken by the beam remnant. If the shower initiator is coloured, also is the beam remnant that is therefore connected to the rest of the event and has to be fragmented and reconstructed coherently.

3.2 The GRAPE generator

GRAPE–Dilepton [55] is a Monte Carlo event generator for di–lepton production in *ep* collisions. GRAPE stands for "GRAce–based generator for Proton–Electron collisions", since the FORTRAN code used to calculate the Feynman amplitudes is generated by the GRACE program [56]. This is the first time for GRACE to be applied to the case where there is a composite particle (the proton) in the initial state.

The generator has the following features:

- The cross–section calculation is based on the exact matrix elements in the electroweak theory at tree level. The Bethe–Heitler process is included, with all its 2γ, γZ^0 and Z^0Z^0 collisions, as well as the QED–Compton and the Z^0 on/off shell production. In the case of di–electrons, the interference between the like–sign leptons in the final state is taken into account.
- The fermion masses are kept non–zero; this makes it possible to use GRAPE with arbitrary small scattering angles of $e^{\pm}$ and/or small invariant masses of di–lepton.
- The calculation of the proton vertex covers the whole kinematic region by dividing it into three categories: elastic, quasi–elastic, DIS. This will be explained in detail in the next section.
- Both the initial state radiation (ISR) and final state radiation (FSR) can be included.

Physical aspects

The GRAPE generator simulates the $e^{\pm}p \to e^{\pm}l^+l^-X$ process. The phase–space is divided into three regions, depending on the opposite of the squared 4-momentum transferred at the proton vertex (Q_p^2) and the invariant mass of the hadronic system ($M_{\rm had}$):

$$Q_p^2 \equiv -[p_e - (p_{e'} + p_{l^+} + p_{l^-})]^2, \tag{3.1}$$

$$M_{\rm had}^2 \equiv [(p_e + p_p) - (p_{e'} + p_{l^+} + p_{l^-})]^2, \tag{3.2}$$

where p_e and p_p are the 4-momenta of the incoming particles (electron and proton), after ISR, whereas $p_{e'}$, p_{l^+} and p_{l^-} are the 4-momenta of the outgoing leptons, before the FSR. The three regions are

- *elastic:* $M_{\mathrm{had}} = M_p$,
- *quasi–elastic:* $Q_p^2 < Q_{\mathrm{min}}^2$, or $M_p + M_{\pi^0} < M_{\mathrm{had}} < M_{\mathrm{cut}}$,
- *DIS:* $Q_p^2 > Q_{\mathrm{min}}^2$ and $M_{\mathrm{had}} > M_{\mathrm{cut}}$,

where M_p and M_{π^0} are the masses of the proton and the neutral pion, respectively. Q_{min} is set to around 1 GeV depending on the parton density function used in the DIS process. The recommended value for M_{cut} is 5 GeV.

In the elastic case, the matrix element is calculated accordingly to (1.8), where the proton charge and momentum substitute the ones of the quark, and the Rosenbluth formula is used for the proton–proton–photon vertex (see [3], Sect. 8.2):

$$\Gamma^{\mu}_{pp\gamma} = e_p \left(\mu_p G_E^p(Q_p^2)\gamma^{\mu} - \frac{p_p^{\mu} + p_{p'}^{\mu}}{2M_p} \frac{k_p}{1 + Q_p^2/4M_p^2} G_E^p(Q_p^2) \right). \tag{3.3}$$

e_p indicates the proton electric charge, $\mu_p = (1 + k_p)\mu_B$, k_p is the anomalous magnetic moment of the proton, μ_B is the Bohr magneton, $p_{p'}$ is the 4-momentum of the outgoing proton, and G_E^p is the *electric form factor* of the proton. This form factor is calculated accordingly to the formula of the dipole fit:

$$G_E^p(Q_p^2) = \left(1 + \frac{Q_p^2}{0.71\,\mathrm{GeV}^2} \right)^{-2}. \tag{3.4}$$

In the quasi–elastic case, the hadron tensor $W_{\mu\nu}$ (see Eq. (1.20)) is calculated making use of the electromagnetic structure functions

$$W_1 = \frac{F_1}{M_p}, \tag{3.5}$$

$$W_2 = F_2 \frac{M_p}{p_p \cdot q}, \tag{3.6}$$

as parameterised by Brasse et al. [57] for $M_{\mathrm{had}} < 2$ GeV, or by ALLM97 [58] for $M_{\mathrm{had}} > 2$ GeV. The exclusive hadronic final state is generated using the MC event generator Sophia [59].

In the DIS case, the Bethe–Heitler, Cabibbo–Parisi and Drell–Yan diagrams involving an electron and a quark are calculated. The parton densities are calculated by PDFLIB [60] with Q_p^2 as a QCD scale. The simulation of the proton remnant and the hadronisation are performed by Pythia. In the region

$$u \equiv |[p_q - (p_{l^+} + p_{l^-})]^2| \lesssim 25 \ \mathrm{GeV}^2, \tag{3.7}$$

where p_q is the 4-momentum of the incoming quark, the process should be treated as a Drell–Yan interaction between the quark and the resolved photon; this is not implemented in Grape, and the explicit cut $u > 25$ GeV^2 is applied.

The effect of ISR is included in the cross–section calculation using the structure function method described in [61], where the squared 4-momentum transfer at the lepton vertex $(p'_e - p_e)^2$ is used as a QED scale. FSR is performed by Pythia using the parton shower method.

3.3 The LPAIR generator

The LPAIR generator [62] simulates only the two–photon Bethe–Heitler process (Fig. 1.9a); this process is dominant in most of the phase space (e.g. see Fig. 1.11). It is however expected that in the region of low invariant masses of the di–lepton system, Cabibbo–Parisi processes become dominant. In the high mass region, also the contribution from the Z^0 production has to be considered. In case of di–electron production, the interference of identical particles in the final state is neglected.

Also here the phase space is divided into three regions, depending on the proton vertex description:

- *elastic:* used for the coherent, elastic scattering of the proton. As GRAPE does, LPAIR uses the Rosenbluth formula to describe the proton form factor.
- *inelastic:* for inelastic scattering. The cross–section is integrated by an empirical fit [57] to the resonance region ($M_{\rm had} < 1.99$ GeV, $Q_p^2 < 5$ GeV^2) and a structure function fit [63] elsewhere.
- *DIS:* as a complement to the inelastic form factors, an option to use PDFLIB is implemented, but makes only sense for high Q_p^2 values due to the validity range ($Q_p^2 > 2...5$ GeV^2) of the PDFLIB functions.

3.4 The DJANGOH generator

The event generator DJANGOH [64] is an interface of the Monte Carlo programs HERACLES [65] and LEPTO [66].

HERACLES simulates neutral and charged current *ep* interactions at HERA; it optionally treats the *ep* scattering either by means of structure function parameterizations or on the basis of parton distribution functions in the framework of the quark–parton model. It includes QED and QCD radiative corrections, comprising single photon emission from the lepton or the quark line as well as self energy corrections and the complete set of one–loop weak corrections. These corrections are sufficient to describe the cross-section with either an accuracy of a few percent or less than 1% if $Q^2 \leq 2 \times 10^3$ GeV^2.

LEPTO is used to simulate the hadronic final state; first order QCD matrix elements for gluon radiation and boson–gluon fusion are implemented and higher order QCD radiation is treated using parton showers. Hadronisation is performed using the Lund string model, implemented in JETSET/PYTHIA [67]. Rapidity gap events are generated through a model based on soft colour interactions.

3.5 The COMPTON generator

The COMPTON program generates $ep \to e\gamma X$ events (Fig. 3.2) accordingly to an approximated cross section obtained by neglecting Q^2/W^2 dependence (Q^2 and

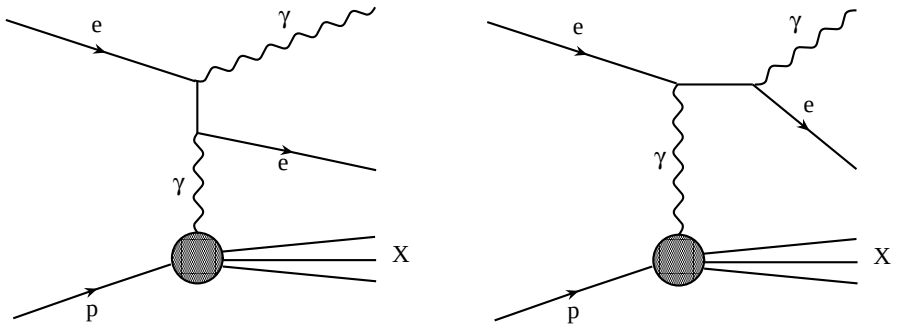

Figure 3.2: Feynmann diagrams for the reaction $ep \to e\gamma X$, s (left) an t–channel (right).

W^2 are defined in Sect. 1.1) and the mass of the electron. This is only a dynamical approximation, since all physical quantities (including Q^2) are generated and the kinematics is derived in an exact way. The generation is performed over the whole experimentally available phase space (which is determined by the detector acceptance).

In a second stage the exact cross section for the processes depicted in Fig. 3.2 is calculated, and a weight for the event is obtained as the ratio of this cross section and the approximated one, used for the generation. This procedure allows, in principle, to provide an exact Monte Carlo; however, the more Q^2/W^2 increases the larger are the event weights. Obviously events with large weights must be rejected since otherwise the statistical accuracy would decrease and it would become difficult to provide an output of individual (unweighted) events. Compton events with relatively small weights can be selected by applying an acoplanarity cut ($|180^\circ - \Delta\phi_{e\gamma}| < 45^\circ$ being the default) and limiting the polar acceptance (being $3.6^\circ < \theta_{e,\gamma} < 176^\circ$ the default).

3.6 The detector simulation

All the event generators supported in ZEUS are gathered in a software program called AMADEUS. The user can choose the event generator, which gives as output all the four–momenta of the particles produced in the hard scattering process and all the relevant kinematic variables.

The data produced by an event generator are the input to the ZEUS detector and trigger simulation program, MOZART[1]. MOZART is based on the GEANT [68] package, whose kernel contains a description of all the detector components, including the material they are made of, their shapes and positions. The program traces the particles through the whole detector, simulating its response and

[1]MOnte Carlo for ZEUS Analysis Reconstruction and Triggering.

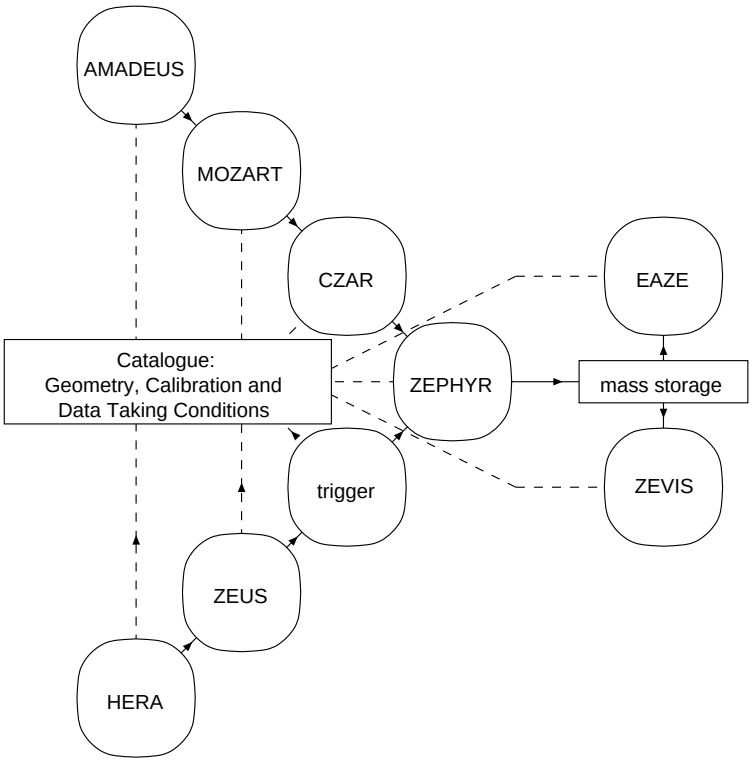

Figure 3.3: A schematic diagram of ZEUS data and Monte Carlo reconstruction chain.

keeping into account physical processes such as energy loss, multiple scattering and particle decays in flight.

The events pass then through the CZAR[2] package, that simulates the trigger logic as implemented in the data taking.

As a final step, the generated sample is processed by the ZEUS reconstruction program, ZEPHYR[3]. This program reconstructs the event variables, like particle momenta and energies, treating the data and the Monte Carlo in the same way. All the information coming from the different detectors making up ZEUS are taken as inputs by ZEPHYR.

All the ZEUS data are organized using the ADAMO[4] [69] data management system, used for the data storage in memory or on external media and for their documentation.

The access to the data by the users is done with the EAZE[5] program; the ZEVIS[6] program generates 2D and 3D representations of the real or simulated

[2]Complete ZGANA Analysis Routine; ZGANA stands for ZEUS GEANT ANALYSIS.
[3]ZEus PHYsics Reconstruction.
[4]Aleph DAta MOdel.
[5]Effortless Analysis of ZEUS Events.
[6]Zeus Event VISualization.

events. A diagram of the ZEUS reconstruction scheme for data and Monte Carlo is shown in Fig. 3.3.

3.7 MC samples for multi–electron search

Di–electron production was simulated by using the GRAPE MC. Some LPAIR samples were generated too, in order to compare the prediction of this generator to the one of GRAPE. The neutral current DIS background was generated by the DJANGOH program, whereas the QED–Compton background was simulated by using the COMPTON generator. In the next section a detailed list of the generated samples follows.

3.7.1 GRAPE samples

GRAPE: $e^+p \to e^+e^+e^-X$, **1996–97 ZEUS configuration**			
Type	Cuts	Cross–section [pb]	Lumi [pb^{-1}]
Elastic	elastic process	(1.2649±0.0012)E+01	2.372E+03
Quasi–elastic	$1.08 < M_{\mathrm{had}} < 5$ GeV	(5.5466±0.0091)E+00	1.803E+03
	$M_{\mathrm{had}} > 5$ GeV	(1.9450±0.0041)E−01	1.542E+04
DIS	eu scattering	(3.196±0.011)E+01	1.252E+03
	$e\bar{u}$ scattering	(7.915±0.023)E+00	1.516E+03
	ed and es scattering	(6.185±0.019)E+00	1.617E+03
	$e\bar{d}$ and $e\bar{s}$ scattering	(3.563±0.011)E+00	1.401E+03
Common cuts: 1 electron with $5^\circ < \theta_e < 175^\circ$ and $P_T^e > 5$ GeV			

GRAPE: $e^+p \to e^+e^+e^-X$, **1996–97 ZEUS configuration**			
Type	Cuts	Cross–section [pb]	Lumi [pb^{-1}]
Elastic	elastic process	(1.5401±0.0020)E+00	1.947E+04
Quasi–elastic	$1.08 < M_{\mathrm{had}} < 5$ GeV	(7.2213±0.0066)E−01	4.154E+3
	$M_{\mathrm{had}} > 5$ GeV	(7.790±0.032)E−03	3.851E+05
DIS	eu scattering	(5.608±0.016)E+00	5.350E+03
	$e\bar{u}$ scattering	(1.1176±0.0031)E+00	8.943E+03
	ed and es scattering	(9.781±0.037)E−01	1.022E+04
	$e\bar{d}$ and $e\bar{s}$ scattering	(5.155±0.018)E−01	9.700E+03
Common cuts: 1 electron with $5^\circ < \theta_e < 175^\circ$ and $P_T^e > 10$ GeV			

GRAPE: $e^-p \to e^-e^+e^-X$, **1998–99 ZEUS configuration**			
Type	Cuts	Cross–section [pb]	Lumi [pb^{-1}]
Elastic	elastic process	(1.3365±0.0011)E+01	7.890E+02
Quasi–elastic	$1.08 < M_{\mathrm{had}} < 5$ GeV	(5.7675±0.0085)E+00	1.039E+03
	$M_{\mathrm{had}} > 5$ GeV	(2.1945±0.0046)E−01	1.367E+04
DIS	eu scattering	(3.330±0.011)E+01	1.017E+03
	$e\bar{u}$ scattering	(8.025±0.023)E+00	1.059E+03
	ed and es scattering	(6.430±0.019)E+00	1.005E+03
	$e\bar{d}$ and $e\bar{s}$ scattering	(3.701±0.012)E+00	1.073E+03
Common cuts: 1 electron with $5^\circ < \theta_e < 175^\circ$ and $P_T^e > 5$ GeV			

GRAPE: $e^-p \to e^-e^+e^-X$, **1998–99 ZEUS configuration**			
Type	Cuts	Cross–section [pb]	Lumi [pb^{-1}]
Elastic	elastic process	(1.6653±0.0019)E+00	1.800E+04
Quasi–elastic	$1.08 < M_{\mathrm{had}} < 5$ GeV	(7.7043±0.0079)E−01	3.894E+03
	$M_{\mathrm{had}} > 5$ GeV	(9.435±0.036)E−03	1.060E+06
DIS	eu scattering	(6.169±0.032)E+00	4.863E+03
	$e\bar{u}$ scattering	(1.1462±0.0040)E+00	8.716E+03
	ed and es scattering	(1.0674±0.0038)E+00	9.359E+03
	$e\bar{d}$ and $e\bar{s}$ scattering	(5.600+-0.015)E−01	8.929E+03
Common cuts: 1 electron with $5^\circ < \theta_e < 175^\circ$ and $P_T^e > 10$ GeV			

GRAPE: $e^+p \to e^+e^+e^-X$, **1999–2000 ZEUS configuration**			
Type	Cuts	Cross–section [pb]	Lumi [pb^{-1}]
Elastic	elastic process	(1.3391±0.0013)E+01	2.240E+03
Quasi–elastic	$1.08 < M_{\mathrm{had}} < 5$ GeV	(5.755±0.047)E+00	2.607E+03
	$M_{\mathrm{had}} > 5$ GeV	(2.1979±0.0034)E−01	4.540E+04
DIS	eu scattering	(3.3565±0.017)E+01	8.936E+02
	$e\bar{u}$ scattering	(8.497±0.028)E+00	1.765E+03
	ed and es scattering	(6.547±0.019)E+00	1.527E+03
	$e\bar{d}$ and $e\bar{s}$ scattering	(3.489±0.011)E+00	2.592E+03
Common cuts: 1 electron with $5^\circ < \theta_e < 175^\circ$ and $P_T^e > 5$ GeV			

GRAPE: $e^+p \to e^+e^+e^-X$, **1999–2000 ZEUS configuration**			
Type	Cuts	Cross–section [pb]	Lumi [pb^{-1}]
Elastic	elastic process	(1.665±0.019)E+00	8.997E+03
Quasi–elastic	$1.08 < M_{\mathrm{had}} < 5$ GeV	(7.7044±0.0079)E−01	1.947E+04
	$M_{\mathrm{had}} > 5$ GeV	(9.431±0.036)E−03	1.059E+06
DIS	eu scattering	(5.932±0.019)E+00	5.002E+03
	$e\bar{u}$ scattering	(1.2344±0.0036)E+00	1.215E+04
	ed and es scattering	(1.0443±0.0031)E+00	9.579E+03
	$e\bar{d}$ and $e\bar{s}$ scattering	(5.694±0.024)E−01	1.544E+04
Common cuts: 1 electron with $5^\circ < \theta_e < 175^\circ$ and $P_T^e > 10$ GeV			

3.7.2 LPAIR samples

LPAIR: $e^+p \to e^+e^+e^-X$, **1996–97 ZEUS configuration**			
Type	Cuts	Cross–section [pb]	Lumi [pb^{-1}]
Elastic	$0 < P^e_{T,\max} < 5$ GeV	(6.308±0.004)E+01	6.341E+02
	$5 < P^e_{T,\max} < 10$ GeV	(8.337±0.007)E+00	1.199E+03
	$10 < P^e_{T,\max} < 20$ GeV	(1.050±0.001)E+00	4.760E+03
	$20 < P^e_{T,\max} < 50$ GeV	(9.63±0.01)E−02	3.115E+04
	$P^e_{T,\max} > 50$ GeV	(1.202±0.001)E−03	8.319E+05
Common cuts: 2 electrons with $10^\circ < \theta_e < 170^\circ$ and $E_e > 3$ GeV			
Quasi–elastic	$0 < P^e_{T,\max} < 5$ GeV	(8.058±0.006)E+00	1.241E+03
	$5 < P^e_{T,\max} < 10$ GeV	(1.2067±0.0006)E+00	4.144E+03
	$10 < P^e_{T,\max} < 20$ GeV	(1.8360±0.0010)E−01	5.447E+03
	$20 < P^e_{T,\max} < 50$ GeV	(1.933±0.001)E−02	5.173E+04
	$P^e_{T,\max} > 50$ GeV	(1.969±0.001)E−04	5.069E+06
Common cuts: 2 electrons with $10^\circ < \theta_e < 170^\circ$ and $E_e > 3$ GeV $Q^2_p < 1$ GeV^2 and $1.07 < M_{\mathrm{had}} < 2.2$ GeV			
DIS	$0 < P^e_{T,\max} < 5$ GeV	(2.339±0.002)E+1	4.275E+02
	$5 < P^e_{T,\max} < 10$ GeV	(6.411±0.004)E+00	1.560E+03
	$10 < P^e_{T,\max} < 20$ GeV	(1.1722±0.0007)E+00	4.254E+03
	$20 < P^e_{T,\max} < 50$ GeV	(1.3009±0.0008)E−1	7.617E+03
	$P^e_{T,\max} > 50$ GeV	(1.683±0.001)E−3	5.894E+05
Common cuts: 2 electrons with $10^\circ < \theta_e < 170^\circ$ and $E_e > 3$ GeV $Q^2_p > 1$ GeV^2 and $M_{\mathrm{had}} > 1.07$ GeV			

3.7.3 DJANGOH samples

DJANGOH: **NC DIS, 1996–97 ZEUS configuration**		
Cuts	Cross–section [pb]	Lumi [pb^{-1}]
$Q^2 > 100$ GeV^2	7.582E+3	4.428E+1
$Q^2 > 400$ GeV^2	1.097E+3	5.645E+2
$Q^2 > 1250$ GeV^2	1.821E+2	5.343E+2
$Q^2 > 2500$ GeV^2	5.312E+1	5.635E+2
$Q^2 > 5000$ GeV^2	1.292E+1	6.178E+2

DJANGOH: **NC DIS, 1998–99 ZEUS configuration**		
Cuts	Cross–section [pb]	Lumi [pb^{-1}]
$Q^2 > 100$ GeV^2	8.158E+3	4.590E+1
$Q^2 > 400$ GeV^2	1.197E+3	1.670E+2
$Q^2 > 1250$ GeV^2	2.169E+2	1.567E+2
$Q^2 > 2500$ GeV^2	7.170E+1	1.394E+2
$Q^2 > 5000$ GeV^2	2.163E+1	1.151E+2

DJANGOH: **NC DIS, 1999–2000 ZEUS configuration**		
Cuts	Cross–section [pb]	Lumi [pb^{-1}]
$Q^2 > 100$ GeV^2	8.122E+3	1.157E+2
$Q^2 > 400$ GeV^2	1.168E+3	6.648E+2
$Q^2 > 1250$ GeV^2	1.975E+2	7.078E+2
$Q^2 > 2500$ GeV^2	5.893E+1	6.780E+2
$Q^2 > 5000$ GeV^2	1.484E+1	6.728E+2

3.7.4 COMPTON MC samples

COMPTON: **QED Compton, 1996–97 ZEUS configuration**		
Cuts	Cross–section [pb]	Lumi [pb^{-1}]
$1 < M_{e\gamma} < 10$ GeV	1.752E+2	5.128E+2
$10 < M_{e\gamma} < 20$ GeV	9.627E+1	5.190E+2
$20 < M_{e\gamma} < 50$ GeV	3.331E+1	8.997E+2
$50 < M_{e\gamma} < 100$ GeV	3.579	5.586E+3
$M_{e\gamma} > 100$ GeV	3.36E−1	2.954E+4
Common cuts: $0 < \theta_{e,\gamma} < 170°$ and $E_{e,\gamma} > 3$ GeV and $\pi - \Delta\phi_{e\gamma} < 45°$		

COMPTON: **QED Compton, 1998–99 ZEUS configuration**		
Cuts	Cross–section [pb]	Lumi [pb^{-1}]
$1 < M_{e\gamma} < 10$ GeV	1.784E+2	5.039E+2
$10 < M_{e\gamma} < 20$ GeV	9.833E+1	5.085E+2
$20 < M_{e\gamma} < 50$ GeV	3.466E+1	5.770E+2
$50 < M_{e\gamma} < 100$ GeV	3.777	2.645E+3
$M_{e\gamma} > 100$ GeV	3.91E−1	2.558E+4
Common cuts: $0 < \theta_{e,\gamma} < 170°$ and $E_{e,\gamma} > 3$ GeV and $\pi - \Delta\phi_{e\gamma} < 45°$		

3.8 MC samples for di–muon search

Di–muon production was simulated by using the GRAPE MC. Some LPAIR samples were generated too, in order to compare the prediction of this generator to the one of GRAPE.

3.8.1 GRAPE samples

GRAPE: $e^+p \to e^+\mu^+\mu^-X$, **1996–97 ZEUS configuration**			
Type	Cuts	Cross–section [pb]	Lumi [pb^{-1}]
Elastic	elastic process	(2.7029±0.0014)E+02	9.249E+01
Quasi–elastic	$Q_p^2 < 100$ GeV^2 and $M_{\text{had}} < 20$ GeV	(1.4263±0.0009)E+02	1.746E+02
Common cuts: 2 muons with $5° < \theta_\mu < 175°$, $E_\mu > 0.5$ GeV and $P_T^\mu > 0.5$ GeV $M_{\mu\mu} > 3$ GeV and $Q^2 < 4$ GeV^2			

GRAPE: $e^+p \to e^+\mu^+\mu^-X$, **1996–97 ZEUS configuration**			
Type	Cuts	Cross–section [pb]	Lumi [pb^{-1}]
Elastic	elastic process	(9.6538±0.0065)E+00	3.108E+03
Quasi–elastic	$1.08 < M_{\mathrm{had}} < 5$ GeV	(4.7605±0.0036)E+00	2.101E+03
	$M_{\mathrm{had}} > 5$ GeV	(1.4609±0.0023)E−01	2.048E+04
DIS	eu scattering	(1.2172±0.0014)E+01	1.642E+03
	$e\bar{u}$ scattering	(2.3806±0.0030)E+00	2.100E+03
	ed and es scattering	(2.1608±0.0025)E+00	2.312E+03
	$e\bar{d}$ and $e\bar{s}$ scattering	(1.1227±0.0014)E+00	2.670E+03
Common cuts: 1 muon with $5^\circ < \theta_\mu < 175^\circ$ and $P_T^\mu > 5$ GeV			

GRAPE: $e^+p \to e^+\mu^+\mu^-X$, **1996–97 ZEUS configuration**			
Type	Cuts	Cross–section [pb]	Lumi [pb^{-1}]
Elastic	elastic process	(1.1893±0.0008)E+00	2.522E+04
Quasi–elastic	$1.08 < M_{\mathrm{had}} < 5$ GeV	(6.0586±0.0043)E−01	1.642E+04
	$M_{\mathrm{had}} > 5$ GeV	(5.002±0.027)E−03	5.998E+05
DIS	eu scattering	(1.7514±0.0022)E+00	1.142E+04
	$e\bar{u}$ scattering	(2.2965±0.0032)E−01	2.177E+04
	ed and es scattering	(2.6504±0.0034)E−01	1.885E+04
	$e\bar{d}$ and $e\bar{s}$ scattering	(1.1512±0.0016)E−01	2.606E+04
Common cuts: 1 muon with $5^\circ < \theta_\mu < 175^\circ$ and $P_T^\mu > 10$ GeV			

GRAPE: $e^-p \to e^-\mu^+\mu^-X$, **1998–99 ZEUS configuration**			
Type	Cuts	Cross–section [pb]	Lumi [pb^{-1}]
Elastic	elastic process	(2.7832±0.0014)E+02	8.935E+01
Quasi–elastic	$Q_p^2 < 100$ GeV^2 and $M_{\mathrm{had}} < 20$ GeV	(1.4621±0.0010)E+02	1.710E+02
Common cuts: 2 muons with $5^\circ < \theta_\mu < 175^\circ$, $E_\mu > 0.5$ GeV and $P_T^\mu > 0.5$ GeV $M_{\mu\mu} > 3$ GeV and $Q^2 < 4$ GeV^2			

GRAPE: $e^-p \to e^-\mu^+\mu^-X$, **1998–99 ZEUS configuration**			
Type	Cuts	Cross–section [pb]	Lumi [pb^{-1}]
Elastic	elastic process	(1.0198±0.0008)E+01	1.078E+03
Quasi–elastic	$1.08 < M_{\mathrm{had}} < 5$ GeV	(4.9679±0.0040)E+00	1.006E+03
	$M_{\mathrm{had}} > 5$ GeV	(1.6661±0.0030)E−01	1.798E+04
DIS	eu scattering	(1.3033±0.0014)E+01	1.074E+03
	$e\bar{u}$ scattering	(2.6570±0.0031)E+00	1.127E+03
	ed and es scattering	(2.3637±0.0026)E+00	1.269E+03
	$e\bar{d}$ and $e\bar{s}$ scattering	(1.2187±0.0014)E+00	2.458E+03
Common cuts: 1 muon with $5^\circ < \theta_\mu < 175^\circ$ and $P_T^\mu > 5$ GeV			

GRAPE: $e^-p \to e^-\mu^+\mu^- X$, **1998–99 ZEUS configuration**			
Type	Cuts	Cross–section [pb]	Lumi [pb^{-1}]
Elastic	elastic process	(1.2846±0.0009)E+00	7.785E+03
Quasi–elastic	$1.08 < M_{\text{had}} < 5$ GeV	(6.5070±0.0049)E−01	7.644E+03
	$M_{\text{had}} > 5$ GeV	(6.256±0.056)E−03	7.992E+05
DIS	eu scattering	(1.9124±0.0024) E+00	5.224E+03
	$e\bar{u}$ scattering	(2.5538±0.0035)E−01	1.175E+04
	ed and es scattering	(2.9104±0.0040)E−01	1.028E+04
	$e\bar{d}$ and $e\bar{s}$ scattering	(1.3005±0.0017)E−01	2.305E+04
Common cuts: 1 muon with $5^\circ < \theta_\mu < 175^\circ$ and $P_T^\mu > 10$ GeV			

GRAPE: $e^+p \to e^+\mu^+\mu^- X$, **1999–2000 ZEUS configuration**			
Type	Cuts	Cross–section [pb]	Lumi [pb^{-1}]
Elastic	elastic process	(2.7831±0.0014)E+02	8.980E+01
Quasi–elastic	$Q_p^2 < 100$ GeV^2 and $M_{\text{had}} < 20$ GeV	(1.4621±0.0010)E+02	1.709E+02
Common cuts: 2 muons with $5^\circ < \theta_\mu < 175^\circ$, $E_\mu > 0.5$ GeV and $P_T^\mu > 0.5$ GeV $M_{\mu\mu} > 3$ GeV and $Q^2 < 4$ GeV^2			

GRAPE: $e^+p \to e^+\mu^+\mu^- X$, **1999–2000 ZEUS configuration**			
Type	Cuts	Cross–section [pb]	Lumi [pb^{-1}]
Elastic	elastic process	(1.01979±0.00076)E+01	2.059E+03
Quasi–elastic	$1.08 < M_{\text{had}} < 5$ GeV	(4.9679±0.0040)E+00	2.012E+03
	$M_{\text{had}} > 5$ GeV	(1.6661±0.0030)E−01	1.801E+04
DIS	eu scattering	(1.2977±0.0014)E+01	2.004E+03
	$e\bar{u}$ scattering	(2.6815±0.0032)E+00	2.049E+03
	ed and es scattering	(2.3725±0.0027)E+00	2.105E+03
	$e\bar{d}$ and $e\bar{s}$ scattering	(1.2127±0.0014)E+00	2.470E+03
Common cuts: 1 muon with $5^\circ < \theta_\mu < 175^\circ$ and $P_T^\mu > 5$ GeV			

GRAPE: $e^+p \to e^+\mu^+\mu^- X$, **1999–2000 ZEUS configuration**			
Type	Cuts	Cross–section [pb]	Lumi [pb^{-1}]
Elastic	elastic process	(1.2846±0.0009)E+00	2.335E+04
Quasi–elastic	$1.08 < M_{\text{had}} < 5$ GeV	(6.5068±0.0049)E−01	2.305E+04
	$M_{\text{had}} > 5$ GeV	(6.2541±0.0057)E−03	4.783E+05
DIS	eu scattering	(1.8940±0.0023)E+00	1.583E+04
	$e\bar{u}$ scattering	(2.5964±0.0036)E−01	5.777E+04
	ed and es scattering	(2.9149±0.0037)E−01	3.427E+04
	$e\bar{d}$ and $e\bar{s}$ scattering	(1.2940±0.0018)E−01	7.724E+04
Common cuts: 1 muon with $5^\circ < \theta_\mu < 175^\circ$ and $P_T^\mu > 10$ GeV			

3.8.2 LPAIR samples

LPAIR: $e^-p \to e^-\mu^+\mu^-X$, **1998–99 ZEUS configuration**			
Type	Cuts	Cross–section [pb]	Lumi [pb^{-1}]
Elastic	elastic process	(4.2306±0.0033)E+1	9.448E+2
Quasi–elastic	$Q_p^2 < 16$ GeV^2 and $1.08 < M_{\mathrm{had}} < 5$ GeV	(2.1367±0.0019)E+1	9.331E+2
DIS	$Q_p^2 < 16$ GeV^2 and $M_{\mathrm{had}} > 5$ GeV	(6.3608±0.0039)E+1	9.411E+2
Common cuts: 1 lepton with $4^\circ < \theta_l < 175^\circ$ and $P_T^l > 3$ GeV			

Chapter 4

Reconstruction and selection of events

The first half of this chapter is devoted to the description of the reconstruction algorithms; they are needed to identify particles and reconstruct their energies and trajectories. The algorithms used in the analysis will be reviewed.

In the second part the criteria used for event selection are presented. The first selection is done by requests at the trigger level; the trigger chains used for selecting multi–electron and di–muon events are shortly described. A detailed description is instead reported in Appendix A. A further selection is performed offline, by requirements on the reconstructed variables; these cuts will be described at the end of the chapter.

4.1 The EM electron finder

The task of an electron finder is to analyse energy deposits in the calorimeter and distinguish electromagnetic from hadronic clusters, making use of EMC and HAC cells, and tracking information when available. The EM [70] electron finder is based on detailed parameterisations of the detector response for electrons. Seven variables (four calorimetric and three tracking variables) are used to evaluate whether or not a calorimeter cluster is an electron:

- f_{HAC}, the fraction of energy in the HAC layers,
- f_{CLeak}, the fraction of EMC energy outside the highest energy cell strip pair. A cell strip is a set of EMC cells which have the same tower number, cell and calorimeter type. If t is the tower number and $1 \leq k \leq 4$ is the cell type, the strip number is defined as $s = 4(t-1)+k$; if $f_{\mathrm{C}}(s)$ is the fraction of the EMC energy contained in strip s, and $s_{\max}$ is the strip with highest energy, then

$$f_{\mathrm{CLeak}} = 1 - \left[f_{\mathrm{C}}(s_{\max}) + \max\left(f_{\mathrm{C}}(s_{\max}-1), f_{\mathrm{C}}(s_{\max}+1) \right) \right],$$

- f_{MLeak}, the fraction of energy outside the highest energy module pair can be defined in terms of $f_{\mathrm{M}}(m)$, the energy fraction in module m and m_{max}, the highest energy module, as

$$f_{\mathrm{MLeak}} = 1 - \left[f_{\mathrm{M}}(m_{\mathrm{max}}) + \max\left(f_{\mathrm{M}}(m_{\mathrm{max}} - 1), f_{\mathrm{M}}(m_{\mathrm{max}} + 1) \right) \right],$$

- E_{cone}, the energy which is not assigned to the candidate, but which lies within a cone, centred around the candidate, of radius 0.8 in the $\eta\phi$ plane,
- $\delta\theta = |\theta_{\mathrm{Trk}} - \theta_{\mathrm{Cal}}|$,
- $\delta\phi = |\phi_{\mathrm{Trk}} - \phi_{\mathrm{Cal}}|$,
- $\delta_{1/P} = |1/E - 1/P_{\mathrm{Trk}}|$.

For candidates which are outside the tracking acceptance, or which do not have a matching track, only the first four quantities are used.

The distributions of each of the seven variables are parameterised separately for each of the three calorimeters. The RCAL and BCAL parameterisations were derived from ZEUS data. Due to the low rate of FCAL electrons, neutral current DIS Monte Carlo was used for the FCAL parameterisation. For several of these variables, the parameterisations depend on auxiliary variables as described below.

- The distribution of f_{HAC} depends on the distance of the candidate from the module edge.
- For FCAL and RCAL candidates, the distribution of the track match variables $\delta\theta$, $\delta\phi$ and $\delta_{1/P}$ depends on the radius at which the track exits the CTD.
- Separate parameterisations are done for negative and positive values of $(\phi_{\mathrm{Trk}} - \phi_{\mathrm{Cal}})$ and $(1/E - 1/P_{\mathrm{Trk}})$ to account for the asymmetric distributions caused by the final state radiation.

4.1.1 Calculation of sub–probabilities

Each of the variables is transformed into a sub–probability. If the variable x is in the range $0 < x < x_{\mathrm{max}}$ and has the sub–probability density $f(x)$, the corresponding probability $P(x)$ is given by

$$P(x) = \int_{x}^{x_{\mathrm{max}}} \mathrm{d}t f(t). \tag{4.1}$$

Since $\int_0^{x_{\mathrm{max}}} \mathrm{d}t f(t) = 1$, the sub–probability $P(x)$ is uniformly distributed between 0 and 1 for real electrons. A higher value of $P(x)$ corresponds to a lower x and therefore a better electron (fake electrons tend to have larger values for each of the variables as they have been defined).

4.1.2 Combination of sub–probabilities

Using the approximation that the various sub–probabilities p_i, where $1 \leq i \leq N$, are uniformly distributed between 0 and 1 and are not correlated to each other, the product of N sub–probabilities, $P = \prod_{i=1}^{N} p_i$ can be transformed into the variable Q,

$$Q = P \sum_{k=0}^{N-1} \frac{(-\log P)^k}{k!}. \tag{4.2}$$

The variable Q is uniformly distributed between 0 and 1. This is the method used to compute, for example, the calorimeter probability P_{Cal} from the sub–probabilities $p(f_{\mathrm{HAC}})$, $p(f_{\mathrm{CLeak}})$, $p(f_{\mathrm{MLeak}})$ and also to compute the *grand probability* from all seven sub–probabilities.

4.1.3 Outline of the algorithm

The algorithm which EM applies to an event is, schematically:

1. Calorimeter cells are grouped in clusters (*islands*).

2. A loop over islands is done. An island is accepted if it passes these three cuts:

   - the energy of the island exceeds emEMin (default 4 GeV),
   - f_{HAC} is less than emFHACmax(fbr) (fbr=1,2,3 for FCAL, BCAL, RCAL). The default value is emFHACmax = (0.3,0.5,0.3).
   - the calorimeter probability $P_{\mathrm{Cal}}(f_{\mathrm{HAC}}, f_{\mathrm{MLeak}}, f_{\mathrm{CLeak}})$ exceeds emCalProbMin (default is 10^{-5}).

3. If the polar angle of the candidate satisfies $0.3 < \theta_e < 2.85$, a matching track in the CTD is searched for. Only tracks which satisfy the following criteria are considered:

   - $P_t > 0.1$ GeV,
   - the distance of closest approach to the beam line is less than 2 cm,
   - the distance of closest approach to the CAL position is less than 50 cm,
   - $|\delta\theta| < \pi/4$,
   - $|\delta\phi| < \pi/4$.

   For tracks passing these cuts, the track match is accepted if $P_{\mathrm{Trk}}(\delta\theta, \delta\phi, \delta_{1/P})$ exceeds emTrackProbMin (default is 10^{-3}).

4. The grand probability is calculated as follows:

$0.3 < \theta_e < 2.85$?	Matching track?	P_{Grand}
Yes	Yes	$P(f_{\text{HAC}}, f_{\text{MLeak}}, f_{\text{CLeak}}, E_{\text{cone}}, \delta\theta, \delta\phi, \delta_{1/P})$
Yes	No	$(1 - \epsilon_{\text{Trk}})P(f_{\text{HAC}}, f_{\text{MLeak}}, f_{\text{CLeak}}, E_{\text{cone}})$
No	–	$P(f_{\text{HAC}}, f_{\text{MLeak}}, f_{\text{CLeak}}, E_{\text{cone}})$

4.2 Muon reconstruction

Due to the different structure of the BRMUON and FMUON detectors (see Sects. 2.2.4 and 2.2.5) two different muon reconstruction algorithms are used, one for muon identification in the barrel and rear region, GLOMU, and one for muons in the forward region, MPMATCH2. These two algorithms are briefly described below. Additional information can be found in the given references.

4.2.1 The GLOMU package

A program for the selection of muons coming from the interaction region must satisfy various requirements; it must be efficient in the detection of the signal, able to reject a large part of the background events, free from bias. The GLOMU program [71], originally developed for the use in the TLT, fulfills all the above requirements. The program combines the information from the inner barrel–rear muon chambers (B/RMUI), the CTD and the calorimeter:

- track segments in the B/RMUI,
- good quality tracks in the CTD,
- minimum ionising particle (MIP) clusters in the UCAL[1].

If all the three detectors see some signal, a matching is attempted, and kept if the χ^2 of the match is satisfactory.

In more detail, the muon search is performed as follows:

- For the B/RMUI detector the ADAMO tables MBSTAR (for the strip view) and MBSGS (for the wire view) [73] are used for the fast reconstruction of track segments in space. At the end one or more tracks are kept (at most one per chamber). For each track the point of entrance in the chamber, together with the polar and azimuthal angles, and the associated errors, are available.
- For the CTD the helix parameters stored in the VCTRHL table are used. Of all the reconstructed tracks only those that satisfy the following requirements are considered:
  - $\chi^2 < 20$,

[1]GLOMU calls the Wai's package [72] to search for minimum ionising particles in the calorimeter.

- $D_H < 10$ cm, to reject cosmic muons[2],
- $|Z_H| \leq 75$ cm[3],
- $\theta_\mu \geq 20°$, since we consider only tracks in the barrel and rear direction,
- $P_T \geq 1$ GeV in the barrel region, or $P \geq 1$ GeV in the rear region.

Once a track satisfies these requirements it is extrapolated from the point of closest approach to the vertex, to a *fiducial surface*[4] external to the CTD via a Runge–Kutta integration. It was decided to use this method because it allows the most precise extrapolation of tracks through regions where the magnetic field is significant for low energy particles. The number of integration steps (20) was dictated by compromising between speed and accuracy. The fiducial surface is a cylinder of radius 94 cm, between $z = -146$ cm and $z = 180$ cm, as derived by a study of the magnetic field map.

For each extrapolated track the position in space, the direction (θ, ϕ), the momentum and the errors are computed at the fiducial surface.

- For the calorimeter, energy deposits typical of a MIP are searched for. The three spatial coordinates and the absolute timing flag (to improve the cosmic rejection) are used.

- In the case that all the three detectors provide objects of the kind described above a matching is attempted. The matching is made separately in the θ and ϕ variables. Five determinations of these two angles are available:

  - (θ, ϕ) from the B/RMUI track,
  - (θ, ϕ) from the CTD,
  - (θ, ϕ) given by the segment connecting the CTD–B/RMUI points (not used),
  - (θ, ϕ) given by the segment connecting the B/RMUI–UCAL points,
  - (θ, ϕ) given by the segment connecting the CTD–UCAL points.

  All the possible combinations of θ and ϕ are considered, and the corresponding χ^2_θ and χ^2_ϕ computed; the total χ^2 is simply the sum of all these contributions. From Monte Carlo studies, a cut of $\chi^2 < 20$ was set in order to accept matches.

The package provides also the possibility to select different kinds of matching, e.g. UCAL–B/RMUI, UCAL–CTD, CTD–B/RMUI, as well as matchings with different χ^2 cuts and different measurement error assumptions.

[2] D_H is the impact parameter, see Section 2.2.1.

[3] Z_H is the z coordinate at the point of closest approach to the vertex, see Section 2.2.1.

[4] The *fiducial surface* corresponds to the surface where the magnetic field becomes less than 1 kGauss.

4.2.2 The MPMATCH2 matching package

The MPMATCH2 package [74] (largely based on the MVMATCH software [75]), has the main purpose to match segments reconstructed by the FMUON detector with tracks reconstructed by the inner tracking devices, mainly the CTD. It has been developed for the selection and the reconstruction of a clean muon sample in inelastic events with non–isolated muons, and therefore the angular coverage is limited to the overlapping region between the FMUON and the CTD.

The search for a match starts from a FMUON reconstructed track, which is defined by five parameters in the ZEUS reference frame: $(x, y, \mathrm{d}x/\mathrm{d}z, \mathrm{d}y/\mathrm{d}z, Q/p)$. This FMUON track, with its parameters and its covariance matrix, is extrapolated backward to the UCAL surface, using the GEANE [76] package. A match is then attempted with tracks found by central trackers and extrapolated to the same surface. Once that a match is found, a Kalman filtering [77] is used to combine the information from the various detectors; later on a vertex fit can be done by extrapolating the track toward the z of the reconstructed vertex, and performing a fit between the parameters of the track and the x and y coordinates of the reconstructed vertex. The procedure is repeated for all available FMUON tracks; if there is more than one possible match with CTD tracks, a choice based on the χ^2 probability is done so that just one track is retained.

4.2.3 Matching of CTD tracks and MIPs

To raise the efficiency in muon finding, a matching of tracks in the central tracker and minimum ionising particle deposits in the UCAL is attempted.

I wrote a simple algorithm to match the CTD tracks, coming from the primary vertex, to the MIPs found by the GLOMU package. The tracks are propagated by means of GEANT to the calorimeter inner surface and the distance of each track to each MIP deposit is evaluated. A track is classified as muon if the closest MIP is less than 25 cm far away.

4.3 Reconstruction of hadronic variables

The kinematic variables of an ep scattering, x, y and Q^2, can be derived from the hadronic final state reconstructed by the calorimeter. Several effects cause a difference between the measured and the true variables, making corrections necessary. In the first part of this section, all the corrections to be applied to the energy measured by the calorimeter will be illustrated:

- rejection of noisy cells and suppression of noise–related effects;
- comparison of the calorimeter response to real data and its simulation;
- simulation of effects related to the UCAL geometry (cracks, dead material, etc.).

Sector	Cell Type	Correction to DATA	
		1994–97	1998–2000
FCAL	EMC	1.04	1.02
	HAC	0.95	0.94
BCAL	EMC	1.04	1.05
	HAC	1.08	1.10
RCAL	EMC	1.022	1.022
	HAC	1.022	1.022

Table 4.1: Correction factors to be applied to data to keep into account the difference in the calorimeter energy scale with respect to Monte Carlo. The correction factors depend on the detector sector, on the cell type and on the year.

Then, in the second part, the algorithms which reconstruct calorimetric variables will be described.

4.3.1 Corrections to calorimetric variables

The first correction applied to the calorimeter measurements is the suppression of badly–working calorimeter cells and of noise–related effects. The list of noisy cells for each year is reported in standard routines, used to correct for these effects. The corrections fall into distinct categories: the removal of noisy cells accordingly to the list, a cut on the cell imbalance[5], and the removal of isolated EMC and HAC cells with energies below 80 and 140 MeV, respectively. The noise associated with the imbalance and isolation cuts is mainly due to sparks in the PMTs, while the noisy cells come mainly from electronic malfunctioning.

A second correction regards the calorimeter energy scale. Comparisons of the calorimeter response and its simulation [78] have shown that there is a factor between the actual calorimeter energy scale and the one simulated in MOZART. This discrepancy can easily be corrected by multiplying the energy as measured on real data by a correction factor, dependent on the sector of the calorimeter (FCAL, BCAL, or RCAL), on the cell type (EMC or HAC) and on the year. These correction factors are summarised in Table 4.1. No correction is applied to the Monte Carlo.

In addition to these effects, that can easily be corrected, systematic discrepancies between the variables measured by the calorimeter and the true ones arise from the calorimeter structure and the way it measures particles: the presence of inactive material in front of the UCAL, cracks between the calorimeter sectors, and the presence of particles like muons and neutrinos which do not release all their energy in the calorimeter are the causes of a systematic shift of the calorimeter measurements toward lower values than the true ones. All these effects have

[5]As described in Sect. 2.2.2, each cell is read on both sides by a photomultiplier. The imbalance is defined as the fractional difference of the two independent measurements.

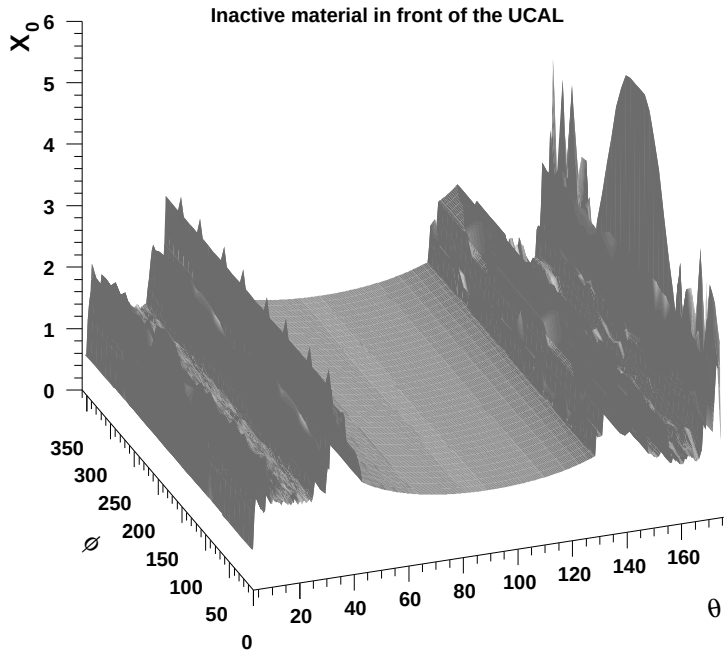

Figure 4.1: Distribution of inactive material in front of the UCAL in units of the radiation length, X_0, in the θ–ϕ plane, as implemented in the simulation of the detector.

to be taken into account in order to correct the calorimetric variables up to the true values. An estimation of the goodness of the corrections can be obtained by comparing the true variables and the corrected ones on a selected Monte Carlo sample.

Suitable routines have been developed in order to correct for the effects reported above. In particular:

- the map of the *dead material* is available and has been used to write correction algorithms. The materials constituting the beam pipe, the tracking devices and the solenoid correspond to a number of radiation lengths varying from 1 to 3 (see Fig. 4.1) and the energy loss of the particles, especially of those having low momenta, can be relevant in such a thickness. Since energy losses due to the presence of the dead material are difficult to be included with sufficient precision in the detector simulation, the correction is applied offline, and is parametrized as a function of the energy and the polar angle of the particles;

- the zones of the cracks between the calorimeter sectors are not well simulated by the Monte Carlo so corrections have been introduced offline;

- pions, kaons and protons having energies below 1 GeV lose all their energy by ionisation before any hadronic interaction. In this case the calorimeter

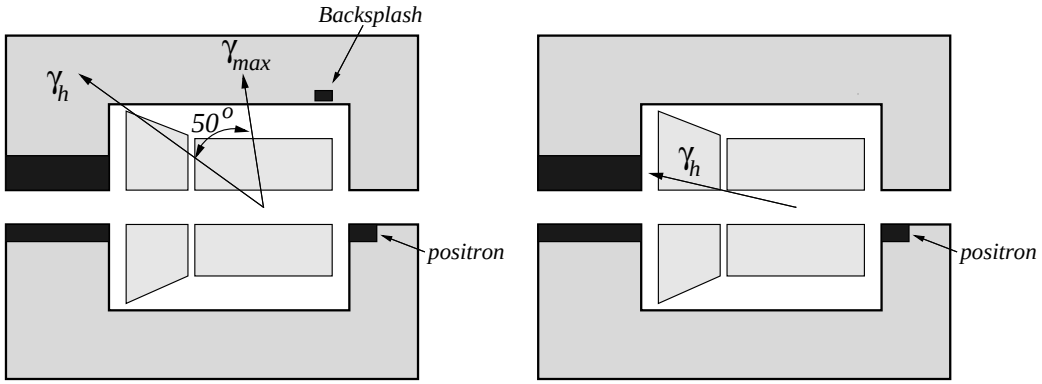

Figure 4.2: (a) Due to small energy deposits in BCAL/RCAL, the measurement of γ_h (the polar angle of the hadronic system) is overestimated. (b) By rejecting energy deposits 50° behind the original γ_h, γ_h is corrected. The scattered electron is shown for completeness.

is no more compensated ($e/h \sim 0.6$) and this causes an overestimation of the energy of the low–energy hadrons.

Corrections for backsplash

$(E - P_z)$ and P_T of the hadronic system are important quantities, as they can be used to compute the kinematical variables x, y and Q^2 of the event. On the other hand, small deposits in the rear part of the calorimeter, often not originated by the hard interaction, may vary considerably the value of $(E - P_z)$ in low–y events. As an example, a rear deposit of 500 MeV contributes with ∼1 GeV to the total $(E - P_z)$; in an event having $y_{\text{true}} = 0.002$, thus $(E - P_z) = 100$ MeV, the measured value will be $y_{\text{meas}} = 0.02$, one order of magnitude higher than the true value.

These low–energy deposits may come from the so called backsplash (low–energy neutral particles may be emitted from a high–energy shower in the FCAL and reach BCAL or RCAL), from noisy cells, from showering in inactive material (e.g. beam pipe, CTD inner wall), from overlay interactions.

The backsplash correction is applied by removing cells which:

- have a polar angle $\gamma > \gamma_h + 50°$
  (γ_h is the polar angle of the hadronic system, as calculated by the clustering algorithm);
- are in RCAL or BCAL;
- have $E < 3$ GeV;
- have not an associated track coming from the primary vertex.

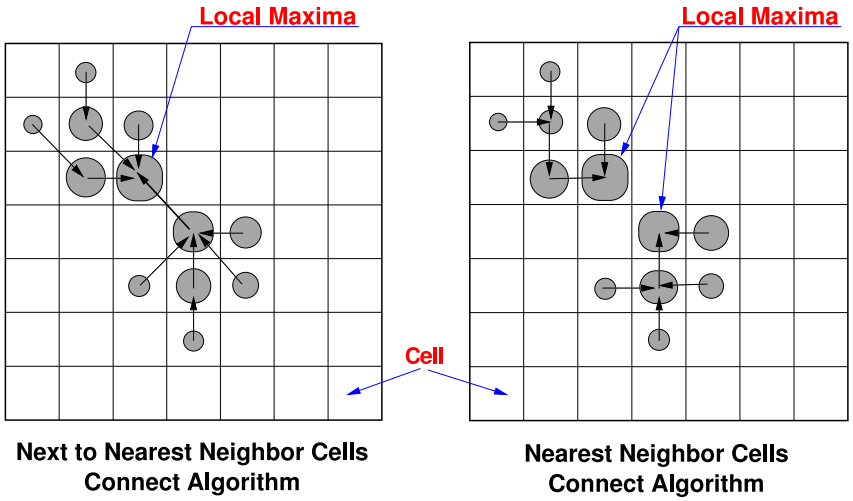

Figure 4.3: Schematic representation of the cell island clustering, with two different definition of neighbourhood.

The angle γ_h is recomputed after the cell removal, then the procedure, sketched in Fig. 4.2, is iterated at most three times or until the angle γ_h changes less than 1%.

4.3.2 The clustering algorithm

Particles entering the calorimeter will shower and deposit their energy in several adjacent cells. The role of a clustering algorithm is to merge all the cells belonging to the shower of a single particle.

The clustering algorithm used at ZEUS works in two steps [79]: first the *cell islands* are formed, then these objects are used to obtain the *cone islands*. The reason for this procedure stems from the fact that the ZEUS calorimeter is divided into three spatially separated sections (FCAL, BCAL, RCAL) and a single particle can split its energy among two of them; an algorithm with two stages of clustering, one local and one global, is therefore needed.

The cell island algorithm starts considering each cell above an energy threshold and its local neighbourhood (eight or four cells, depending on the definition of neighbourhood). The cell is connected to the highest energy cell in the neighbourhood, and the procedure is repeated for each cell, until every cell is uniquely assigned to an island (Fig. 4.3). The algorithm looks for cell islands in each layer of the calorimeter separately (FEMC, FHAC1, FHAC2, BEMC, BHAC1, BHAC2, REMC, RHAC).

The cone island algorithm has the purpose to collect the cell islands which belong to a shower of a single particle or to a jet of particles. This algorithm has as input the cell islands and performs a clustering in the θ–ϕ plane. The matching starts from cell islands in the HAC2 layer and goes inward. For each

HAC2 cell island, the angular separation from all HAC1 cell islands is determined and translated into a probability accordingly to a distribution obtained from a single pion Monte Carlo. The HAC1 cell island with highest probability is taken and matched to the HAC2 cell island if the probability is higher than a fixed cut. If no valid HAC1 cell island is found, an attempt is done of a matching with an EMC cell island.

In a second step, a similar procedure is followed for the HAC1 cell islands, in order to find a match with an EMC island. As third and final step, EMC cell islands can be connected to each other. After this linking, HAC cell islands matched to the same EMC cell island are joined to give a cone island. The centre of gravity of the cells forming the cone island is used as estimation of the cluster position. To obtain a better precision in the estimation, the positions of the cell centres are corrected by using the energy imbalance (see Footnote 5), and a weight logarithmic in the energy is used, instead of a linear one [79].

4.3.3 The CorAndCut algorithm

CorAndCut is an algorithm that reconstructs the hadronic final state by using the calorimeter only. It applies noise suppression and energy corrections to the calorimeter cells, then makes use of the cone island method to group the cells into clusters; the corrections for backsplash are also included.

The kinematic variables are calculated by using the *Jacquet–Blondel* method [80]:

$$\begin{aligned} y_{\mathrm{JB}} &= \frac{E - P_z}{2E_e}, \\ Q^2_{\mathrm{JB}} &= \frac{P_T^2}{1 - y_{\mathrm{JB}}}, \\ x_{\mathrm{JB}} &= \frac{Q^2\mathrm{JB}}{s y_{\mathrm{JB}}}. \end{aligned} \tag{4.3}$$

In order to achieve a better precision in the evaluation, the constraints $0 \leq y_{\mathrm{JB}} \leq 1$ and $0 \leq Q^2_{\mathrm{JB}} \leq s$ are applied; this procedure is called *regularisation of Jacquet–Blondel variables*.

4.3.4 The ZUFOs algorithm

The ZUFOs algorithm (ZEUS Unidentified Flowing Objects, [81]) is based on the fact that the hadronic energy has both a charged particle and a neutral particle component. Both are measured by the calorimeter, but a large fraction of the charged particles is also measured by the tracking detectors. In some cases, especially when the charged particles have low energies, or when they cross a large thickness of dead material before being detected, the resolution of the tracking devices is better than that of the calorimeter (see Fig. 4.4).

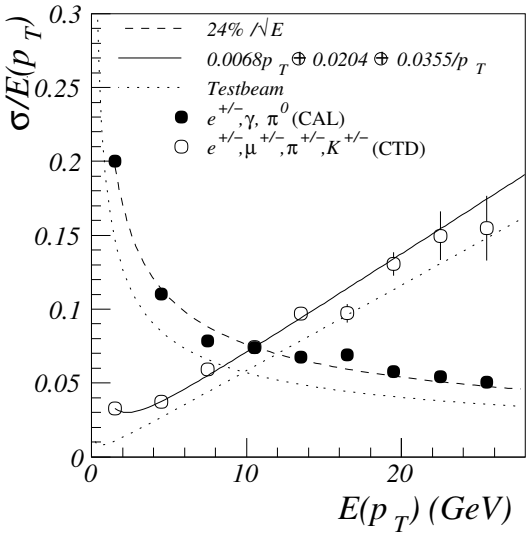

Figure 4.4: The resolution on the measurement of the electromagnetic energy E in the EMC calorimeter (full dots) and the transverse momentum p_T in the CTD (empty dots), obtained from single particle Monte Carlo, $(e^{\pm}, \pi^0, \gamma)$ and $(e^{\pm}, \pi^{\pm}, \mu^{\pm}, K^{\pm})$, respectively. Also the estimated resolutions and test beam results are reported.

The ZUFOs algorithm reconstructs cone islands, applying the noise suppression and all the corrections described above, then associates calorimetric clusters and "good" CTD tracks[6] (an example is shown in Fig. 4.5). In the reconstruction of hadronic quantities the tracking information is used when its resolution is better than the one of the calorimeter deposit; also unmatched cone islands, as well as unmatched good tracks, are used in the evaluation of the hadronic energy and momentum.

4.4 Trigger chain for multi–electron events

Events with two or more electrons in the final state have been selected by using three different trigger chains. Only one of these was specifically designed for the selection of di–electron events, the other two were thought for neutral current events and events with a sizable transverse energy deposited in the calorimeter. Nevertheless, the use of all these trigger chains helps in having an higher efficiency in the data selection, that is of particular importance for an analysis in which we do not expect a large number of events in the final sample.

In all the trigger selections, some veto criteria have to be fulfilled: the timing

[6]In the algorithm a track is considered good if it comes from the primary vertex, passes at least 4 superlayers and owns $0.1 < P_T < 20$ GeV (the P_T upper cut is raised to 25 GeV if the track crosses more than 7 CTD superlayers).

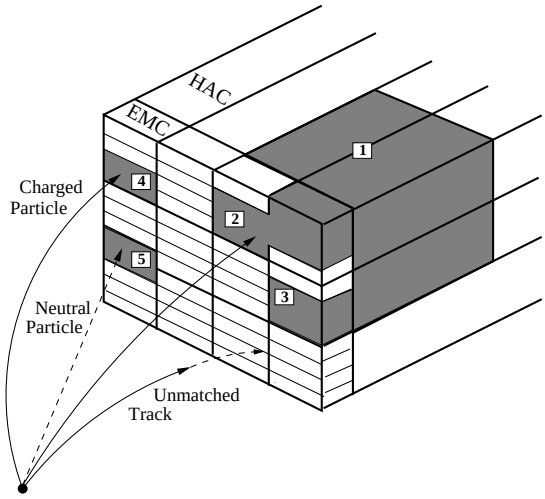

Figure 4.5: Neighbouring calorimeter cells are clustered into cell islands. This schematic picture shows four EMC cell islands and one HAC cell island. EMC cell islands 2 and 3 are joined with HAC cell island 1 to form a cone island. Then the cone islands are matched to CTD tracks.

in the C5 counter and in the SRTD has to be consistent with physical events and not with that of beam–gas events, and no coincidence of the inner and outer veto wall has to be found.

In the following the trigger chains are introduced; they will be fully described in Appendix A.

4.4.1 Trigger for the selection of di–electron events

Elastic di–electrons are selected at the SLT by looking for an *elastic* topology (i.e. an event having few tracks in the CTD and low energy around the forward beam pipe), low hadronic energy measured by the calorimeter, and two electrons or a sizable energy deposit in the electromagnetic calorimeter. At the TLT a "good vertex" is required (i.e. close to the nominal interaction point), a cosmic rejection is applied (by means of UCAL timing, number and acollinearity of the CTD tracks, energy deposited in the forward calorimeter), and some additional conditions are required on energy and position of one of the electrons (requirements were applied to both electrons in 1996–97).

Inelastic di–electrons are selected at the SLT by looking for two electrons with large invariant mass ($M_{12} > 4$ or 6 GeV, depending on the year) and a sizable energy deposit in the electromagnetic calorimeter. At the TLT a good vertex is required, the usual cosmic rejection is applied and some additional cuts are applied on energy and position of the two electrons.

4.4.2 Trigger for the selection of neutral current events

Neutral current events are selected at the SLT by requiring a large transverse energy measured by the calorimeter ($E_T > 16$ GeV), an $(E - P_z)$ compatible with an event completely contained in the detector[7] ($E - P_z > 34$ GeV), and applying a beam–gas rejection.

At the TLT a good vertex combined with a calorimeter timing compatible with a physical event are required, or a TLT electron and high–Q^2 ($Q^2 > 200$ or 160 GeV^2, depending on the year).

At the DST level a correct timing, $(E - P_z) > 32$ GeV and an electron with $E_e > 4$ GeV are required. In addition, high E_T (in 1996–97) or high Q^2 (thereafter) are asked for.

4.4.3 Trigger for the selection of events with transverse energy in the UCAL

At the SLT level, high E_T in the calorimeter or an isolated electron are required, in addition to $(E - P_z) > 15$ GeV and a beam–gas rejection.

At the TLT level a good vertex, a time compatible with that of a physical event and $E_T > 20$ GeV are required.

At the DST level, $E_T > 20$ GeV or the TLT fired, and a vertex with $-120 < z_{\text{vtx}} < 60$ cm are required.

4.5 Trigger chain for di–muon events

In the selection of events with more than one muon in the final state, special trigger slots dedicated to muon identification have been used. Due to the difference of the B/RMUON and FMUON detectors different trigger chains are requested for muons in the barrel–rear or in the forward regions. These slots are introduced below, whereas a more detailed treatment can be found in Appendix A.

4.5.1 Trigger for muons in the barrel–rear region

Two trigger chains are defined by using the barrel–rear muon chambers. The first chain looks for activity in the inner chambers, B/RMUI, and in the CTD, the second one require also activity in the outer chambers, B/RMUO.

The first chain starts at FLT by requiring an *elastic* topology (few tracks in the CTD and low energy around the forward beam pipe) and a signal in B/RMUI, or a B/RMUI signal matched in position to a MIP–like deposit in the calorimeter and one (or more) CTD track. At the SLT a timing cut and a beam–gas rejection are applied.

[7] For events in which the scattered electron is measured, $E - P_z$ is equal to the value before the collision, $E - P_z = (E_e^{\text{ini}} + E_p^{\text{ini}}) - (P_e^{\text{ini}} + P_p^{\text{ini}})_z = 2E_e^{\text{ini}} = 55$ GeV, since the incoming proton moves in the positive z direction whereas the electron in the opposite direction.

The second chain require a signal in the barrel or rear muon chambers (inner and outer), a calorimeter activity and at least a CTD track. At the SLT a timing cut is applied.

The TLT requires one of the above SLT fired and a muon found by GLOMU (which matches CTD, UCAL and inner muon chambers information).

4.5.2 Trigger for muons in the forward region

The trigger chain selects, at FLT, events with low track multiplicity and a FMUON hit matched in position to a MIP–like deposit in the calorimeter. At the SLT, the vertex (if any) is required to be in $-75 < z_{\rm vtx} < 75$ cm, the total calorimeter energy to be less than 10 GeV, and the FCAL energy to be predominantly hadronic. The request on the CTD particle multiplicity is renewed. At the TLT a muon matching of the FMUON hits to the CTD or the UCAL is required, and a pair of CTD tracks with invariant mass $M > 1.5$ GeV.

4.6 Offline data selection

4.6.1 Selection of multi–electron events

Preselection

In order to reduce the amount of data to be analysed a preselection is operated by means of global variables, without the necessity of running the electron finding and the other reconstruction algorithms. The requirements are:

- $1 \leq N_{\rm TrkVtx} \leq 9$;
- $\sum_i P_{T,i} > 3$ GeV.

$N_{\rm TrkVtx}$ is the number of CTD tracks coming from the primary vertex. In a multi–electron event I expect at least one of the electrons be central and the track be reconstructed by the CTD; moreover, the final sample will contain events with relatively low multiplicity (see Fig. 4.6, left).

With the second cut the request is on the sum of all transverse momenta measured by CTD for only the tracks coming from the primary vertex.

Selection of EM electrons

Electrons are searched by using EM and are accepted if:

- $E_{\rm cone} < 0.3$ GeV; $E_{\rm cone}$ is the energy, not associated to the electron, contained in a cone of radius 0.3 in the η–ϕ plane centred around the electron;
- $N_{\rm Trk} = 0$; $N_{\rm Trk}$ is the number of tracks in a η–ϕ cone of radius 0.4 around the electron, other than the electron track;

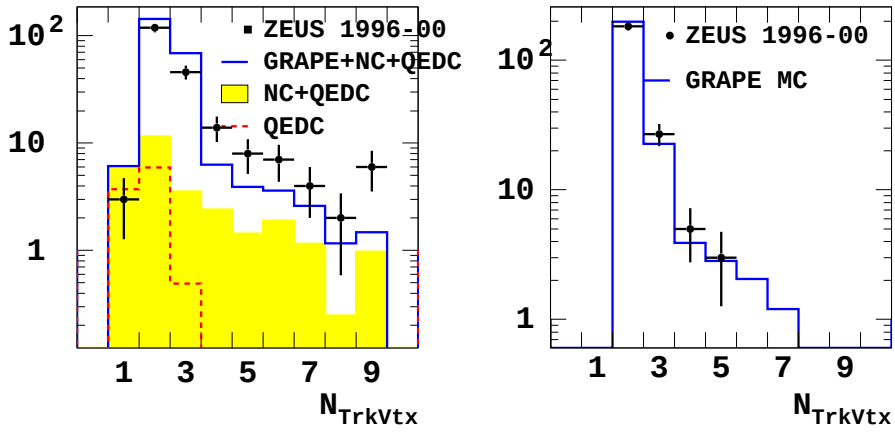

Figure 4.6: (Left) Distribution of the number of CTD tracks coming from the primary vertex, for the multi–electron sample. (Right) The same for the di–muon sample.

- Forward electrons ($\theta_e < 17°$):
  - $E_e > 10$ GeV (E_e is the electron energy),
  - CalProb > 0.1, where CalProb is the probability of the calorimeter deposit;
- Barrel electrons ($17° < \theta_e < 164°$):
  - $E_e > 10$ GeV,
  - GrandProb > 0.01, where GrandProb is the grandprobability from the electron finder,
  - a matched track ($P_{\mathrm{Trk}} > 5$ GeV and DCA < 5 cm);
- Rear electrons ($\theta_e > 164°$):
  - $E_e > 5$ GeV,
  - CalProb > 0.1.

Final event selection

To be selected an event must own:

- a vertex with $|z_{\mathrm{vtx}}| < 50$ cm;
- a barrel electron with transverse energy $E_T^e > 10$ GeV;
- a second barrel electron with $E_T^e > 5$ GeV.

4.6.2 Selection of di–muon events

Preselection

Like for multi–electron search, di–muon events are preselected by cutting on the number of tracks and the P_T:

- $2 \leq N_{\mathrm{TrkVtx}} \leq 7$;
- $\sum_i P_{T,i} > 1.5$ GeV.

The muons are identified by GLOMU in the barrel–rear region and by MPMATCH2 in the forward. The efficiency is raised by looking also for MIPs in the calorimeter.

Selection of GLOMU muons

Muons found by GLOMU are accepted if the matching is good ($\chi^2 < 20$), if the track passes at least three CTD superlayers, if the muon track is in a region where the efficiency of B/RMUON is high and well understood ($0.60 < \theta_\mu < 2.74$ rad), and if the muon has a transverse momentum $P_T^\mu > 5$ GeV and is isolated ($D^\mu_{\mathrm{Trk}} > 1$, where D^μ_{Trk} is the distance of the muon from the closest track in the η–ϕ plane).

Selection of MPMATCH2 muons

Muons found by MPMATCH2 are accepted if the probabilities of the FMUON track and the matching are both greater than 0.01, if the track is in a region where the efficiency of FMUON is high and well reproduced by the Monte Carlo ($0.20 < \theta_\mu < 0.45$ rad), if the muon has high–P_T ($P_T^\mu > 5$ GeV) and is isolated ($D^\mu_{\mathrm{Trk}} > 1$).

Selection of UCAL MIPs

A calorimeter deposit compatible with a MIP is identified as a muon if it owns a high–P_T ($P_T^\mu > 5$ GeV) CTD track matched in position, which passes at least three superlayers and is isolated ($D^\mu_{\mathrm{Trk}} > 1$).

Final event selection

The final selection of di–muon events is done by requiring:

- a muon from GLOMU or MPMATCH2;
- a second muon.

Some additional cuts are necessary to eliminate the cosmic muons from the sample; a vertex close to the nominal interaction point, an acollinearity between the muons and a timing compatible with a physical event are required:

- $|z_{\rm vtx}| < 50$ cm and $\sqrt{x_{\rm vtx}^2 + y_{\rm vtx}^2} < 0.5$ cm;
- an angle Ω between muons such that $\cos\Omega > -0.995$;
- $|t_{\rm up} - t_{\rm down}| < 3\sigma$.

4.7 Resolution on electron variables

The performances of the EM program have been evaluated on the GRAPE sample, after having applied the event selection described above. The reconstructed polar and azimuthal angles of the two electrons were compared to the true values, available in the simulation. The reconstructed angles show a very nice correlation with the true values, as can be seen in Fig. 4.7. The resolution on the polar angle measurement is around 0.5%, as shown by Fig. 4.9.

The reconstructed transverse momenta of the electrons are also well correlated to the true values (Fig. 4.8), although a worse resolution is attained; as can be seen in Fig. 4.9 the resolution on the P_T^e is around 10%. Also in Fig. 4.8 the correlations for $\cos(\Omega)$ and M_{12} are shown, being Ω the angle between the two electrons and M_{12} the invariant mass of the di–electron. The resolutions are 2% on $\cos(\Omega)$ and 10% on the invariant mass (see again Fig. 4.9).

4.8 Resolution on muon variables

Like in the electron case, the performances of the muon finders have been evaluated on the GRAPE sample, after having applied the event selection described in the previous sections. The reconstructed θ and ϕ angles of the two muons were compared to the true values. The reconstructed angles are nicely correlated with the true values, as can be seen in Fig. 4.10. The resolution on the polar angle measurement is 0.3%, as shown by Fig. 4.12.

The reconstructed transverse momenta of the muons are also well correlated to the true values (Fig. 4.11), but again a worse resolution is obtained with respect to the angles; as can be seen in Fig. 4.12 the resolution on the P_T^μ is about 10–15%. Also in Fig. 4.11 the correlations for $\cos(\Omega)$ and $M_{\mu\mu}$ are shown, being Ω the angle between the two muons and $M_{\mu\mu}$ the invariant mass of the di–muon. The resolutions are 1% on $\cos(\Omega)$ and 10% on the invariant mass (see again Fig. 4.12).

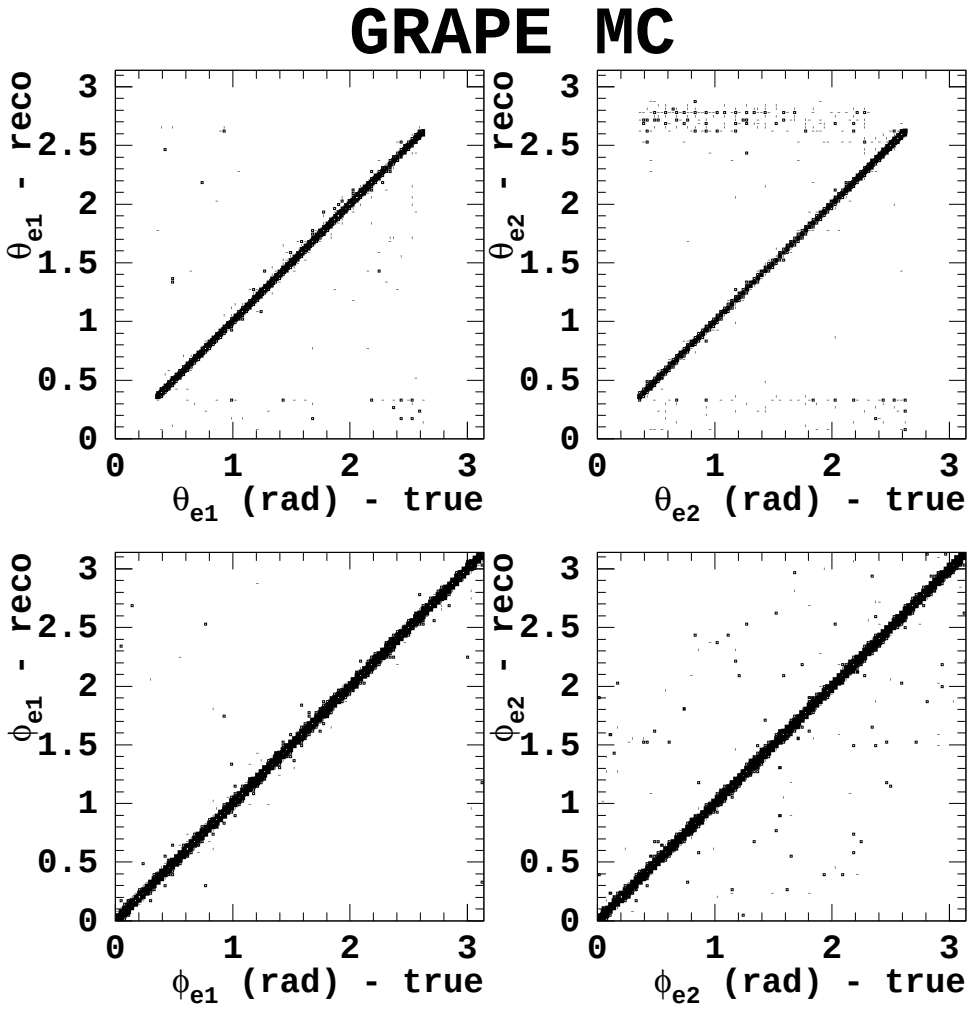

Figure 4.7: Correlation of the variables reconstructed by the EM electron finder and the true variables, obtained on a GRAPE sample. In the first row the results for the polar angles of the two electrons are shown, whereas in the second row the correlations of the azimuthal angles are plotted.

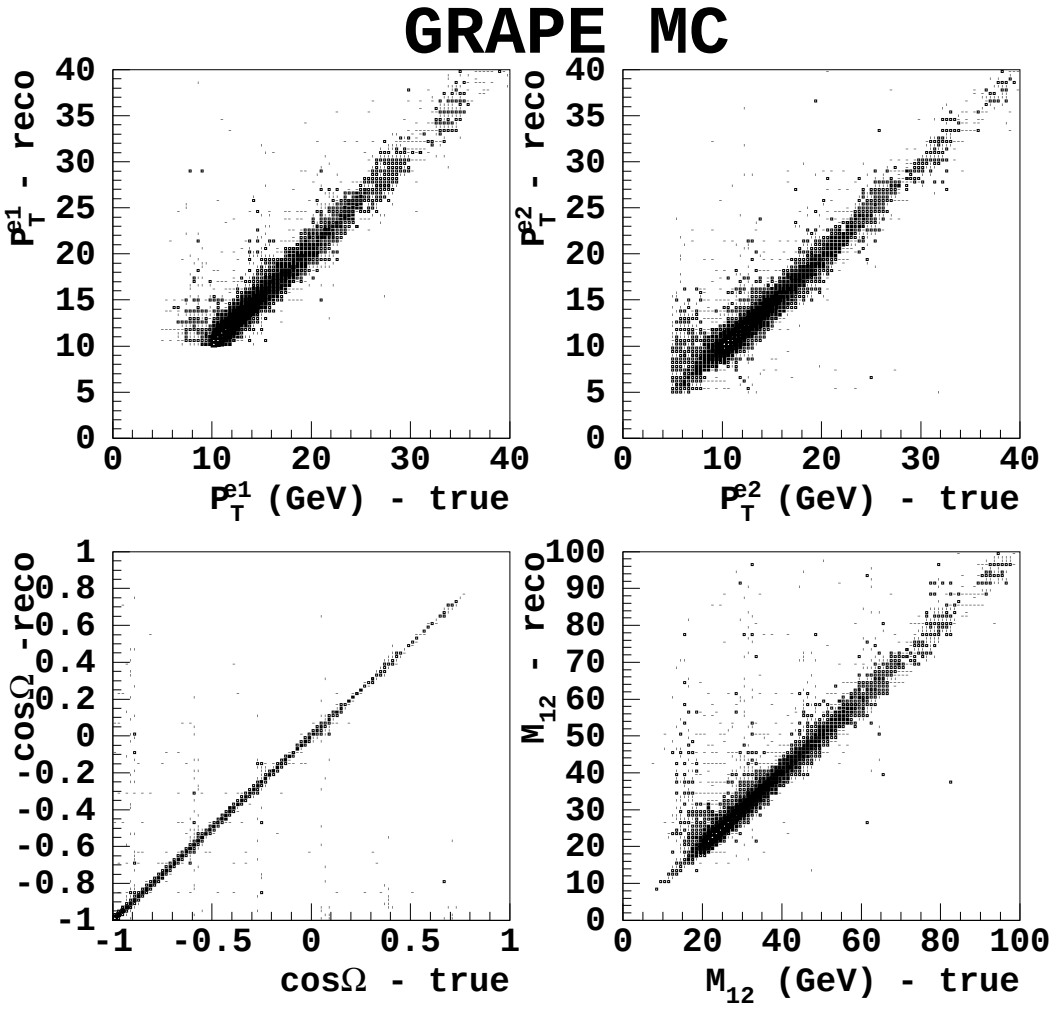

Figure 4.8: Correlation of the variables reconstructed by the EM electron finder and the true variables, obtained on a GRAPE sample. In the first row the results for the transverse momenta of the two electrons are shown, whereas in the second row the correlations of $\cos(\Omega)$ and M_{12} are plotted, being Ω the angle between electrons and M_{12} their invariant mass.

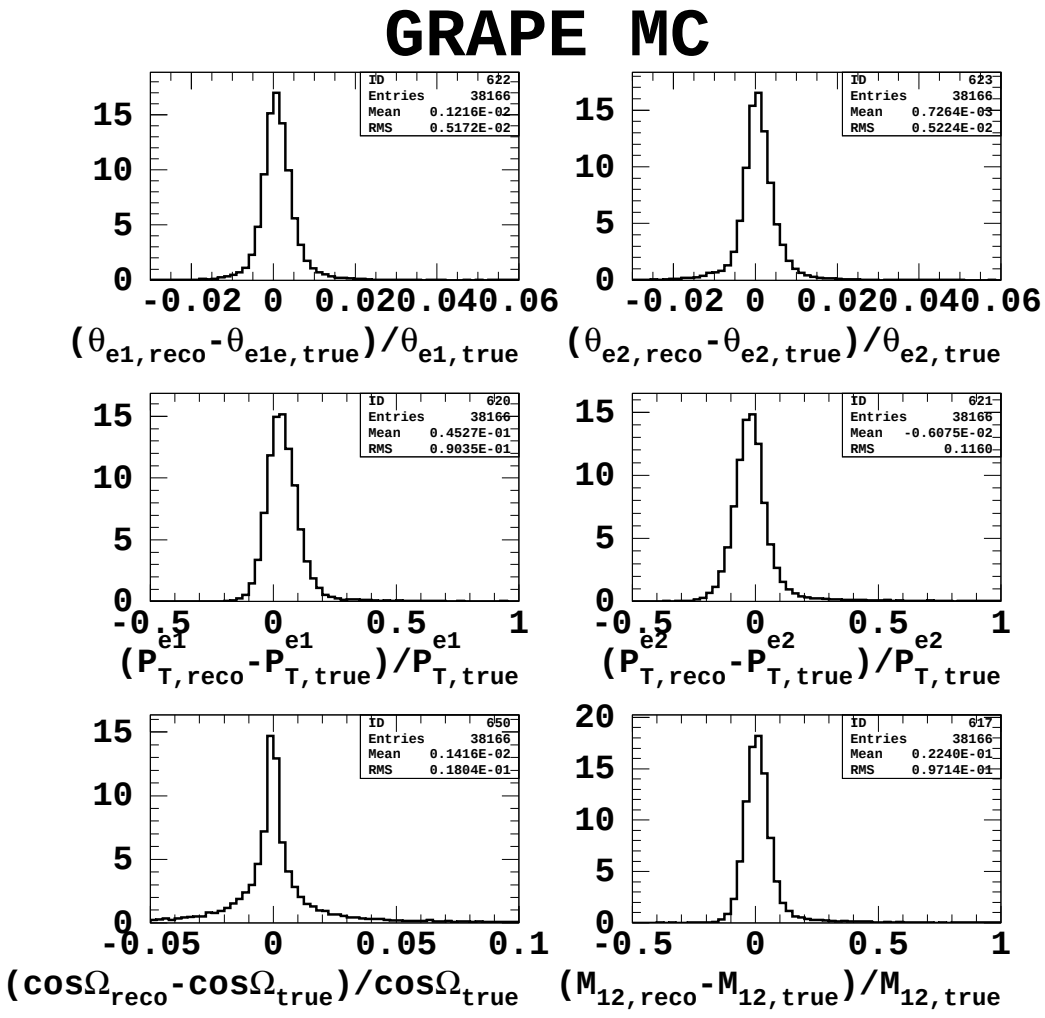

Figure 4.9: Resolution of the variables reconstructed by the electron finder. In the first row the results on the polar angles are shown, in the second row the P_T^e resolution is plotted, in the bottom row the resolutions of cos(Ω) and M_{12} are reported.

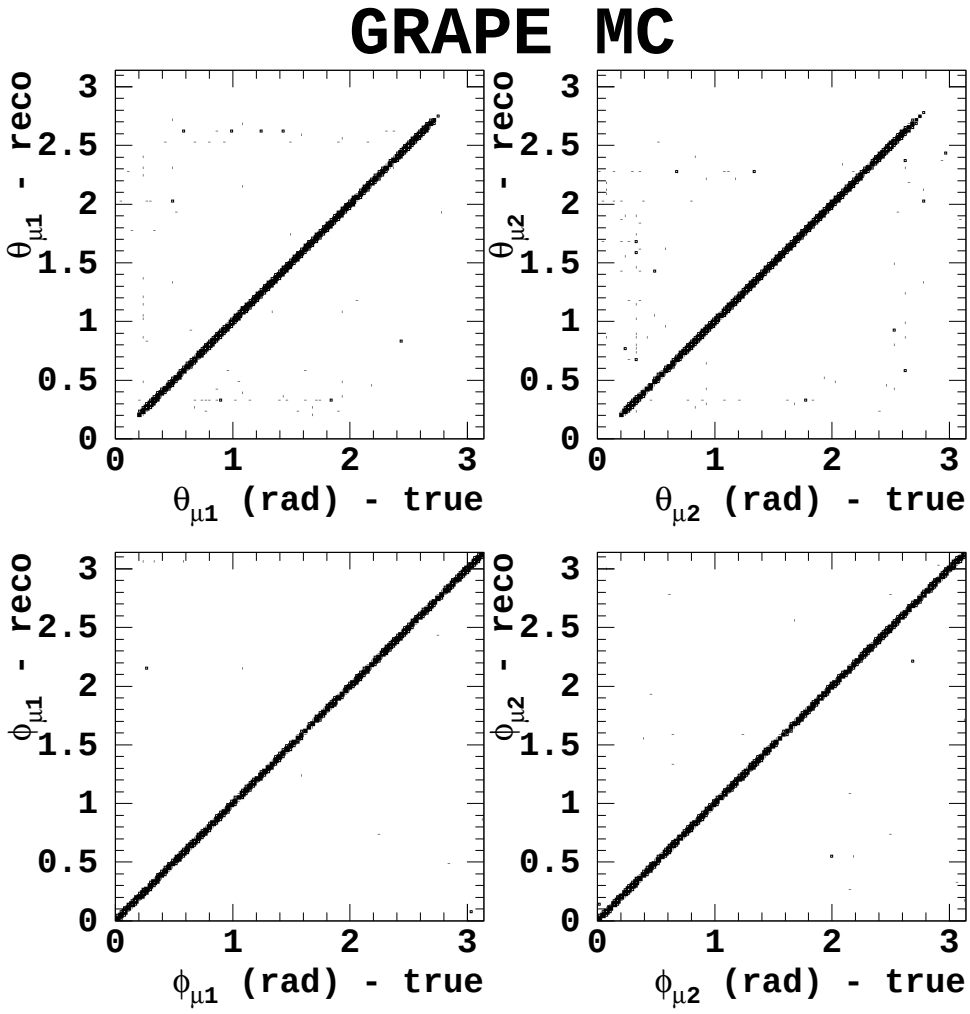

Figure 4.10: Correlation of the variables reconstructed by the muon finders and the true variables, obtained on a GRAPE sample. In the first row the results for the polar angles of the two muons are shown, whereas in the second row the correlations of the azimuthal angles are plotted.

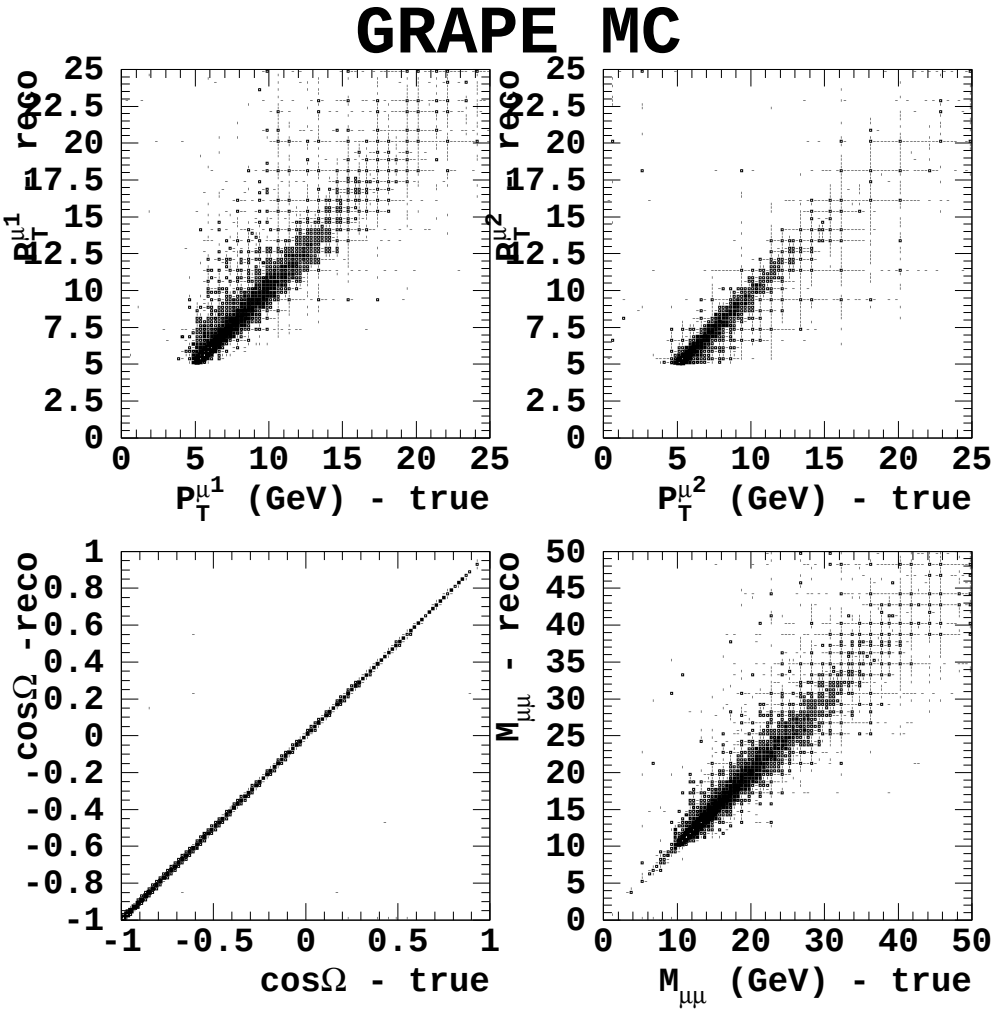

Figure 4.11: Correlation of the variables reconstructed by the muon finders and the true variables, obtained on a GRAPE sample. In the first row the results for the transverse momenta of the two muons are shown, whereas in the second row the correlations of $\cos(\Omega)$ and $M_{\mu\mu}$ are plotted, being Ω the angle between muons and $M_{\mu\mu}$ their invariant mass.

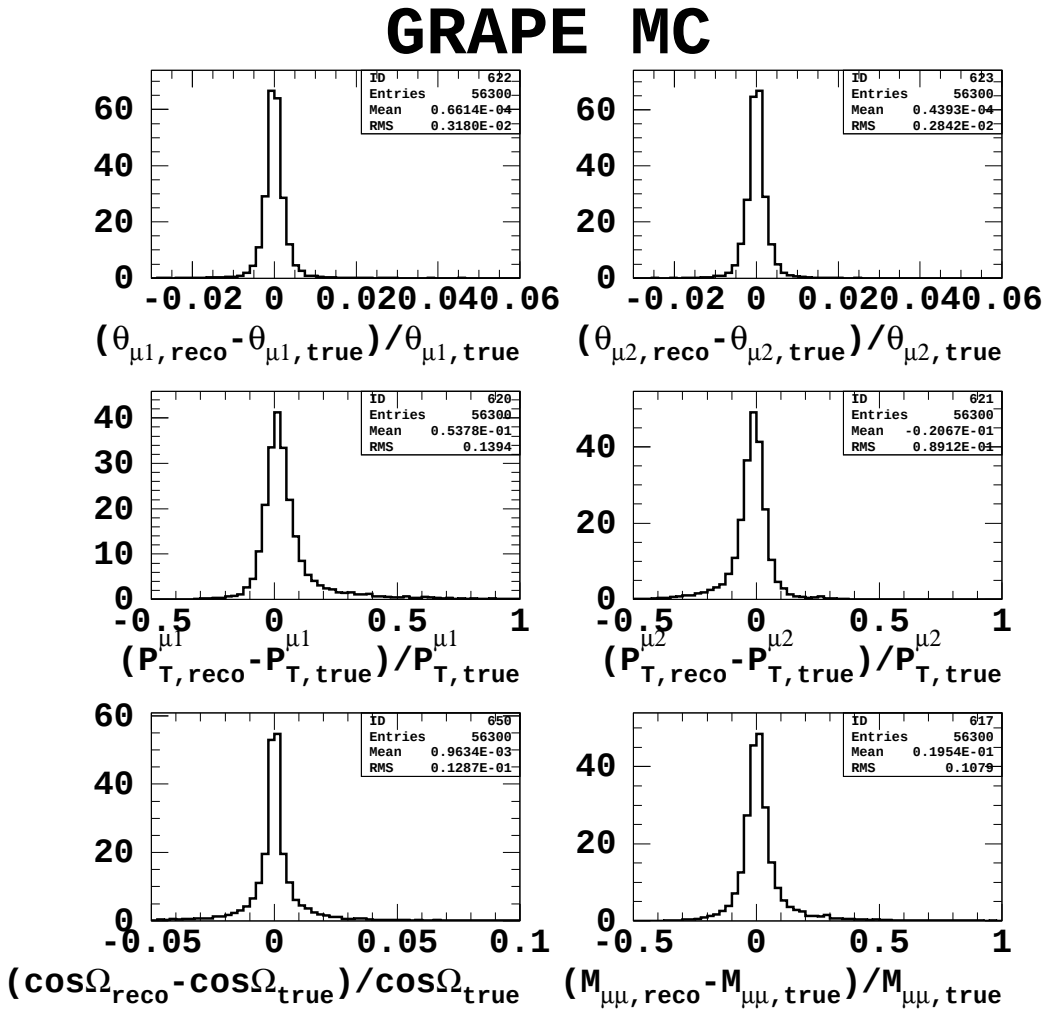

Figure 4.12: Resolution of the variables reconstructed by the muon finders. In the first row the results on the polar angles are shown, in the second row the P_T^μ resolution is plotted, in the bottom row the resolutions of cos(Ω) and $M_{\mu\mu}$ are reported.

Chapter 5

Data results and Monte Carlo comparison

In this chapter I report on the results I have obtained on the multi–lepton search. They were obtained independently and represent an extension of the ICHEP 2002 results reviewed in Sect. 1.6. The chapter is divided in two parts, the first devoted to the multi–electron study, the other one to the di–muons. The measured cross sections will be shown in the next chapter.

5.1 Multi–electron search

All the luminosity collected from year 1996 to 2000 has been used for the multi–electron search. After the selection of runs in which the CTD and the calorimeter were working properly, 120.49 pb^{-1} were left (see Table 5.1).

The events were classified as $2e$ if just two electrons were found or as $3e$ when three electrons were detected. No events with more than three electrons were found in the data sample.

The Standard Model expectation is composed by the di–electron contribution, simulated by the GRAPE Monte Carlo, the neutral current DIS, simulated

Collisions	Period	Lumi (pb^{-1})
e^+p	1996–1997	38.63
e^-p	1998–1999	16.71
e^+p	1999–2000	65.15
$e^\pm p$	1996–2000	120.49

Table 5.1: Integrated luminosity used for the multi–electron analysis. The numbers are first shown separately for the three running periods, then the 1996–2000 luminosity is given. The integrated luminosity is the one available after the selection of runs in which the CTD and the UCAL were working properly.

by DJANGOH and the QED Compton, simulated by the COMPTON program. Neutral current and QED events can survive the selection if a jet or the electromagnetic deposit of a photon are misidentified as an electron. The generators and the samples have already been described in Chapter 3. The ratios of data and Monte Carlo integrated luminosities were used as a weight for the single Monte Carlo events.

The description of the data given by the Standard Model is good. In Fig. 5.1 the transverse energies E_T^e and the polar angles θ_e of the two highest E_T electron are shown for the $2e$ sample; first the distributions for the three running periods are plotted separately, then the cumulative graphics are also plotted. Fig. 5.2 shows the same results as obtained on the $3e$ sample.

In Tables 5.2 and 5.3 the number of events counted in data and in Monte Carlo using the $2e$ and $3e$ selections, respectively, is reported. The contributions of the individual processes are also shown. The agreement of data and Standard Model is good for the $2e$ sample, although a slight deficiency is observed in data in the high mass region ($M_{12} > 50$ GeV, being M_{12} the invariant mass of the di–electron). The agreement of data with Standard Model in the $3e$ is still satisfactory, even if a slight deficiency is seen in the low mass region of real data[1].

Table 5.4 reports the number of events with two or three electrons found, namely the sum of $2e$ and $3e$ samples.

In Fig. 5.3 some variables are plotted for the 1996–2000 data sample. The variables are the invariant mass of the two highest E_T electrons, M_{12}, the angles $|\theta_{e1} - \theta_{e2}|$ and $(\phi_{e1} - \phi_{e2})$, being ϕ_e the azimuthal angle of the electron, and the difference of energy and longitudinal momentum of the two electrons, $(E - P_z)_{ee}$. In the upper left plots the distributions for the $2e$ sample are shown, in the upper right the $3e$, in the bottom the $2e$+$3e$.

In Fig. 5.4 more plots are shown for the 1996–2000 period, $2e$+$3e$ sample. In the upper left the transverse and total energies, and the angles of the first electron are plotted. The same is done for the second electron in the upper right. In the lower left, the hadronic variables coming from CorAndCut are plotted: total energy, $(E - P_z)$, transverse energy and momentum. In the lower right the global variables (electrons+hadrons) are shown: transverse momentum and energy, $(E - P_z)$, $(\phi_{e1} - \phi_{\rm had})$.

As already said, the agreement is satisfactory, both in the shapes of the distribution and in the normalisation. This holds for all the subsamples and all the variables analysed.

The excess observed by H1 in the number of $2e$ and $3e$ events at high mass ($M_{12} > 100$ GeV), see Section 1.6, is not confirmed by this analysis.

5.1.1 Comparison of LPAIR to GRAPE MC

A LPAIR sample was generated using the 1996 detector configuration, and its simulation compared to the GRAPE prediction. The distributions of the electron

[1] In the $3e$ case, the M_{12} mass is calculated for the two highest E_T electrons.

Period	Selection	Data	All SM	GRAPE	NC DIS	QED–C
1996–97	All $2e$	58	56.97	47.39	5.51	4.07
	$M_{12} > 50$ GeV	6	8.28	6.53	1.35	0.40
	$M_{12} > 100$ GeV	0	0.18	0.13	0.00	0.05
1998–99	All $2e$	32	29.47	25.96	2.28	1.23
	$M_{12} > 50$ GeV	2	3.95	3.33	0.40	0.22
	$M_{12} > 100$ GeV	0	0.07	0.05	0.00	0.02
1999–00	All $2e$	93	111.35	95.76	10.78	4.80
	$M_{12} > 50$ GeV	9	15.25	12.82	1.58	0.85
	$M_{12} > 100$ GeV	1	0.43	0.29	0.08	0.06
1996–00	All $2e$	183	197.78	169.11	18.57	10.10
	$M_{12} > 50$ GeV	17	27.47	22.68	3.32	1.47
	$M_{12} > 100$ GeV	1	0.67	0.46	0.08	0.13

Table 5.2: Number of di–electrons ($2e$ selection) measured in the different running periods, compared to the expectation from the Standard Model simulation. The individual contributions from the various processes are also shown: di–electron production (GRAPE), neutral current DIS (NC DIS) and QED Compton (QED–C).

Period	Selection	Data	All SM	GRAPE	NC DIS	QED–C
1996–97	All $3e$	6	10.97	10.91	0.06	0.00
	$M_{12} > 50$ GeV	1	2.28	2.28	0.00	0.00
	$M_{12} > 100$ GeV	0	0.12	0.12	0.00	0.00
1998–99	All $3e$	5	6.19	6.19	0.00	0.00
	$M_{12} > 50$ GeV	1	1.16	1.16	0.00	0.00
	$M_{12} > 100$ GeV	0	0.07	0.07	0.00	0.00
1999–00	All $3e$	15	20.86	20.78	0.08	0.00
	$M_{12} > 50$ GeV	4	4.10	4.02	0.08	0.00
	$M_{12} > 100$ GeV	0	0.26	0.26	0.00	0.00
1996–00	All $3e$	26	38.03	37.88	0.15	0.00
	$M_{12} > 50$ GeV	6	7.54	7.46	0.08	0.00
	$M_{12} > 100$ GeV	0	0.44	0.44	0.00	0.00

Table 5.3: Number of tri–electrons ($3e$ selection) measured in the different running periods, compared to the expectation from the Standard Model simulation. The individual contributions from the various processes are also shown: di–electron production (GRAPE), neutral current DIS (NC DIS) and QED Compton (QED–C).

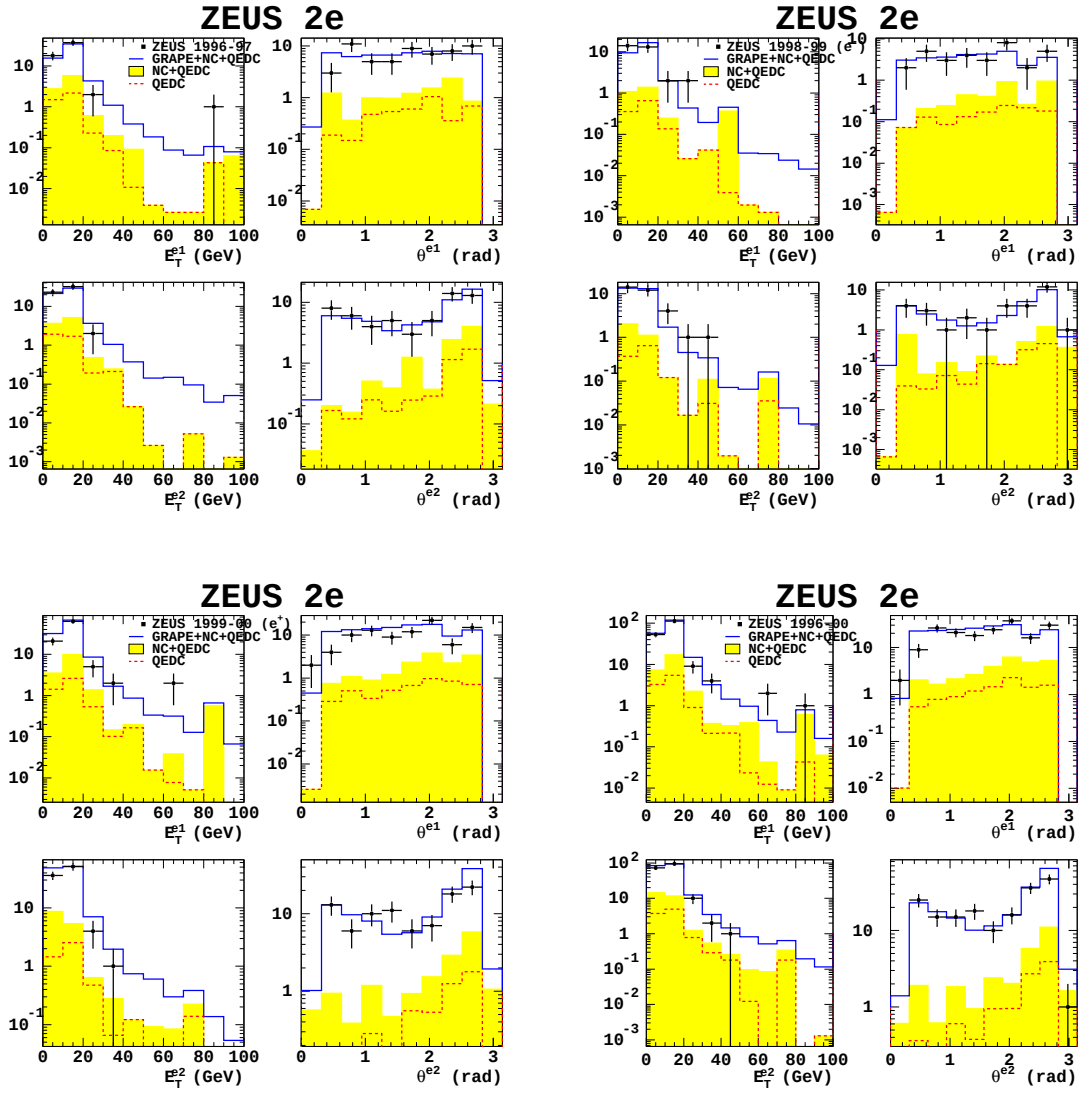

Figure 5.1: Distributions of electron variables for the 1996–97 running period (upper left plots), 1998–99 (upper right), 1999–2000 (lower left) and 1996–2000 (lower right). For each running period the transverse energy E_T^e and the polar angle θ_e of the two electrons with highest E_T are plotted. The sample considered is the "2e".

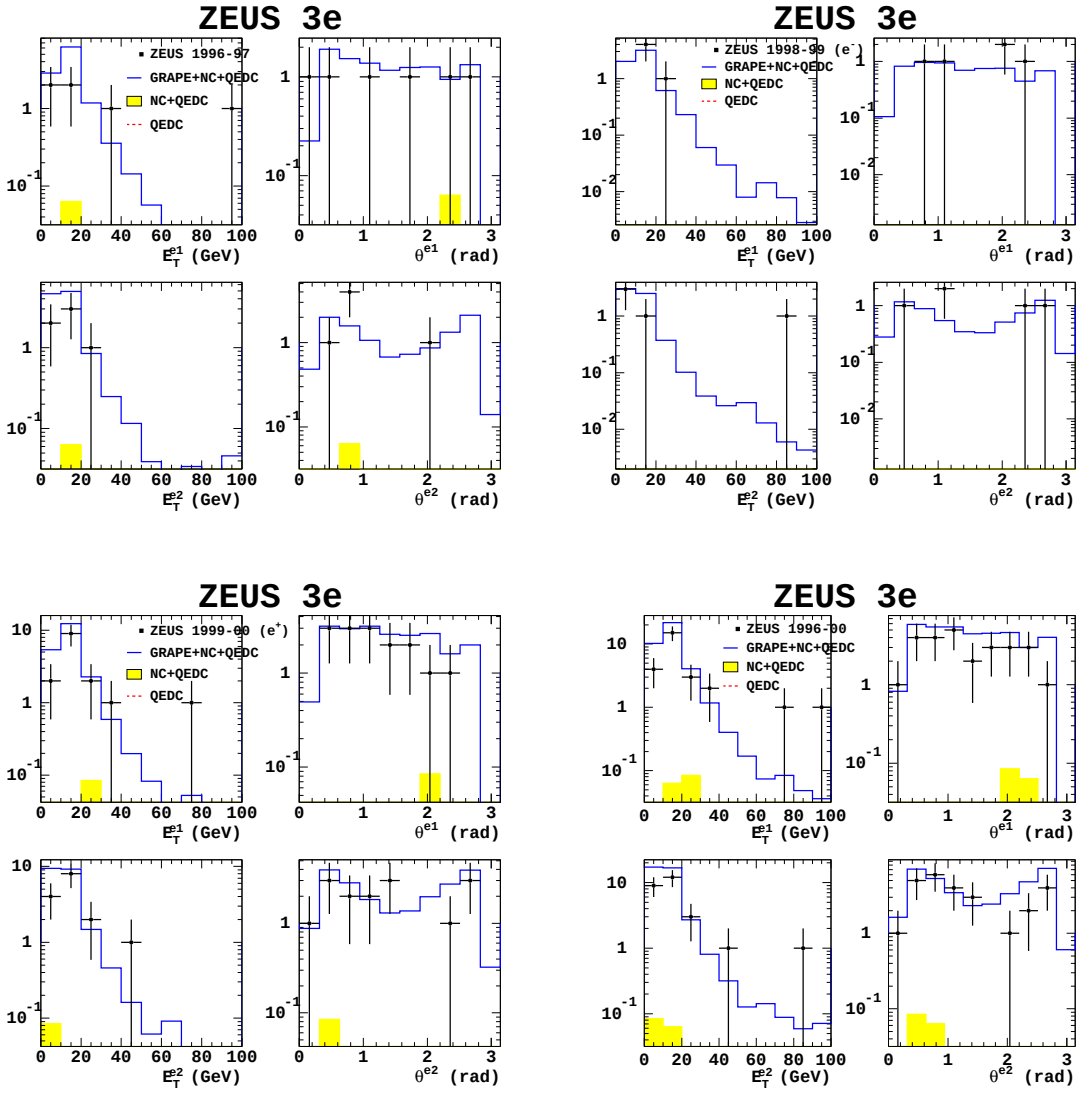

Figure 5.2: Distributions of electron variables for the 1996–97 running period (upper left plots), 1998–99 (upper right), 1999–2000 (lower left) and 1996–2000 (lower right). For each running period the transverse energy E_T^e and the polar angle θ_e of the two electrons with highest E_T are plotted. The sample considered is the "3e".

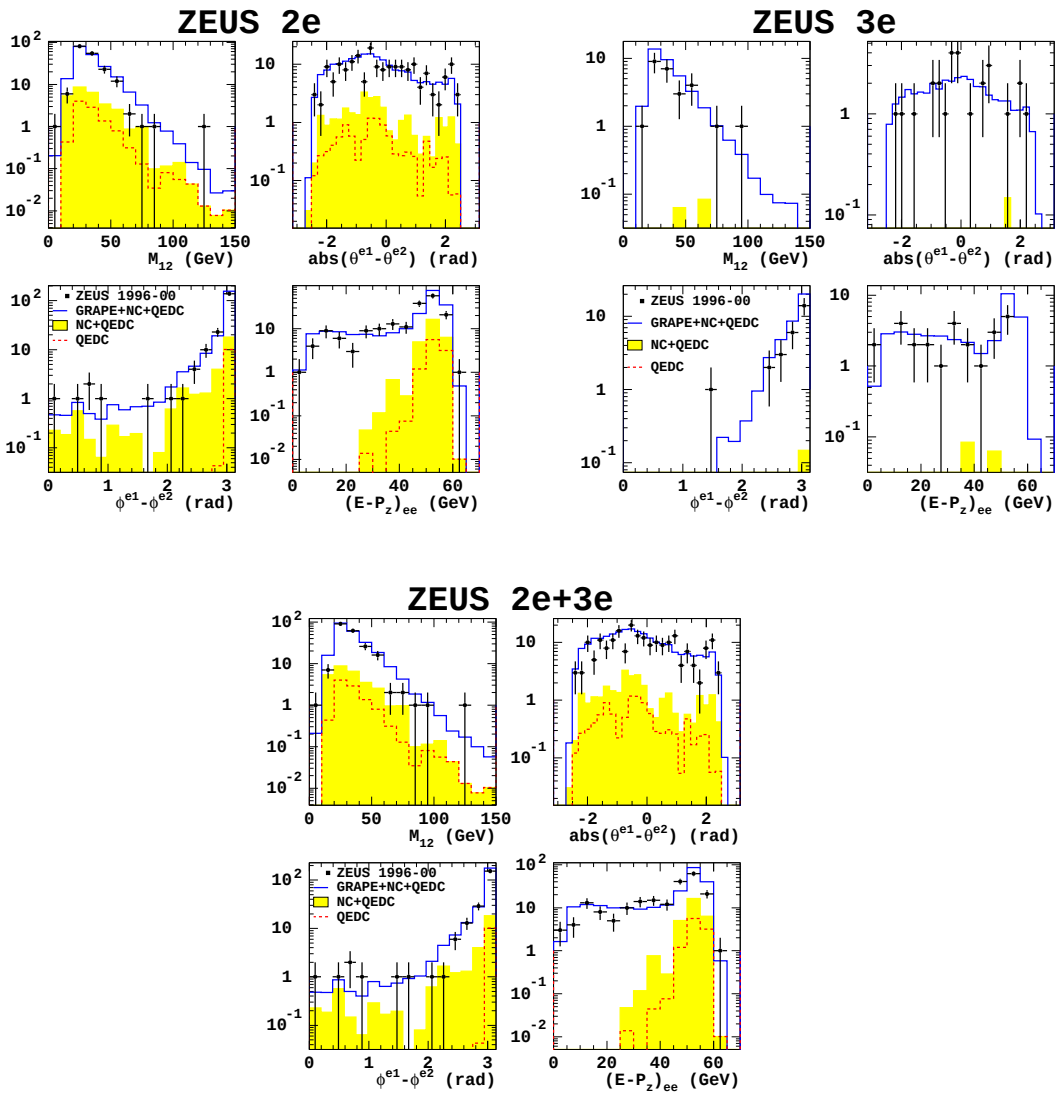

Figure 5.3: Distributions of various electron variables in the 1996–2000 running period, 2e sample (upper left plots), 3e sample (upper right), 2e+3e (bottom). The invariant mass M_{12}, the difference of polar and azimuthal angles, $(E - P_z)$ of the two electrons are plotted.

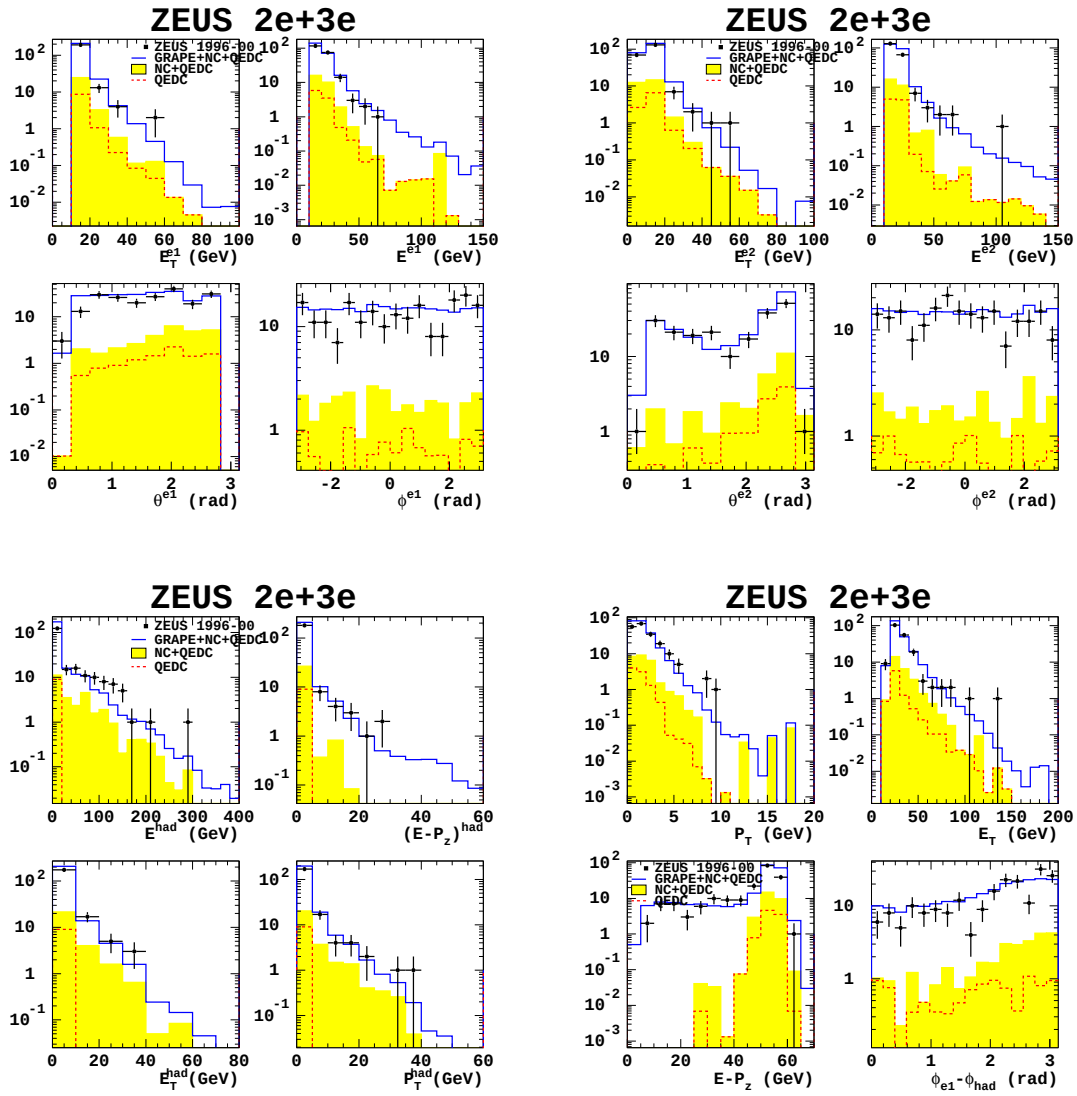

Figure 5.4: Distributions of various electron variables in the 1996–2000 running period, $2e$+$3e$ sample. In the upper left transverse and total energy, polar and azimuthal angles are plotted for the highest E_T electron. The same variables are plotted for the second highest E_T electron in the upper right. In the lower left the hadronic variables, as coming from CorAndCut, are shown: total energy, $(E-P_z)$, transverse energy and momentum. In the lower right the global variables (electrons+hadrons) of the event are plotted: transverse momentum and energy, $(E-P_z)$, the distance in ϕ of the first electron and the hadronic deposits.

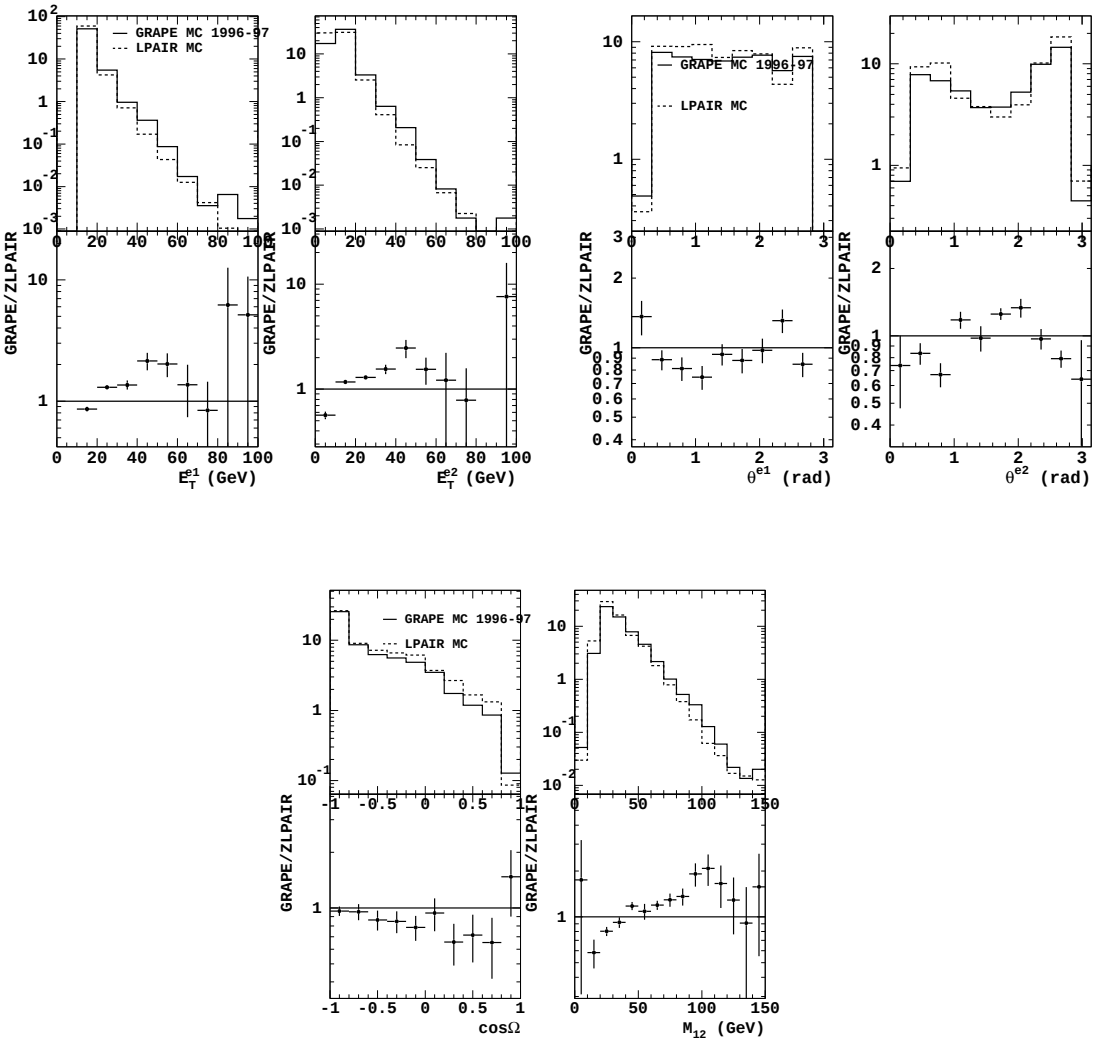

Figure 5.5: Comparison of GRAPE and LPAIR simulations. In the upper left graphs the transverse energy E_T^e of the two electrons is plotted, and the ratio of GRAPE over LPAIR expectations. In the upper right the same is done for the polar angle θ_e. In the bottom the comparison is done for the cos(Ω) and the invariant mass M_{12} of the di–electron.

Period	Selection	Data	All SM	GRAPE	NC DIS	QED–C
1996–97	All $2e$+$3e$	64	67.94	58.30	5.57	4.07
	$M_{12} > 50$ GeV	7	10.56	8.81	1.35	0.40
	$M_{12} > 100$ GeV	0	0.39	0.24	0.00	0.05
1998–99	All $2e$+$3e$	37	35.66	32.15	2.28	1.23
	$M_{12} > 50$ GeV	3	5.11	4.49	0.40	0.22
	$M_{12} > 100$ GeV	0	0.14	0.12	0.00	0.02
1999–00	All $2e$+$3e$	108	132.21	116.54	10.87	4.80
	$M_{12} > 50$ GeV	13	19.35	16.84	1.66	0.85
	$M_{12} > 100$ GeV	1	0.69	0.55	0.08	0.06
1996–00	All $2e$+$3e$	209	235.82	207.00	18.72	10.10
	$M_{12} > 50$ GeV	23	35.01	30.14	3.40	1.47
	$M_{12} > 100$ GeV	1	1.12	0.91	0.08	0.13

Table 5.4: Number of multi–electrons ($2e$+$3e$) measured in the different running periods, compared to the expectation from the Standard Model simulation. The individual contributions from the various processes are also shown: di–electron production (GRAPE), neutral current DIS (NC DIS) and QED Compton (QED–C).

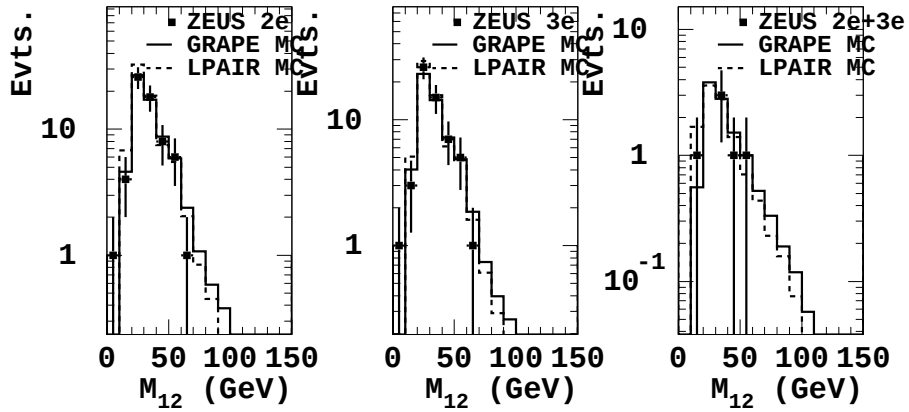

Figure 5.6: Invariant mass (M_{12}) distributions simulated by the GRAPE and LPAIR generators, and measured in 1996–97 data. In the left the $2e$ selection is applied, in the centre the $3e$, in the right the $2e$+$3e$.

MC Type	All $2e$	$M_{12} > 50$ GeV	$M_{12} > 100$ GeV
GRAPE	47.39	6.53	0.126
LPAIR	53.94	5.79	0.071
MC Type	All $3e$	$M_{12} > 50$ GeV	$M_{12} > 100$ GeV
GRAPE	10.91	2.28	0.118
LPAIR	11.09	1.68	0.072
MC Type	All $2e$+$3e$	$M_{12} > 50$ GeV	$M_{12} > 100$ GeV
GRAPE	58.30	8.81	0.244
LPAIR	65.03	7.47	0.143

Table 5.5: $2e$, $3e$ and $2e$+$3e$ events predicted for years 1996–97 by the GRAPE and LPAIR generators. LPAIR is slightly higher than GRAPE at low M_{12}, the opposite happens at high mass.

Collisions	Period	Lumi (pb^{-1})
e^+p	1996–1997	33.55
e^-p	1998–1999	11.93
e^+p	1999–2000	55.99
$e^\pm p$	1996–2000	101.47

Table 5.6: Integrated luminosity used for the di–muon analysis. The numbers are first shown separately for the three running periods, then the 1996–2000 luminosity is given. The integrated luminosity is the one available after the selection of runs in which the CTD, the UCAL and the muon chambers were working properly.

variables (transverse energy and polar angle), of the cosine of the angle between electrons, $\cos(\Omega)$, of the invariant mass M_{12} are plotted in Fig. 5.5, as well as the GRAPE over LPAIR ratio. In Table 5.5 the number of events predicted by the two simulations are compared.

It can be seen that at low mass M_{12} of the di–electron the LPAIR overshoots GRAPE, whereas at high mass the opposite happens. Even if the LPAIR Monte Carlo lacks some diagrams, it is able to describe data as well as GRAPE; the invariant mass distributions of the two generators are compared to the 1996–97 data in Fig. 5.6, using $2e$, $3e$, $2e$+$3e$ selections.

5.2 Di–muon search

All the luminosity collected in years 1996–2000 has been used for the di–muon search. After the selection of runs in which the CTD, the calorimeter and the muon chambers were working properly, 101.47 pb^{-1} were left (see Table 5.6).

Region	Cut	Data/MC ratio	
		Years 1996–97	Years 1998–2000
BMUON	$4.25 < P_T^\mu < 10$ GeV	0.854 ± 0.061	0.709 ± 0.042
RMUON	$5 < P_T^\mu < 10$ GeV	0.819 ± 0.068	0.853 ± 0.050

Table 5.7: B/RMUON efficiencies: the ratio of data and Monte Carlo trigger efficiencies are shown for BMUON (FLT10) and RMUON (FLT11), for 1996–97 and 1998–2000 running periods.

In the case of di–muon search all the background sources were considered to be negligible, as found by H1 in its analysis (see for example Fig. 1.18).

The ratios of data and Monte Carlo integrated luminosities have been taken as weight for Monte Carlo events.

Another weight factor had to be taken into account: in the GEANT simulation of the B/RMUON chambers effects like the degradation of electronics and limited streamer tubes and the effect of a high–voltage that is lower than the design value (to extend the lifetime of LSTs) were not included. For this reason the efficiencies in the trigger selection and the offline muon reconstruction are higher for Monte Carlo events than for real events. In [82] a method for evaluating the ratio of data and Monte Carlo efficiencies is described. In this analysis the trigger efficiencies were corrected using the factors in Table 5.7[2].

The variables of the highest P_T muon are plotted for data and the GRAPE simulation in Fig. 5.7. The upper left plots refer to 1996–97 running period, the upper right to 1998–99, the lower left to 1999–2000; in the lower right graphs the cumulative distributions for 1996–2000 are plotted. The variables considered are the transverse momentum P_T^μ, the distance of the muon from the closest track in $\eta\phi$, $D_{\rm Trk}^\mu$, the polar and azimuthal angles, θ_μ and ϕ_μ. Both the shape and the normalisation of data distributions are well reproduced by the simulation.

The same variables of the second muon are plotted for the same running periods in Fig. 5.8. Also here the description of the data given by GRAPE is good.

In Fig. 5.9 more distributions are shown, for the 1996–2000 period. In the upper plots the angles $\Delta\theta = (\theta_{\mu 1} - \theta_{\mu 2})$ and $|\Delta\phi| = |\phi_{\mu 1} - \phi_{\mu 2}|$, $\cos(\Omega)$, being Ω the angle between the two muons, and the invariant mass $M_{\mu\mu}$ of the di–muon are shown. In the lower left the energies measured by the calorimeter, corrected for the noisy cells and different energy scale in data and Monte Carlo (Sect. 4.3.1), are plotted for the various calorimeter sections. In the lower right the hadronic variables as obtained by the ZUFOs algorithm are plotted: transverse energy E_T and momentum P_T, $(E - P_z)$ and the polar angle γ of the hadronic system. The data sample is well described by the simulation; the only significant feature are the three events crowding at $M_{\mu\mu} \sim 50$ GeV.

[2]M. Turcato and A. Bertolin, private communication.

Period	Selection	Data	GRAPE
1996–97	All	74	81.01
	$M_{\mu\mu} > 50$ GeV	2	1.27
	$M_{\mu\mu} > 100$ GeV	0	0.07
1998–99	All	27	28.12
	$M_{\mu\mu} > 50$ GeV	1	0.49
	$M_{\mu\mu} > 100$ GeV	0	0.04
1999–00	All	117	132.01
	$M_{\mu\mu} > 50$ GeV	3	2.14
	$M_{\mu\mu} > 100$ GeV	0	0.12
1996–00	All	218	241.14
	$M_{\mu\mu} > 50$ GeV	6	3.91
	$M_{\mu\mu} > 100$ GeV	0	0.23

Table 5.8: Number of di–muons measured in the different running periods, compared to the expectation from the Standard Model simulation.

MC Type	All	$M_{\mu\mu} > 50$ GeV	$M_{\mu\mu} > 100$ GeV
GRAPE	28.12	0.494	0.035
LPAIR	27.79	0.383	0.013

Table 5.9: Di–muon events predicted for years 1998–99 by the GRAPE and LPAIR generators.

These three events were scanned (Fig. 5.10); the first and the third have the two muons found by the muon chambers, the second has a muon found by the RMUON detector and another one identified by a track and a MIP–like deposit in the calorimeter. They all resemble genuine di–muon events.

The number of events counted in the data samples and in the simulations is summarised in Table 5.8. The process is well simulated by the GRAPE generator.

5.2.1 Comparison of LPAIR to GRAPE MC

A LPAIR sample was generated using the 1998 detector configuration, and its simulation compared to the GRAPE prediction. The distributions of the muon variables (transverse momentum, polar angle and distance of the closest track), of the cosine of the angle between electrons, $\cos(\Omega)$, and the invariant mass $M_{\mu\mu}$ are plotted in Fig. 5.11, as well as the GRAPE over LPAIR ratio. All distributions agree nicely. In Table 5.9 the number of events predicted by the two simulations are compared. The expectations are very close at low mass, whereas at higher mass they are still in agreement even if the statistics is poor.

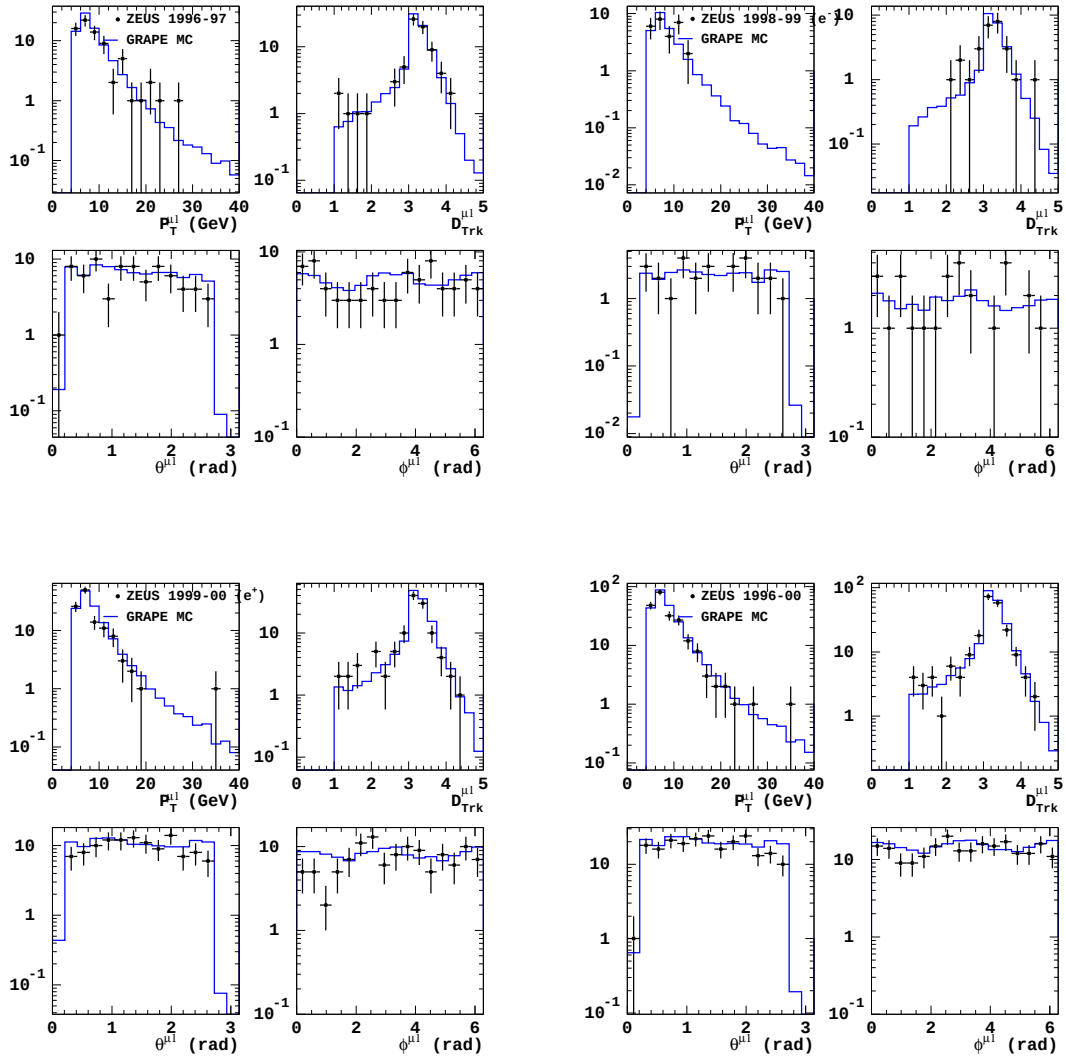

Figure 5.7: Distributions of variables of the highest P_T muon, for the 1996–97 running period (upper left plots), 1998–99 (upper right), 1999–2000 (lower left) and 1996–2000 (lower right). For each running period the transverse momentum P_T^μ, the distance of the closest track $D_{\rm Trk}^\mu$, the polar (θ_μ) and azimuthal (ϕ_μ) angles are plotted.

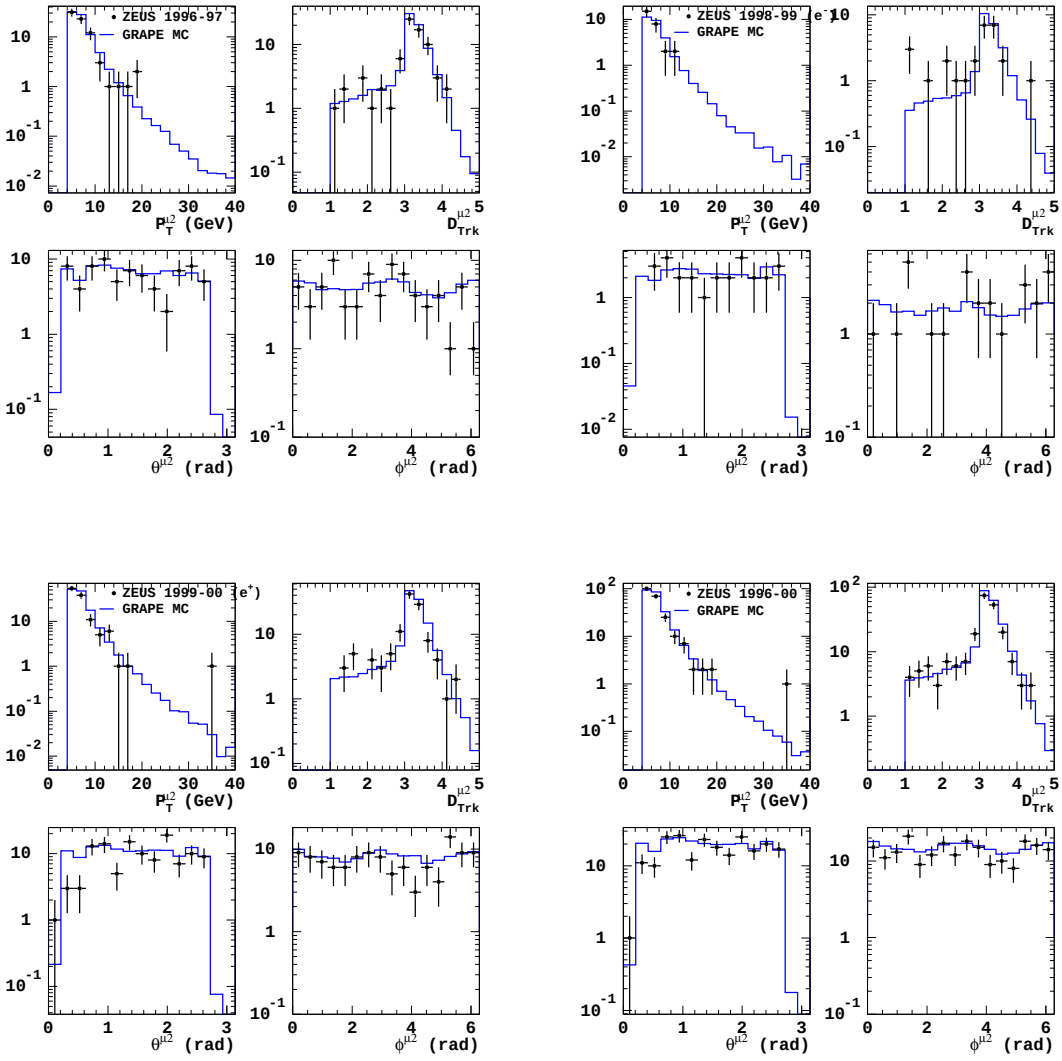

Figure 5.8: Distributions of variables of the second muon, for the 1996–97 running period (upper left plots), 1998–99 (upper right), 1999–2000 (lower left) and 1996–2000 (lower right). For each running period the transverse momentum P_T^{μ}, the distance of the closest track $D_{\rm Trk}^{\mu}$, the polar (θ_μ) and azimuthal (ϕ_μ) angles are plotted.

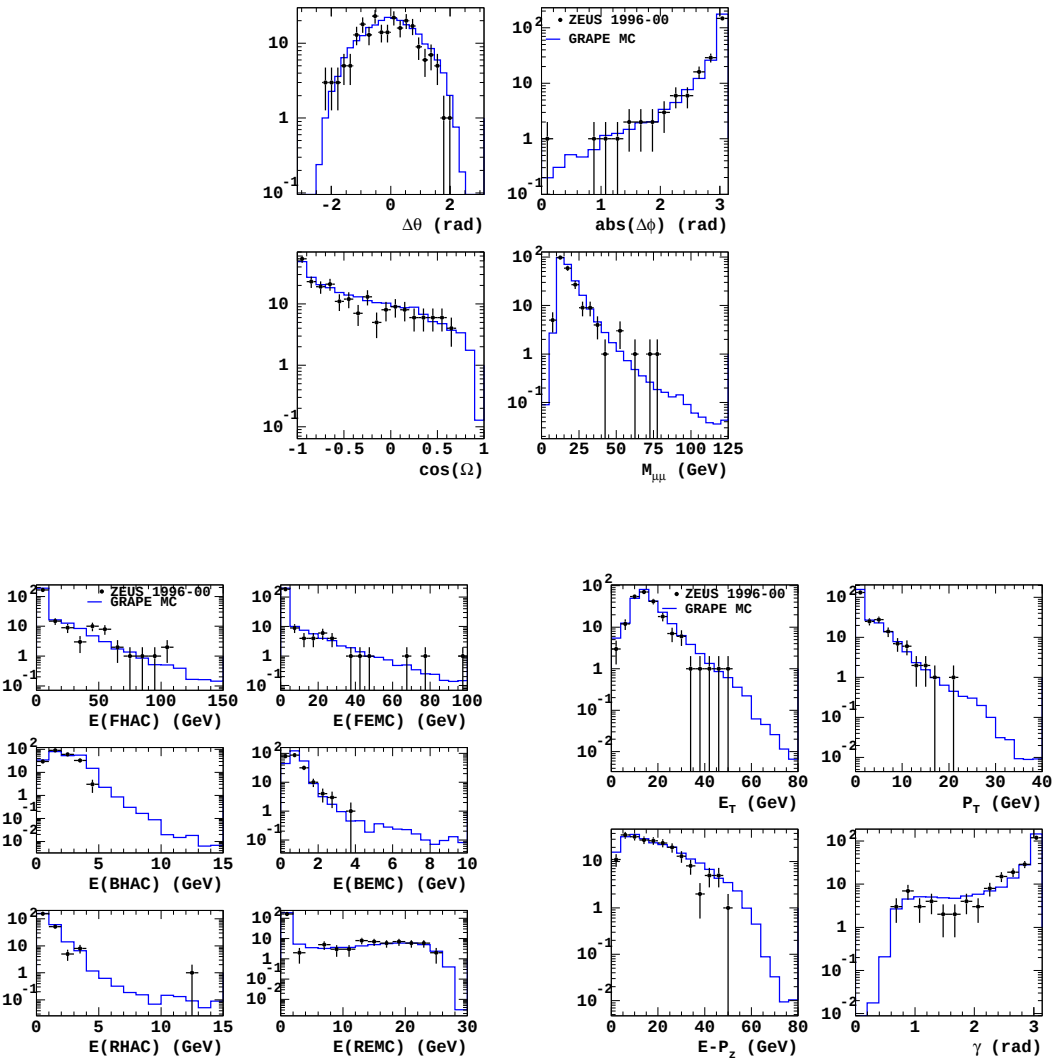

Figure 5.9: Distributions of variables for the 1996–2000 running period. In the upper plots the angles $\Delta\theta$ and $|\Delta\phi|$, the $\cos(\Omega)$ and the invariant mass $M_{\mu\mu}$ are shown. In the lower left the energies measured by the various section of the calorimeter are reported. In the lower right the hadronic variables as reconstructed by the ZUFOs algorithm are plotted: total transverse energy and momentum, $(E - P_z)$, polar angle (γ) of the hadronic system.

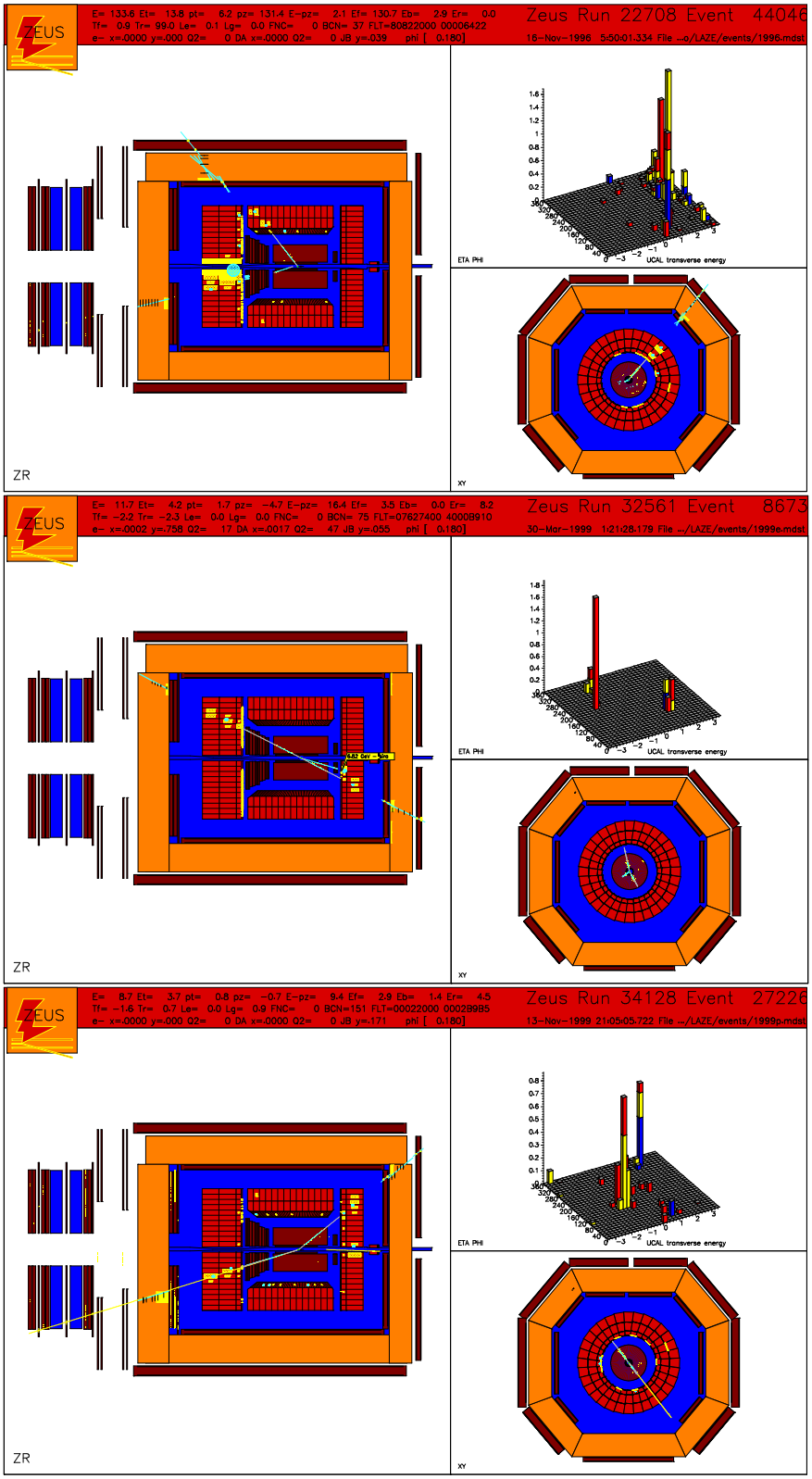

Figure 5.10: The three di–muons found with invariant mass around 50 GeV. They have $M_{\mu\mu}$ = 50.3, 51.3, 51.5 GeV, respectively. All of them are clean events with activity in the muon chambers; in the second event a muon is outside the angular acceptance of the muon detectors and is identified by a CTD track and a MIP–like deposit in the UCAL.

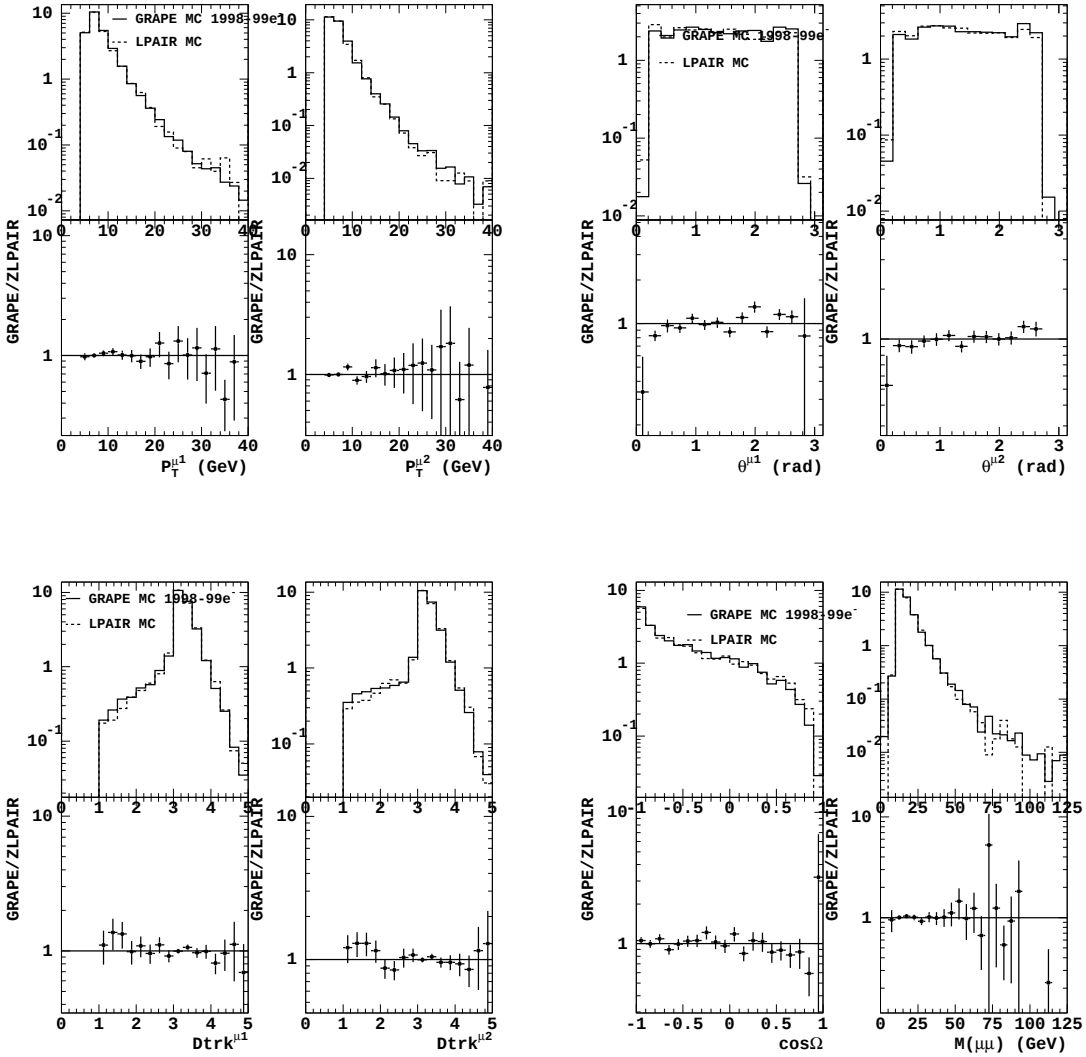

Figure 5.11: Comparison of GRAPE and LPAIR simulations. In the upper left graphs the transverse momentum P_T^μ of the two muons is plotted, and the ratio of GRAPE over LPAIR expectations. In the upper right the same is done for the polar angle θ_μ. In the lower left the comparison is done for the distance D^μ_{Trk}, in the lower right for the $\cos(\Omega)$ and the invariant mass $M_{\mu\mu}$ of the di–muon.

Chapter 6

Cross section measurement

In this chapter the measurement of the di–electron and di–muon production cross sections will be described. The phase space, the method used and the results obtained will be presented.

6.1 Di–electron production

In order to evaluate the cross section of the di–electron production, the signal has to be separated from the background (neutral current DIS and QED Compton). The variable that permits to distinguish between the two is $(E - P_z)$.

For events in which the scattered electron is measured, this quantity equals the value before the collision:

$$E - P_z = (E_e^{\text{ini}} + E_p^{\text{ini}}) - (P_e^{\text{ini}} + P_p^{\text{ini}})_z = 2E_e^{\text{ini}} = 55 \text{ GeV}, \tag{6.1}$$

since the incoming proton moves in the z direction ($P_{p,z}^{\text{ini}} = E_p^{\text{ini}}$) whereas the electron in the opposite direction ($P_{e,z}^{\text{ini}} = -E_e^{\text{ini}}$). When the scattering angle is small and the electron escapes the detection, a significant deficiency is observed in $(E - P_z)$. The proton constituents which go through the hole in the FCAL do not contribute to the $(E - P_z)$ since they have $P_z \simeq E$.

The neutral current and QED Compton events which are misidentified as di–electrons have the scattered electron measured and their $(E - P_z)$ peaks at 55 GeV (see Fig. 5.4). The genuine multi–electrons have also a peak at 55 GeV, but the distribution have a sizable number of events below this value; they are events in which the scattered electron is undetected while the other two electrons are measured.

Selection of $\gamma\gamma$ sample

A cut $(E - P_z) < 45$ GeV has been established in order to reject the background. This subsample of $2e$ events has been called "$\gamma\gamma$", accordingly to the name used by H1, Sect. 1.6.

The kinematic region selected for the cross section measurement is therefore:

Period	Selection	Data	All SM	GRAPE	NC DIS	QED–C
1996–97	All $\gamma\gamma$	15	14.07	13.98	0.07	0.02
	$M_{12} > 50$ GeV	2	0.88	0.86	0.00	0.02
	$M_{12} > 100$ GeV	0	0.03	0.03	0.00	0.00
1998–99	All $\gamma\gamma$	4	8.12	8.11	0.00	0.01
	$M_{12} > 50$ GeV	0	0.38	0.37	0.00	0.01
	$M_{12} > 100$ GeV	0	0.01	0.01	0.00	0.00
1999–00	All $\gamma\gamma$	32	30.68	30.62	0.00	0.06
	$M_{12} > 50$ GeV	1	1.63	1.57	0.00	0.06
	$M_{12} > 100$ GeV	0	0.06	0.05	0.00	0.01
1996–00	All $\gamma\gamma$	51	52.86	52.71	0.07	0.08
	$M_{12} > 50$ GeV	3	2.88	2.80	0.00	0.08
	$M_{12} > 100$ GeV	0	0.09	0.08	0.00	0.01

Table 6.1: Number of di–electrons ($\gamma\gamma$ selection) measured in the different running periods, compared to the expectation from the Standard Model simulation. The individual contributions from the various processes are also shown: di–electron production (GRAPE), neutral current DIS (NC DIS) and QED Compton (QED–C).

- two electrons in $17^\circ < \theta_e < 164^\circ$,
- $E_T^{e1} > 10$ GeV and $E_T^{e2} > 5$ GeV,
- $M_{12} > 5$ GeV,
- $E - P_z < 45$ GeV.

The number of events found in this region is reported in Table 6.1; again a nice description of the data is given by GRAPE. The shapes of the distributions are also well reproduced (see Fig. 6.1).

Measured cross section

After having defined a certain region in the phase space, the following quantities are considered in order to calculate the cross section:

- N_g, the number of Monte Carlo events generated in the region;
- N^r, the number of MC events reconstructed in the region;
- N_g^r, the number of MC events generated and reconstructed in the region;
- N_d, the number of events selected in data samples.

With the use of the following definitions:

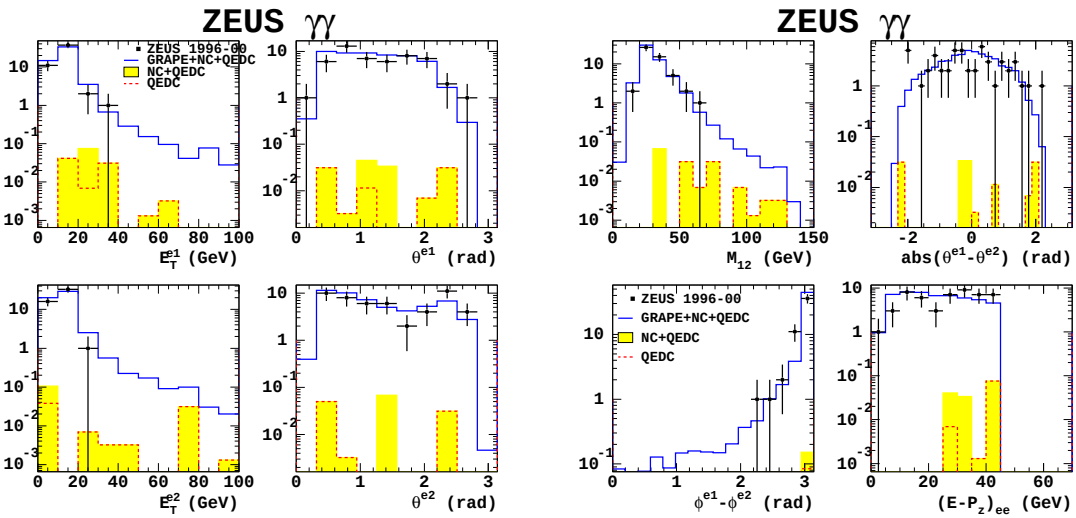

Figure 6.1: Distributions for the $\gamma\gamma$ sample, 1996–2000 period. Transverse energy E_T^e and polar angle θ_e of the two electrons are plotted on the left. The invariant mass of the di–electron, M_{12}, the angles $|\Delta\theta|$ and $\Delta\phi$, $(E - P_z)$ of the di–electron are plotted on the right.

- efficiency: $\epsilon = N_g^r/N_g$,
- purity: $p = N_g^r/N^r$,
- acceptance: $a = \epsilon/p = N^r/N_g$,

the predicted and measured cross sections are obtained:

$$\sigma_{\rm MC} = \frac{N_g}{L}, \tag{6.2}$$

$$\sigma_{\rm DATA} = \frac{N_d}{a \cdot L}, \tag{6.3}$$

being L the integrated luminosity.

In the case of the differential cross section, if x is a physical quantity and Δx the chosen width of the bin, we can also define:

$$\frac{{\rm d}\sigma_{\rm MC}}{{\rm d}x} = \frac{N_g}{L\ \Delta x}, \tag{6.4}$$

$$\frac{{\rm d}\sigma_{\rm DATA}}{{\rm d}x} = \frac{N_d}{a\ L\ \Delta x}. \tag{6.5}$$

In Table 6.2 purities, acceptances and total cross sections (with their statistical and systematic errors) are presented, separately for the running periods. The cross section for the 1998–99 is affected by a huge statistical uncertainty because

Period	Purity	Acceptance	$\sigma_{\rm DATA}$ (pb)	$\sigma_{\rm MC}$ (pb)
1996–97	0.825	0.234	$1.66 \pm 0.43^{+0.18}_{-0.14}$	1.55
1998–99	0.773	0.292	$0.82 \pm 0.41^{+0.13}_{-0.12}$	1.66
1999–00	0.790	0.283	$1.73 \pm 0.31^{+0.22}_{-0.17}$	1.66
1996–00			$1.62 \pm 0.23^{+0.21}_{-0.16}$	

Table 6.2: Measurement of the di–electron production cross section. The purity, the acceptance, the measured and predicted cross sections are reported separately for the three running periods. The first and second uncertainty given for the cross sections are the statistical and the systematic ones, respectively. The three measurements are then combined to give a cross section referred to $\sqrt{s} = 318$ GeV.

four events only are found in data. The procedure to combine the running periods to get a global "1996–2000" cross section is described in the next section. The list of checks for systematic effects is reported afterward.

Combination of running periods

Since the centre–of–mass energy is different in the different running periods, the Monte Carlo cross section and the acceptances (Table 6.2) are also different. The data cross section can be referred to $\sqrt{s} = 318$ GeV by using the Monte Carlo cross sections:

$$\sigma^{318}_{xxxx} \equiv \frac{\sigma^{\rm MC}_{99-00}}{\sigma^{\rm MC}_{xxxx}} \sigma^{\rm DATA}_{xxxx}, \tag{6.6}$$

where $xxxx$ is the running period, 96–97 or 98–99.

The three cross sections are then combined by taking a mean averaged on the integrated luminosity:

$$\sigma_{9600} = \frac{\sigma^{318}_{9697} L_{9697} + \sigma^{318}_{9899} L_{9899} + \sigma^{\rm DATA}_{9900} L_{9900}}{L_{9697} + L_{9899} + L_{9900}}. \tag{6.7}$$

The value of the total cross section is reported in Table 6.2, with its uncertainties. It shows a nice agreement with the GRAPE prediction.

The differential cross sections, together with the acceptances, are plotted in Fig. 6.2, whereas the numerical values are listed in Appendix B. The cross sections are measured as a function of the mass M_{12}, the electron transverse momentum P^e_T and the electron polar angle θ_e. A fair agreement can be also seen for these differential distributions.

6.1.1 Effect of the systematic uncertainties

Various systematic uncertainties may affect the results presented above. The sources which have been studied for this work are:

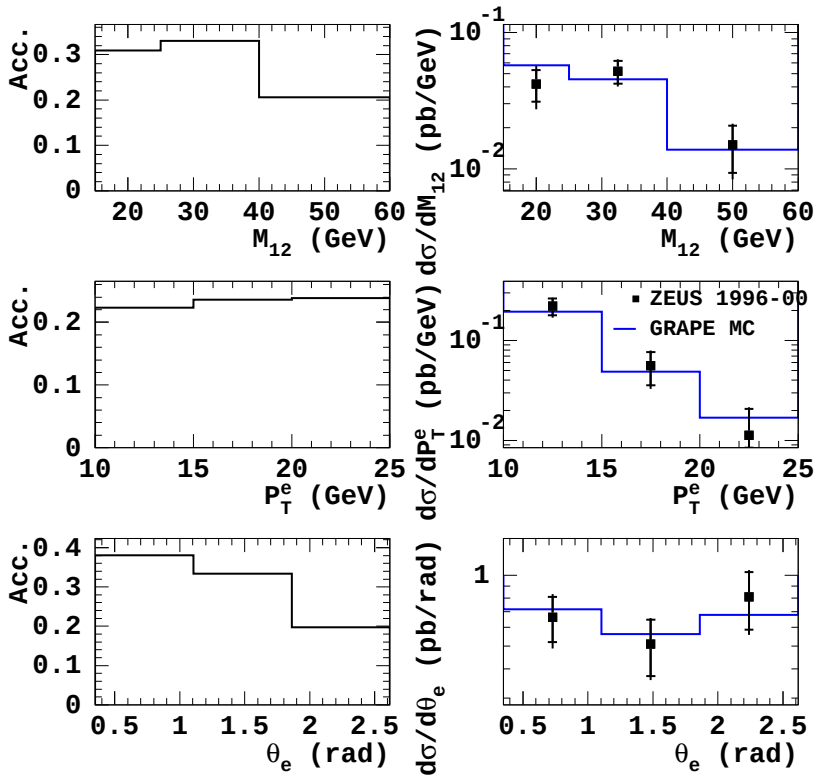

Figure 6.2: Acceptances and differential cross sections for di–electron production. The acceptances are obtained on a GRAPE simulation at $\sqrt{s} = 318$ GeV. All 1996–00 data, corrected for different $\sqrt{s}$, are used for the cross section calculation. The statistical (internal error bars) and total (statistical+systematic, external error bars) uncertainties are reported for the measurements.

- **Luminosity measurement:** the luminosity is measured with an uncertainty varying from 1.1 to 2.25% (depending on the year). The uncertainty on the integrated luminosity, and therefore on the cross section, is here around 2%.

- **Calorimeter energy scale:** the calorimeter energy scale is not accurately simulated in the Monte Carlo; some scale factors have been applied, see Sect. 4.3.1. Nonetheless, an uncertainty on the energy scale persists; a 5% indetermination of the Monte Carlo energy scale has been assumed. The effect on the total cross section is a variation of $^{+9.4}_{-4.1}$%.

- **Fake electron simulation:** the electron finder might behave differently on fake electrons in data and in background Monte Carlo; this is taken into account by varying the cuts on the identification probabilities: CalProb $>$ 0.2 (instead of 0.1) for forward/rear electrons and GrandProb $>$ 0.1 (instead of 0.01) for barrel electrons have been used. The effect on the cross section is a variation of -4.8%.

- For the same reason, a different isolation cut has been applied: $E_{\rm cone} <$ 0.2 GeV instead of $E_{\rm cone} < 0.3$ GeV. The effect on the cross section is a variation of $+7.3$%.

- **Mass resolution:** The invariant mass M_{12} is reconstructed with an 8% uncertainty. The value of the mass cut M_{12} has been varied accordingly. There is no variation in the total cross section, since events with a mass M_{12} around the cut value are anyway removed by the E_T^e cuts.

The relative variation in the data over Monte Carlo ratio is shown in Fig. 6.3, as a function of the invariant mass M_{12}. The variation due to systematic uncertainties is represented by the solid line; for comparison, the statistical uncertainty has been shown as a dashed line. Almost everywhere the variation due to systematic uncertainties is well below the statistical error.

The systematic uncertainty on the total cross section, as coming from the above enumerated sources, is $^{+13}_{-10}$%. This has to be compared to a ± 14% statistical uncertainty.

6.2 Di–muon production

The kinematic region selected for the cross section measurement is defined by:

- two muons,
- $P_T^\mu > 5$ GeV,
- $15^\circ < \theta_\mu < 164^\circ$,
- $M_{\mu\mu} > 5$ GeV.

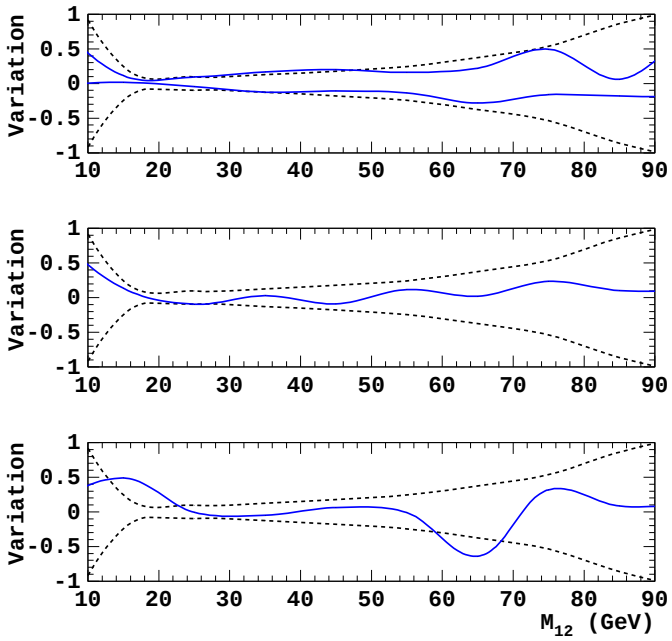

Figure 6.3: Relative variation in the data over Monte Carlo ratio, due to the systematic uncertainties, for the "$\gamma\gamma$" di–electron sample. In the upper plot the Monte Carlo energy scale has been varied by $\pm 5\%$. In the middle plot the probability cuts have been changed in the electron identification. In the lower plot the isolation cut of the electron has been varied. The solid line represents the variation due to systematic uncertainties, wheres the statistical uncertainty has been reported as a dashed line for comparison.

Period	Purity	Acceptance	$\sigma_{\rm DATA}$ (pb)	$\sigma_{\rm MC}$ (pb)
1996–97	0.953	0.436	$4.65 \pm 0.56^{+0.35}_{-0.31}$	5.31
1998–99	0.956	0.438	$4.97 \pm 0.98^{+0.29}_{-0.27}$	5.21
1999–00	0.968	0.427	$4.81 \pm 0.45^{+0.35}_{-0.33}$	5.32
1996–00			$4.79 \pm 0.33^{+0.35}_{-0.32}$	

Table 6.3: Measurement of the di–muon production cross section. The purity, the acceptance, the measured and predicted cross sections are reported separately for the three running periods. The first and second uncertainty given for the cross sections are the statistical and the systematic, respectively. The three measurements are then combined to give a cross section referred to $\sqrt{s} = 318$ GeV.

The procedure for calculating the cross section is the same described in the di–electron section. In Table 6.3 the purities, acceptances and total cross sections (with their statistical and systematic errors) are presented, separately for running periods. The measured cross sections agree nicely with the GRAPE simulation.

The differential cross sections together with the acceptances are plotted in Fig. 6.4, whereas the numerical values are listed in Appendix B. The cross sections are measured as a function of the mass $M_{\mu\mu}$, the muon transverse momentum P_T^{μ} and the muon polar angle θ_{μ}. A fair agreement can also be seen in these differential distributions.

6.2.1 Effect of the systematic uncertainties

Various systematic uncertainties may affect the results presented above. The sources which have been studied for this work are:

- **Luminosity measurement:** the luminosity is measured with an uncertainty varying from 1.1 to 2.25% (depending on the year). The uncertainty on the integrated luminosity, and therefore on the cross section, is $\sim$2%.

- **Muon chambers efficiency:** the B/RMUON efficiency has been measured with an uncertainty of 7.5% in 1996–97 and 6.0% in 1998–00. This gives a variation of $^{+5.4}_{-4.8}$% in the total cross section.

- $\cos(\Omega)$ **resolution:** The $\cos(\Omega)$ is reconstructed with a 1% accuracy. The cut has been varied accordingly to $\cos(\Omega) > -0.985$, bringing to a +2.8% variation in the total cross section.

- **Isolation cut:** the cut $D^{\mu}_{\rm Trk} > 2$ has been applied instead of $D^{\mu}_{\rm Trk} > 1$; in this way the total cross section changes by +4%.

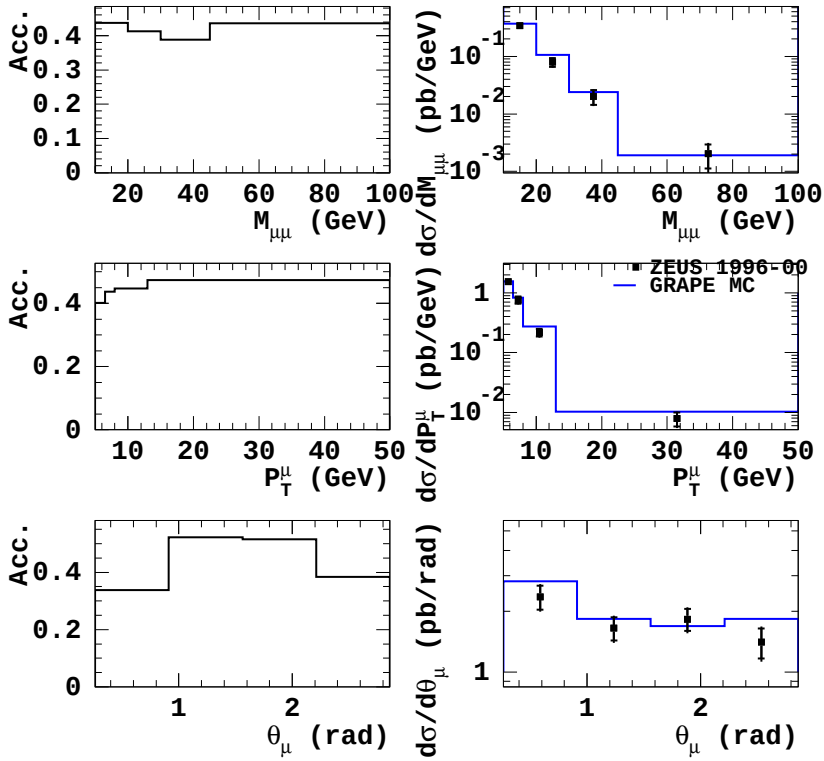

Figure 6.4: Acceptances and differential cross sections for di–muon production. The acceptances are obtained on a GRAPE simulation at $\sqrt{s} = 318$ GeV. All 1996–00 data, corrected for different $\sqrt{s}$, are used for the cross section calculation. The statistical (internal error bars) and total (statistical+systematic, external error bars) uncertainties are reported for the measurements.

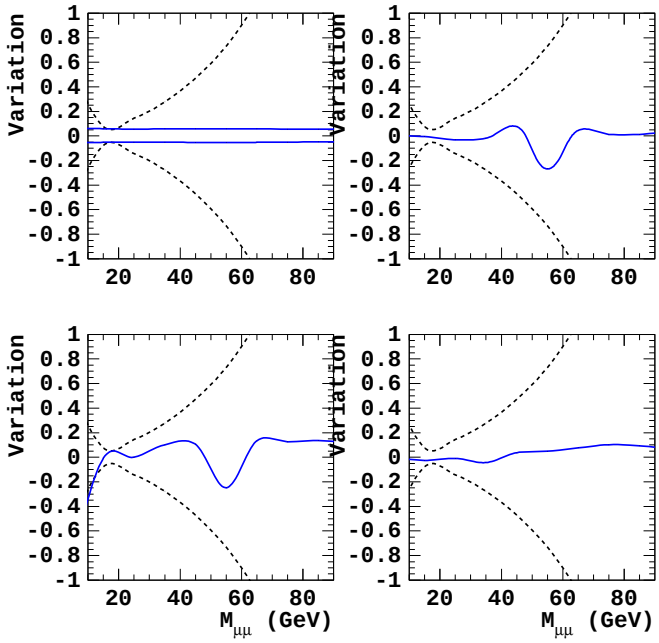

Figure 6.5: Relative variation in the data over Monte Carlo ratio, due to the systematic uncertainties, for the di–muon sample. In the upper left plot efficiencies of muon chambers have been varied on Monte Carlo events by ±7.5% (for 1996–97) or ±6.0% (for 1998–2000). In the upper right plot the cos(Ω) cut has been changed. In the lower left plot the isolation cut of the muon has been varied. In the lower right plot the probability cuts have been changed in the muon selection. The solid line represents the variation due to systematic uncertainties, wheres the statistical uncertainty has been reported as a dashed line for comparison.

- **Probability cut:** in GLOMU the cut $\chi^2 < 10$ has been applied instead of $\chi^2 < 20$; in MPMATCH2 the cut Prob > 0.05 has been applied instead of Prob > 0.01; this changes the total cross section by -0.4%.

The relative variation in the data over Monte Carlo ratio is shown in Fig. 6.5, as a function of the invariant mass $M_{\mu\mu}$. The variation due to systematic uncertainties is represented by the solid line; for comparison, the statistical uncertainty has been shown as a dashed line. Almost everywhere the variation due to systematic uncertainties is well below the statistical error.

The systematic uncertainty on the total cross section, as coming from the above enumerated sources, is $^{+7.2}_{-6.6}\%$. This has to be compared with a ±6.9% statistical uncertainty.

6.3 Comments

The cross sections of di–electron and di–muon production have been measured. The total cross sections were measured separately for the running periods and then combined in a cross section referred to a unique centre–of–mass energy $\sqrt{s} = 318$ GeV. The differential cross sections were quoted by using all the statistics, in order to reduce the statistical uncertainties.

The di–electron measured total cross sections agree with the GRAPE predictions; the only discrepancy is observed in the 1998–99 period, where 4 events were selected and 8.1 are expected. This difference is fully compatible with a statistical fluctuation. The result obtained by using the full statistics is

$$\sigma(e^+p \to e^+e^+e^-X) = 1.62 \pm 0.23^{+0.21}_{-0.16} \text{ pb}$$

(the first uncertainty is the statistical, the second one is the systematic), which is in agreement with the GRAPE prediction:

$$\sigma(\text{GRAPE}) = 1.66 \text{ pb}.$$

The differential distributions are well reproduced, both in shapes and normalisation, by the Monte Carlo simulation.

The di–muon measured total cross section is in agreement with the GRAPE value for all the running periods. The value measured by using all the statistics

$$\sigma(e^+p \to e^+\mu^+\mu^-X) = 4.79 \pm 0.33^{+0.35}_{-0.32} \text{ pb},$$

is in agreement with the GRAPE prediction:

$$\sigma(\text{GRAPE}) = 5.32 \text{ pb}.$$

The differential distributions are well reproduced, both in shapes and normalisation, by the Monte Carlo simulation.

This work represents an extension of the results presented by the collaboration at the ICHEP 2002 conference, and will be the basis for the future publication of ZEUS on the di–muon and di–electron production.

Appendix A

Description of the trigger chains

The trigger chains for multi–electron and di–muon selection, previously introduced in Chapter 4, are here described in more detail. I will start with the trigger chain for the multi–electron selection, then the chain for di–muons will follow.

A.1 Trigger chain for multi–electron events

Events with two or more electrons in the final state have been selected by using three different trigger chains. Only one of these was specifically designed for the selection of di–electron events, the other two were thought for neutral current events and events with a sizable transverse energy deposited in the calorimeter. Nevertheless, the use of all these trigger chains helps in having a higher efficiency in the data selection, that is of particular importance for an analysis in which we do not expect a large number of events in the final sample. The three trigger chains are defined in some detail below.

In all the trigger selections, some veto criteria have to be fulfilled: the timing in the C5 counter and in the SRTD has to be consistent with physical events and not with that of beam–gas events, and no coincidence of the inner and outer veto wall has to be found.

A.1.1 Trigger for the selection of di–electron events

At the second level of the ZEUS trigger, these events are selected by two different slots, depending on the production mechanism of the electron pair, elastic on inelastic:

- **SLT6:** selects events with elastic di–electron production. The requirements of this trigger are different in 1996–97 and 1998–2000 data taking due to the different running conditions. In 1996–97 the requests were the following:
  - the energy in the forward calorimeter around the beam pipe has to be small, $E_{\mathrm{Fbp}} < 3.750$ GeV;

- at least one good track has to be found in the central tracker;
- the number of tracks has to be $1 \leq N_{\mathrm{Trk}} < 4$;
- an energy deposit has to be found in the electromagnetic calorimeter;
- the hadronic energies in FCAL and RCAL have to be $E_{\mathrm{FHAC}} < 2$ GeV and $E_{\mathrm{RHAC}} < 2$ GeV[1];
- either the energy in the barrel calorimeter is $E_{\mathrm{BCAL}} < 5$ GeV or the ratio between the electromagnetic and total energy in the BCAL has to be $E_{\mathrm{BEMC}}/E_{\mathrm{BCAL}} > 0.7$;
- a pair of electrons has to be found, each electron with an energy $E_e > 1$ GeV, having an invariant mass $M_{12} > 2$ GeV;

  or (starting from end of 1996)

  the hadronic energy in the FCAL has to be $E_{\mathrm{FHAC}} < 2$ GeV, whereas the electromagnetic component has to be $E_{\mathrm{FEMC}} > 10$ GeV.

In 1998–2000 to be accepted the events had to fulfill the following requirements:

- at least one good track present in the central tracker, and activity in the calorimeter;
- $E_{\mathrm{FHAC}} < 2$ GeV or $E_{\mathrm{FEMC}}/E_{\mathrm{FCAL}} > 0.9$;
- $E_{\mathrm{RHAC}} < 2$ GeV or $E_{\mathrm{REMC}}/E_{\mathrm{RCAL}} > 0.9$;
- $E_{\mathrm{BCAL}} < 5$ GeV or $E_{\mathrm{BEMC}}/E_{\mathrm{BCAL}} > 0.7$;
- a pair of electrons has to be found, each electron with an energy $E_e > 2$ GeV, or $E_e > 1$ GeV and polar angle $\theta_e > 2$ rad, having an invariant mass $M_{12} > 3\,\mathrm{GeV}$;

  or

  two electrons from the FLT, of which one fulfilling the above request and $E_{\mathrm{FEMC}} > 2$ GeV;

  or

  two electrons from the FLT and $E_{\mathrm{FEMC}} > 4$ GeV;

  or

  $E_{\mathrm{FEMC}} > 20$ GeV.

- **SLT7:** selects inelastic di–electron events; the requirements are:

[1] E_{Fxxx}, E_{Bxxx}, E_{Bxxx}, indicates the energies in the forward, barrel and rear calorimeter, respectively. "xxx" can be "EMC" when we refer to the electromagnetic energy, "HAC" when we are talking about the hadronic, "CAL" when the total energy is referred to.

- a significant energy deposit has to be found in the electromagnetic calorimeter;
- at least one good track in the central chamber has to be present;
- until the end of 1996 a pair of electrons has to be found, each electron with an energy $E_e > 2$ GeV, having an invariant mass $M_{12} > 4$ GeV. Later the two electrons were asked to have $E_e > 4$ GeV and invariant mass $M_{12} > 6$ GeV.

At the third level of the ZEUS trigger, two dedicated slots select elastic and inelastic di–electron events:

- **TLT1:** selects elastic di–electron events. The following requirements are common for the two data–taking periods:
  - SLT6 has to be fired;
  - a "good vertex" has to be found (i.e. the coordinates of the vertex satisfy $|z_{\rm vtx}| < 60$ cm and $\sqrt{x^2_{\rm vtx} + y^2_{\rm vtx}} < 10$ cm);
  - in order to reject cosmic events, a cut is applied on the timing of the upper and lower part of the calorimeter (see Sect. 2.2.7). Moreover, at least one of the following three conditions has to be satisfied: $N_{\rm Trk} > 3$ or $E_{\rm FCAL} > 1$ GeV or the acollinearity angle between the two highest–P_T tracks has to be $\Omega < 3.1216$ rad.

  The requests on the electron tracks in 1996–97 were defined as:
  - the two electron tracks have to fulfill each the following requirements on transverse momentum P_T, distance of closest approach to the interaction point $D_{\rm ca}$, and z coordinate at the distance of closest approach $z_{\rm ca}$:

    $$1)\, P^1_T > 0.5 \text{ GeV}, \quad D^1_{\rm ca} < 1.5 \text{ cm}, \quad |z^1_{\rm ca}| < 60 \text{ cm};$$
    $$2)\, P^2_T > 0.2 \text{ GeV}, \quad D^2_{\rm ca} < 1.5 \text{ cm}, \quad |z^2_{\rm ca}| < 60 \text{ cm}.$$

  Starting from 1998, request were applied only to one of the two tracks:
  - $P^1_T > 0.5\,\text{GeV}, \quad D^1_{\rm ca} < 1.5$ cm, $\quad |z^1_{\rm ca}| < 60$ cm.
- **TLT14:** selects inelastic di–electron events. The criteria are:
  - SLT7 has to be fired;
  - a "good vertex" has to be found, as described for TLT1;

- the two electron tracks have to fulfill the following requirements on transverse momentum P_T, distance of closest approach to the interaction point $D_{\rm ca}$, and z coordinate at the distance of closest approach $z_{\rm ca}$:

$$1)\ P_T^1 > 1.0\ \text{GeV},\quad D_{\rm ca}^1 < 1.5\ \text{cm},\quad |z_{\rm ca}^1| < 60\ \text{cm};$$
$$2)\ P_T^2 > 0.5\ \text{GeV},\quad D_{\rm ca}^2 < 1.5\ \text{cm},\quad |z_{\rm ca}^2| < 60\ \text{cm};$$

- same cuts for cosmic events as for TLT1.

After the third level trigger, the di–electron events are asked to fulfill the requests of the following DST bit:

- **DST115:** selects di–lepton events.
  - TLT1 or TLT14 have to be fired.

A.1.2 Trigger for the selection of neutral current events

At the second level of the ZEUS trigger, neutral current events are selected by:

- **SLT3:** selects neutral current high–E_T events:
  - $E_T(-2ir) > 16$ GeV, where $E_T(-2ir)$ is the transverse energy deposited in the calorimeter, with the exception of the first two rings of cells around the forward beam pipe;
  - $E - P_z > 34\,\text{GeV}$;
  - the vertex of the event has to fulfill standard requirements for beam–gas rejection.

At the third level of the ZEUS trigger, the selection of neutral current processes is carried on looking for high–E_T and high–Q^2 events:

- **TLT4**: selects high–E_T neutral current events:
  - SLT3 has to be fired;
  - a "good vertex" has to be found, as described for TLT1;
  - the timing in the upper and lower part of the calorimeter has to be consistent with that of a physical event.
- **TLT7**: selects high–Q^2 neutral current events. The following requirements are common to all the data–taking periods:
  - $E - P_z > 32$ GeV, where E and P_z are the ones reconstructed by the central tracking devices;
  - beam–gas rejection: $z_{\rm vtx} > -80$ cm or $N_{\rm Trk} < 5$;

- at least one electron candidate has to be found by one of the electron finders used at the TLT;
- the electron energy has to be $E_e > 10$ GeV, and its position in the UCAL has to satisfy one of the following:

$$\sqrt{x_e^2 + y_e^2} > 30 \text{ cm} \quad \text{or} \quad z_e > -120 \text{ cm},$$

that means that if the particle is in the rear calorimeter, has to be outside a circle of radius 30 cm around the beam pipe.

At some point in 1996 the following conditions were added to the previous ones:

- the transverse momentum P_T^e and the polar angle θ_e of the candidate electron have to satisfy one of the following:

$$P_T^e > 2 \text{ GeV} \quad \text{or} \quad \theta_e > 0.3 \text{ rad}.$$

The requirement on the event Q^2 in 1996–97 was:

- $Q^2 > 200\,\text{GeV}^2$,

while starting from 1998 the threshold was lowered:

- $Q^2 > 160\,\text{GeV}^2$.

As last step, the events are requested to fulfill the requirement of the following DST bit:

- **DST32:** selects neutral current events. These requests are common to the two data–taking periods:
  - TLT4 or TLT7 fired;
  - the timing in the upper and lower part of the calorimeter consistent with that of a physical event;
  - $E - P_z > 32$ GeV;
  - a candidate electron found by one of the electron finders, having energy $E_e > 4$ GeV.

  In 1996–97, the following conditions had also to be satisfied for an event to be accepted:
  - $E_T > 10$ GeV, where E_T is the transverse energy deposited in the calorimeter.

  In 1998–2000, these were the additional conditions to be fulfilled:
  - $P_T^e > 2$ GeV, P_T^e being the electron transverse momentum;
  - $Q^2 > 160$ GeV^2.

A.1.3 Trigger for the selection of events with transverse energy in the UCAL

At the second level of the ZEUS trigger, events are selected having a significant transverse energy measured in the UCAL:

- **SLT1:** $E_T(-2ir) > 35$ GeV, where $E_T(-2ir)$ is the transverse energy deposited in the calorimeter, with the exception of the first two rings of cells around the forward beam pipe;
- **SLT2:**
  - $E_T(-2ir) > 25$ GeV,

    or

    at least an isolated electron in the FCAL or in the BCAL, and a good track in the central tracking detector;
  - $E - P_z > 15$ GeV;
  - the vertex of the event has to fulfill standard requirements for beam–gas rejection.

At the third level of the ZEUS trigger, cleaning cuts are applied and high–E_T is required:

- **TLT15:**
  - SLT1 or SLT2 fired;
  - a "good vertex" has to be found, as described for TLT1;
  - the timing in the upper and lower part of the calorimeter has to be consistent with that of physical events;
  - the transverse energy measured by the UCAL, excluding the islands in the FCAL with radius < 30 cm, has to be $E_T > 20$ GeV.

At the DST bit level, the same requests are applied to the more refined variables evaluated offline:

- **DST35:** selects events with high–E_T in the UCAL:
  - TLT15 fired, or the transverse energy measured by the calorimeter, excepted the islands with $\theta < 7°$, has to be $E_T > 20$ GeV;
  - -60 cm $< z_{\text{vtx}} < 120$ cm.

A.2 Trigger chain for di–muon events

In the selection of events with more than one muon in the final state, special trigger slots dedicated to muon identification have been used. Due to the difference of the B/RMUON and FMUON detectors different trigger chains are requested for muons in the barrel–rear or in the forward regions. These slots are described in some detail below.

A.2.1 Trigger for muons in the barrel–rear region

Two trigger chains are defined by using the barrel–rear muon chambers. The first chain looks for activity in the inner chambers, B/RMUI, and in the CTD, the second one require also activity in the outer chambers, B/RMUO.

The first chain starts at the first level trigger with:

- **FLT8**, elastic B/RMUI:
  - a signal, compatible with the crossing of a charged particle, has to be found in B/RMUI;
  - the energy in the forward calorimeter around the beam pipe is required to be small: $E_{\mathrm{Fbp}} < 3.750$ GeV;
  - in the CTD no more than five tracks have to be found, and at least one track coming from the vertex.
- **FLT10**, BMUI:
  - a signal compatible with the crossing of a charged particle has to be found in any of the BMUI chambers;
  - the BCAL have to present an energy deposit, compatible with a MIP; the deposit has to be in a octant[2] whose θ–ϕ position matches the active muon chamber;
  - at least one track has to be found by the central tracker, coming from the event vertex.
- **FLT11**, RMUI:
  - a signal compatible with the crossing of a charged particle has to be found in any of the RMUI chambers;
  - a MIP–like deposit has to be found in the RCAL, in a quadrant[3] whose θ–ϕ position matches the active muon chamber;

[2]The BCAL is divided in octants; each of the barrel muon chambers is matched to a set of BCAL octants close in θ–ϕ.

[3]The RCAL is divided in quadrants; each rear muon chamber is matched to a subset of these quadrants.

- at least one track, coming from the vertex, has to be found by the central tracker.

The slot MUO1 is required at the second level trigger:

- **SLT MUO1:**
  - FLT8, FLT10 or FLT11 fired;
  - if the energy deposited in the calorimeter is above 1 GeV, the timing of the deposit has to be compatible with a physical event;
  - $P_z/E < 0.96$ has to be fulfilled; E is the total energy measured by the UCAL, $P_z = \sum_i E_i \cos\theta_i$ where E_i is the energy of the i–th calorimeter cell and θ_i is its polar angle in the ZEUS reference. This condition removes mainly halo–muon events and proton beam gas collisions.

The second trigger chain starts at the first level trigger with

- **FLT14**, BMUO:
  - a signal compatible with the crossing of a charged particle has to be found in the BMUI and BMUO chambers;
  - the calorimeter has to detect at least 464 MeV in any of the trigger towers;
  - at least one track, coming from the vertex, has to be found by the central tracker.
- **FLT15**, RMUO:
  - a signal compatible with the crossing of a charged particle has to be found in the RMUI and RMUO chambers;
  - the calorimeter has to detect at least 464 MeV in any of the trigger towers;
  - at least one track, coming from the vertex, has to be found by the central tracker.

The requirement at the second level trigger is

- **SLT MUO2:**
  - FLT14 or FLT15 fired;
  - if the energy deposited in the calorimeter is above 1 GeV, the timing of the deposit has to be compatible with a physical event.

$P_z/E < 0.96$ is not required in this chain because the rates of FLT slots 14 and 15 are much lower than for 8, 10 and 11.

These two chains are then merged in the same third level trigger slot:

- **TLT MUO03:**
  - SLTs MUO1 or MUO2 fired;
  - the TLT version of GLOMU have to find a match between muon chambers hits and CTD tracks or calorimeters MIP–like deposits.

A.2.2 Trigger for muons in the forward region

At the first level of the ZEUS trigger, events with hits in the forward muon detector are selected:

- **FLT4:**
  - at least one good track and no more than four tracks have to be found in the central tracking detector;
  - at least one hit has to be found in the FMUON detector;
  - a deposit compatible with a MIP has to be present in the FCAL, in a quadrant[4] whose θ–ϕ position matches the active muon chamber; if $\theta > 20°$, the deposit must fulfill $E_{\mathrm{FHAC}} > 1$ GeV.

These are the requirements the events have to fulfill at the second level of the ZEUS trigger:

- **SLT MUO3:**
  - the vertex, if any, must have $-75 \text{ cm} < z_{\mathrm{vtx}} < 75 \text{ cm}$;
  - $N_{\mathrm{Trk}} < 5$;
  - $E_{\mathrm{CAL}} < 10$ GeV, E_{CAL} being the total UCAL energy;
  - $E_{\mathrm{FHAC}} > 1.5\ E_{\mathrm{FEMC}}$.

At the third level of the ZEUS trigger, the information from the various detectors are used to perform a matching:

- **TLT MUO04:**
  - a muon matching algorithm, MAMMA [83], is used to match a hit in FMUON with a MIP–like deposit in the calorimeter or a track in the CTD or both; at least one matching is required;
  - a pair of CTD tracks with invariant mass $M > 1.5$ GeV has to be found.

[4]The FCAL is divided in quadrants; each forward muon chamber is matched to a subset of these quadrants.

Appendix B

Differential cross sections

In this appendix, the values of the measured di–lepton cross sections are reported in tables together with the Standard Model predictions.

B.1 Di–electron production

The di–electron cross section has been measured in the kinematic region defined by:

- two electrons in $17^\circ < \theta_e < 164^\circ$,
- $E_T^{e1} > 10$ GeV and $E_T^{e2} > 5$ GeV,
- $M_{12} > 5$ GeV,
- $E - P_z < 45$ GeV.

The values which have been obtained for the purity, the acceptance, the differential cross section are:

Bin definition	Pur.	Acc.	$\frac{d\sigma_{DATA}}{dx}$ (pb/[x])	$\frac{d\sigma_{MC}}{dx}$ (pb/[x])
$15 < M_{12} < 25$ GeV	0.723	0.309	$(4.2 \pm 1.1 \pm 1.0)$E−02	5.7E−02
$25 < M_{12} < 40$ GeV	0.840	0.330	$(5.2 \pm 1.0 \pm 0.6)$E−02	4.5E−02
$40 < M_{12} < 60$ GeV	0.803	0.206	$(1.50 \pm 0.57^{+0.34}_{-0.32})$E−02	1.38E−02
$10 < P_T^e < 15$ GeV	1.154	0.223	$(2.20 \pm 0.42^{+0.28}_{-0.20})$E−01	1.94E−01
$15 < P_T^e < 20$ GeV	1.073	0.236	$(5.6 \pm 2.1^{+1.1}_{-1.0})$E−02	4.9E−02
$20 < P_T^e < 25$ GeV	0.924	0.239	$(1.13 \pm 0.93^{+0.45}_{-0.43})$E−02	1.69E−02
$0.349 < \theta_e < 1.105$ rad	0.831	0.381	$(6.6 \pm 1.4^{+1.0}_{-0.9})$E−01	7.2E−01
$1.105 < \theta_e < 1.862$ rad	0.828	0.334	$(5.1 \pm 1.4 \pm 0.6)$E−01	5.6E−01
$1.862 < \theta_e < 2.618$ rad	0.681	0.198	$(8.1 \pm 2.2^{+1.2}_{-1.0})$E−01	6.8E−01

The cross sections are reported with their statistical and systematic uncertainties.

B.2 Di–muon production

In the case of di–muon production, the kinematic region for the cross section measurement has been defined as:

- two muons,
- $P_T^\mu > 5$ GeV,
- $15^\circ < \theta_\mu < 164^\circ$,
- $M_{\mu\mu} > 5$ GeV.

The values which have been obtained for the purity, the acceptance, the differential cross section are:

Bin definition	Pur.	Acc.	$\frac{d\sigma_{DATA}}{dx}$ (pb/[x])	$\frac{d\sigma_{MC}}{dx}$ (pb/[x])
$10 < M_{\mu\mu} < 20$ GeV	0.968	0.437	$(3.44 \pm 0.28^{+0.24}_{-0.22})$E−01	3.70E−01
$20 < M_{\mu\mu} < 30$ GeV	0.977	0.412	$(8.0 \pm 1.4^{+0.8}_{-0.7})$E−02	10.7E−02
$30 < M_{\mu\mu} < 45$ GeV	0.928	0.388	$(2.02 \pm 0.58^{+0.32}_{-0.31})$E−02	2.40E−02
$45 < M_{\mu\mu} < 100$ GeV	0.787	0.437	$(2.04 \pm 0.91 \pm 0.65)$E−03	1.90E−03
$5 < P_T^\mu < 6.5$ GeV	0.949	0.401	$1.53 \pm 0.16^{+0.11}_{-0.10}$	1.55
$6.5 < P_T^\mu < 8$ GeV	1.009	0.437	$(7.6 \pm 1.1^{+0.6}_{-0.5})$E−01	8.3E−01
$8 < P_T^\mu < 13$ GeV	0.994	0.447	$(2.17 \pm 0.31^{+0.23}_{-0.22})$E−01	2.72E−01
$13 < P_T^\mu < 50$ GeV	0.885	0.473	$(7.9 \pm 2.1^{+1.3}_{-1.2})$E−03	10.3E−03
$0.262 < \theta_\mu < 0.912$ rad	0.963	0.339	$2.36 \pm 0.42^{+0.18}_{-0.17}$	2.81
$0.912 < \theta_\mu < 1.562$ rad	0.977	0.523	$1.65 \pm 0.22^{+0.13}_{-0.12}$	1.83
$1.562 < \theta_\mu < 2.212$ rad	0.970	0.516	$1.83 \pm 0.23^{+0.14}_{-0.13}$	1.69
$2.212 < \theta_\mu < 2.862$ rad	0.963	0.385	$1.41 \pm 0.24^{+0.14}_{-0.13}$	1.84

The cross sections are reported with their statistical and systematic uncertainties.

Part II

VCMVD: an algorithm for MVD tracking at TLT

Chapter 7

Introduction

7.1 The VCTRAK package

The tracks, the primary and secondary vertices are found at ZEUS by the VCTRAK package [84]. Each reconstructed track must use CTD hits, although information from other tracking detectors (VXD, SRTD, RTD, FTD) may also be exploited. VCTRAK is a component of the offline reconstruction program, ZEPHYR. Online, it participates to the Third Level Trigger (in a limited CTD–only mode for speed).

After the installation of the Micro–Vertex Detector in the year 2001 (see Sect. 2.3), the necessity arose of using in the VCTRAK code the information of this newly installed detector. This is important for example for studying heavy quarks, which have a pathlength measurable by the MVD but not by the CTD; in addition to the obvious advantage of a heavy quark tagging based on the secondary vertices found in the offline, new Third Level Triggers (TLTs) may greatly improve the performances of the online selection.

In this part of the thesis I will describe the VCMVD (VCtrak+MVD) FORTRAN package; this algorithm, which updates the VCTRAK package by adding the information from the barrel MVD, has been developed for the use in the TLT.

7.2 The VCMVD package

The VCMVD software was mainly intended for the online use but can also be run offline; what the program does is first to read the list of tracks found by VCTRAK and their parameters; these tracks are propagated inwards through the MVD; hits measured by the detector are used to update the track parameters. The working units used by the program are: centimeters (distance), radians (angle), Tesla (magnetic field) and GeV/c (momentum).

In the next section the parameterisation of the particle trajectories will be described in a certain depth.

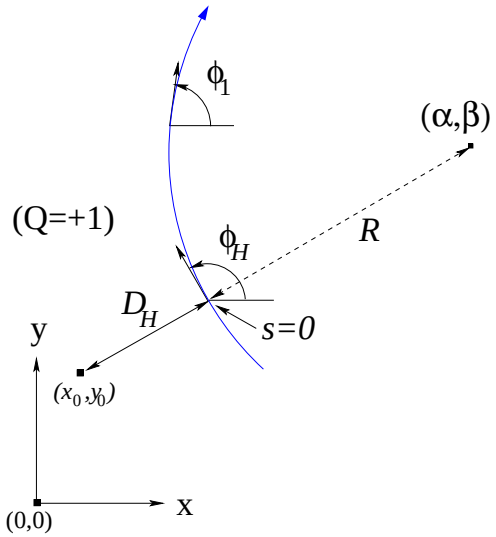

Figure 7.1: Charged particles follow helix–like trajectories in the xy plane.

7.3 Mathematics of particle trajectories

The ZEUS inner detectors, for example CTD and MVD, are plunged in the magnetic field generated by the superconducting coil. A charged particle follows therefore a helix–like trajectory[1] (see Fig. 7.1). Let me indicate by s the path-length of the particle; $s = 0$ corresponds to the point of closest approach to the *reference point* (x_0, y_0). The helix is described by five parameters a_ν:

- a_1, or ϕ_H: the azimuthal angle of the tangent to the helix, at $s = 0$;
- $a_2 = Q/R$, where Q is the charge number, R is the radius of the helix; $|a_2|$ represents the helix curvature;
- $a_3 = Q\ D_H$, where D_H is the distance of closest approach of the particle to the reference point (x_0, y_0);
- a_4, or Z_H: the z coordinate at $s = 0$;
- $a_5 = \cot\theta$; θ is the polar angle of the tangent at $s = 0$.

VCMVD reads the parameters within the routine VCTHLX of the VCTRAK package:

- Reference point: (XREFO,YREFO) $\rightarrow (x_0, y_0)$;
- PARH50(5) $\rightarrow a_\mu$;

[1]Here – and in the following – a constant magnetic field directed along z: $\vec{B} = (0, 0, B_z)$=(0,0,1.43) T, will be assumed.

- HELSUM $\rightarrow \chi^2$;
- HELDER(5) $\rightarrow B_\mu$;
- HELMAT(15) $\rightarrow U_{\mu\nu}$.

χ^2 represents the goodness of the trajectory fit performed by VCTRAK, B_μ and $U_{\mu\nu}$ are related to χ^2 first and second derivative, respectively; the exact definitions are given in Sect. 10.3.

The position of the particle on the helix can be identified by using an angle ϕ (Eqs. 3–4–5 in reference [84]):

$$x(\phi) = x_0 + \left(a_3 + \frac{1}{a_2}\right)\sin a_1 - \frac{\sin\phi}{a_2}, \tag{7.1}$$

$$y(\phi) = y_0 - \left(a_3 + \frac{1}{a_2}\right)\cos a_1 + \frac{\cos\phi}{a_2}, \tag{7.2}$$

$$z(\phi) = a_4 - \frac{a_5}{a_2}\left(\phi - a_1\right). \tag{7.3}$$

ϕ represents the azimuthal angle of the tangent to the helix (see Fig. 7.1). The relation between ϕ and the pathlength s is given in [84], Eq. 2:

$$s = -\frac{\phi - a_1}{a_2}. \tag{7.4}$$

It is worth to notice that, for a positive charged particle ($a_2 > 0$), the angle ϕ decreases along the trajectory, while for a negative charged particle ($a_2 < 0$), the angle increases. The z coordinate can be written as

$$z(\phi) = a_4 + s \cdot a_5. \tag{7.5}$$

7.3.1 Trajectory swimming: parameters

The change of reference point $(x_0, y_0) \rightarrow (x_0', y_0')$ changes the value of the parameters a_ν. The trajectory is indeed the same, but the parameterisation is different. The radius is obviously unaffected:

$$a_2' = \frac{Q}{R} = a_2, \tag{7.6}$$

and so is the polar angle θ:

$$a_5' = \cot\theta = a_5. \tag{7.7}$$

In the xy plane the trajectory is a circumference (Fig. 7.1), whose centre is (α, β); in terms of $\vec{a}$ the coordinates of the centre can be expressed as

$$\begin{aligned} \alpha &= x_0 + \left(a_3 + \frac{1}{a_2}\right)\sin a_1 \\ \beta &= y_0 - \left(a_3 + \frac{1}{a_2}\right)\cos a_1. \end{aligned} \tag{7.8}$$

The same expressions holds for the new reference, so that[2] (see Section B.3 for details)

$$a_1' = \mathrm{ATAN2}\left(\sin a_1 - \frac{x_0' - x_0}{a_3 + 1/a_2}, \cos a_1 + \frac{y_0' - y_0}{a_3 + 1/a_2}\right). \tag{7.9}$$

The pathlength to the new reference point is

$$s' = \frac{a_1 - a_1'}{a_2} = \frac{a_1 - \mathrm{ATAN2}(...)}{a_2}, \tag{7.10}$$

so that I can rewrite

$$a_1' = a_1 - s' a_2. \tag{7.11}$$

The parameter a_4 is straightforward to obtain

$$a_4' = a_4 + s' a_5, \tag{7.12}$$

while a_3' requires some more calculations (see again Section B.3); in the end the expression is

$$a_3' = -(x_0' - x_0)\sin a_1' + (y_0' - y_0)\cos a_1' + \left(a_3 + \frac{1}{a_2}\right)\cos(s' a_2) - \frac{1}{a_2}. \tag{7.13}$$

7.3.2 Trajectory swimming: derivatives

If I neglect the uncertainty on the swimming distance s', the derivatives of the swum parameters with respect to the original ones are simply

$$\left\{\frac{\partial a_1'}{\partial a_\nu}\right\} = \{1, -s', 0, 0, 0\} \tag{7.14}$$

$$\left\{\frac{\partial a_2'}{\partial a_\nu}\right\} = \{0, 1, 0, 0, 0\} \tag{7.15}$$

$$\begin{aligned}\left\{\frac{\partial a_3'}{\partial a_\nu}\right\} &= \left\{-(x_0' - x_0)\cos a_1' - (y_0' - y_0)\sin a_1', -s'\frac{\partial a_3'}{\partial a_1} + \right. \\ &+ \left. \frac{1 - \cos(s' a_2)}{a_2^2} - s'\left(a_3 + \frac{1}{a_2}\right)\sin(s' a_2), \cos(s' a_2), 0, 0\right\}\end{aligned} \tag{7.16}$$

$$\left\{\frac{\partial a_4'}{\partial a_\nu}\right\} = \{0, 0, 0, 1, s'\} \tag{7.17}$$

$$\left\{\frac{\partial a_5'}{\partial a_\nu}\right\} = \{0, 0, 0, 0, 1\} \tag{7.18}$$

[2] With ATAN2() I refer to the namesake FORTRAN function.

Chapter 8

MVD geometry and dead materials effect

The ZEUS Micro–Vertex Detector (MVD) has already been described in detail in Sect. 2.3.1; here I will just recall the main features.

The Micro–Vertex Detector (see Fig. 8.1) is divided into two main parts: the Barrel region (BMVD) and the Forward region (FMVD). The BMVD covers the central region around the interaction point, and is composed by 30 *ladders* (arranged in three layers) whose axes are parallel to the z axis of ZEUS reference frame. Each ladder is made up of 5 modules (see Fig. 2.23); each module, in turn, is composed by four silicon wafers; the signal is read–out by 512 strips on each wafer. On each side of the module there is a wafer with read–out strips parallel to z ($r\phi$ detectors) and one with read–out strips orthogonal to z (z detectors), in order to measure two coordinates for each particle traversing the module.

The forward MVD is composed of four wheels. I will not give further details since the use of FMVD hits has not yet been implemented in VCMVD.

8.1 The ADAMO Data System

The ZEUS software is mainly written in FORTRAN. While the FORTRAN language is well–suited to write algorithms its very simple data structures are completely inadequate to deal with the complexity and amount of data of a high energy physics experiment.

The ADAMO Data System [69], originally developed for the ALEPH experiment at LEP, provides a way of defining tabular data structures and manipulating and validating them from FORTRAN. It uses a form of the *Entity–Relationship* model and allows the structure of the tables and the relationships between them to be readily represented in pictorial form as a diagram (e.g. see Fig. 8.2, from ADAMO manual). The underlying physical structure is still complex, and indeed it is managed by a memory manager, but this is of no concern at all to the ADAMO programmer who thinks only in terms of the tables.

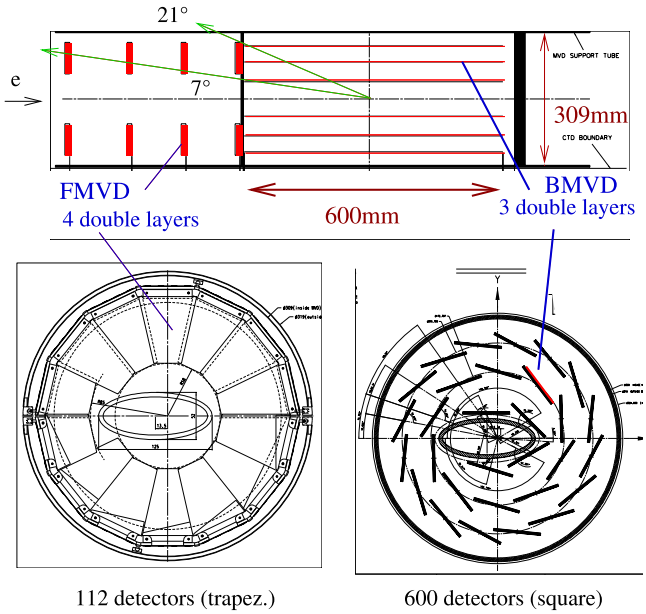

Figure 8.1: Layout of the MVD along the beam line (upper figure). A MVD forward wheel (lower left) and a BMVD section in the $r\phi$ plane (lower right).

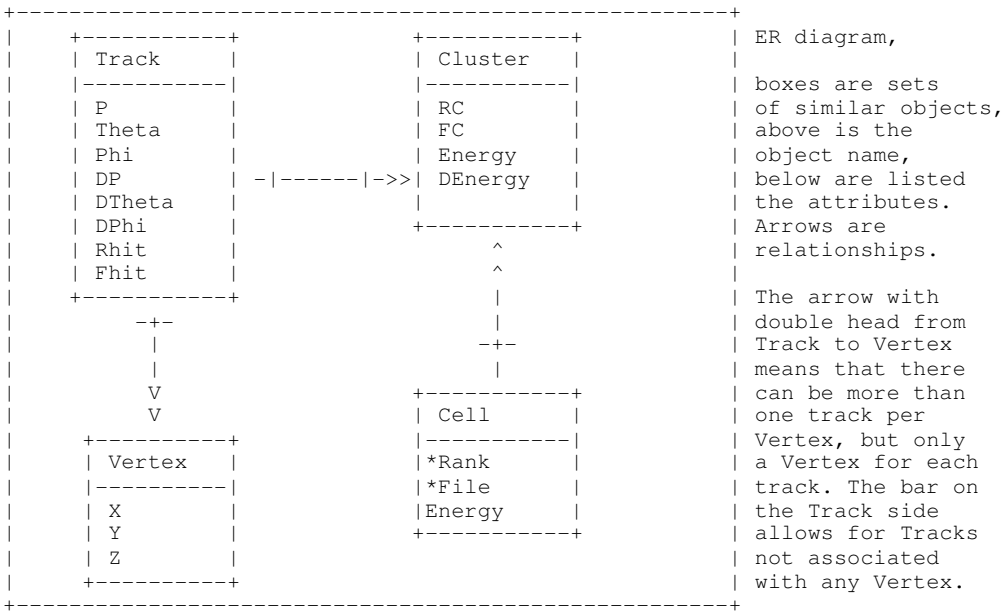

Figure 8.2: ADAMO uses a form of the *Entity–Relationship* model and allows data to be represented as a diagram.

Central to ADAMO is a user–created dictionary from which both the data structure and the FORTRAN COMMON blocks used to access the data are automatically generated. Since the same dictionary also provides part of the documentation, this procedure ensures that data structure and documentation are in step.

The FORTRAN interface consists of data manipulation and validation routines and the way in which these access the data ensures that the data structure cannot be corrupted. Tables can be moved between a storage medium and memory and also to and from an ORACLE database. Interactive look–up and update of stored tables are provided.

8.2 The ADAMO table MVWAF

The MVD geometry, corrected for alignments, is stored in the ADAMO table MVWAF. The table has an entry for each silicon wafer, and supplies various information about position and orientation of that detector. The geometry is referred to the ZEUS reference frame.

The quantities of interest for VCMVD are:

- MVWAF_Pos(3): (x, y, z) at the centre of the wafer (i.e. the centre of strip No. 255.5),
- MVWAF_Mdir(3): the three projections of the wafer x axis over the axes of ZEUS reference frame (Fig. 8.3),
- MVWAF_Dm: the read–out strip pitch in centimeters.

The position of a strip in the wafer reference frame is:

$$\xi = (\text{Strip No.} - 255.5) \cdot \text{MVWAF\_Dm}. \tag{8.1}$$

The position in the ZEUS reference of a $r\phi$ strip is obtained as

$$\begin{array}{rcl} x & = & \text{MVWAF\_Pos}(1) + \xi \cdot \text{MVWAF\_MDir}(1) \\ y & = & \text{MVWAF\_Pos}(2) + \xi \cdot \text{MVWAF\_MDir}(2) \\ z & = & \text{undefined} \end{array} \tag{8.2}$$

while the position in ZEUS of a z strip is

$$\begin{array}{rcl} x & = & \text{undefined} \\ y & = & \text{undefined} \\ z & = & \text{MVWAF\_Pos}(3) + \xi \cdot \text{MVWAF\_MDir}(3). \end{array} \tag{8.3}$$

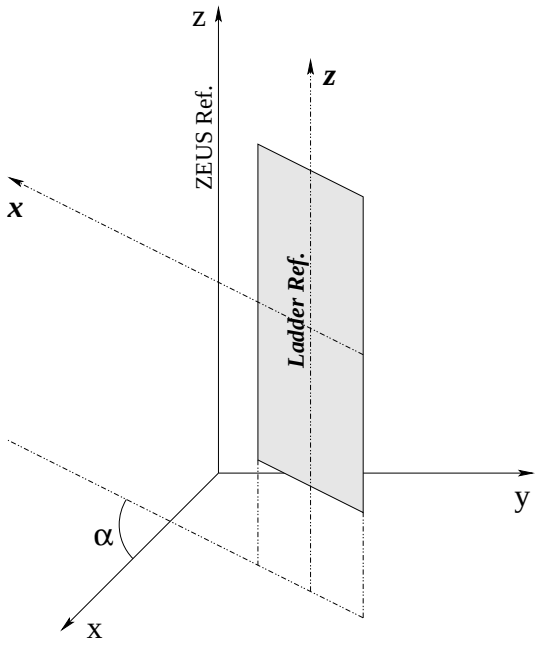

Figure 8.3: Wafer and ZEUS reference frames.

8.3 Dead Materials

The knowledge of dead material distribution is essential for the evaluation of multiple scattering (Sect. 8.4), and energy loss (Sect. 8.5). The dead materials considered in VCMVD are the BMVD ladders, the MVD support tube, the beam pipe. Their conformations are approximated by using simple geometrical shapes (rectangular boxes, cylinders).

8.3.1 The Ladders

BMVD ladders are represented by using rectangular boxes; their z axes are parallel to the ZEUS one, the x axes form an angle α (different for each ladder) with the x of the ZEUS coordinates system (see again Fig. 8.3); α is determined by

$$\tan\alpha = \frac{\text{MVWAF\_MDir(2)}}{\text{MVWAF\_MDir(1)}}. \tag{8.4}$$

If ϕ is the azimuthal angle of the tangent to the helix in the point of intersection with the ladder, and t is the ladder thickness, the xy projection of the thickness of the material traversed by the particle is (Fig. 8.4):

$$D_{2D} = \frac{t}{|\cos\gamma|} = \frac{t}{|\sin(\alpha-\phi)|}; \tag{8.5}$$

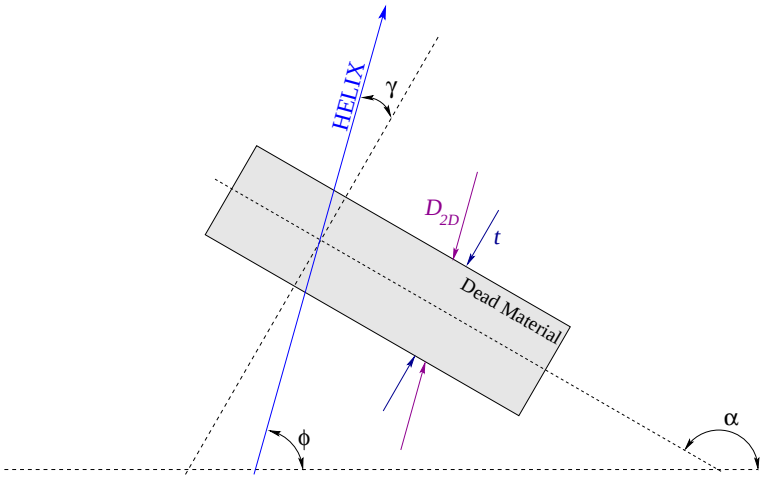

Figure 8.4: Thickness of dead material traversed by a particle.

the 3D thickness is therefore

$$D = \frac{D_{2D}}{|\sin\theta|} = \frac{t\sqrt{1+a_5^2}}{|\sin(\alpha-\phi)|}. \tag{8.6}$$

8.3.2 The Support Tube

The inner wall of CTD and the MVD support tube are considered to be a cylinder of radius R_S whose axis is parallel to z. The helix intersects the cylinder after a pathlength s_{int} as is calculated in (10.7); the intersection point $\big(x(s_{int}), y(s_{int})\big)$ is given by (10.6), by making the substitution $R_L \to R_S$.

The angular coefficient of the tangent to the cylinder in the point of intersection is

$$\tan\alpha = \frac{x(s_{int})}{-y(s_{int})}, \tag{8.7}$$

as derived in Section B.6; the thickness of material traversed by the particle is given again by Equations (8.5)–(8.6).

8.3.3 The beam pipe

The xy cross section of the beam pipe is approximately an ellipse whose axes are a and b (see Fig. 8.5). The pathlength at the intersection point is determined by (B.44) and (B.45); the angular coefficient of the tangent in that point is given in Sect. B.7 of the Appendix:

$$\tan\alpha = -\left(\frac{b}{a}\right)^2 \frac{x(s_{int}) - x_E}{y(s_{int})}. \tag{8.8}$$

The thickness of the dead material is derived consequently.

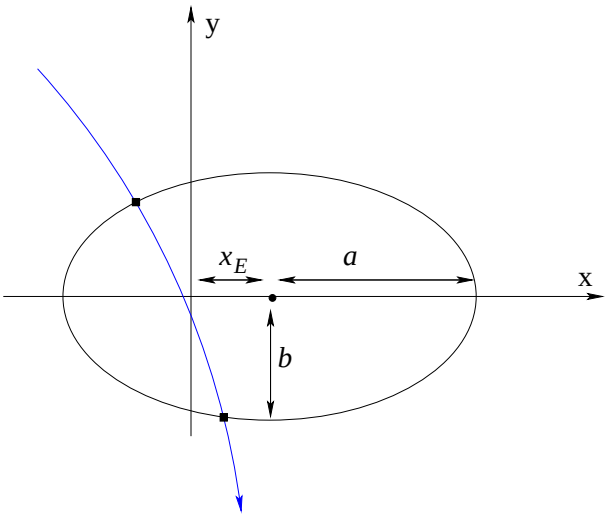

Figure 8.5: Intersections between a particle helix and the beam pipe.

8.4 Multiple Scattering

Being D the thickness of dead material traversed by the particle, in radiation lengths (Eq. 8.6), the 2D rms scattering angle and its projection onto the $r\phi$ plane are [85]:

$$\begin{aligned} \delta_{2D} &= \frac{0.0136}{p\ [\mathrm{GeV}]}\sqrt{D}\ (1+0.0038\ln D), \\ \delta_{RMS} &= \frac{\delta_{2D}}{|\sin\theta|} = \delta_{2D}\sqrt{1+a_5^2}. \end{aligned} \tag{8.9}$$

Some auxiliary quantities are needed:

$$\begin{aligned} k &= -\frac{\partial}{\partial\theta}a_5 = 1+a_5^2, \\ \nu &= a_1 - \phi = s\ a_2, \\ h &= x_0\cos a_1 + y_0\sin a_1 + \frac{\sin(s\ a_2)}{a_2} - \frac{s}{2}. \end{aligned} \tag{8.10}$$

As explained in [84], Sect. 5.12.2, the multiple scattering in $r\phi$ affects covariances of a_1 and a_3:

$$\begin{aligned} \mathrm{cov}(1,1) &\rightarrow \mathrm{cov}(1,1) + \delta^2_{RMS}, \\ \mathrm{cov}(1,3) &\rightarrow \mathrm{cov}(1,2) + Q\ s\ \delta^2_{RMS}, \\ \mathrm{cov}(3,3) &\rightarrow \mathrm{cov}(1,3) + (s\ \delta_{RMS})^2, \end{aligned} \tag{8.11}$$

whereas multiple scattering in z affects a_4 and a_5, and, indirectly (through the changing of transverse momentum), a_1 to a_3:

$$
\begin{array}{lcl}
\mathrm{cov}(1,1) & \rightarrow & \mathrm{cov}(1,1) + (\nu\ a_5\ \delta_{2D})^2 \\
\mathrm{cov}(1,2) & \rightarrow & \mathrm{cov}(1,2) + \nu\ a_2\ (a_5\ \delta_{2D})^2 \\
\mathrm{cov}(1,3) & \rightarrow & \mathrm{cov}(1,3) + h\ (\nu\ a_5\ \delta_{2D})^2 \\
\mathrm{cov}(1,4) & \rightarrow & \mathrm{cov}(1,4) - \nu\ a_5\ k\ s\ \delta_{2D}^2 \\
\mathrm{cov}(1,5) & \rightarrow & \mathrm{cov}(1,5) + \nu\ a_5\ k\ \delta_{2D}^2 \\
\mathrm{cov}(2,2) & \rightarrow & \mathrm{cov}(2,2) + (a_2\ a_5\ \delta_{2D})^2 \\
\mathrm{cov}(2,3) & \rightarrow & \mathrm{cov}(2,3) + h\ \nu\ a_2\ (a_5\ \delta_{2D})^2 \\
\mathrm{cov}(2,4) & \rightarrow & \mathrm{cov}(2,4) - a_2\ a_5\ k\ s\ \delta_{2D}^2 \\
\mathrm{cov}(2,5) & \rightarrow & \mathrm{cov}(2,5) + a_2\ a_5\ k\ \delta_{2D}^2 \\
\mathrm{cov}(3,3) & \rightarrow & \mathrm{cov}(3,3) + (h\ \nu\ a_5\ \delta_{2D})^2 \\
\mathrm{cov}(3,4) & \rightarrow & \mathrm{cov}(3,4) - h\ \nu\ a_5\ k\ s\ \delta_{2D}^2 \\
\mathrm{cov}(3,5) & \rightarrow & \mathrm{cov}(3,5) + h\ \nu\ a_5\ k\ \delta_{2D}^2 \\
\mathrm{cov}(4,4) & \rightarrow & \mathrm{cov}(4,4) + (s\ k\ \delta_{2D})^2 \\
\mathrm{cov}(4,5) & \rightarrow & \mathrm{cov}(4,5) - s\ (k\ \delta_{2D})^2 \\
\mathrm{cov}(5,5) & \rightarrow & \mathrm{cov}(5,5) + (k\ \delta_{2D})^2
\end{array}
\tag{8.12}
$$

Here s is the path–length from a_1 to the dead material location.

8.5 Energy Loss

8.5.1 Bethe–Bloch formula

The energy loss rate (also known as stopping power) is calculated accordingly to the Bethe–Bloch formula (see Sect. 23.2 in [85]):

$$
-\frac{\mathrm{d}E}{\mathrm{d}x} = Kz^2 \frac{Z}{A} \frac{1}{\beta^2} \left[\frac{1}{2} \ln \frac{2m_e c^2 \beta^2 \gamma^2 T_{\max}}{I^2} - \beta^2 - \frac{\delta}{2} \right], \tag{8.13}
$$

where

- $K = 3.07075 \cdot 10^{-4}\ \mathrm{GeV\,cm^2\ mol^{-1}}$,
- z is the charge number of the incident particle (± 1),
- βc is the particle speed, and $\gamma = 1/\sqrt{1-\beta}$,
- Z and A are respectively the atomic number and the atomic mass of the medium; $Z/A \simeq 0.5$ for all the elements except hydrogen;
- $m_e = 511\,\mathrm{keV}$ is the mass of electron,
- I is the mean excitation energy of the medium,
- δ is the density effect correction.

The dependence on the mass M of the incident particle is due to:

$$
T_{\max} = \frac{2m_e c^2 \beta^2 \gamma^2}{1 + 2\gamma m_e / M}. \tag{8.14}
$$

In VCMVD a pion mass $M_\pi = 0.139570\ \mathrm{GeV}$ is assumed.

Material	Z	Z/A	I (eV)	ρ (g/cm^2)	$-C$	X_0	X_1	a	m	δ_0
Be	4	0.44384	63.7	1.848	2.7847	0.0592	1.6922	0.80392	2.4339	0.14
C	6	0.49954	78.0	2.000	2.9925	-0.0351	2.4860	0.20240	3.0036	0.10
Al	13	0.48181	166.0	2.699	4.2395	0.1708	3.0127	0.08024	3.6345	0.12
Si	14	0.49848	173.0	2.330	4.4351	0.2014	2.8715	0.14921	3.2546	0.14

Table 8.1: Density effect parameters for some elements.

8.5.2 Density effect correction

The density effect correction is parameterised as [86]:

$$\delta = \begin{cases} 2X\ln(10) + C & \text{if } X \geq X_1 \\ 2X\ln(10) + a(X_1 - X)^m + C & \text{if } X_0 \leq X < X_1 \\ \delta_0\ 10^{2\ (X - X_0)} & \text{if } X < X_0 \end{cases} \tag{8.15}$$

where X is defined as

$$X = \log_{10}(\beta\gamma); \tag{8.16}$$

parameters X_0, X_1, a, m, δ_0 are given in Table 8.1 (again from [86]) for some elements.

As an example, the stopping power for pions in beryllium is plotted in Fig. 8.6, with and without density effect correction.

8.5.3 Energy Loss in VCMVD

The energy loss is calculated by using

$$\Delta E = \frac{\mathrm{d}E}{\mathrm{d}x}\ D, \tag{8.17}$$

where D is the thickness (8.6) expressed in grams $\cdot\,\mathrm{cm}^{-2}$.

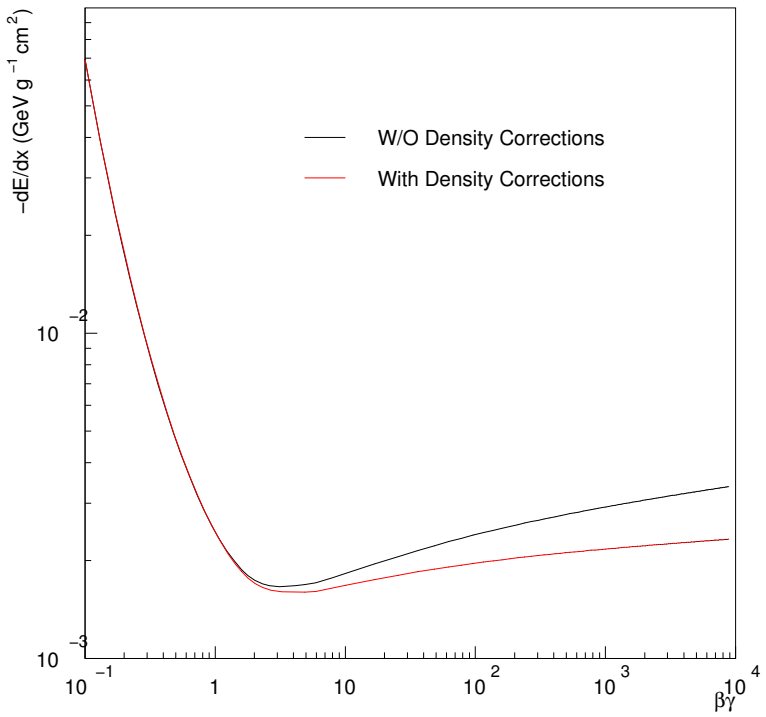

Figure 8.6: Stopping power for pions in Beryllium.

Chapter 9

Reconstruction of MVD clusters

The read–out of MVD strips is collected by ADCs and stored in the MVRAWS ADAMO table. The ADCs also run a clustering algorithm, described in the next section, on these strip data, and store the results in the MVRAWC table. These two tables are available in the Second Level Trigger, and the strip table is transferred to the TLT too. The suitability of transferring the MVRAWC table from SLT to TLT was discussed inside the collaboration; the main drawback is the amount of data to be transferred and the consequent dead time. The MVRAWC table is currently available in the TLT, and VCMVD reads cluster information from it; in case of a removal of the clusters table, VCMVD was provided with a clustering routine which runs over MVRAWS strips and uses the same logic as the ADCs do.

9.1 The clustering algorithm

Calibration runs are taken regularly for the calculation of pedestals of read–out channels; let me name PED(i) the value read for the channel i. Then, the *common mode* is defined by:

- N(good strips) = N(strips) − N(dead channels);
- $\text{Common} = \sum_{i=1}^{\text{N(strips)}} \text{PED}(i)/\text{N(good strips)}$.

Pedestals and common mode are subtracted from the ADC read–out value, ADC(i), to obtain the PedSub array which will be used for clustering:

- $\text{PedSub}(i) = \max\big(\, 0, \text{ADC}(i) - \text{PED}(i) \,\big)$;
- for dead channels, PED(i) is set to 0x3FF (the maximum value possible for the ADC read–out), so that $\text{PedSub}(i) \equiv 0$;
- $\text{ComSub}(i) = \max\big(\, 0, \text{PedSub}(i) - \text{Common} \,\big)$.

A threshold Thresh(i) is set for each strip, depending on its noise; strips are grouped in clusters respecting the following rules:

- Strip i is "beginning of a cluster" if one of the three cases below holds:
  (1) (ComSub($i-1$) $\leq$ Thresh($i-1$)) AND (ComSub(i) $\leq$ Thresh(i)) AND (ComSub($i+1$) $>$ Thresh($i+1$));
  (2) ($i = 0$ i.e. silicon edge) AND (ComSub(i) $\leq$ Thresh(i)) AND (ComSub($i+1$) $>$ Thresh($i+1$));
  (3) ($i = 0$ i.e. silicon edge) AND (ComSub(i) $>$ Thresh(i)).
- Similarly, strip j is "end of a cluster" if one of the three cases below is true:
  (1) (ComSub($j-1$) $>$ Thresh($j-1$)) AND (ComSub(j) $\leq$ Thresh(j)) AND (ComSub($j+1$) $\leq$ Thresh($j+1$));
  (2) (ComSub($j-1$) $>$ Thresh($j-1$)) AND (ComSub(j) $\leq$ Thresh(j)) AND ($j = 511$ i.e. silicon edge);
  (3) (ComSub(j) $>$ Thresh(j)) AND ($j = 511$ i.e. silicon edge).
- Then, strips i to j make one cluster.

The cluster is kept if the length is $(j-i+1) > 16$ or the sum of ComSubs between i and j is above a given threshold.

The efficiency of cluster reconstruction has been evaluated on a Monte Carlo simulation of single muons. The number of reconstructed clusters is equal to the number of GEANT hits in the MVD (Fig. 9.1) in most of the cases. In some cases more clusters are seen, due to the noise.

Structure of MVRAWS

The table MVRAWS contains a list of all fired strips, in particular the strip ID, the layer, ladder and module numbers, and the read–out value after pedestal and common mode subtraction, ComSub(i), are stored.

Structure of MVRAWC

The table MVRAWC contains an entry for each MVD cluster; the quantities recorded are (1 and n are the first and the last strip in the cluster):

- the layer, ladder and module numbers;
- the total ADC count for the cluster, $\sum_{i=0}^{n}$ ComSub(i);
- the strip ID and ComSub for $i = 0,\ n+1$;
- the ComSub for $i = 1,\ n$;

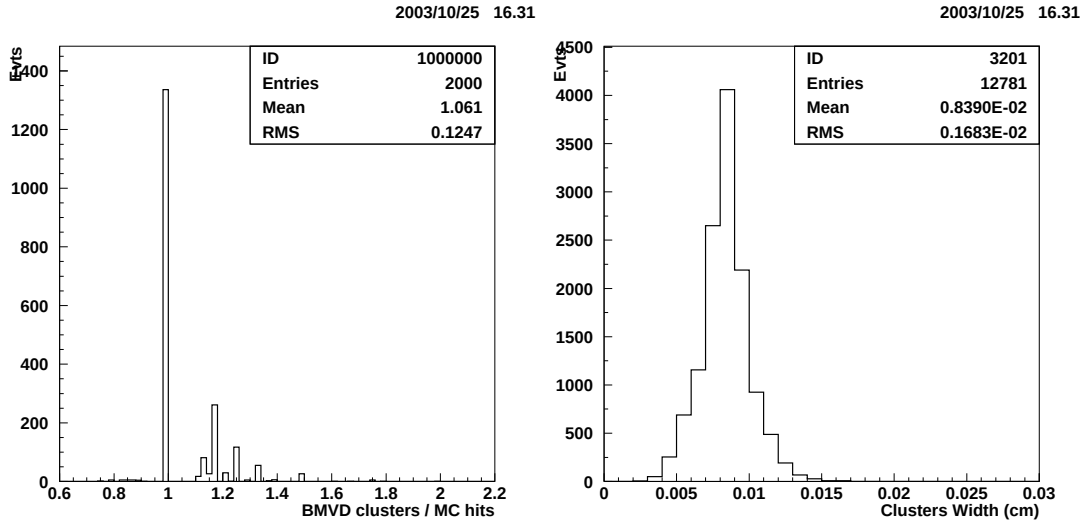

Figure 9.1: On the left the efficiency of cluster reconstruction, obtained on a Monte Carlo of single muons, is shown. It is calculated as the number of reconstructed clusters over the number of GEANT MVD hits. On the right the distribution of cluster widths, calculated on the same MC sample by using the centre–of–gravity, is plotted.

The whole information about the first two and the last two strips is stored; for the remaining ones only the total ADC count is available. This is enough for characterising the cluster since large clusters are rare, and for those the central strips have quite a constant ADC count (Fig. 9.2).

Once a list of the clusters is available, VCMVD calculates centres and widths, in the ZEUS reference frame, by means of the *centre of gravity algorithm*.

9.2 The Centre of Gravity algorithm

Let me call $\xi(i)$ the position, in the wafer reference, of the i–th strip of a cluster, and ADCSUM the total ADC count over the cluster:

$$\text{ADCSUM} = \sum_{i=0}^{n+1} \text{ComSub}(i). \tag{9.1}$$

The centre and the width of the cluster can be evaluated by using the centre of gravity algorithm:

$$\langle \xi \rangle = \frac{1}{\text{ADCSUM}} \sum_{i=0}^{n+1} \text{ComSub}(i)\ \xi(i), \tag{9.2}$$

$$\sigma^2(\xi) = \frac{1}{\text{ADCSUM}} \sum_{i=0}^{n+1} \text{ComSub}(i)\ [\xi(i) - \langle \xi \rangle]^2. \tag{9.3}$$

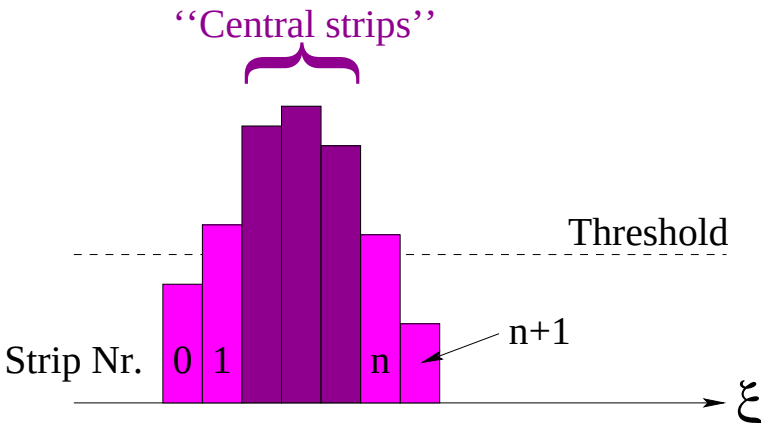

Figure 9.2: Clustering in the MVD. 1 and n are the first and last strip above threshold.

If $n > 2$, the $(n-2)$ central strips are considered like a single strip having

$$\xi_c = \frac{1}{2}[\xi(0) + \xi(n+1)], \tag{9.4}$$

$$\begin{aligned} \mathrm{ComSub}_c &= \mathrm{ADCSUM} - \mathrm{ComSub}(0) - \mathrm{ComSub}(1) \\ &- \mathrm{ComSub}(n) - \mathrm{ComSub}(n+1). \end{aligned} \tag{9.5}$$

The distribution of cluster widths, obtained on a Monte Carlo simulation of single muons, is plotted in Fig. 9.1. The mean value is around 80 μm.

9.3 Cluster position in ZEUS frame

As explained in the MVD section (Sect. 2.3.1), the $r\phi$ and z sensors composing an half–module are read by the same HELIX chip; there is consequently an ambiguity due to the fact that you do not know if the fired strip is on a $r\phi$ or a z wafer. This has to be taken into account in the pattern recognition procedure described in the next chapter.

An $r\phi$ position, Eq. 8.2 and a z, Eq. 8.3, is associated to each cluster; of course only one out of the two has a physical meaning, whereas the other is a *ghost* due to the ambiguity of the read–out.

Chapter 10

Trajectory fit

The trajectory fit is performed separately for the three layers of the BMVD; three steps can be individuated in this iterative procedure.

For the layer 2, the external one:

- all the tracks found by VCTRAK are propagated inwards, from the reference point (outside the MVD) until they intercept the BMVD outer layer; the coordinates of the intersection are calculated in the wafer reference frame;
- the clusters reconstructed on the layer 2 are assigned to the trajectories; each track may collect two clusters, an $r\phi$ and a z, on every ladder, and each cluster can be used just once;
- the track parameters are updated by making use of the position of the assigned clusters; the reference point is then transported to coincide with the cluster position.

The procedure is repeated for the layers 1 (the middle one) and 0 (the most internal), and the reference point is finally transported to the nominal interaction point, the origin of the ZEUS reference frame.

The three steps of the fitting procedure are described in the next sections.

10.1 Trajectory–Ladder intersections

As a first approximation, the BMVD layer is considered as a circular cylinder (which is quite true for layers 1 and 2, whereas for the layer 0 an ellipsoidal cylinder would be more appropriated). The intersection of the particle helix and this cylinder is found: $B \equiv (x_{int}^{LAY}, y_{int}^{LAY})$, Fig. 10.1, then the ladders whose centres (x_{mvd}, y_{mvd}) are close enough to the intersection, namely

$$\Delta xy = \sqrt{(x_{int}^{LAY} - x_{mvd})^2 + (y_{int}^{LAY} - y_{mvd})^2} < 4.5 \text{ cm}, \tag{10.1}$$

are inspected to verify if the helix really intersects them.

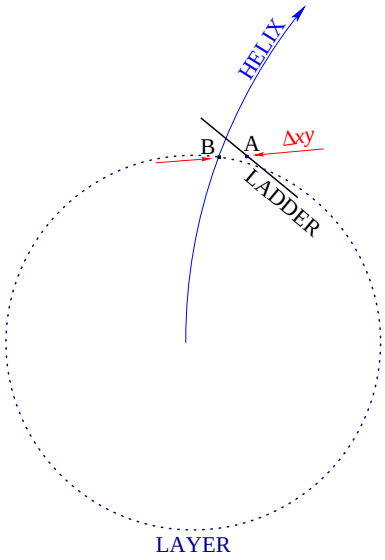

Figure 10.1: Distance Δxy between ladder centre (A) and the intersection (B) of helix and layer cylinder.

10.1.1 Helix–Layer intersections

The three layers are assumed to be cylinders with radii $R_L = 4.0$, 8.5, 12.0 cm. Two different approaches are used, depending on the ratio a_3^0/R_L[1].

"Small" a_3^0

a_3^0 is regarded as "small" when

$$a_3^0 < 0.3\ R_L.$$

In this case a_3^0 is neglected with respect to R_L, therefore (see Fig. 10.2)

$$\frac{1}{2}R_L = R\ \tan\left(\frac{\delta\phi^0}{2}\right) = \frac{1}{|a_2|}\tan\left(\frac{\delta\phi^0}{2}\right),$$

and the angle $\delta\phi^0$ is given by

$$\delta\phi^0 = 2\arctan\left(\frac{R_L\ |a_2|}{2}\right). \tag{10.2}$$

The angle at the intersection point is

$$\phi_{int} = a_1^0 - Q\ \delta\phi^0, \tag{10.3}$$

while the Cartesian coordinates are

$$\begin{array}{rcrcl} x_{int}^{LAY} & = & (a_3^0 + 1/a_2)\sin a_1^0 & - & \sin(\phi_{int})/a_2 \\ y_{int}^{LAY} & = & -(a_3^0 + 1/a_2)\cos a_1^0 & + & \cos(\phi_{int})/a_2 \end{array} \tag{10.4}$$

[1]With the notation a_ν^0 the parameter a_ν, swum to (0,0), is indicated.

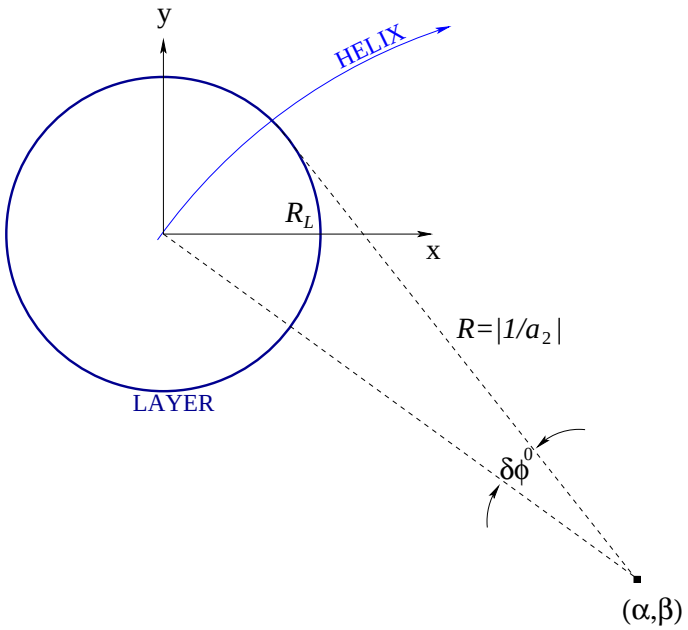

Figure 10.2: Intersection between the particle trajectory and a layer of the barrel MVD. a_3^0 is neglected.

"Large" a_3^0

In the case $a_3^0 \geq 0.3\ R_L$, $\delta\phi = \phi - a_1 \ll 1$ is assumed; for energetic particles it is quite correct, since (see Eq. B.7),

$$|\delta\phi| = |a_1 - \phi| = |s\ a_2| = \frac{|s|\ 0.003\ B_z}{P_T}, \tag{10.5}$$

and for $s = 5\,\text{cm}$ and $P_T = 100\,\text{MeV}$ it is $|\delta\phi| \simeq 0.2$.

Using this assumption,

$$\begin{array}{rcccl} \sin\phi & = & \sin(a_1 + \delta\phi) & \simeq & \sin a_1 + \cos a_1\ \delta\phi \\ \cos\phi & = & \cos(a_1 + \delta\phi) & \simeq & \cos a_1 - \sin a_1\ \delta\phi \end{array}$$

and the particle trajectory becomes (remember $s = -\delta\phi/a_2$):

$$\begin{array}{rcl} x(s) & = & x_0 + a_3\ \sin a_1 + s\ \cos a_1 \\ y(s) & = & y_0 - a_3\ \cos a_1 + s\ \sin a_1 \end{array} \tag{10.6}$$

The s at the intersection point with the layer is (see Section B.4 for details):

$$\begin{array}{rcl} B & = & x_0 \cos a_1 + y_0 \sin a_1 \\ \Delta & = & R_L^2 - (x_0 \sin a_1 - y_0 \cos a_1 + a_3)^2 \\ s_{int} & = & -B + \sqrt{\Delta} \end{array} \tag{10.7}$$

and the Cartesian coordinates come from Equation (10.6)

$$\left\{ \begin{array}{rcl} x_{int}^{LAY} & = & x(s_{int}) \\ y_{int}^{LAY} & = & y(s_{int}) \end{array} \right. \tag{10.8}$$

10.1.2 Helix–Ladder intersections

Each ladder can be represented in the ZEUS reference by a thick rectangle whose major axis is parallel to z:

$$\begin{aligned} x(\xi) &= x_{mvd} + \xi \cos\alpha \\ y(\xi) &= y_{mvd} + \xi \sin\alpha \end{aligned} \tag{10.9}$$

The width of each ladder is $|\xi| < 3.07\,\text{cm}$ and the height is considered as infinite. To find out the intersections between the particle helices (Eqs. 7.1 and 7.2) and the ladders, some auxiliary variables are needed:

$$\begin{aligned} B &= \left(a_3 + \frac{1}{a_2}\right)\sin(\alpha - a_1) + (x_{mvd} - x_0)\cos\alpha + \\ &+ (y_{mvd} - y_0)\sin\alpha, \end{aligned} \tag{10.10}$$

$$\begin{aligned} C &= \left(a_3 + \frac{1}{a_2}\right)^2 - \left(\frac{1}{a_2}\right)^2 + 2\left(a_3 + \frac{1}{a_2}\right)[(y_{mvd} - y_0)\cos a_1 - \\ &- (x_{mvd} - x_0)\sin a_1] + (x_{mvd} - x_0)^2 + (y_{mvd} - y_0)^2. \end{aligned} \tag{10.11}$$

The parameters ξ and ϕ at the intersection point (see Section B.5 for details) are:

$$\xi_{int} = -B \pm \sqrt{B^2 - C}, \tag{10.12}$$

$$\begin{aligned} \phi_{int} &= \text{ATAN2}\left\{Q\left[\left(a_3 + \frac{1}{a_2}\right)\sin a_1 - (x_{mvd} - x_0) - \xi_{int}\cos\alpha\right],\right. \\ &\left. Q\left[-\left(a_3 + \frac{1}{a_2}\right)\cos a_1 + (y_{mvd} - y_0) + \xi_{int}\sin\alpha\right]\right\}, \end{aligned} \tag{10.13}$$

thus the pathlength from a_1 to ϕ_{int} is

$$s_{int} = -\frac{\phi_{int} - a_1}{a_2}, \tag{10.14}$$

and the coordinates comes from (7.5) and (10.9).

From the mathematical point of view any intersection between a plane and a helix has two solutions in ξ; the solutions in ϕ are infinite (due to periodicity of tangent). The physical intersection is the one with:

- $|\phi_{int} - a_1| < 2\pi$,
- $s_{int} < 0$, since the propagation is backward,
- $|s_{int}|$ is the minimum between the possible values.

Layer	Ladder	k_x	k_y
0	0	+	+
	1	+	+
	2	−	−
	3	+	−
1	0	+	+
	1	+	+
	2	+	+
	3	−	+
	4	−	+
	5	−	−
	6	−	−
	7	−	−
	8	+	−
	9	+	−
2	0	+	−
	1	+	+
	2	+	+
	3	+	+
	4	+	+
	5	−	+
	6	−	+
	7	−	+
	8	−	+
	9	−	−
	10	−	−
	11	−	−
	12	−	−
	13	+	−
	14	+	−
	15	+	−

Table 10.1: Sign of the corrections to x_{int} and y_{int}, as a function of the layer and ladder numbers.

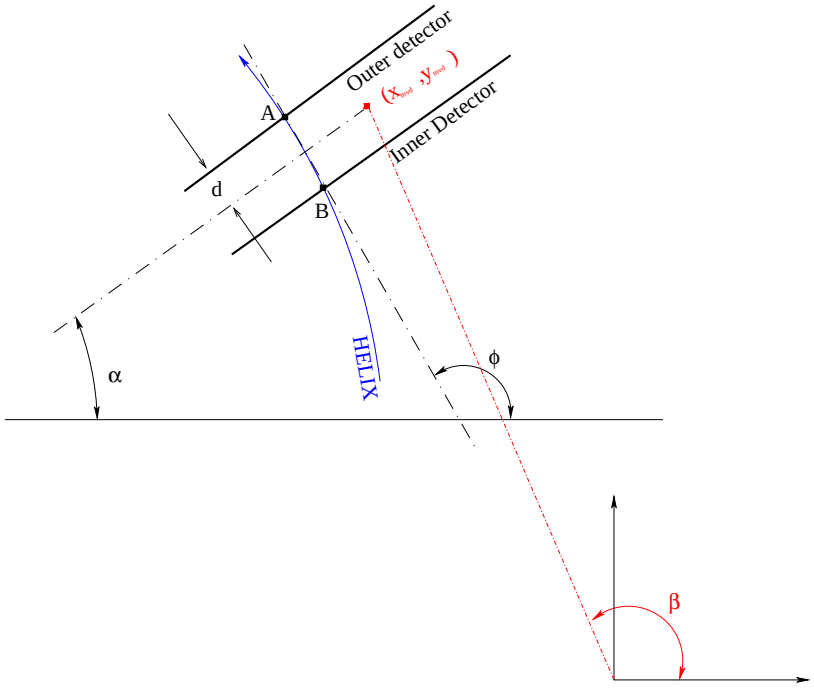

Figure 10.3: Corrections to ξ_{int} and z_{int} due to Inner/Outer detector.

Corrections to ξ_{int} and z_{int}

Each ladder is composed by an inner detector and an outer one (Fig. 10.3) spaced by $d = 0.13$ or 0.27 cm, depending on the z coordinate. The intersections ξ_{int} and z_{int} are calculated on the middle plane (dashed–dotted line). To bring the intersection to the inner or to the outer detector, corrections have to be applied. For example, the centre of the outer detector has coordinates:

$$x^{out}_{mvd} = x_{mvd} + k_x \cdot d \,|\sin\alpha| \equiv x_{mvd} + \delta x^{out}_{mvd},$$
$$y^{out}_{mvd} = y_{mvd} + k_y \cdot d \,|\cos\alpha| \equiv y_{mvd} + \delta y^{out}_{mvd}.$$

k_x and k_y give the sign of the correction and are listed in Table 10.1, as a function of the layer and ladder numbers.

Eqs. 10.10 and 10.11 acquire the corrections:

$$\begin{aligned}
\delta B^{out} &= \delta x^{out}_{mvd}\ \cos\alpha + \delta y^{out}_{mvd}\ \sin\alpha = \\
&= d\ \left[k_x\ |\sin\alpha|\cos\alpha + k_y\ |\cos\alpha|\sin\alpha\right] \\
\delta C^{out} &= 2\left(a_3 + \frac{1}{a_2}\right)(\cos a_1\ \delta y_{mvd} - \sin a_1\ \delta x_{mvd}) + 2\ (x_{mvd} - x_0)\ \delta x_{mvd} + \\
&+ \ 2\ (y_{mvd} - y_0)\ \delta y_{mvd} = \\
&= 2d\left(a_3 + \frac{1}{a_2}\right)(k_y\ \cos a_1|\cos\alpha| - k_x\ \sin a_1|\sin\alpha|) + \\
&+ \ 2\ k_x\ (x_{mvd} - x_0)|\sin\alpha| + 2\ k_y\ (y_{mvd} - y_0)|\cos\alpha|
\end{aligned} \tag{10.15}$$

and ξ_{int} gets a correction

$$\delta\xi_{int}^{out} = -\delta B^{out}\left[1 \mp \frac{B}{\sqrt{B^2 - C}}\right] \mp \frac{\delta C^{out}}{2\sqrt{B^2 - C}}. \tag{10.16}$$

When the intersection lies on the inner detector, the correction is

$$\delta\xi_{int}^{in} = -\delta\xi_{int}^{out}. \tag{10.17}$$

The pathlength within the two detectors is approximately

$$\overline{AB} = \frac{2d}{|\sin(\phi_{int} - \alpha)|},$$

and since $z = a_4 + s\ a_5$ the corrections to z_{int} are:

$$\delta z_{int}^{out} = a_5\ \frac{\overline{AB}}{2} = \frac{a_5\ d}{|\sin(\phi_{int} - \alpha)|}, \tag{10.18}$$

$$\delta z_{int}^{in} = -\delta z_{int}^{out}. \tag{10.19}$$

Uncertainty on the intersections

The uncertainty on the intersections is obtained from a_ν's uncertainties and from the derivatives of ξ and z with respect to the helix parameters (see Section B.5 for details):

$$\begin{aligned}\sigma^2(\xi_{int}) &= \left(\frac{\partial\xi}{\partial a_1}, \frac{\partial\xi}{\partial a_2}, \frac{\partial\xi}{\partial a_3}\right)\begin{pmatrix} \sigma^2(a_1) & \mathrm{cov}(1,2) & \mathrm{cov}(1,3) \\ \mathrm{cov}(1,2) & \sigma^2(a_2) & \mathrm{cov}(2,3) \\ \mathrm{cov}(1,3) & \mathrm{cov}(2,3) & \sigma^2(a_3) \end{pmatrix} \\ &\times \begin{pmatrix} \partial\xi/\partial a_1 \\ \partial\xi/\partial a_2 \\ \partial\xi/\partial a_3 \end{pmatrix},\end{aligned} \tag{10.20}$$

and

$$\sigma^2(z_{int}) = \left(\frac{\partial z}{\partial a_4}, \frac{\partial z}{\partial a_5}\right)\begin{pmatrix} \sigma^2(a_4) & \mathrm{cov}(4,5) \\ \mathrm{cov}(4,5) & \sigma^2(a_5) \end{pmatrix}\begin{pmatrix} \partial z/\partial a_4 \\ \partial z/\partial a_5 \end{pmatrix}. \tag{10.21}$$

10.2 Pattern recognition

The *pattern recognition* is the procedure which:

1. pick up clusters to be assigned to each trajectory;
2. get rid of multiple assignments of clusters, making a decision on the track to which these clusters have to be assigned and either they have to be used as $r\phi$ or as z.

I will illustrate how VCMVD copes with these two facts in the next two sections.

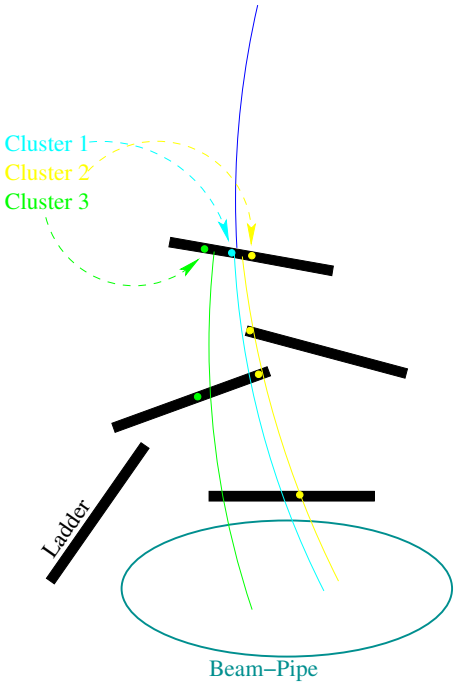

Figure 10.4: The strategy used by VCMVD for pattern recognition. Only part of the BMVD is sketched.

10.2.1 Collection of clusters

These steps are taken for each layer, 2, 1 and 0:

- each helix m is propagated inwards until intercepts a ladder, as described in the previous section;
- the $r\phi$ and z "distances",
  $(C^{\xi}_{mj})^2 = \left(\xi^m_{int} - \xi^j_{clu}\right)^2/\sigma^2_{\xi}$ and
  $(C^{z}_{mj})^2 = \left(z^m_{int} - z^j_{clu}\right)^2/\sigma^2_{z}$,
  are calculated for each cluster j in the ladder;
- all the clusters within $(C^{\xi}_{mj})^2 < 50$ from the track are collected and stored in a $r\phi$ list;
- all the clusters within $(C^{z}_{mj})^2 < 50$ from the track are collected and stored in a z list;
- the clusters are sorted in terms of $(C_{mj})^2$; for example, in Fig. 10.4 the ordering is (clu1, clu2, clu3).

This instruction is applied to the external layer only:

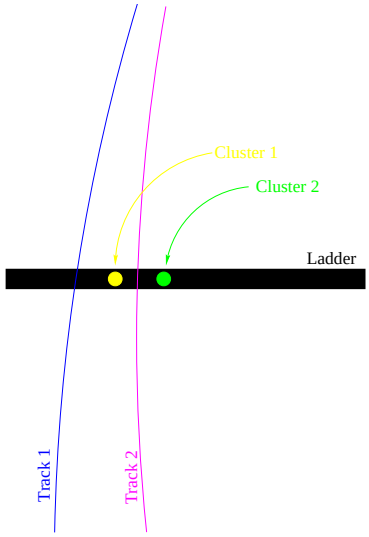

Figure 10.5: How VCMVD get rid of multiple assignment of clusters. Initially cluster 1 is assigned to both track 1 and track 2; in the end cluster 2 is associated to track 2.

- a fast helix fit (3 parameters in $r\phi$, 2 parameters in z) is performed; $r\phi$ clusters in the list are used to update a_1–a_2–a_3 and the list is reordered, preferring clusters which drive to other clusters in the inner layers. For example the $r\phi$ list of Fig. 10.4 becomes (clu2, clu3, clu1). The same is done for z clusters, which are used for updating a_4 and a_5. The helix parameters from the fast fit are not stored, they are only used for the reordering.

10.2.2 Multiple assignments

Before doing an update of the 5 parameters, VCMVD has to get rid of multiple assignments of clusters. For each helix m and every cluster j in the ladder, the distance is calculated

$$(C^{\xi}_{mj})^2 = \frac{\left(\xi^m_{int} - \xi^j_{clu}\right)^2}{\sigma(\xi)^2}; \tag{10.22}$$

the same is done for z coordinate.

A distance $(C^{\xi,z}_{mj})^2 \equiv 10^7$ is assumed every time a cluster is not in the list of candidates.

For every pair of helices m and n, it is checked that the closest cluster is not the same; the fact that a cluster can be used either as $r\phi$ or z is also considered. If the cluster is the same for the two tracks, a decision has to be taken for the assignment and the second closest cluster of each helix is considered. See for example Fig. 10.5: the same $r\phi$ cluster (clu1), is the closest one to both helix 1 (trk1) and helix 2 (trk2); the second closest cluster in $r\phi$ is clu2. The procedure is followed:

- if $C_{12}^2 + C_{21}^2 \leq C_{11}^2 + C_{22}^2$, the assignments are clu2 → trk1 and clu1 → trk2;
- if $C_{12}^2 + C_{21}^2 > C_{11}^2 + C_{22}^2$, the assignments are clu1 → trk1 and clu2 → trk2; in Fig. 10.5 this case holds;

the procedure is iterated until there are no more multiple assignments.

Before proceeding with the pattern recognition in the next layer, a complete (5 parameters) fit of the helix parameters is performed, using the 1st cluster in the list. The fitting procedure is described in the next section.

10.3 Parameters Fit

The general formalism

Let me introduce

- a list of N measurements: $\{F_m,\ 1 \leq m \leq N\}$;
- σ_m^2, the variance of the measurement F_m;
- $f(m;\vec{a})$, the function that fits the measurements; in the case treated by VCMVD the function is a helix.

The χ^2 of the fit depends on the parameters a_ν and is defined by:

$$\chi^2(\vec{a}) = \sum_{m=1}^{N} \frac{[F_m - f(m;\vec{a})]^2}{\sigma_m^2}. \tag{10.23}$$

The first and second derivatives of χ^2 define the two quantities B_μ and $U_{\mu\nu}$,

$$B_\mu(\vec{a}) = -\frac{1}{2}\frac{\partial\chi^2(\vec{a})}{\partial a_\mu} = \sum_{m=1}^{N} \frac{F_m - f(m;\vec{a})}{\sigma_m^2}\frac{\partial f(m;\vec{a})}{\partial a_\mu}, \tag{10.24}$$

$$U_{\mu\nu}(\vec{a}) = -\frac{\partial B_\mu(\vec{a})}{\partial a_\nu} = \sum_{m=1}^{N} \frac{1}{\sigma_m^2}\frac{\partial f(m;\vec{a})}{\partial a_\mu}\frac{\partial f(m;\vec{a})}{\partial a_\nu}; \tag{10.25}$$

the second derivative of $f(m;\vec{a})$ is neglected.

The initial value of $\vec{a}$ is the one from VCTRAK, or the one from the last fit done by VCMVD.

The best estimation of the parameters after the insertion of the new measurement is obtained by minimising the new χ^2; the hypothesis of a small variation of $\vec{a}$ is assumed:

$$\chi^2(\vec{a} + \delta\vec{a}) = \chi^2(\vec{a}) - 2B_\mu(\vec{a})\ \delta a_\mu, \tag{10.26}$$

$$\frac{\partial\chi^2(\vec{a} + \delta\vec{a})}{\partial a_\mu} = 0. \tag{10.27}$$

From this couple of equations the following relation can be derived,

$$-2B_\mu(\vec{a}) + 2U_{\mu\nu}(\vec{a})\ \delta a_\nu = 0, \tag{10.28}$$

which leads to

$$\delta a_\mu = U^{-1}_{\mu\nu}(\vec{a})\ B_\nu(\vec{a}). \tag{10.29}$$

The new, minimised, χ^2 is

$$\begin{aligned}\chi^2(\vec{a}+\delta\vec{a}) &= \chi^2(\vec{a}) + \frac{\partial\chi^2(\vec{a})}{\partial a_\mu}\ \delta a_\mu + \frac{1}{2}\frac{\partial^2\chi^2(\vec{a})}{\partial a_\mu \partial a_\nu}\ \delta a_\mu\ \delta a_\nu = \\ &= \chi^2(\vec{a}) - 2B_\mu(\vec{a})\ \delta a_\mu + \delta a_\mu\ U_{\mu\nu}(\vec{a})\ \delta a_\nu. \end{aligned}\tag{10.30}$$

Since $U_{\mu\nu}(\vec{a})\ \delta a_\nu = B_\mu(\vec{a})$, this rewrites

$$\chi^2(\vec{a}+\delta\vec{a}) = \chi^2(\vec{a}) - B_\mu(\vec{a})\ \delta a_\mu. \tag{10.31}$$

The updated B_μ is zero by definition

$$B_\mu(\vec{a}+\delta\vec{a}) = -\frac{1}{2}\frac{\partial\chi^2(\vec{a}+\delta\vec{a})}{\partial a_\mu} = 0. \tag{10.32}$$

Finally,

$$\begin{aligned}U_{\mu\nu}(\vec{a}+\delta\vec{a}) &= \frac{1}{2}\frac{\partial^2}{\partial a_\mu \partial a_\nu}\chi^2(\vec{a}+\delta\vec{a}) = \frac{1}{2}\frac{\partial^2}{\partial a_\mu \partial a_\nu}\left[\chi^2(\vec{a}) - B_\rho(\vec{a})\ \delta a_\rho\right] \\ &= U_{\mu\nu}(\vec{a}) - \frac{1}{2}\delta a_\rho \frac{\partial^2}{\partial a_\mu \partial a_\nu} B_\rho(\vec{a}), \end{aligned}\tag{10.33}$$

where, neglecting second derivatives,

$$\frac{\partial^2}{\partial a_\mu \partial a_\nu} B_\rho(\vec{a}) = -\frac{\partial U_{\nu\rho}(\vec{a})}{\partial a_\mu} = -\frac{\partial}{\partial a_\mu}\sum_{m=1}^{N}\frac{1}{\sigma_m^2}\frac{\partial f(m;\vec{a})}{\partial a_\nu}\frac{\partial f(m;\vec{a})}{\partial a_\rho} = 0. \tag{10.34}$$

The new value of $U_{\mu\nu}$ is equal to the old one:

$$U_{\mu\nu}(\vec{a}+\delta\vec{a}) = U_{\mu\nu}(\vec{a}). \tag{10.35}$$

Parameters fit in VCMVD

In VCMVD there are $r\phi$ and z clusters; in the first case the measurement to be fitted is $F_m = \xi_{clu}$ and the fitting function is $\xi_{int}(\vec{a})$, Equation (10.12); in the second case the measurement is z_{clu} and the fitting function is $z_{int}(\vec{a})$, Equation (7.5). The derivatives of the fitting functions are given in Section B.5 of the Appendix.

Chapter 11

Results

The VCMVD package hasn't yet been used online; it was tested in the offline simulation of the TLT, and will be included in the next release of the trigger software. Presumably it will be tested online in the very next months of data taking, after the March–October 2003 shutdown of the HERA accelerator.

In the meanwhile the software performances have been evaluated offline, by using Monte Carlo samples and real data. The samples which have been used are:

- a single $\mu^{\pm}$ Monte Carlo, $P_{\mu} = 0.5$–1.5 GeV, $\theta_{\mu} = 45$–$135°$,
- a b–$\bar{b}$ Monte Carlo,
- Data: run 43182 (MVRAWC available), run 43183 (only MVRAWS available); both were taken on November 26$^{\text{th}}$ 2002.

No selection was applied to the events, only some cuts were applied on the tracks reconstructed by VCTRAK, in order to select particles that pass through the barrel MVD:

- $P_T > 100$ MeV,
- $-29 < Z_H < 31$ cm,
- $|D_H| < 4$ cm,
- $34° < \theta < 146°$.

11.1 Execution Times

The execution time of VCMVD is in average around 40% of VCTRAK time for single muons, and 11% for b–$\bar{b}$ (Fig. 11.1); VCTRAK does a hard work for finding tracks in complex events, while VCMVD does not worry about track finding and is not slowed down that much. In real data the relative execution time is in between the two cases above, higher when table MVRAWS is used (25%) than when MVRAWC is present (20%).

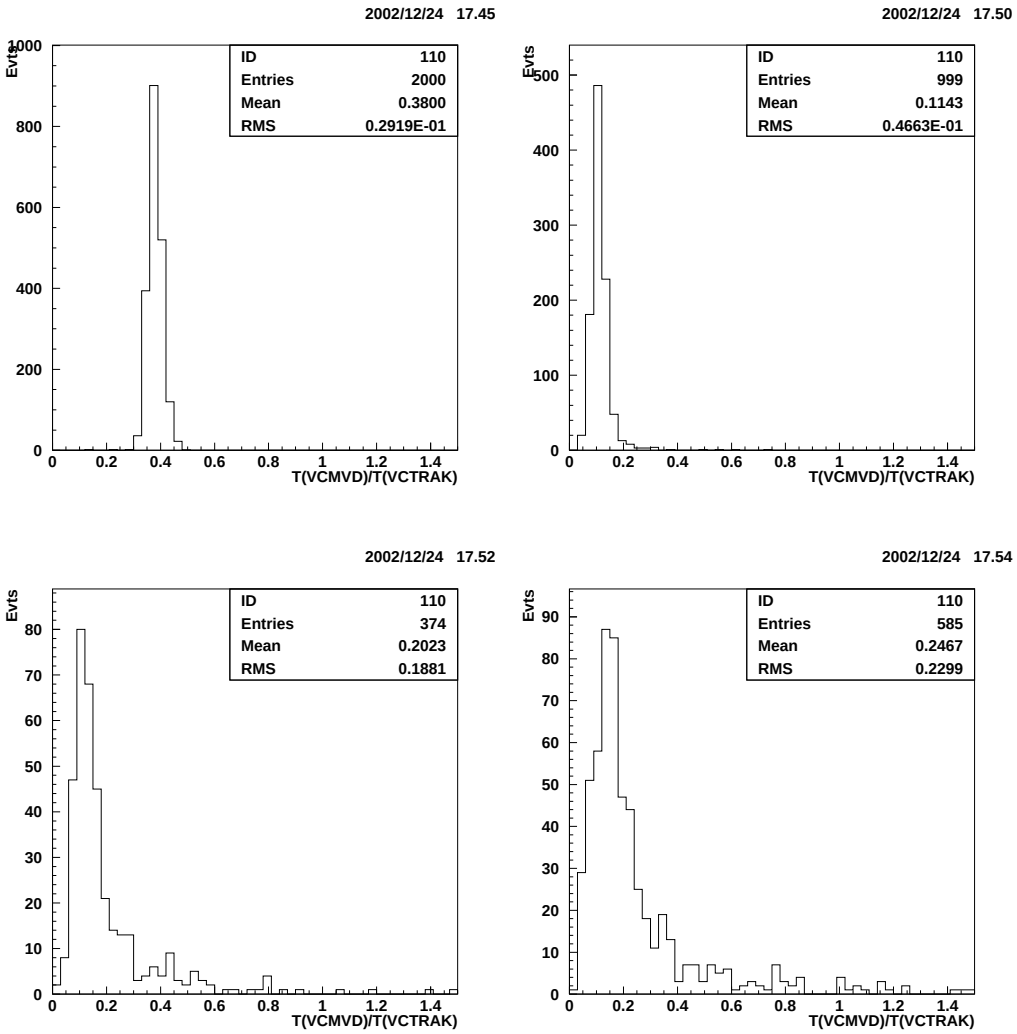

Figure 11.1: Execution time of VCMVD, expressed as a fraction of the VCTRAK execution time. Upper left plot is for single muons MC, upper right for b–$\bar{b}$ MC, lower left plot is for run 43182 (using MVRAWC) and lower right for run 43183 (using MVRAWS).

11.2 Efficiency: assigned clusters

The barrel MVD covers about 72° in azimuthal angle with two ladders, while the remaining is covered by three or more ladders. This means that, for uniformly distributed tracks I expect the number of intersections with ladders to be, in average,

$$\langle \text{No. of intersect.} \rangle \gtrsim \frac{2 \cdot 72^\circ + 3 \cdot (360^\circ - 72^\circ)}{360^\circ} = 2.8. \qquad (11.1)$$

VCMVD has a very high efficiency in finding clusters for single tracks, (see Fig. 11.2):

$$\langle n(R\phi) \rangle = 2.90 \qquad \langle n(Z) \rangle = 2.92,$$

and is still reasonably efficient for b–$\bar{b}$ Monte Carlo:

$$\langle n(R\phi) \rangle = 2.46 \qquad \langle n(Z) \rangle = 2.41.$$

In real data the efficiency is slightly lower, maybe due to inefficiencies of the detector not simulated in the Monte Carlo:

$$\langle n(R\phi) \rangle = 2.01 \qquad \langle n(Z) \rangle = 2.02 \qquad \text{(run 43182)},$$

$$\langle n(R\phi) \rangle = 2.04 \qquad \langle n(Z) \rangle = 2.03 \qquad \text{(run 43183)}.$$

11.3 Uncertainty on D_H

At low momenta the uncertainty on D_H is dominated by the multiple scattering. In the sample of single muons ($P_T = 0.5$–1.5 GeV) the uncertainty is $\langle \sigma(D_H) \rangle = 650$ μm for tracks found by VCTRAK and goes down to 300 μm after VCMVD (Fig. 11.3).

In the b–$\bar{b}$ sample the momentum reach higher values, and the result is $\langle \sigma(D_H) \rangle = 100$–$200$ μm when $P_T > 3$ GeV.

For real data the result is similar.

11.4 Uncertainty on Z_H

The uncertainty on the parameter Z_H is generally of the order of several millimeters after VCTRAK; VCMVD is able to reduce dramatically this uncertainty. In the sample of single muons the uncertainty is $\langle \sigma(Z_H) \rangle = 3.2$ mm for VCTRAK tracks, and goes down to 0.26 mm after VCMVD (Fig. 11.4).

In the b–$\bar{b}$ sample and in real data the distributions are broader, anyway the most probable value of $\sigma(Z_H)$ after VCMVD is well below 1 mm.

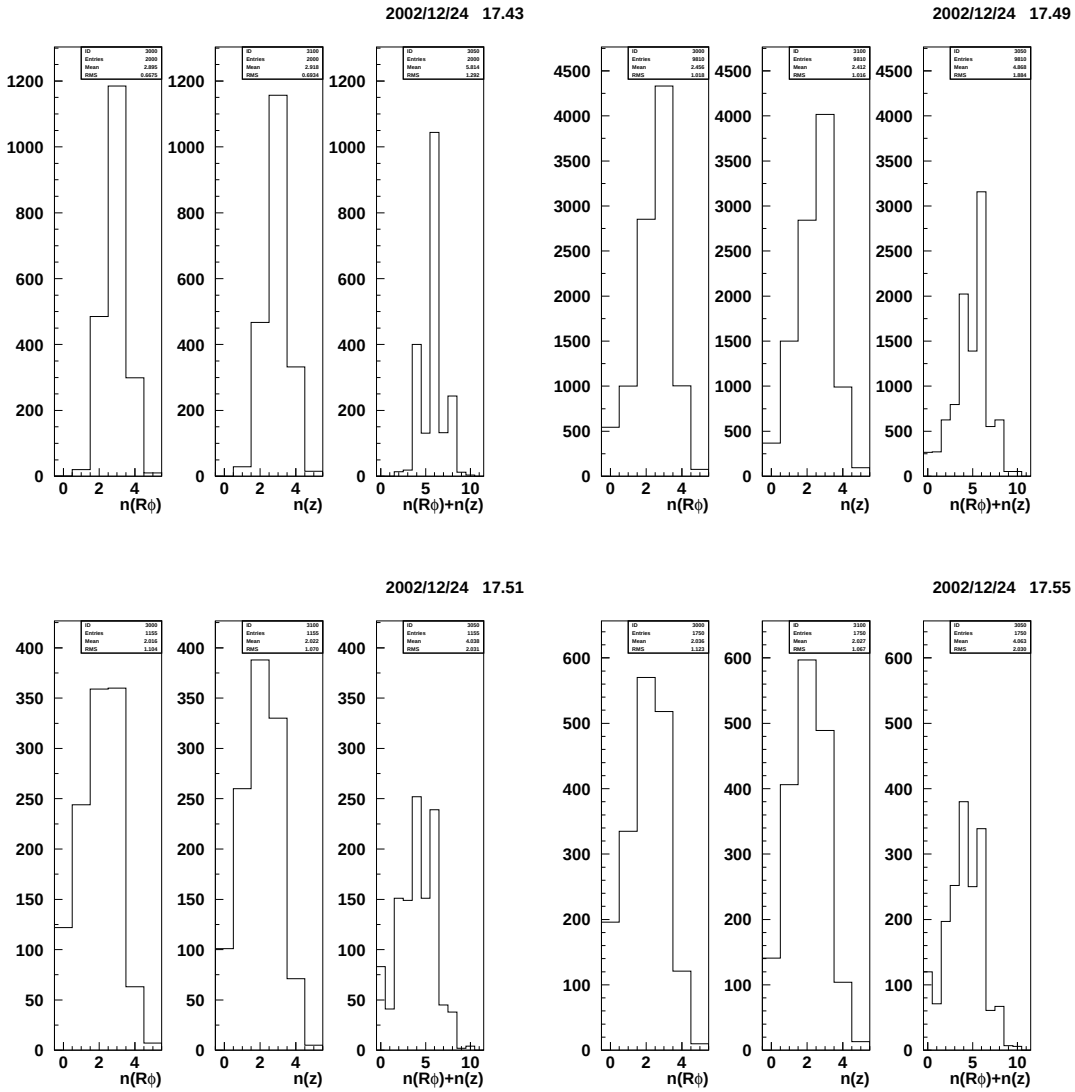

Figure 11.2: Distribution of the number of clusters used in VCMVD fit; the geometrical limit is $n \simeq 2.8$. Upper left plot is for single muons MC, upper right for b–$\bar{b}$ MC, lower left plot is for run 43182 (using MVRAWC) and lower right for run 43183 (using MVRAWS).

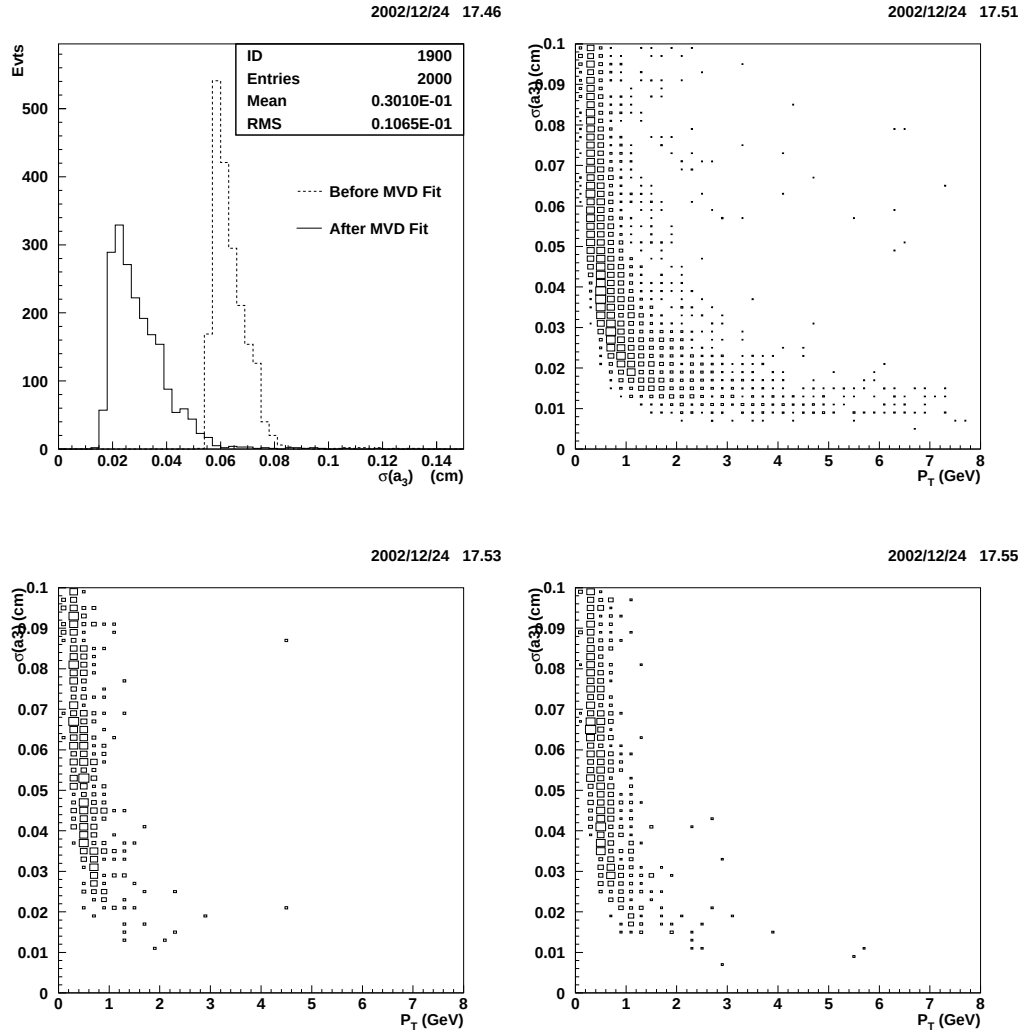

Figure 11.3: Uncertainty on the parameter D_H (a_3); the helix is referred to (0,0). Upper left plot is for single muons MC. In the upper right graph $\sigma(D_H)$ is plotted as a function of P_T, for b–$\bar{b}$ MC. On the bottom, the same is done for run 43182 (on the left, with the use of MVRAWC) and run 43183 (on the right, with the use of MVRAWS).

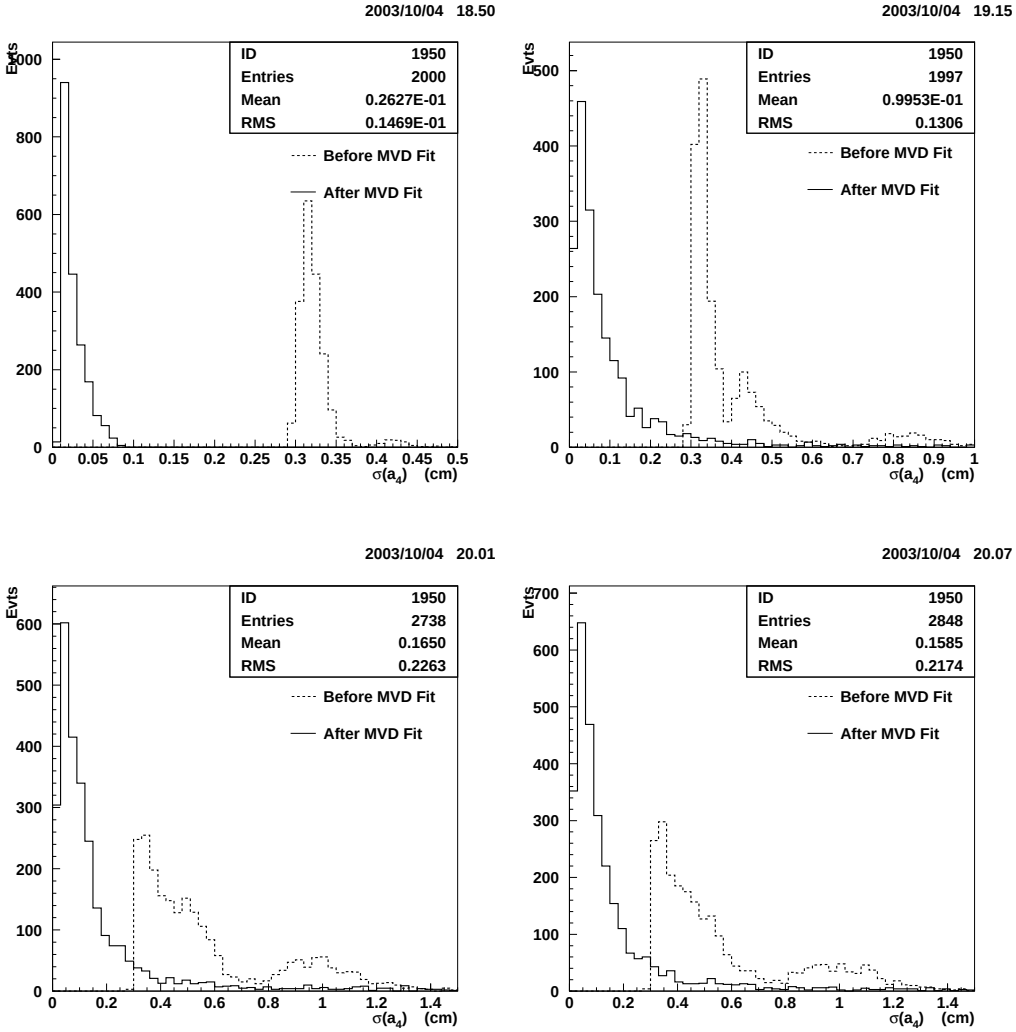

Figure 11.4: Uncertainty on the parameter Z_H (a_4); the reference point is (0,0). Upper plots refer to Monte Carlo simulations, single muon on the left and b–$\bar{b}$ on the right. On the bottom, $\sigma(Z_H)$ is plotted for run 43182 (on the left, with the use of MVRAWC) and run 43183 (on the right, with the use of MVRAWS).

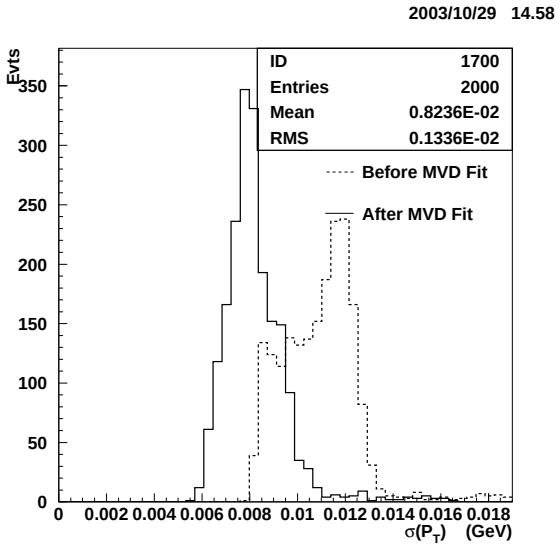

Figure 11.5: Uncertainty on the transverse momentum P_T for a Monte Carlo of single muons.

11.5 Uncertainty on P_T

For the Monte Carlo simulation of single muons, the uncertainty on the transverse momentum P_T goes down from $\langle\sigma(P_T)\rangle = 11$ MeV to $\langle\sigma(P_T)\rangle = 8$ MeV (Fig. 11.5).

11.6 Probability distributions

In Fig. 11.6 are plotted the probability distributions for the five quantities

$$C_\nu^2 = \left(\frac{a_\nu^{\mathrm{FIT}} - a_\nu^{\mathrm{TRUE}}}{\sigma(a_\nu, \mathrm{FIT})}\right)^2$$

The probabilities are evaluated in the assumption that the fitted parameters a_ν^{FIT} are normally distributed around the true values a_ν^{TRUE} and have a standard deviation given by the fit uncertainty, $\sigma(a_\nu^{\mathrm{FIT}})$.

The probabilities are quite flat, except from some excess at low values (indicating non–Gaussian tails of a_ν^{FIT} distributions); this flatness is a hint that the covariance matrix and the fitted a_ν are consistent the one with the others and the fitting procedure is correct.

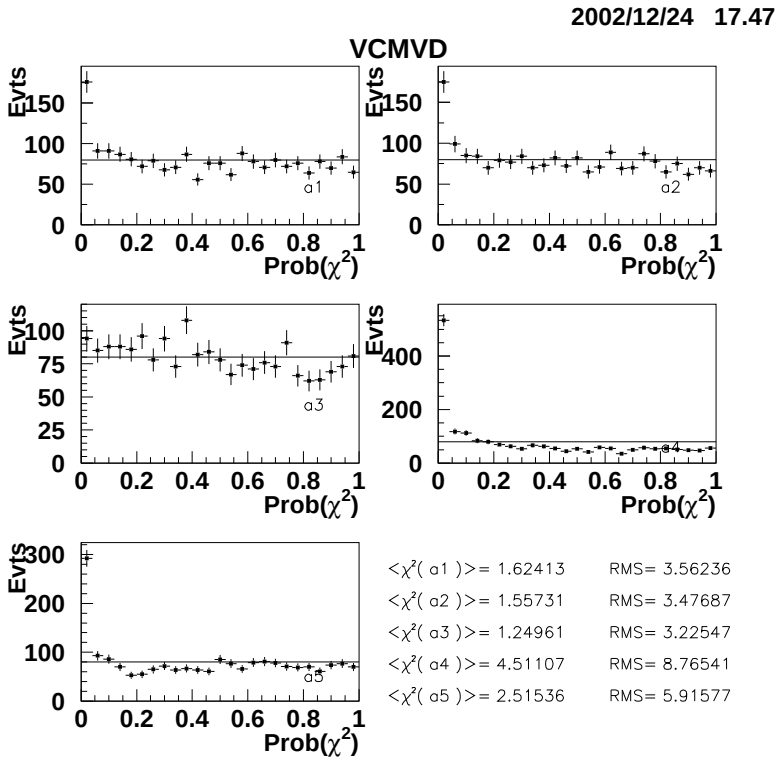

Figure 11.6: Probability distributions for the fitted parameters a_ν in a Monte Carlo simulation of single muons; the five distributions (one for each parameter a_ν) are reasonably flat, except for some events with low probability coming from non–Gaussian tails.

Appendix A

The data file mvdcmn.inc

All the results obtained by VCMVD are stored in common blocks; the commons are defined in the data file "mvdcmn.inc" which is described here.

The clustering results are written in the common block "BClu":

- nmvrc = Number of BMVD clusters;

⋆ For each cluster i:

- mvrc_adc0(i) = ADC counts in strip 0;
- mvrc_adc1(i) = ADC counts in strip 1;
- mvrc_adcn(i) = ADC counts in strip n;
- mvrc_adcn1(i) = ADC counts in strip $n+1$;
- mvrc_sum(i) = ADC counts in the whole cluster;
- nclstrip(i) = Cluster width (in strips) = $n+2$;
- mvrc_strip0(i) = Position (in strip units) of strip 0;
- mvrc_stripn1(i) = Position (in strip units) of strip $n+1$;
- mvrc_det(i) = Inner (1) or Outer (0) Detector;
- mvrc_mod(i) = Module number (0–4);
- mvrc_lad(i) = BMVD ladder (0–3 or 0–9 or 0–15);
- mvrc_lay(i) = BMVD layer (0–2);
- mvrc_csi(i) = Cluster centre in sensor frame, $(-3.066, 3.066)$ cm;
- mvrc_sigcsi(i) = RMS width of cluster (cm);
- mvrc_xx(i), mvrc_exx(i) = x position and RMS width in ZEUS frame;

- mvrc_yy(i), mvrc_eyy(i) = y position and RMS width in ZEUS frame;
- mvrc_zz(i), mvrc_ezz(i) = z position and RMS width in ZEUS frame.

The quantities relative to the helices are stored in the common block "mvdpar":

- ntrk = Number of tracks (≡ numext from VCTRAK);

⋆ For each helix m:

- Ndof_tr = No. of degrees of freedom of the fit (VCTRAK+VCMVD);
- x0_tr(m), y0_tr(m) = Reference point coordinates;
- a0_tr(μ,m) = a_μ helix parameters, updated with MVD hits;
- s_tr(m) = χ^2 after MVD fit;
- u_tr(1–15,m) = $U_{\mu\nu}$, updated and packed (see Sect. B.9);
- inv_u_tr(1–15,m) = Covariance matrix for a_μ, updated and packed.

Finally, in the common block "aClus" the list of clusters associated to each track is recorded:

- ntrk2 = Number of tracks (≡ numext from VCTRAK);

⋆ For each helix m:

- n_rphi(m) = No. of $r\phi$ MVD clusters associated to the helix;
- n_z(m) = No. of z MVD clusters associated to the helix;
- RPhi_aClus(1-5,m) = list of $r\phi$ clusters, out of BClu, associated to the helix;
- Z_aClus(1-5,m) = list of z clusters, out of BClu, associated to the helix.

Two flags are available to act on VCMVD functioning; they can be fed into VCMVD by using control cards. The flags are:

- TLTMVD = 0 (skip VCMVD code), 1 (run VCMVD, default);
- MVD_DM = 0 (no dead material effect), 1 (energy loss + multiple scattering, default), 2 (energy loss only), 3 (multiple scattering only).

Appendix B

Mathematical details

Details of the calculations, skipped in the previous sections, are reported here.

B.1 From vertex and momentum to helix parameters

Helix parameters can be obtained from the position of the vertex $V = (V_x, V_y, V_z)$, and momentum $\vec{P} = (P_x, P_y, P_z)$ of a particle.

Since the reference point is arbitrary, $(x_0, y_0) = (V_x, V_y)$ is chosen; the reference can be changed successively as reported in Section 7.3.1. The initial direction of the particle is given by the momentum in the production vertex:

$$a_1 = \text{ATAN2}(P_y, P_x), \tag{B.1}$$

$$a_5 = \cot\theta = \frac{P_z}{P_T}, \tag{B.2}$$

where $P_T = \sqrt{P_x^2 + P_y^2}$ is the transverse momentum. The radius of curvature is related to P_T by:

$$R = \frac{P_T}{0.003\ B_z} \tag{B.3}$$

(see Eq. 25.20, [85]); P_T has to be expressed in GeV and B_z in Tesla; the parameter a_2 (cm) is then

$$a_2 = \frac{Q}{R} = \frac{0.003\ Q\ B_z}{P_T}. \tag{B.4}$$

By definition, the distance of closest approach and the initial z coordinate are:

$$a_3 = 0, \tag{B.5}$$

$$a_4 = V_z. \tag{B.6}$$

B.2 From $\vec{a}$ to momentum

Transverse and total momenta can be derived from the helix parameters; from Equation (B.3),

$$P_T = 0.003\ R\ B_z = \frac{0.003\ B_z}{|a_2|} \tag{B.7}$$

and

$$P = \frac{P_T}{|\sin\theta|} = P_T\ \sqrt{1 + a_5^2}. \tag{B.8}$$

B.3 Details on parameter swimming

The change of reference point $(x_0, y_0) \to (x_0', y_0')$ changes the value of the parameters a_ν. The trajectory is indeed the same, but the parameterisation is different.

Equation (7.8) holds for both reference points, therefore

$$\begin{aligned}
\left(a_3' + \frac{1}{a_2'}\right)\sin a_1' &= -(x_0' - x_0) + \left(a_3 + \frac{1}{a_2}\right)\sin a_1, \\
\left(a_3' + \frac{1}{a_2'}\right)\cos a_1' &= \quad (y_0' - y_0) + \left(a_3 + \frac{1}{a_2}\right)\cos a_1.
\end{aligned}$$

and consequently

$$\begin{aligned}
\left|a_3' + \frac{1}{a_2'}\right|\sin a_1' &= \left|a_3 + \frac{1}{a_2}\right|\sin a_1 - Q(x_0' - x_0), \\
\left|a_3' + \frac{1}{a_2'}\right|\cos a_1' &= \left|a_3 + \frac{1}{a_2}\right|\cos a_1 + Q(y_0' - y_0).
\end{aligned}$$

By dividing everything by $\left|a_3 + \frac{1}{a_2}\right|$, sine and cosine of a_1' are obtained, from which the angle itself is derived:

$$a_1' = \mathrm{ATAN2}\left(\sin a_1 - \frac{x_0' - x_0}{a_3 + 1/a_2}, \cos a_1 + \frac{y_0' - y_0}{a_3 + 1/a_2}\right). \tag{B.9}$$

The curvature

$$a_2' = Q/R = a_2 \tag{B.10}$$

is unchanged by the swimming.

For a_3', (7.8) is used again

$$\begin{aligned}
a_3' \sin a_1' &= -(x_0' - x_0) + \left(a_3 + \frac{1}{a_2}\right)\sin a_1 - \frac{1}{a_2}\sin a_1', \\
a_3' \cos a_1' &= \quad (y_0' - y_0) + \left(a_3 + \frac{1}{a_2}\right)\cos a_1 - \frac{1}{a_2}\cos a_1'.
\end{aligned}$$

Then I multiply the first term by $\sin(a_1')$ and the second by $\cos(a_1')$ and I sum them up

$$\begin{aligned} a_3' &= -(x_0' - x_0)\sin a_1' + \left(a_3 + \frac{1}{a_2}\right)\sin a_1 \sin a_1' - \frac{1}{a_2}\sin^2 a_1' + \\ &+ (y_0' - y_0)\cos a_1' + \left(a_3 + \frac{1}{a_2}\right)\cos a_1 \cos a_1' - \frac{1}{a_2}\cos^2 a_1' = \\ &= -(x_0' - x_0)\sin a_1' + (y_0' - y_0)\cos a_1' + \left(a_3 + \frac{1}{a_2}\right)\cos(s' a_2) - \\ &- \frac{1}{a_2}. \end{aligned} \tag{B.11}$$

The pathlength from a_1 to the new angle a_1' is

$$s' = \frac{a_1 - a_1'}{a_2}; \tag{B.12}$$

from this I obtain

$$a_4' = a_4 + s' a_5 \tag{B.13}$$

Finally, the a_5 is untouched by the swimming:

$$a_5' = \cot\theta = a_5. \tag{B.14}$$

B.4 Intersection between a track and a layer

The layer is approximated by a cylinder of radius R_L (Fig. B.1); its equation is

$$x^2 + y^2 = R_L^2. \tag{B.15}$$

The equations of the particle trajectory,

$$x(\phi) = x_0 + \left(a_3 + \frac{1}{a_2}\right)\sin a_1 - \frac{\sin\phi}{a_2} \tag{B.16}$$

$$y(\phi) = y_0 - \left(a_3 + \frac{1}{a_2}\right)\cos a_1 + \frac{\cos\phi}{a_2} \tag{B.17}$$

in the hypothesis $\delta\phi = \phi - a_1 \ll 1$ (see Sect. 10.1.1), can be written

$$\begin{aligned} x(s) &= x_0 + a_3 \sin a_1 + \frac{1}{a_2}[\sin a_1 - (\sin a_1 + \cos a_1\ \delta\phi)] = \\ &= x_0 + a_3 \sin a_1 - \frac{\delta\phi}{a_2}\cos a_1 \end{aligned} \tag{B.18}$$

and

$$\begin{aligned} y(s) &= y_0 - a_3 \cos a_1 + \frac{1}{a_2}[(\cos a_1 - \sin a_1\ \delta\phi) - \cos a_1] = \\ &= y_0 - a_3 \cos a_1 - \frac{\delta\phi}{a_2}\sin a_1. \end{aligned} \tag{B.19}$$

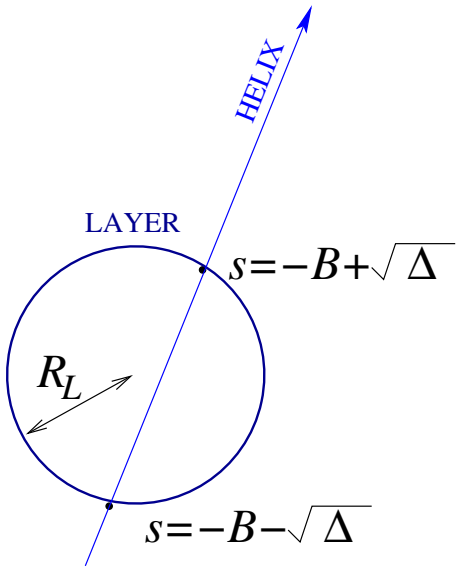

Figure B.1: Intersection between a particle helix and a layer. The curvature a_2 is neglected.

They can be expressed in terms of s by using $s = -(\phi - a_1)/a_2 = -\delta\phi/a_2$,

$$\begin{aligned} x(s) &= x_0 + a_3 \sin a_1 + s \cos a_1 \\ y(s) &= y_0 - a_3 \cos a_1 + s \sin a_1 \end{aligned} \tag{B.20}$$

The intersections between (B.15) and (B.20) are given by the formula

$$(x_0 + a_3 \sin a_1 + s \cos a_1)^2 + (y_0 - a_3 \cos a_1 + s \sin a_1)^2 = R_L^2. \tag{B.21}$$

This last equation can be written

$$\begin{aligned} s^2 + 2Bs + C &= 0 \\ B &= x_0 \cos a_1 + y_0 \sin a_1 \\ C &= x_0^2 + y_0^2 + a_3^2 - R_L^2 + 2a_3(x_0 \sin a_1 - y_0 \cos a_1) \end{aligned} \tag{B.22}$$

If $\Delta = B^2 - C \geq 0$ two solutions exist, but only the one with greater s is the correct one:

$$s_{int} = -B + \sqrt{\Delta}. \tag{B.23}$$

B.5 Intersection between a track and a ladder

A ladder of the BMVD is represented as a thick rectangle

$$\begin{aligned} x(\xi) &= x_{mvd} + \xi \ \cos\alpha \\ y(\xi) &= y_{mvd} + \xi \ \sin\alpha \end{aligned} \tag{B.24}$$

The intersections of the particle helix, Eq. B.20, with this rectangle are the solutions of

$$\begin{aligned} x_0 + \left(a_3 + \frac{1}{a_2}\right)\sin a_1 - \frac{\sin\phi}{a_2} &= x_{mvd} + \xi\ \cos\alpha \\ y_0 - \left(a_3 + \frac{1}{a_2}\right)\cos a_1 + \frac{\cos\phi}{a_2} &= y_{mvd} + \xi\ \sin\alpha \end{aligned} \tag{B.25}$$

The ξ coordinate can be obtained by getting $\sin(\phi)/a_2$ from the first of the relations, $\cos(\phi)/a_2$ from the second, and adding them up in quadrature. By doing that

$$\begin{aligned} \frac{1}{a_2^2} &= (x_0 - x_{mvd})^2 + \left(a_3 + \frac{1}{a_2}\right)^2 \sin^2 a_1 + \xi^2\cos^2\alpha + 2(x_0 - x_{mvd}) \\ &\times \left(a_3 + \frac{1}{a_2}\right)\sin a_1 - 2\xi(x_0 - x_{mvd})\cos\alpha - 2\xi\left(a_3 + \frac{1}{a_2}\right)\sin a_1 \\ &\times \cos\alpha + (y_0 - y_{mvd})^2 + \left(a_3 + \frac{1}{a_2}\right)^2\cos^2 a_1 + \xi^2\sin^2\alpha - \\ &- 2(y_0 - y_{mvd})\left(a_3 + \frac{1}{a_2}\right)\cos a_1 - 2\xi(y_0 - y_{mvd})\sin\alpha + \\ &+ 2\xi\left(a_3 + \frac{1}{a_2}\right)\cos a_1 \sin\alpha. \end{aligned} \tag{B.26}$$

Terms in ξ^2, ξ and ξ^0 are grouped together

$$\begin{aligned} &\xi^2 + 2\xi\left[\left(a_3 + \frac{1}{a_2}\right)(\sin\alpha\cos a_1 - \cos\alpha\sin a_1) + (x_{mvd} - x_0)\cos\alpha + \right. \\ &+ \left. (y_{mvd} - y_0)\sin\alpha\right] + \left\{\left(a_3 + \frac{1}{a_2}\right)^2 - \frac{1}{a_2^2} + (x_{mvd} - x_0)^2 + (y_{mvd} - y_0)^2 + \right. \\ &+ \left. 2\left(a_3 + \frac{1}{a_2}\right)[-(x_{mvd} - x_0)\sin a_1 + (y_{mvd} - y_0)\cos a_1]\right\}, \end{aligned} \tag{B.27}$$

from which

$$\begin{aligned} B &= \left(a_3 + \frac{1}{a_2}\right)\sin(\alpha - a_1) + (x_{mvd} - x_0)\cos\alpha + \\ &+ (y_{mvd} - y_0)\sin\alpha, \end{aligned} \tag{B.28}$$

$$\begin{aligned} C &= \left(a_3 + \frac{1}{a_2}\right)^2 - \left(\frac{1}{a_2}\right)^2 + 2\left(a_3 + \frac{1}{a_2}\right)[(y_{mvd} - y_0)\cos a_1 - \\ &- (x_{mvd} - x_0)\sin a_1] + (x_{mvd} - x_0)^2 + (y_{mvd} - y_0)^2, \end{aligned} \tag{B.29}$$

$$\xi_{int} = -B \pm \sqrt{B^2 - C}. \tag{B.30}$$

Sine and cosine of ϕ_{int} are extracted from (B.25):

$$\begin{aligned} \frac{\sin\phi_{int}}{a_2} &= -(x_{mvd}-x_0)+\left(a_3+\frac{1}{a_2}\right)\sin a_1-\xi_{int}\cos\alpha, \\ \frac{\cos\phi_{int}}{a_2} &= (y_{mvd}-y_0)-\left(a_3+\frac{1}{a_2}\right)\cos a_1+\xi_{int}\sin\alpha. \end{aligned} \tag{B.31}$$

and the ϕ_{int} is obtained from there:

$$\begin{aligned} \phi_{int} = \mathrm{ATAN2}\Bigg\{ & Q\left[\left(a_3+\frac{1}{a_2}\right)\sin a_1-(x_{mvd}-x_0)-\xi_{int}\cos\alpha\right], \\ & Q\left[-\left(a_3+\frac{1}{a_2}\right)\cos a_1+(y_{mvd}-y_0)+\xi_{int}\sin\alpha\right]\Bigg\}. \end{aligned} \tag{B.32}$$

Derivatives of $\xi(a_\nu)$ and $z(a_\nu)$

The equations of the helix, (B.16) and (B.17), can be expressed in terms of the pathlength as:

$$x(s) = x_0+\left(a_3+\frac{1}{a_2}\right)\sin a_1-\frac{\sin(a_1-s\ a_2)}{a_2}, \tag{B.33}$$

$$y(s) = y_0-\left(a_3+\frac{1}{a_2}\right)\cos a_1+\frac{\cos(a_1-s\ a_2)}{a_2}. \tag{B.34}$$

In the point of intersection, also (B.24) are valid; from this equivalence it can be derived:

$$\begin{aligned} \xi_{int}\cos\alpha &= x_0-x_{mvd}+\left(a_3+\frac{1}{a_2}\right)\sin a_1-\frac{\sin(a_1-s_{int}\ a_2)}{a_2} \\ \xi_{int}\sin\alpha &= y_0-y_{mvd}-\left(a_3+\frac{1}{a_2}\right)\cos a_1+\frac{\cos(a_1-s_{int}\ a_2)}{a_2} \end{aligned} \tag{B.35}$$

Assuming the uncertainty on s_{int} to be negligible, the derivatives of ξ_{int} with respect to the various a_ν are:

$$\begin{aligned} \cos\alpha\left(\frac{\partial\xi}{\partial a_1}\right)_{int} &= \left(a_3+\frac{1}{a_2}\right)\cos a_1-\frac{\cos\phi_{int}}{a_2}, \\ \cos\alpha\left(\frac{\partial\xi}{\partial a_2}\right)_{int} &= \frac{\sin\phi_{int}-\cos a_1}{a_2^2}+s_{int}\frac{\cos\phi_{int}}{a_2}, \\ \cos\alpha\left(\frac{\partial\xi}{\partial a_3}\right)_{int} &= \sin a_1. \end{aligned} \tag{B.36}$$

Another way to express the derivatives is

$$\begin{aligned}
\sin\alpha \left(\frac{\partial\xi}{\partial a_1}\right)_{int} &= \left(a_3 + \frac{1}{a_2}\right)\sin a_1 - \frac{\sin\phi_{int}}{a_2}, \\
\sin\alpha \left(\frac{\partial\xi}{\partial a_2}\right)_{int} &= \frac{\cos a_1 - \cos\phi_{int}}{a_2^2} + s_{int}\frac{\sin\phi_{int}}{a_2}, \\
\sin\alpha \left(\frac{\partial\xi}{\partial a_3}\right)_{int} &= -\cos a_1.
\end{aligned} \tag{B.37}$$

The other derivatives are

$$\begin{aligned}
\left(\frac{\partial\xi}{\partial a_4}\right) &= \left(\frac{\partial\xi}{\partial a_5}\right) = 0 \\
\left(\frac{\partial z}{\partial a_1}\right) &= \left(\frac{\partial z}{\partial a_2}\right) = \left(\frac{\partial z}{\partial a_3}\right) = 0 \\
\left(\frac{\partial z}{\partial a_4}\right) &= 1 \\
\left(\frac{\partial z}{\partial a_5}\right)_{int} &= s_{int}
\end{aligned} \tag{B.38}$$

B.6 Intersection between a track and the support tube

The support tube is a cylinder with radius R_S. The (B.22) and (B.23) are still valid here (with the substitution $R_L \to R_S$). The angular coefficient of the tangent to the tube in the point of intersection is

$$\tan\alpha = \frac{x(s_{int})}{-y(s_{int})} \tag{B.39}$$

where $x(s_{int})$ and $y(s_{int})$ come from (B.20).

B.7 Intersection between a track and the beam pipe

The xy cross section of the beam pipe has approximately the shape of an ellipse in the barrel region (Fig. 8.5):

$$\begin{aligned}
x(\gamma) &= x_E + a\cos\gamma \\
y(\gamma) &= b\sin\gamma
\end{aligned} \tag{B.40}$$

The particle trajectory is described by (B.20), so that the intersection is

$$\begin{aligned}
x_E + a\cos\gamma &= x_0 + a_3\sin a_1 + s\cos a_1 \\
b\sin\gamma &= y_0 - a_3\cos a_1 + s\sin a_1
\end{aligned} \tag{B.41}$$

Let me define $x'_0 = (x_0 + a_3 \sin a_1)$ and $y'_0 = (y_0 - a_3 \cos a_1)$, therefore

$$\begin{aligned} \cos\gamma &= \frac{x'_0 - x_E + s\cos a_1}{a} \\ \sin\gamma &= \frac{y'_0 + s\sin a_1}{b} \end{aligned} \tag{B.42}$$

The problem can be solved by squaring and adding up the two equations:

$$As^2 + 2Bs + C = 0, \tag{B.43}$$

where the parameters A, B and C are:

$$\begin{aligned} A &= \frac{\cos^2 a_1}{a^2} + \frac{\sin^2 a_1}{b^2}, \\ B &= \frac{(x'_0 - x_E)\cos a_1}{a^2} + \frac{y'_0 \sin a_1}{b^2}, \\ C &= \frac{(x'_0 - x_E)^2}{a^2} + \frac{{y'_0}^2}{b^2} - 1. \end{aligned} \tag{B.44}$$

If $\Delta = B^2 - AC \geq 0$ the solution exists:

$$s_{int} = \frac{-B + \sqrt{\Delta}}{A}. \tag{B.45}$$

The tangent to the beam pipe in the point of intersection is

$$\tan\alpha = \frac{y'(\gamma_{int})}{x'(\gamma_{int})} = \frac{b\cos\gamma_{int}}{-a\sin\gamma_{int}} = -\left(\frac{b}{a}\right)^2 \frac{x(s_{int}) - x_E}{y(s_{int})}. \tag{B.46}$$

B.8 Matrix inversion

The determinant of a 2×2 symmetric matrix A

$$A = \begin{pmatrix} A_{11} & A_{12} \\ A_{12} & A_{22} \end{pmatrix}$$

is

$$\det(A) = A_{11}\ A_{22} - A_{12}^2 \tag{B.47}$$

from which the inverse matrix is obtained:

$$A^{-1} = \frac{1}{\det(A)} \begin{pmatrix} A_{22} & -A_{12} \\ -A_{12} & A_{11} \end{pmatrix}. \tag{B.48}$$

The determinant of a 3×3 symmetric matrix B

$$B = \begin{pmatrix} B_{11} & B_{12} & B_{13} \\ B_{12} & B_{22} & B_{23} \\ B_{13} & B_{23} & B_{33} \end{pmatrix}$$

is

$$\begin{aligned} \det(B) &= B_{11}(B_{22}B_{33} - B_{23}^2) - B_{12}(B_{12}B_{33} - B_{13}B_{23}) + \\ &+ B_{13}(B_{12}B_{23} - B_{13}B_{22}) \end{aligned} \tag{B.49}$$

from which the inverse matrix is obtained:

$$B^{-1} = \frac{1}{\det(B)} \begin{pmatrix} B_{22}B_{33} - B_{23}^2 & B_{12}B_{23} - B_{12}B_{33} & B_{12}B_{23} - B_{13}B_{22} \\ B_{12}B_{23} - B_{12}B_{33} & B_{11}B_{33} - B_{13}^2 & B_{13}B_{12} - B_{11}B_{23} \\ B_{12}B_{23} - B_{13}B_{22} & B_{13}B_{12} - B_{11}B_{23} & B_{11}B_{22} - B_{12}^2 \end{pmatrix}.$$

The inversion of 5×5 matrices is performed by using the routine TRSINV from the CERNLIB [87] FORTRAN library.

B.9 Packing of symmetric matrices

Any 5×5 symmetric matrix can be expressed by using 15 components only. In VCTRAK and in CERNLIB two different packing standards are used. Let me name $U(5,5)$ the symmetric matrix, while $V(15)$ and $C(15)$ are the packed matrices (VCTRAK and CERNLIB standard, respectively). The matrix U is expressed in terms of V and C as

$$\begin{aligned} U &= \begin{pmatrix} V(1) & V(2) & V(3) & V(4) & V(5) \\ V(2) & V(6) & V(7) & V(8) & V(9) \\ V(3) & V(7) & V(10) & V(11) & V(12) \\ V(4) & V(8) & V(11) & V(13) & V(14) \\ V(5) & V(9) & V(12) & V(14) & V(15) \end{pmatrix} = \\ &= \begin{pmatrix} C(1) & C(2) & C(4) & C(7) & C(11) \\ C(2) & C(3) & C(5) & C(8) & C(12) \\ C(4) & C(5) & C(6) & C(9) & C(13) \\ C(7) & C(8) & C(9) & C(10) & C(14) \\ C(11) & C(12) & C(13) & C(14) & C(15) \end{pmatrix} \end{aligned} \tag{B.50}$$

The conversion between the two standards is

$$\begin{aligned} C &= \big(V(1), V(2), V(6), V(3), V(7), V(10), V(4), V(8), V(11), V(13), \\ &\quad V(5), V(9), V(12), V(14), V(15)\big) \end{aligned} \tag{B.51}$$

$$\begin{aligned} V &= \big(C(1), C(2), C(4), C(7), C(11), C(3), C(5), C(8), C(12), C(6), \\ &\quad C(9), C(13), C(10), C(14), C(15)\big) \end{aligned} \tag{B.52}$$

Conclusions

The production of di–electrons and di–muons has been studied analysing the collisions collected by the ZEUS detector at HERA in the 1996–2000 period. All the usable luminosity, 121.30 pb^{-1} for the multi–electron search, 101.47 pb^{-1} for the di–muons, has been made use of. The prominent contribution to the process is expected to come from the production of a photon pair and its consequent conversion in a lepton–antilepton pair. Being this a QED process, the Standard Model expectation is very well predictable. The study has shown a nice agreement in all the multi–lepton variables and in all the subsamples. The excess observed by H1 in the number of $2e$ and $3e$ events at high mass ($M_{12} > 100$ GeV), see Section 1.6, is not confirmed by this analysis.

The di–electron cross section has been measured at a centre–of–mass energy $\sqrt{s} = 318$ GeV, in the phase space defined by:

- two electrons in $17° < \theta_e < 164°$,
- $E_T^{e1} > 10$ GeV and $E_T^{e2} > 5$ GeV,
- $M_{12} > 5$ GeV,
- $E - P_z < 45$ GeV.

The measured value is:

$$\sigma(e^+p \to e^+e^+e^-X) = 1.62 \pm 0.23^{+0.21}_{-0.16} \text{ pb}$$

(the first uncertainty is the statistical, the second one is the systematic), which is in good agreement with the Standard Model expectation:

$$\sigma_{\text{SM}} = 1.66 \text{ pb}.$$

The differential cross sections

$$\frac{\text{d}\sigma}{\text{d}M_{12}}, \frac{\text{d}\sigma}{\text{d}P_T^e}, \frac{\text{d}\sigma}{\text{d}\theta_e},$$

have been measured and found in agreement with the SM predictions.

The di–muon cross section has been measured at a centre–of–mass energy $\sqrt{s} = 318$ GeV, in the phase space defined by:

- two muons,
- $P_T^\mu > 5$ GeV,
- $15^\circ < \theta_\mu < 164^\circ$,
- $M_{\mu\mu} > 5$ GeV.

The measured value is:

$$\sigma(e^+p \to e^+\mu^+\mu^- X) = 4.79 \pm 0.33^{+0.35}_{-0.32} \text{ pb}$$

(the first uncertainty is the statistical, the second one is the systematic), which is in agreement with the Standard Model expectation:

$$\sigma_{\text{SM}} = 5.32 \text{ pb}.$$

The differential cross sections

$$\frac{\mathrm{d}\sigma}{\mathrm{d}M_{\mu\mu}}, \frac{\mathrm{d}\sigma}{\mathrm{d}P_T^\mu}, \frac{\mathrm{d}\sigma}{\mathrm{d}\theta_\mu},$$

have been measured and found in agreement with the SM predictions.

This work represents an extension of the results presented by the collaboration at the ICHEP 2002 conference, and will be the basis for the future publication of ZEUS on the di–muon and di–electron production.

In the second part of the thesis, the development of a third level trigger algorithm for the tracking in the newly installed ZEUS Micro–Vertex Detector has been described. This algorithm has been tested offline giving excellent results in terms of speed in execution and in the improvement of the tracking. When run on real data, it uses in average 20–25% of the time used for the tracking in the central chamber. On a sample of single muons, the uncertainty on the impact parameter goes down from 650 μm (using the central tracker only) to 300 μm in the xy plane, whereas goes down from 3.2 mm to 0.26 mm in z. In the very next months the algorithm will be tested in the online data processing.

References

[1] M. Gell-Mann, Phys. Lett. **8**, 214 (1964).

[2] Particle Data Group, K. Hagiwara et al., Phys. Rev. **D 66**, 010001 (2002).

[3] F. Halzen and A.D. Martin, *Quarks and Leptons: An Introductory Course in Modern Particle Physics*. John Wiley & Sons, Inc, 1984.

[4] C.G. Callan and D.J. Gross, Phys. Rev. Lett. **22**, 156 (1969).

[5] J.I. Friedman and H.W. Kendall, Annual Review of Nuclear Science **22**, 203 (1972).

[6] ZEUS Coll., S. Chekanov et al., Eur. Phys. J. **C 21**, 443 (2001).

[7] R.K. Ellis, W.J. Stirling and B.R. Webber, *QCD and Collider Physics*, Cambridge Monographs on Particle Physics, Nuclear Physics and Cosmology, Vol. 8. Cambridge University Press, 1996.

[8] V.N. Gribov and L.N. Lipatov, Sov. J. Nucl. Phys. **15**, 438 (1972);
L.N. Lipatov, Sov. J. Nucl. Phys. **20**, 94 (1975);
G. Altarelli and G. Parisi, Nucl. Phys. **B 126**, 298 (1977);
Yu.L. Dokshitzer, Sov. Phys. JETP **46**, 641 (1977).

[9] V.S. Fadin, E.A. Kuraev and L.N. Lipatov, Phys. Lett. **B 60**, 50 (1975).

[10] E.A. Kuraev, L.N. Lipatov and V.S. Fadin, Sov. Phys. JETP **44**, 443 (1976).

[11] E.A. Kuraev, L.N. Lipatov and V.S. Fadin, Sov. Phys. JETP **45**, 199 (1977).

[12] Ya.Ya. Balitskiĭ and L.N. Lipatov, Sov. J. Nucl. Phys. **28**, 822 (1978).

[13] M. Ciafaloni, Nucl. Phys. **B 296**, 49 (1988).

[14] S. Catani, F. Fiorani and G. Marchesini, Phys. Lett. **B 234**, 339 (1990).

[15] S. Catani, F. Fiorani and G. Marchesini, Nucl. Phys. **B 336**, 18 (1990).

[16] H1 Coll., C. Adloff et al., Eur. Phys. J. **C 19**, 269 (2001).

[17] H1 Coll., C. Adloff et al., Z. Phys. **C 74**, 191 (1997).

[18] ZEUS Coll., J. Breitweg et al., Z. Phys. **C 74**, 207 (1997).

[19] H1 Coll., V. Andreev et al., Phys. Lett. **B 561**, 241 (2003).

[20] H1 Coll., A. Aktas et al., Preprint hep-ex/0307015, 2003.

[21] H. Bethe and W. Heitler, Proc. Roy. Soc. Lond. **A 146**, 83 (1934).

[22] L.D. Landau and E. Lifshitz, Physikalische Zeitschrift der Sowjetunion **6**, 244 (1934).

[23] G. Barbiellini et al., Phys. Rev. Lett. **32**, 385 (1974).

[24] N. Arteaga-Romero, C. Carimalo and P. Kessler, Z. Phys. **C 52**, 289 (1991).

[25] P. Kessler, Nuovo Cimento **17**, 809 (1960);
P. Kessler, Acta Physica Austriaca **41**, 141 (1975).

[26] D. Hoffmann and L. Favart, *Lepton pair Monte Carlo generators for HERA physics*. Monte Carlo Workshop for HERA Physics, DESY - Hamburg 1998/1999, 1999, available on `http://www.desy.de/~heramc/proceedings/wg70/lpp.ps.gz`. Appears in DESY-PROC-1999-02.

[27] U. Baur, J.A.M. Vermaseren and D. Zeppenfeld, Nucl. Phys. **B 375**, 3 (1992).

[28] B. Dutta and R.N. Mohapatra, Phys. Rev. **D 59**, 015018 (1999).

[29] E. Accomando and S. Petrarca, Phys. Lett. **B 323**, 212 (1994).

[30] E. Accomando, M. Iori and M. Mattioli, Preprint hep-ph/9505274, 1995.

[31] L. Willmann et al., Phys. Rev. Lett. **82**, 49 (1999).

[32] OPAL Coll., G. Abbiendi et al., Phys. Lett. **B 526**, 221 (2002).

[33] C. Diaconu for H1 and ZEUS Collaborations, *Amsterdam 2002, ICHEP*, S. Bentvelsen et al. (ed.), pp. 224–227. North-Holland (2003). Also in preprint hep-ex/0210017.

[34] ZEUS Coll., U. Holm (ed.), *The ZEUS Detector*. Status Report (unpublished), DESY (1993), available on `http://www-zeus.desy.de/bluebook/bluebook.html`.

[35] G.A. Voss and B.H. Wiik, Ann. Rev. Nucl. Part. Sci. **44**, 413 (1994).

[36] *Future Physics at HERA Volumes I and II*, ed. G. Ingelman, A. De Roeck, R. Klanner, 1996.

[37] M. Seidel, *The Upgraded Interaction Regions of HERA* (unpublished). DESY-HERA-00-01.

[38] N. Harnew et al., Nucl. Inst. Meth. **A 279**, 290 (1989);
B. Foster et al., Nucl. Phys. Proc. Suppl. **B 32**, 181 (1993);
B. Foster et al., Nucl. Inst. Meth. **A 338**, 254 (1994).

[39] M. Derrick et al., Nucl. Inst. Meth. **A 309**, 77 (1991);
A. Andresen et al., Nucl. Inst. Meth. **A 309**, 101 (1991);
A. Caldwell et al., Nucl. Inst. Meth. **A 321**, 356 (1992);
A. Bernstein et al., Nucl. Inst. Meth. **A 336**, 23 (1993).

[40] E. Iarocci, Nucl. Inst. Meth. **217**, 30 (1983).

[41] G. Abbiendi et al., Nucl. Inst. Meth. **A 333**, 342 (1993).

[42] H. Bethe and W. Heitler, Proc. Roy. Soc. Lond. **A146**, 83 (1934).

[43] H. A. Bethe, Phys. Rev. **89**, 1256 (1953).

[44] ZEUS Coll., R. Carlin et al., Nucl. Inst. Meth. **A 379**, 542 (1996).

[45] F. Chlebana, *Description of the ZEUS Global Second Level Trigger in 1994* (unpublished), 1994, available on `http://www-zeus.desy.de/ZEUS_ONLY/zeus_notes/ZEUS_NOTES/ZEUS-94-102.ps`. ZEUS-94-102.

[46] INMOS Limited, *Transputer Reference Manual*. Prentice Hall, 1988.

[47] A. Garfagnini, Nucl. Inst. Meth. **A 435**, 34 (1999).

[48] D. Dannheim et al., Nucl. Inst. Meth. **A 505**, 663 (2003).

[49] ZEUS Coll., *A microvertex Detector for ZEUS* (unpublished), 1997, available on `http://www-zeus.desy.de/ZEUS_ONLY/zeus_notes/ZEUS_NOTES/ZEUS-97-006.ps`. ZEUS-97-006, DESY-PRC 97/01.

[50] U. Kotz et al., Nucl. Inst. Meth. **A 235**, 481 (1985).

[51] M. Feuerstack-Raible, Nucl. Inst. Meth. **A 447**, 35 (2000).

[52] J.P. Collins, D.E. Soper and G. Sterman, Nucl. Phys. **B 308**, 833 (1988).

[53] G. Marchesini et al., Comp. Phys. Comm. **67**, 465 (1992).

[54] T. Sjöstrand et al., Comp. Phys. Comm. **135**, 238 (2001).

[55] T. Abe, Comp. Phys. Comm. **136**, 126 (2001).

[56] T. Ishikawa et al., Preprint KEK-92-19, 1993.

[57] F.W. Brasse et al., Nucl. Phys. **B 110**, 413 (1976).

[58] H. Abramowicz and A. Levy, Preprint DESY-97-251 (hep-ph/9712415), DESY, 1997.

[59] A. Mücke et al., Comp. Phys. Comm. **124**, 290 (2000).

[60] H. Plothow-Besch, Comp. Phys. Comm. **75**, 396 (1993).

[61] J. Fujimoto et al., Prog. Theor. Phys. Suppl. **100**, 1 (1990).

[62] S.P. Baranov et al., *Proc. Workshop on Physics at HERA*, W. Buchmüller and G. Ingelman (eds.), Vol. 3, p. 1478. DESY, Hamburg, Germany (1991).

[63] A. Suri and D.R. Yennie, Ann. Phys. **72**, 243 (1972).

[64] H. Spiesberger, HERACLES *and* DJANGOH*: Event Generation for ep Interactions at HERA Including Radiative Processes*, 1998, available on `http://www.desy.de/~hspiesb/djangoh.html`.

[65] A. Kwiatkowski, H. Spiesberger and H.-J. Möhring, Comp. Phys. Comm. **69**, 155 (1992). Also in *Proc. Workshop Physics at HERA*, 1991, DESY, Hamburg.

[66] G. Ingelman, A. Edin and J. Rathsman, Comp. Phys. Comm. **101**, 108 (1997).

[67] T. Sjöstrand, Comp. Phys. Comm. **82**, 74 (1994).

[68] R. Brun et al., GEANT3, Technical Report CERN-DD/EE/84-1, CERN, 1987.

[69] S.M. Fisher and P. Palazzi, *ADAMO Programmers Manual – Version 3.2.* CERN ECP and RAL, available on `http://adamo.web.cern.ch/Adamo/programmers_manual/TOC_of_adamo.html`.

[70] A. López-Durán Viani and S. Schlenstedt, *Electron Finder Efficiencies and Impurities. A Comparison Between SINISTRA95, EM and EMNET* (unpublished). ZEUS-99-077, internal ZEUS note, 1999.

[71] G. Abbiendi et al., *Observation of J/psi* $\rightarrow \mu^+\mu^-$ *in the first 275* nb^{-1} *of 1993 run* (unpublished), 1993, available on `http://www-zeus.desy.de/ZEUS_ONLY/zeus_notes/ZEUS_NOTES/ZEUS-93-120.ps`. ZEUS-NOTE-93-120.

[72] L. Wai, *A muon separator* (unpublished). ZEUS-93-12, 1993.

[73] S. Limentani, M. Posocco and L. Stanco, *Muon Barrel Reconstruction* (unpublished), 1992, available on http://www-zeus.desy.de/ZEUS_ONLY/zeus_notes/ZEUS_NOTES/ZEUS-92-027.pdf. ZEUS-92-027.

[74] M. Corradi, *MPMATCH2 Web Page*, available on http://www-zeus.desy.de/∼corradi/ZEUS_ONLY/mpmatch/mpmatch2.html.

[75] L. Bellagamba, *MVMATCH: A package to match FMUON tracks with Central Detectors* (unpublished), 1996, available on http://www-zeus.desy.de/ZEUS_ONLY/zeus_notes/ZEUS_NOTES/ZEUS-96-051.ps. ZEUS-96-051.

[76] V. Innocente, M. Maire and E. Nagy, *MC91: Detector and event simulation in high energy physics*, pp. 58–78. Amsterdam (1991).

[77] R. Frühwirth, Nucl. Inst. Meth. **A 262**, 444 (1987).

[78] J. Repond, *Jet Energy Corrections* (unpublished). ZEUS Note96-104.

[79] G.M. Briskin, *Diffractive Dissociation in ep Deep Inelastic Scattering.* Ph.D. Thesis, Tel Aviv University, 1998. (Unpublished).

[80] F. Jacquet and A. Blondel, *Proceedings of the Study for an ep Facility for Europe*, U. Amaldi (ed.), p. 391. Hamburg, Germany (1979). Also in preprint DESY 79/48.

[81] N. Tuning, *ZUFOs: Hadronic Final State Reconstruction with Calorimeter, Tracking and Backsplash Correction* (unpublished). ZEUS-Note-01-021, 2001.

[82] M. Turcato, *Open beauty photoproduction at HERA.* Ph.D. Thesis, Università di Padova, 2002.

[83] G. Bruni, *Muons And Mips MAtcher.* DESY, available on http://www-zeus.desy.de/~zeusbo/ZEUS_ONLY/private/offline/mfmamma.html.

[84] G. F. Hartner, *VCTRAK Briefing: Program and Math* (unpublished). Zeus-98-058, internal ZEUS-note, 1998.

[85] Particle Data Group, C. Caso et al., Eur. Phys. J. **C3**, 1 (1998).

[86] R.M. Sternheimer, M.J. Berger and S.M. Seltzer, At. Data Nucl. Data Tables **30**, 261 (1984).

[87] CERN, *CERNLIB documentation*, available on http://wwwasdoc.web.cern.ch/wwwasdoc/.

List of Figures

List of Tables

Acknowledgments

I would like to first thank all the people involved in the work I have presented in the previous pages. It's likely that someone will be forgotten: I beg their pardon since now.

For the di–lepton analysis, I have to mention the coordinators of the "Exotics and Rare Phenomena" Physics group at ZEUS, Elisabetta Gallo and Katarzyna Klimek, who gave me important directions during the analysis work. Of course I have also to thank Alessandro Bertolin and Riccardo Brugnera from Padova University, who were of fundamental importance to understand the functioning of the B/RMUON detector and how to use it in a physical analysis. Massimo Corradi and Davide Boscherini contributed by revealing me the secrets of the FMUON detector.

Several people were involved as well in the development of the VCMVD software. I would like to mention the coordinator of the "MVD Offline" group, Tobias Haas. A special thank goes to Gerd Hartner, the author of the VCTRAK package: the birth of the VCMVD was possible because of his notes and hints. Erik Maddox from NIKHEF, who developed the offline tracking package for the MVD, and Alessandro Polini from Bologna University also gave me some useful information. For the implementation in the trigger software I have to thank all the trigger team: Adrian Mirea, Mara Soares, Nichol Brummer.

My most felt gratitude is for my supervisor, Luca Stanco, for having followed me in three years of Ph.D.

Now I move to thank people not (directly) involved in my thesis:

- Prof. Silvia Limentani, for the experience she puts at our service;
- Stefano Dusini who worked with me, here in Padova, in the first months of my Ph.D. and taught me various helpful things;
- Roberto Carlin, now Deputy Spokesman of ZEUS collaboration, who knows so well the B/RMUON hardware and was a reference point during my shifts;
- Giuseppe Barbagli, my supervisor when I was in Florence, who furnished me a lot of good music and shared with me nights of work and amusement;
- Enrico (Borsato) and Flavio, for the dinners we shared in Hamburg and the help in the work;
- all my present and past office–mates: Andrea (Longhin), Alvise, Fulvio, Marcello, Moreno, Federico, Enrico (Feltresi), Enrico (Carrara), Melisa, Roberto (Righetto), Daniele, Paolo, Antonio, Laura;
- Silvia and Anna, my apartment–mates;
- the Italian friends in DESY: Alessandro (Montanari), Vincenzo, Nicola, Devis, Luigi.

A special thank goes to my parents and my sister for supporting me even if, in this last times, we met too rarely.

A very special thank is devoted to Monica, who worked with me in the first stages of VCMVD, discussed with me several aspects of the di–lepton analysis, helped me during BMUON shifts, shared the same office in Padova and Hamburg. But more than all I thank her for having shared with me two years of her life. I hope it is just the beginning.

“Non senza fatiga si giunge al fine”

Girolamo Frescobaldi,
toccata No. IX from “Secondo Libro di Toccate” (1627)